



COPYRIGHT AND CITATION CONSIDERATIONS FOR THIS THESIS/ DISSERTATION



- Attribution — You must give appropriate credit, provide a link to the license, and indicate if changes were made. You may do so in any reasonable manner, but not in any way that suggests the licensor endorses you or your use.
- NonCommercial — You may not use the material for commercial purposes.
- ShareAlike — If you remix, transform, or build upon the material, you must distribute your contributions under the same license as the original.

How to cite this thesis

Surname, Initial(s). (2012). Title of the thesis or dissertation (Doctoral Thesis / Master's Dissertation). Johannesburg: University of Johannesburg. Available from: <http://hdl.handle.net/102000/0002> (Accessed: 22 August 2017).

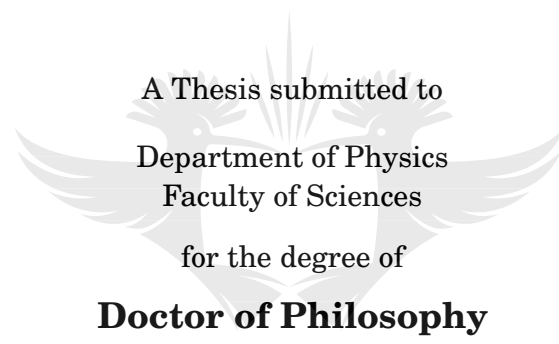
Gamma-ray bursts as probes of cosmological parameters at high redshifts

Author:

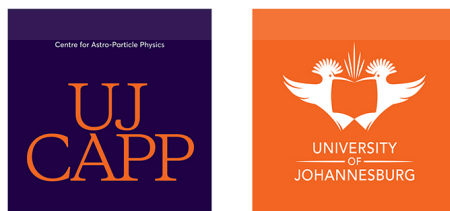
Feraol Fana Dirirsa

Supervisor:

Prof. Soebur Razzaque



UNIVERSITY
OF
JOHANNESBURG



Centre for Astro-Particle Physics (CAPP)
University of Johannesburg
Johannesburg
South Africa

2018

CERTIFICATE

This is to certify that the thesis entitled "Gamma-ray bursts as probes of cosmological parameters at high redshifts" submitted by Feraol Fana Dirirsa for the award of the degree of Doctor of Philosophy of University of Johannesburg is his original work. This has not been published or submitted to any other University for any other Degrees or Diploma.



Prof. Soebur Razzaque
Thesis Supervisor and Director (CAPP)

Dr. Emanuela Carleschi
Head of Department (Physics)

UNIVERSITY
OF
JOHANNESBURG

Centre for Astro-Particle Physics, and Department of Physics
University of Johannesburg
PO Box 524 - Auckland Park 2006
Johannesburg
South Africa

DECLARATION

I, Feraol Fana Dirirsa, declare that the work reported in this thesis entitled “Gamma-ray bursts as probes of cosmological parameters at high redshifts”, is entirely original. This thesis was composed independently by me, based on the research carried out under the supervision of Prof. Soebur Razzaque in the Department of Physics at the University of Johannesburg. I further declare that the work enclosed in this thesis is my own contribution and where other's ideas or words have been included, I have adequately cited and referenced the original sources.

Signed: _____

Date: 16 November 2018

UNIVERSITY
OF
JOHANNESBURG

ABSTRACT

Gamma-ray bursts are powerful astronomical transient events emitting large energy in γ -rays within a short period of time. Their emission dominates in the keV–MeV range. High luminosity with values up to 10^{54} erg s $^{-1}$ and huge isotropic energy release in the prompt emission phase can make gamma-ray bursts (GRBs) detectable up to a high redshift, $z \sim 9.4$. If emission from GRBs can be standardized, like Supernovae (SNe) Type Ia and which have been observed only up to a redshift of $z < 2$, they have the potential to be used as cosmological probes and help us to understand the nature of dark-energy when the universe was much younger than today. With GRBs as standard candles, we can extend our understanding of the universe's mysterious expansion over cosmic time.

The main aim of this thesis is to explore radiation characteristics from GRBs and utilize them to use GRBs as cosmological standard candles, similar to SNe Type Ia. The standardization of GRBs rests on phenomenological correlations between the spectral properties and energetics, of which one strongly relies on the cosmological model. The fascinating correlation between isotropically radiated energy with the intrinsic peak energy of the νF_ν spectrum in the cosmological source frame can be traced back to the Amati relation. In 2004, Yonetoku proposed another correlation between the isotropic peak luminosity and intrinsic peak energy (so-called Yonetoku relation). Besides, over the past sixteen years, many scholars have anticipated studying other correlations of GRB observables. The studied correlations were not tight enough to be used independently to construct the extended GRB Hubble diagram and constrain the cosmological parameters using the parameters obtained from the observational data of SNe Type Ia or cosmic microwave background. In spite of that, using the phenomenological correlations of the combined sample of GRBs detected by different telescopes and also by combining with the SNe Type Ia data, we can construct the extended GRB Hubble diagram that can be used to constrain cosmological parameters at high redshift.

In this thesis work, we use high-quality samples of long GRBs to study the Yonetoku relation. These samples were collected from the *Fermi* Gamma-ray Burst Monitor (GBM) and *Swift*-Burst Alert Telescope (BAT) until the end of December 2017, whose spectroscopic or photometric redshifts were measured. These GRBs also have well-defined spectra to use for correlation study. In both samples, we have found a strong partial correlation between the peak luminosity and intrinsic peak energy. Using the slope and normalization obtained from the Yonetoku correlation, we estimated the cosmological parameters of the Hubble constant (H_0) and dark-energy density

(Ω_Λ) , first, for the samples of GRBs alone and then together with the latest union SNe Ia data. The obtained values of H_0 and Ω_Λ for the best-fit spectral model of the present GBM and BAT samples of GRBs combining with the latest SNe Type Ia data provide $H_0 = 69.908^{+0.533}_{-0.517} \text{ km s}^{-1} \text{ Mpc}^{-1}$ and $\Omega_\Lambda = 0.715^{+0.027}_{-0.030}$ in 1σ confidence intervals. The obtained result in 1σ confidence level is consistent with the currently acceptable ranges of H_0 and Ω_Λ but the errors on parameters are rather large that arise due to the large extrinsic systematics scattering associated to the simulated sample. The Hubble diagram was also plotted using these best-fit values, obtained from both the GRB and SNe data. The obtained result has shown a substantial refinement in the robustness of the Yonetoku relation.

We have also studied the Amati relation by performing spectral analysis of 26 GRBs with measured redshift that have been detected by the *Fermi*-Large Area Telescope (LAT) during its nine years of operations from July 2008 to September 2017, thus extending the computation of isotropically radiated energy in the 100 MeV range. We found that multiple components are required to fit the spectra of a number of GRBs. The Amati relation is satisfied by the 25 long GRBs, with fitting parameters similar to previous studies that used data from different satellite instruments, while the only short GRB 090510 detected by LAT with known redshift is an outlier. However, there is large scatter in fit parameters, dominated by unknown extrinsic systematics, that may be due to the hidden parameters related to the physical origin of the Amati relation. We have also performed fits to the Amati relation using the *Fermi* data together with another sample of 94 GRBs (W2016) to explore the redshift dependence. Using the Amati relation we extend the Hubble diagram and constrain the Hubble constant and dark-energy density in the flat Λ CDM cosmological model. These exercises are done with the sample of GRBs alone and with the latest SNe Type Ia data. For the combined GRB samples (*Fermi* and W2016) with the Type Ia data, we obtained good fit to the cosmological parameters of $H_0 = 69.95^{+0.54}_{-0.45} \text{ km s}^{-1} \text{ Mpc}^{-1}$ and $\Omega_\Lambda = 0.72 \pm 0.03$. We have also fitted cosmological parameters using GRBs with $z > 1.414$ and SNe U2.1 sample obtaining $H_0 = 70.03^{+0.48}_{-0.54} \text{ km s}^{-1} \text{ Mpc}^{-1}$ and $\Omega_\Lambda = 0.72 \pm 0.03$. The obtained results are consistent with the presently suitable ranges of those cosmological parameters. We have also studied the sensitivity of the Amati relation to the initial choice of the cosmological parameters.

The results from our research indicate that phenomenological correlations such as Amati and Yonetoku relations for long GRBs can potentially be useful to standardize GRBs for cosmological studies.

Key words: Gamma-ray bursts, prompt emission–phenomenological correlations: extended Hubble diagram, cosmological parameters–Hubble constant, dark-energy density

ACKNOWLEDGEMENTS

I am grateful to my thesis supervisor, Prof. Soebur Razzaque for his kind support and his strong encouragement, which were crucial to my progress on this fascinating Astrophysics research area.

I would also like to thank the NASA *Fermi* collaboration, especially the LAT group, for building a magnificent instrument and developing *Fermi* science tools which reshaped our understanding of energetic Gamma-ray bursts.

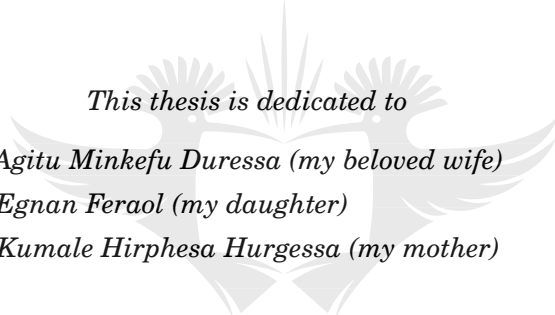
I appreciate the support from Dr. Richard Britto, who has enabled me to understand the *Fermi* data analysis and introduced me to the relevant software. I would like to thank Dr. Reetanjali Moharana for her valuable discussions in my research and encouragement. Thanks go to excellent members of the University of Johannesburg Centre for Astro-Particle Physics: Dr. Jagdish Joshi, Dr. Salvador Miranda-Palacios, Mr. Mfuphi Ntshatsha and Mr. Lutendo Nyadzani for helpful discussions and friendships in any condition during my study.

I would like to take this chance to thank Prof. Frédéric Piron for his mentor-ship at the Université Montpellier, France. I learned a lot about the process of the maximum binned likelihood analysis and the physics of GRBs. I would also like to acknowledge the Erasmus+ MIC for the internship research opportunity and financial support they awarded me. I also acknowledge the National Research Foundation (NRF) of South Africa, Department of Physics, and the University of Johannesburg for their generous financial support.

I must also thank several persons who contributed directly or indirectly for my studies during this period. I have to thank all the academics of the Physics Department for all the support I have received from each and every one of them. I owe thanks especially to Dr. Emanuela Carleschi (HOD), Prof. Hartmut Wikler and Prof. Chris Engelbrecht for supporting me with their valuable comments for different applications of postgraduate funding.

My friends, a special collective thanks goes to Dr. Abey Sherif, Yonas Habtegiorghies, Segni Kebede, Shimeles Zeleke, Tarekegn Heliso, Tagesse Meke, Eleni Berhe, Yared Zeleke and Jonie Addisu, I sincerely thank all of you for your moral support and encouragement.

Most of all, I thank my wife Agitu Minkefu, for encouraging me and providing support to finalize this thesis. Above all, I thank my mother Kumale (Hirkoo) Hirphesa, and my siblings Dejene Hirpha, Shewaye, Beshadu, Beksisa, Naol, Kidane, Sena, Bontu, Andinet and Chalchissa Gelana for their unconditional love, blessings and prayers which always led me through my life and I thank Almighty God for being with me to complete one of the great dreams of my life.



This thesis is dedicated to

*Agitu Minkefu Duressa (my beloved wife)
Egnan Feraol (my daughter)
Kumale Hirphesa Hurgessa (my mother)*

UNIVERSITY
OF
JOHANNESBURG

ABBREVIATIONS

<u>Acronym</u>	<u>Definition</u>
Band	Band model (§2.6.2)
BAT	Burst Alert Telescope
BATSE	Burst And Transient Source Experiment
BB	Blackbody model (§2.6.2)
BGO	Bismuth Germanate Oxide
CGRO	Compton Gamma-Ray Observatory
Comp	Comptonized model (power-law with an exponential cutoff, §2.6.2)
dof	Degrees of Freedom
EGRET	Energetic Gamma-Ray Experiment Telescope (§2.3.1)
FoV	Field of View
GCN	Gamma Ray Burst Coordinates Network
GBM	Gamma-ray Burst Monitor
GRB	Gamma Ray Burst
HE	High Energy
IRF	Instrument Response Function
LAT	Large Area Telescope
LGRBs	Long Gamma Ray Bursts
ph	photon
PL	Power-Law (§2.6.2)
SBPL	Smoothly Broken Power-Law model (§2.6.2)
SED	Spectral Energy Distribution
sr	Steradian
SGRB	Short Gamma Ray Burst

TABLE OF CONTENTS

	Page
1 Introduction	1
1.1 Motivation for the study	3
1.2 Objectives of the research	4
1.3 Summary of the main results	5
1.3.1 Yonetoku relation	5
1.3.2 Amati relation	5
1.4 Organization of the thesis	6
2 Historical background and phenomenology	9
2.1 Early observations	10
2.1.1 The Interplanetary Network	11
2.1.2 The Burst and Transient Source Experiment	11
2.1.3 <i>Konus-Wind</i>	13
2.2 Observations in the afterglow era	14
2.2.1 <i>BeppoSAX</i>	14
2.2.2 HETE-2	14
2.2.3 The <i>Swift</i> mission	15
2.3 Observations of high-energy emission	16
2.3.1 <i>Energetic Gamma-Ray Experiment Telescope</i>	16
2.3.2 <i>INTEGRAL</i>	18
2.3.3 <i>AGILE</i>	19
2.3.4 <i>Fermi</i>	20
2.4 GRB alerts in the future from space-based detectors	25
2.5 Ground-based air cherenkov telescopes for GRB detections	25
2.6 GRB phenomenology	29
2.6.1 Prompt emission	29
2.6.2 Spectral models	31
2.6.3 Prompt emission spectra in the keV/MeV–GeV range	33
2.6.4 Fluences and Fluxes	34

TABLE OF CONTENTS

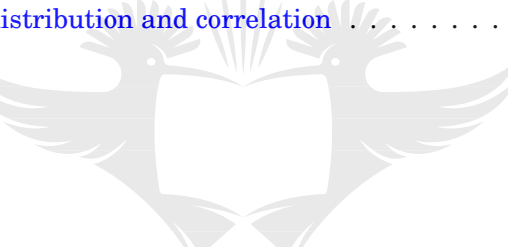
2.6.5	Afterglow emission	35
2.6.6	GRB emission mechanism	36
2.7	Summary	38
3	The <i>Fermi</i> Gamma-ray Space Telescope	39
3.1	<i>Fermi</i> mission overview	39
3.2	Source model and instrument response functions	40
3.2.1	LAT event classifications	42
3.3	Maximum likelihood analysis of the LAT data	45
3.3.1	The unbinned maximum likelihood analysis	45
3.3.2	The binned likelihood analysis	47
3.4	On orbit and ground processing	49
3.4.1	On orbit processing	49
3.4.2	Ground processing	50
3.4.3	GRB detection	50
3.5	Detection of new LAT GRBs	51
3.6	The Gamma-ray Burst Monitor performance	53
3.6.1	GBM spectral analysis	53
3.6.2	LAT and GBM joint spectral analysis	55
3.7	Summary	57
4	Gamma-ray Burst Cosmology	59
4.1	Introduction	59
4.1.1	Connection between Supernovae and GRBs	61
4.2	Cosmological parameters	61
4.2.1	Distance measures in cosmology	64
4.2.2	Distance modulus	65
4.3	Lambda-Cold Dark Matter model	66
4.4	Using GRBs as standard candles	68
4.4.1	Amati relation	69
4.4.2	Yonetoku relation	71
4.4.3	Decorrelation energy	72
4.5	Extended Hubble diagram	73
4.5.1	Construction of the Hubble diagram from the Amati relation	73
4.5.2	Construction of the Hubble diagram from the Yonetoku relation	75
4.6	Constraints on the dark-energy and the Hubble constant	75
4.7	Evolution of the Amati relation with redshift	76
4.8	Summary	78

TABLE OF CONTENTS

5 Yonetoku relation for <i>Fermi</i>-GBM and <i>Swift</i>-BAT GRBs	81
5.1 Introduction	82
5.2 Observational data from <i>Fermi</i> -GBM and <i>Swift</i> -BAT	83
5.3 Intrinsic peak energy and isotropic luminosity calculations	85
5.4 Samples of GRBs	86
5.4.1 Common GRBs (GBM and BAT)	86
5.4.2 GBM GRBs fitted with Comp and Band models	87
5.4.3 The combined sample of GBM and BAT GRBs of the best-fit model	89
5.5 The Yonetoku relation between $E_{i,p}$ and L_{iso}	92
5.5.1 Fitted model	92
5.5.2 Partial correlation analysis	93
5.5.3 Likelihood analysis of $E_{i,p}$ and L_{iso}	93
5.6 Constraints on cosmological parameters and the extended Hubble diagram	96
5.6.1 Constraints on dark-energy and Hubble parameters	96
5.6.2 The extended Hubble diagram	98
5.7 Summary	99
6 Amati relation for <i>Fermi</i>-LAT GRBs	101
6.1 Introduction	102
6.2 Data sets	103
6.2.1 GRB samples	103
6.2.2 <i>Fermi</i> data preparation	104
6.3 Spectral analysis	105
6.3.1 Spectral fitting	105
6.3.2 Isotropic energy calculation	106
6.4 Amati relation between E_{iso} and $E_{i,p}$	109
6.4.1 Fitted model	109
6.4.2 Likelihood analysis	111
6.5 The Hubble diagram and constraints on cosmological parameters	114
6.5.1 Sensitivity on the initial choice of cosmological parameters	116
6.5.2 Joint fits with SNe U2.1 data	117
6.6 Discussion and Summary	119
7 Summary and future directions	121
7.1 Summary of results	121
7.1.1 Cosmological constraints from calibrated Yonetoku relation	122
7.1.2 Cosmological constraints from calibrated Amati relation	123
7.2 Future directions	125

TABLE OF CONTENTS

A Derivation of SBPL	127
A.1 Smoothly-Broken Power Law	127
B The <i>Fermi</i>-GBM and <i>Swift</i>-BAT spectral fitting parameters, and reanalysis of W2016 data	129
B.1 The best-fit spectral parameters of the <i>Swift</i> -BAT sample	129
B.2 The best-fit spectral parameters of the <i>Fermi</i> -GBM sample	130
B.3 The Comp (F_{Comp}) spectral fitting parameters of the <i>Fermi</i> -GBM sample	133
B.4 The Band (F_{Band}) spectral fitting parameters of the <i>Fermi</i> -GBM sample	135
B.5 Reanalysis of W2016 data	137
C Decorrelation energy and multivariate normal distribution	141
C.1 The decorrelation energy	141
C.1.1 The computed decorrelation energy for different samples	142
C.1.2 The plots of the computed decorrelation energy for different samples	143
C.2 Multivariate normal distribution and correlation	144
List of publications	147
Bibliography	149



UNIVERSITY
OF
JOHANNESBURG

LIST OF TABLES

TABLE	Page
2.1 Main GRB detector of the past, present, and future satellites.	17
2.2 GBM instrument characteristics and performance (Meegan et al., 2009).	22
2.3 Parameters of LAT telescope and estimated performance (Atwood et al., 2009).	24
2.4 The T_{90} distributions of the GRB prompt emission discovered by <i>Fermi</i> -GBM <i>Swift</i> -BAT and BATSE instruments until December, 2017.	31
3.1 The result of T_{90} time-integrated spectral analysis.	55
3.2 GRB 160509A, GRB 150403A and GRB 090902B as jointly measured by GBM and LAT (or LLE) and results from the spectral model fits of time-integrated flux within T_{90} . . .	57
4.1 The best-fit parameters of the $E_{\text{iso}} - E_{\text{i,p}}$ correlation fits to the samples of A2008 and G008 for different redshift bins. The Spearman rank correlation coefficient (Spearman, 1904) is done with ρ_{sp} and χ^2_{red} , which is the reduced χ^2	78
5.1 The $E_{\text{i,p}}$ and L_{iso} of the <i>Fermi</i> -GBM sample of 76 GRBs in the cosmological rest frame which are computed using the best-fit model with their redshift. Also calculated are distance modulus μ	89
5.2 The $E_{\text{i,p}}$ and L_{iso} of the <i>Swift</i> -BAT sample of 38 long GRBs in the cosmological rest frame which are computed using the best-fit model with their redshift. The distance modulus μ is also shown.	91
5.3 The best-fit parameters of the $E_{\text{i,p}} - L_{\text{iso}}$ correlation for five categories of GRB samples. The $\rho_{\text{p}E_{\text{i,p}},L_{\text{iso},z}}$, $\rho_{\text{p}E_{\text{i,p}},L_{\text{iso}}}$, $\rho_{\text{p}L_{\text{iso}},z}$ and $\rho_{\text{p}E_{\text{i,p}},z}$ are the Pearson correlation coefficients defined in Eqs. (5.11), (5.12), (5.13) and (5.14), respectively.	95
5.4 Constraints on H_0 and $\Omega_\Lambda \in (0.0, 0.85)$ in 1σ confidence level in the flat universe. . . .	97
6.1 <i>Fermi</i> sample of 25 LGRBs and 1 SGRB with selected detectors and results from the spectral model fits of Time-integrated Flux within T_{90}	105
6.2 Intrinsic Peak Energy, $E_{\text{i,p}}$, and Isotropic radiated Energy, E_{iso} , for the <i>Fermi</i> GRB sample.	109
6.3 The best-fit parameters of the Amati relation fits to the full samples of GRBs and GRBs with redshift $z > 1.414$. $\rho_{E_{\text{i,p}},E_{\text{iso}},z}$ is the partial correlation coefficient (see Eq. 5.11).	112

LIST OF TABLES

6.4 Constraints on (H_0, Ω_Λ) for a flat universe from the Amati relation, and reduced χ^2/dof of the fits.	116
B.1 The result of the Comp spectral fitting parameters of the <i>Swift</i> -BAT sample integrated over T_{peak} for 38 GRBs (e.g., <i>Swift</i> -BAT catalog, Lien et al., 2016). The z , L_{iso} and μ for each GRB is listed in Tab. 5.2.	129
B.2 The result of the best-fit spectral fitting parameters of the <i>Fermi</i> -GBM sample integrated over T_{peak} for 76 GRBs (e.g., <i>Fermi</i> -GBM catalog, Gruber et al., 2014; von Kienlin et al., 2014; Narayana Bhat et al., 2016a). The z , L_{iso} and μ for each GRB is listed in Tab. 5.1.	131
B.3 The result of the Comp (F_{Comp}) spectral fitting parameters of the <i>Fermi</i> -GBM sample integrated over T_{peak} for 90 GRBs (e.g., <i>Fermi</i> -GBM catalog, Gruber et al., 2014; von Kienlin et al., 2014; Narayana Bhat et al., 2016a).	133
B.4 The result of the Band (F_{Band}) spectral fitting parameters of the <i>Fermi</i> -GBM sample integrated over T_{peak} for 46 GRBs (e.g., <i>Fermi</i> -GBM catalog, Gruber et al., 2014; von Kienlin et al., 2014; Narayana Bhat et al., 2016a).	136
B.5 The W2016 sample of 94 GRBs with E_{iso} updated from Amati et al. (2008, 2009); Wang et al. (2016). Instruments: SW = <i>Suzaku</i> -WAM, KW = <i>Konus</i> -Wind, SB = <i>Swift</i> -BAT, FG = <i>Fermi</i> GBM, HET = HETE-2, GRO = CGRO/BATSE and SAX = <i>BeppoSAX</i> . . .	137
C.1 The result of curve fitting of the <i>Fermi</i> -GBM and <i>Swift</i> -BAT samples.	142

UNIVERSITY
 OF
 JOHANNESBURG

LIST OF FIGURES

FIGURE	Page
2.1 GRB 670702 light curve (Robert & Jerry, 2000)	10
2.2 <i>Left side</i> : locations of 2702 GRBs triggered by <i>CGRO/BATSE</i> in Galactic coordinates and Hammer-Aitoff projection. <i>Right side</i> : hardness ratio HR_{32} of SGRBs and LGRBs with the T_{90} scattering plot. The dashed vertical lines (crimson) and (blue) correspond to the mean of HR_{32} of the long and short GRBs (Briggs et al., 1996; Paciesas et al., 1999).	11
2.3 Diverse light curves of the GRBs prompt emission detected by BATSE instrument. This sample includes short and long events. https://gammaray.nsstc.nasa.gov/batse/grb/lightcurve/	13
2.4 <i>Left panel</i> : sky distribution of 1199 <i>Swift-BAT</i> GRBs detected from November 2014 to March 2018 (magenta stars, Lien et al., 2016) and 2702 <i>CGRO/BATSE</i> (magenta stars, Meegan et al., 1996; Paciesas et al., 1999) detected GRBs in Galactic coordinates and Hammer-Aitoff projection. <i>Right panel</i> : the redshift distributions of 405 GRBs detected by <i>Swift-BAT</i> . The vertical dashed line shows the mean (~ 2.03) of the redshift distributions.	16
2.5 History of observational gamma-ray astronomy from Vela satellites in the early 1960s to the future mission SVOM satellite, scheduled for launch in 2021 (see Tab. 2.1).	18
2.6 <i>Left panel</i> : sky distribution of 83 MCAL GRBs (i.e., 17 SGRBs with green stars, 61 LGRBs with magenta stars and 5 unknown GRBs with cyan stars) in Galactic coordinates and using Hammer-Aitoff projection. The data is taken from Galli et al. (2013). <i>Right panel</i> : energy of the photons from the direction of GRB 080514B detected by the <i>GRID</i> (Giuliani et al., 2008).	20
2.7 Schematics of orientation and location of the GBM detectors (Meegan et al., 2009). Twelve NaI detectors (right panel) are indexed 0–11 (n0–n11) and two BGO detectors (left panel) are denoted by 12 (b0) and 13 (b1) in the figure. The gray box of the middle Figure shows the location of LAT instrument.	21
2.8 The schematic diagram of different part of <i>Fermi</i> satellite. (Credit: http://fermi.sonoma.edu/multimedia/gallery/)	23

<p>2.9 <i>Left panel:</i> comparison of the effective areas of γ-ray instruments with wide FoV (Yamaoka et al., 2017) between the <i>Fermi</i>-LAT (Atwood et al., 2009), <i>Fermi</i>-GBM (Meegan et al., 2009), <i>Swift</i>-BAT (Barthelmy et al., 2005), <i>CGRO</i>-BATSE (Fishman et al., 1985), <i>Konus</i>-Wind (Terekhov et al., 1998) and <i>Suzaku</i>-WAM (Yamaoka et al., 2009). <i>Right panel:</i> comparison of the effective areas of VERITAS, MAGIC, CTA optimistic and CTA realistic (Gilmore et al., 2013).</p> <p>2.10 The differential sensitivity of CTA and LAT at different energies versus time. Each of the lines shown was generated for a minimum number of 25 events in the 5σ significance of detection (Cherenkov Telescope Array Consortium et al., 2017).</p> <p>2.11 The highest energy photons of GRBs detected by <i>Fermi</i>-LAT with maximum energy $E_{\max} > 20$ GeV. The color bar represents the E_{\max} of the GRBs.</p> <p>2.12 The T_{90} distribution for the <i>Fermi</i>-GBM (Gruber et al., 2014; von Kienlin et al., 2014; Narayana Bhat et al., 2016b), <i>Swift</i>/BAT (Lien et al., 2016) and BATSE (Meegan et al., 1996; Paciesas et al., 1999) GRBs. Their distributions of a statistical data sets are reported in Tab. 2.4. The vertical dashed line shows the value of T_{90} at 2 s.</p> <p>2.13 The prompt emission spectral of GRB 090926A modeled at different time intervals (bottom panel) as well as for the time-integrated prompt emission (top panel) (Ackermann et al., 2011).</p> <p>2.14 <i>Left panel:</i> distribution of the fluences of 2231 GBM (10–1 MeV, Gruber et al., 2014; von Kienlin et al., 2014; Narayana Bhat et al., 2016a), 135 LAT (from Fermi.gsfc.nasa.gov, 2017) and 1154 BAT (15–150 keV, Lien et al., 2016) GRBs collected from the catalog until December 2017. <i>Right panel:</i> the energy fluxes of 2115 GBM (10–1 MeV), 132 LAT and 1154 BAT (15–150 keV).</p> <p>2.15 The <i>Swift</i>-XRT light curves for which their prompt emission were simultaneously detected by <i>Fermi</i>-LAT, except GRB 050315 and 050502B (from the <i>Swift</i>-XRT GRB light curve repository Swift-XRT, 2018). We used the segmented indices (α) of the power-law as defined by Zhang et al. (2006).</p> <p>2.16 Schematic fireball model of GRBs, and emission regions of a collapsing star and compact merger (Gomboc, 2012).</p> <p>3.1 The spectral energy coverage of GBM, LLE, and LAT.</p>	<p>26</p> <p>28</p> <p>28</p> <p>30</p> <p>34</p> <p>35</p> <p>36</p> <p>37</p> <p>40</p>
-----------------------------------------------------------------------------------------------------------------------------------------------------------------------------------------------------------------------------------------------------------------------------------------------------------------------------------------------------------------------------------------------------------------------------------------------------------------------------------------------------------------------------------------------------------------------------------------------------------------------------------------------------------------------------------------------------------------------------------------------------------------------------------------------------------------------------------------------------------------------------------------------------------------------------------------------------------------------------------------------------------------------------------------------------------------------------------------------------------------------------------------------------------------------------------------------------------------------------------------------------------------------------------------------------------------------------------------------------------------------------------------------------------------------------------------------------------------------------------------------------------------------------------------------------------------------------------------------------------------------------------------------------------------------------------------------------------------------------------------------------------------------------------------------------------------------------------------------------------------------------------------------------------------------------------------------------------------------------------------------------------------------------------------------------------------------------------------------------------------------------------------------------------------------------------------------------------------------------------------------------------------------------------------------------------------------------------------------------------------------------------------------------------------------------------------------------------------------------------------------------------------------------------------------------------------------------------------------------------------------------------------------------------------------------------	-------------------------------------------------------------------------------------------

LIST OF FIGURES

3.2	The top two panels and the bottom left panel plots show the performance comparison of the P7REP_SOURCE_V15 with P8R2_SOURCE_V6 event classes. <i>Top left panel</i> : comparison of the effective area integrated in the FoV (acceptance) between Pass 7 and Pass 8 SOURCE events classes. <i>Top right panel</i> : comparison of the effective area between Pass 7 and Pass 8 SOURCE events classes. <i>Bottom left panel</i> : comparison of the angular resolution between Pass 7 and Pass 8 SOURCE event classes. <i>Bottom right panel</i> : the on-axis comparison of the effective area as a function of energy for three distinct Pass 8 SOURCE classes of event. From the source: http://www.slac.stanford.edu/exp/glast/groups/canda/lat_Performance.htm	43
3.3	The <i>Fermi</i> spacecraft orbit: The blue hatched polygon band is representing the South Atlantic Anomaly (SAA) boundary, in which the detectors are turned off, the solid red curve is the path of the spacecraft over one orbit path from West to East and the horizontal dashed blue lines show the maximum of the inclination of $\pm 26^\circ$ (Fitzpatrick et al., 2012).	49
3.4	The test statistic distribution of 134 LAT GRBs (from Fermi.gsfc.nasa.gov, 2017).	51
3.5	<i>Left panel</i> : the energy distribution of GRB 160625B with respect to the best localization of (RA, DEC) = (308.56°, 6.93°). The color bar indicates the photon energy in MeV. <i>Right panel</i> : the <i>TS</i> map of GRB 160625B. The color bar denotes the <i>TS</i> at a given location. (Credit: Flare Advocate (FA) <i>Fermi</i> tool)	52
3.6	<i>Left panel</i> : the light curves of short GRB 090510 for different GBM detectors. The hatched band indicates the interval $T_{90} = T_{05} - T_{95}$ (s) from the GBM trigger T_0 . <i>Right panel</i> : the Band, SBPL, Comp, PL and BB spectral models performed to fit the spectra of short GRB 090510.	54
3.7	<i>Top panel</i> : the vF_v joint spectral fitting of GBM and LAT data of GRB 160509A. <i>Top middle panel</i> : the vF_v joint spectral fit of GBM and LLE data of GRB 150403A. <i>Bottom panel</i> : the vF_v joint spectral fitting of GBM and LAT data of GRB 090902B. The lower panels show the residual of the spectral fit. The fit results are summarized in Tab. 3.2.	56
4.1	<i>Left panel</i> : photons from a GRB and its afterglow travel on its way to us through the surrounding burst medium, host galaxy medium, and other intervening absorbers. GRBs may probe the properties and environment of the first stars and galaxies in the universe (http://www.armaghplanet.com/blog/the-big-bounce-theory-what-is-it.html). <i>Right panel</i> : the luminosity distance, d_L , of different astrophysical objects in Λ CDM cosmology with standard parameters vs. redshift. The upper x -axis shows the time (Gyr) since Big Bang.	60
4.2	<i>Left panel</i> : the density evolution of the main constituents of the universe with the scale factor. The hatched band in maroon color represents $w_{de} = -1 \pm 0.2$. <i>Right panel</i> : the energy density of each cosmic component illustrated with different line colors, as labeled in the legend. A vertical shaded region corresponds to the current epoch.	63

4.3 <i>Left panel:</i> the distribution of d_L for different values of the dark matter parameters. <i>Right panel:</i> the distribution of d_L with different values of the dark-energy parameters, assuming a flat universe.	65
4.4 <i>Left panel:</i> the Λ CDM model: 1σ , 2σ and 3σ confidence levels in the $(\Omega_m, \Omega_\Lambda)$ plane from SNe U2.1 combined with the constraints from BAO and CMB. <i>Right panel:</i> Hubble diagram of the SNe U2.1 sample. The solid line represents the best-fit cosmology for a flat Λ CDM universe from the SNe U2.1 data (Suzuki et al., 2012).	68
4.5 <i>Left panel:</i> the Amati relation for 12 LGRBs (Amati et al., 2002). <i>Right panel:</i> 12 LGRB data updated with sub-energetic bursts (GRB 980425 and GRB 031203) and the two short GRB 050709 and GRB 051221 (Amati, 2006a).	70
4.6 The Yonetoku relation using the reference energy of $E_0 = 100$ keV (blue line) and the decorrelation energy of $E_{0,\text{dec}} = 1000$ keV (green line). The butterfly is the $\sigma_{L_{\text{iso}}}$ contour of the L_{iso} analysis.	74
4.7 <i>Left panel:</i> the Amati relation for 68 GRBs. Data taken from Amati et al. (2008) and 74 GRBs from Ghirlanda et al. (2008) fitted by a power-law. <i>Right panel:</i> the distribution of the $E_{i,p}$ with respect to the redshift.	76
4.8 <i>Left panel:</i> the correlation of $E_{i,p}$ and E_{iso} for different redshift bins for the A2008 sample which consists of 68 LGRBs. <i>Right panel:</i> the correlation of $E_{i,p}$ and E_{iso} for the redshift binned into four groups for the G2008 sample containing 74 GRBs. For both samples, the results of the best-fit parameters are reported in Tab. 4.1.	77
4.9 The best-fit parameters for each of the binning for the A2008 and G2008 samples with their Spearman's rank correlation coefficient ρ_{sp} (first panel). The result of parameters for each bin of the A2008 sample obtained from the PL fit (magenta hexagon symbols) and G2008 sample (cyan diamond symbols).	79
5.1 <i>Left panel:</i> GRB spectral energy coverage of the GBM and BAT. <i>Right panel:</i> GRBs detected by the <i>Fermi</i> -GBM (green symbols, Gruber et al., 2014; von Kienlin et al., 2014; Narayana Bhat et al., 2016a) and <i>Swift</i> -BAT (gray symbols, Lien et al., 2016) are isotropically distributed in the sky.	82
5.2 <i>Left panel:</i> the energy flux histograms of GBM (green hatched, 2115 GRBs) and BAT (gray hatched, 1154 GRBs) data collected until December 2017. <i>Right panel:</i> the L_{iso} distribution of GBM (green symbols) and <i>Swift</i> (gray symbols) computed in the 1 keV–10 MeV energy range extrapolated based on the best-fit model over the time range of the peak flux of the bursts with respect to their redshifts. The L_{iso} and redshift distributions for GBM (green dotted histogram) and for BAT (gray histogram).	84

LIST OF FIGURES

- 5.3 *Left panel:* comparison of $E_{i,p}$ measured by the GBM and BAT for 12 GRBs detected in common. *Right panel:* the correlation between L_{iso} of GBM and BAT sample. Blue symbols correspond to the BAT and GBM GRBs fitted with the same Comp spectral model while the green symbols indicate the fit with different spectral models. The dashed line indicates the equality of L_{iso} measured with the GBM and BAT. 86
- 5.4 *Top panel:* distribution of the bolometric flux F_{bolo} as the GBM GRB spectrum modeled by both Comp (blue histogram) and Band (green histogram) models. *Bottom panel:* redshift of 43 GRBs. 87
- 5.5 *Left panel:* the correlation between L_{iso} of GBM Comp and Band samples. *Right panel:* the correlation between $E_{i,p}$ of GBM Comp and Band samples. The dashed line denotes the equality of L_{iso} and $E_{i,p}$ measured with GBM Comp and Band function. 88
- 5.6 *Left panel:* distribution of the L_{iso} statistic for the Comp and Band models. A value less than 1 indicates the L_{iso} values are inside errors. *Right panel:* distribution of the $E_{i,p}$ statistic for the Comp and Band models. A value < 1 indicates the $E_{i,p}$ values are inside errors. 88
- 5.7 Distributions of the fitting parameters of the Yonetoku relation estimated using MCMC method for different GRB samples. k , m and σ_{ext} are the coefficients of the Yonetoku relation defined in Eq. (5.9) during the MCMC sampling run. *Top left panel:* the estimated parameters of the observational F_{Comp} sample (green). *Top right panel:* the estimated parameters for F_{Band} sample (blue). *Middle left panel:* the estimated parameters for $F_{\text{best-model}}$ sample (magenta). *Middle right panel:* the estimated parameters for S_{Comp} (gray). *Bottom panel:* the estimated parameters for $FS_{\text{best-model}}$ sample of 76 GRBs. The parameter of the highest likelihood found during the run is indicated by the cross lines. 94
- 5.8 The correlation between L_{iso} and $E_{i,p}$ and the best-fit curves of the Yonetoku relation. *Top left panel:* the measured parameters of the observational F_{Comp} sample (green). *Top middle panel:* the measured parameters for F_{Band} sample (blue). *Top right panel:* the measured parameters for $F_{\text{best-model}}$ sample (magenta). *Bottom left panel:* the measured parameters for S_{Comp} (gray). *Bottom right panel:* the joint 78 GBM sample of GRBs (black points with error bars) and 26 BAT sample of GRBs (red points with error bars) with the best-fit model, which are not simultaneously detected by the GBM ($FS_{\text{best-model}}$). 96

5.9 Constraints on the cosmological parameters from the fitting of the Yonetoku relation for different samples of LGRBs. <i>Top left panel</i> : the Ω_Λ and H_0 obtained for the observational F_{Comp} sample (green). <i>Top middle panel</i> : the Ω_Λ and H_0 obtained with the observational F_{Band} sample (blue). <i>Top right panel</i> : the Ω_Λ and H_0 obtained from the observational $F_{\text{best-model}}$ sample (magenta). <i>Bottom left panel</i> : the Ω_Λ and H_0 obtained with the observational S_{Comp} sample (gray). <i>Bottom right panel</i> : the $\Omega_\Lambda - H_0$ obtained from the observational $FS_{\text{best-model}}$ sample (black). The 1σ and 2σ confidence levels of the pair of cosmological parameters determined by following $\Delta\chi^2 \equiv \chi^2 - \chi^2_{\min} \leq 2.30$ and 6.18 , respectively. The plus sign indicates the best-fit location, which found within range.	97
5.10 Contours of likelihood in the (H_0, Ω_Λ) plane for SNe U2.1 (black color) and SNe U2.1 with $FS_{\text{best-model}}$ (maroon color) samples in 1σ and 2σ confidence levels. The plus signs show the location of the best-fit.	98
5.11 Combined SNe and GRB Hubble diagram for the $FS_{\text{best-model}} + \text{SNe U2.1}$ sample. The black curved line is plotted using the estimated cosmological parameters $H_0 = 69.908 \text{ km s}^{-1} \text{ Mpc}^{-1}$ and $\Omega_\Lambda = 0.715$ obtained from the joint $FS_{\text{best-model}} + \text{SNe U2.1}$ data. The vertical broken line is plotted at the maximum redshift $z = 1.414$ of the SNe U2.1 data.	98
5.12 Comparison of the coefficients of the Yonetoku relation of our current work with the previous work done by Schaefer & Collazzi (2007); Zitouni et al. (2014); Lin et al. (2016).	100
6.1 <i>Left panel</i>: redshift distribution for our sample of 26 (25 long and 1 short) <i>Fermi</i> GRBs (maroon histogram) and the W2016 sample of 94 GRBs (gray histogram). The cumulative distribution function (CDF) of the <i>Fermi</i> (median: $z = 1.66$, mean: $z = 1.79$) and W2016 (median: $z = 2.30$, mean: $z = 2.57$) samples are indicated in the inset with maroon and gray lines, respectively. <i>Right panel</i> : the luminosity distance d_L of 26 <i>Fermi</i> GRBs in ΛCDM cosmology with standard parameters vs. redshift. The upper x-axis shows the time (Gyr) since the Big Bang.	103
6.2 vF_v spectra of <i>Fermi</i>-LAT/GBM GRBs with known redshift resulting from the time-integrated spectral analysis over the T_{90} duration. The top left panel shows the Band or Band + BB model fits, while the top right panel shows SBPL or SBPL + BB model fits. The bottom panels show more complex models along with their components. The 1σ confidence regions of the models are shown with shades of the same color as the model lines.	107

LIST OF FIGURES

6.3	The top four panels show the distribution of the parameters from the simulated 10,000 spectra that obtained from the best-fit Band model of GRB 150514A. $S_{\text{bolo}}^*(\text{F10})$ and $S_{\text{bolo}}^*(\text{F100})$ are the bolometric fluences corresponding to the energy interval 1– 10^4 keV and 1– 10^5 keV, respectively. The results are presented in Tab. 6.2. The mean values represented as the solid vertical magenta lines and the 68.27% errors as the vertical broken magenta lines.	108
6.4	<i>Top panels:</i> distributions of bolometric fluence and isotropic energy of <i>Fermi</i> (F10, S_{bolo} and E_{iso} computed in the 1 keV–10 MeV energy range and F100, the same computed in the 1 keV–100 MeV energy range) and of W2016 samples. <i>Bottom panels:</i> distributions of the observed peak energy (left) and of intrinsic peak energy (right) for the <i>Fermi</i> and W2016 bursts.	110
6.5	Amati relation fits (solid lines) to different data samples in the $\log E_{\text{iso}} - \log E_{\text{i,p}}$ plane. The shaded regions correspond to 1σ scatter. <i>Top left panel:</i> <i>Fermi</i> 25 LGRBs with $E_{\text{iso}}^*(\text{F10})$ computed in the 1 keV–10 MeV energy range. <i>Top right panel:</i> <i>Fermi</i> 25 LGRBs with $E_{\text{iso}}^*(\text{F100})$ computed in the 1 keV–100 MeV energy range. <i>Bottom left panel:</i> 94 LGRBs in the W2016 sample. <i>Bottom right panel:</i> joint fit to the <i>Fermi</i> F10 and W2016 data reported in Tab. 6.3.	112
6.6	Amati relation fits (solid lines) to different data samples with redshift > 1.414 in the $\log E_{\text{iso}} - \log E_{\text{i,p}}$ plane. The sample descriptions are the same as in Fig. 6.5.	113
6.7	Constraints on the cosmological parameters H_0 and Ω_Λ from the Amati relation for different samples of LGRBs. The top and bottom panels correspond to the samples with all redshifts and with redshifts > 1.414 , respectively. The 1σ and 2σ confidence level contours are determined by following $\Delta\chi^2 \equiv \chi^2 - \chi^2_{\min} \leq 2.30$ and 6.18, respectively. The plus sign indicates the best-fit location.	114
6.8	<i>Left panel:</i> the empirical cumulative distribution functions (ECDF) of the W2016 full sample and W2016 ($z > 1.414$) are indicated in the inset with orange and maroon lines, respectively (K-S Test: $D = 0.11$, p-value = 0.67). <i>Middle panel:</i> ECDF plot showing expression differences for F10 full sample comparing the F10 ($z > 1.414$) sample (K-S Test: $D = 0.44$, p-value = 0.04). <i>Right panel:</i> the ECDF of the F10+W2016 full sample and F10+W2016 ($z > 1.414$) are indicated in the inset with blue and green lines, respectively (K-S Test: $D = 0.28$, p-value = 0.23).	115
6.9	Results from the sensitivity study of the Amati relation and cosmological parameters on the initial choice of H_0 and Ω_Λ to calculate E_{iso} . The gray lines correspond to initial $H_0 = 69.6 \text{ km s}^{-1} \text{ Mpc}^{-1}$ (default case). The blue and green lines correspond to initial values of $H_0 = 100$ and $50 \text{ km s}^{-1} \text{ Mpc}^{-1}$, respectively. The initial value of $\Omega_\Lambda = 0.714$ (default case) is the same for all cases.	117

6.10 Results from the sensitivity study of the Amati relation and cosmological parameters on the initial choice of H_0 and Ω_Λ to calculate E_{iso} . The gray lines correspond to initial $\Omega_\Lambda = 0.714$ (default case). The blue and green lines correspond to initial values of $\Omega_\Lambda = 0.8$ and 0.6 , respectively. The initial value of $H_0 = 69.6 \text{ km s}^{-1} \text{ Mpc}^{-1}$ (default case) is the same for all cases.	117
6.11 The same as Fig. 6.7 but with the SNe U2.1 sample (Suzuki et al., 2012). The top and bottom panels correspond to the GRBs samples with all redshifts and with redshifts > 1.414 , respectively.	118
6.12 Combined SNe and GRB Hubble diagram for the F10 + W2016 + SNe U2.1 sample. The top panel includes all GRBs and the bottom panel includes GRBs with $z > 1.414$, respectively. The black lines are plotted using the estimated cosmological parameters obtained from the joint F10 + W2016 + SNe U2.1 data with 1σ confidence regions (cyan), reported in Tab. 6.4. The vertical broken line indicate $z = 1.414$	118
A.1 The index changes from α to β	128
C.1 <i>Fermi</i> -GBM sample with the Comp model of 90 GRBs. <i>Left panel</i> – The Yonetoku plane using the reference energy of $E_0 = 100 \text{ keV}$. <i>Right panel</i> – The Yonetoku plane after the decorrelation energy $E_{0,\text{dec}} = 1000 \text{ keV}$ is used.	143
C.2 <i>Fermi</i> -GBM sample with the Band spectral fitting model of 46 GRBs. <i>Left panel</i> – The Yonetoku plane using the reference energy of $E_0 = 100 \text{ keV}$. <i>Right panel</i> – The Yonetoku plane after the decorrelation energy $E_{0,\text{dec}} = 900 \text{ keV}$ is used.	143
C.3 <i>Fermi</i> -GBM sample with the best-fit spectral fitting model of 76 GRBs. <i>Left panel</i> – The Yonetoku plane using the reference energy of $E_0 = 100 \text{ keV}$. <i>Right panel</i> – The Yonetoku plane after the decorrelation energy $E_{0,\text{dec}} = 700 \text{ keV}$ is used.	143
C.4 <i>Swift</i> -BAT sample with the Comp spectral fitting model of 38 GRBs. <i>Left panel</i> – The Yonetoku plane using the reference energy of $E_0 = 100 \text{ keV}$. <i>Right panel</i> – The Yonetoku plane after the decorrelation energy $E_{0,\text{dec}} = 350 \text{ keV}$ is used.	144
C.5 <i>Fermi</i> -GBM and <i>Swift</i> -BAT samples with the best-fit model spectral fitting model of 102 GRBs. <i>Left panel</i> – The Yonetoku plane using the reference energy of $E_0 = 100 \text{ keV}$. <i>Right panel</i> – The Yonetoku plane after the decorrelation energy $E_{0,\text{dec}} = 550 \text{ keV}$ is used.	144

INTRODUCTION

Contents

1.1	Motivation for the study	3
1.2	Objectives of the research	4
1.3	Summary of the main results	5
1.3.1	Yonetoku relation	5
1.3.2	Amati relation	5
1.4	Organization of the thesis	6

Gamma-ray bursts (GRBs) are energetic extragalactic events and non-repetitive blasts that emit dominantly in γ -rays. GRBs were serendipitously discovered in the late 1960s by the United States military satellites named Vela, designed to monitor nuclear explosions forbidden by the Nuclear Test Ban Treaty (Klebesadel et al., 1973). Afterwards, several satellites with a large variety of instruments have been launched to detect GRBs for further investigation, in order to fully understand and widen the information of the bursts. GRBs are extremely bright and release an enormous isotropic equivalent radiated energy $E_{\text{iso}} \sim 10^{54}$ erg in a few hundreds of seconds (Piran, 1999; Mészáros, 2002; Tsutsui et al., 2009; Dirirsa et al., 2017a). The energy released by a single GRB is comparable with the total amount of energy released by a Supernovae (SNe) explosion throughout several months (Piran, 2002). Due to their high¹ luminosities $\sim 10^{54}$ erg s⁻¹, GRBs can be visible at a very large distance to explore the early universe, reaching into the era of the massive first-generation stars (Hutchins, 1976). At present, the most distant object known in the universe is galaxy GN-z11 which was observed at $z = 11.1$ (Oesch et al., 2016) while the second distant object is GRB 090429B with a measured redshift $z \sim 9.4$ (Cucchiara et al., 2011). GRBs occur at arbitrary locations in the sky (Fishman et al., 1985) and in all directions of

¹The highest luminous event in the universe is the gravitational wave with a peak luminosity of 3.6×10^{56} erg s⁻¹ (Christensen, 2018).

the universe. This also suggested that the origin of GRBs are at cosmological distances. During the emission, they possibly shine all other objects in the γ -ray sky from milliseconds to several minutes.

The early observations of GRBs can be characterized by a brief phase of intense and distinct flashes of γ -rays and hard X-rays. They usually exhibit a brief (milliseconds to minutes), rapid variability (last from few milliseconds to hundreds of minutes time scale), thermal (Ghirlanda et al., 2003; Ryde, 2004) and non-thermal (Gruber et al., 2014) spectral appearances, and are observed mostly in the (sub-) MeV γ -ray range (Klebesadel et al., 1973; Fishman & Meegan, 1995). An additional thermal component has been also observed in certain GRBs (Guiriec et al., 2011, 2013, 2015b,a), besides, the power-law (PL) component extending to higher and lower energies (i.e., 10 keV–GeV band) observed in the joint spectral analysis of GRBs from the *Fermi*-Large Area Telescope (LAT) and Gamma-ray Burst Monitor (GBM) (Abdo et al., 2009; Ackermann et al., 2010; Tierney et al., 2013) instruments. Another characteristic of GRBs is an extended emission in time, which can be observed up to GeV energy range. Such GRBs exhibit an additional PL component at high energies. After a brief period of emission, GRBs exhibit a long-lasting multi-wavelength emission (i.e., X-ray, optical, infra-red and sometimes also radio) where the observed flux decreases rapidly within hours to weeks (Costa et al., 1997; Frail et al., 1997; Fox et al., 2003; Piron, 2016).

The progenitor systems and the physical circumstances of GRBs, which are needed to cause, and accelerate the relativistic jet are nonetheless remain unclear. The duration of a GRB is determined from the photon flux accumulation over time, typically between 5% and 95% of the fluence, and is called T_{90} . Based on their duration, GRBs are classified as long ($T_{90} \gtrsim 2$ s) and short ($T_{90} \lesssim 2$ s) bursts (Kouveliotou et al., 1993). The progenitors of these two categories are thought to be different: long GRBs (LGRBs) result from the core collapse of massive stars (MacFadyen & Woosley, 1999) while short GRBs (SGRBs) result from the binary merger of compact objects (Eichler et al., 1989). Observational evidence, namely the association of SNe with LGRBs (Kulkarni et al., 1998; Stanek et al., 2003; Soderberg et al., 2006) and association of gravitational waves with SGRB (Abbott et al., 2017) support the progenitor theories of GRBs.

As mentioned above, most GRBs have been found to be located at cosmological distances. If they can be standardized, like Supernovae (SNe) Type Ia (Riess et al., 1998; Perlmutter et al., 1999; Perlmutter & Schmidt, 2003), GRBs can potentially be used as cosmological probes of the distant universe and constrain cosmological models. The standardization of GRBs is based on phenomenological correlations between spectral properties and energetics. The Amati relation (Amati et al., 2002; Amati, 2006b; Amati et al., 2008), which is a correlation between the isotropic emitted energy, E_{iso} , within T_{90} duration and the spectral energy corrected for redshift, $E_{\text{i,p}}$, at which the time-averaged νF_ν spectrum peaks, has been the most studied correlation so far. Only LGRBs follow this correlation but no convincing physical explanation has been given. SGRBs are known to be inconsistent with the $E_{\text{i,p}} - E_{\text{iso}}$ correlation for LGRBs as explored by Ghirlanda

et al. (2009). Selection effects including detector artifacts may also play an important role in the Amati relation (Ghirlanda et al., 2005; Butler et al., 2007; Li, 2007; Ghirlanda et al., 2008; Butler et al., 2009, 2010; Kocevski, 2012; Collazzi et al., 2012). Nevertheless, the strong $E_{i,p}$ - E_{iso} correlation achieved in several studies has not precluded their use as cosmological standard candles. In astronomy, standard candles are the standardized references utilized by cosmologists to measure distances in the expansion of the universe. These are sources that have a known intrinsic luminosity, i.e., how much photon is emitted by the object at cosmological source frame. Then comparing this amount with the apparent luminosity (i.e., amount of photon from the objects reaches the observer), one can measure how far away the object is from an observer.

Another important phenomenological correlation is the Yonetoku relation (Yonetoku et al., 2004), which is a correlation between the $E_{i,p}$ and isotropic peak luminosity L_{iso} of LGRBs. The SGRBs also follow the same correlation (Ghirlanda et al., 2009; Zhang et al., 2012a,b) as LGRBs. The $E_{i,p}$ - L_{iso} correlation has been also carefully studied by others (Ghirlanda et al., 2010; Zitouni et al., 2014) and the interpretation of scattering from the Yonetoku plane as due to the opening angle distribution of GRB jets was explored (Ghirlanda et al., 2005). Besides Nava et al. (2009); Ghirlanda et al. (2010, 2012b); Dainotti & Amati (2018) studied this relation whether it has a physical origin or is due to the instrument selection effects. Their possible origins have also been discussed by Yonetoku et al. (2010) even if they cannot be accountable for the existence of the $E_{i,p}$ - L_{iso} correlation. This correlation can be used as a useful cosmological tool to investigate the physical environment of the early universe (Ghirlanda et al., 2006; Schaefer & Collazzi, 2007) and also as a redshift estimator (Yonetoku et al., 2004).

The correlations between the spectral peak energy and energy output for LGRBs have important implications both for the theoretical understanding of the burst physics and for the application of GRBs possibly as cosmological tools (Ghirlanda et al., 2004a, 2006; Amati et al., 2008; Cardone et al., 2009; Tsutsui et al., 2009; Demianski & Piedipalumbo, 2011; Wang et al., 2016; Demianski et al., 2017). To date, there is no clear consensus has been reached on the physical interpretation of these correlations (Eichler & Levinson, 2004; Levinson & Eichler, 2005). However, interesting progress has been recently made to answer this question by studying the comoving properties of GRBs (Panaitescu, 2009; Ghirlanda et al., 2012a).

1.1 Motivation for the study

Traditionally, SNe Type Ia have been used as standard candles in cosmology because of the relatively predictable intrinsic brightness based on their light curve structure (Riess et al., 1998; Perlmutter et al., 1999; Perlmutter & Schmidt, 2003). However, one can only reach a redshift $z < 2$ using SNe Type Ia as distance ladders. GRBs can be a good candidate to determine dark-energy and cosmic expansion, like SNe Type Ia, once its radiation can be considered as standard candles. The study of GRBs associated with cosmological parameters is a novel research area since they

have been observed up to a very high redshift, $z \sim 9.4$ and their γ -ray emissions are unencumbered by any obstructing dust. The phenomenological Yonetoku (i.e., $E_{i,p} - L_{iso}$) and Amati (i.e., $E_{i,p} - E_{iso}$) relations have been the most studied correlations so far. These phenomenological relations can be used as potential cosmological probes that might help to constrain cosmological parameters (Liang & Zhang, 2005; Ghirlanda et al., 2006; Amati et al., 2008; Cardone et al., 2009; Tsutsui et al., 2009; Demianski & Piedipalumbo, 2011; Wang et al., 2016; Demianski et al., 2017), and to probe the physics of GRBs (Thompson et al., 2007). The reliability of these correlations is being studied to make a big impact on the study of cosmological models with GRBs. Detailed modeling of time-integrated spectra of a uniform bright GRB sample from single spacecraft instruments, such as *Fermi*-GBM/LAT may increase the reliability of $E_{i,p}$ and E_{iso} measurements of the Amati relation to study cosmology. Extending the validity of the Yonetoku relation for the *Fermi*-GBM and the *Swift*-Burst Alert Telescope (BAT) sample of GRBs is also interesting to calibrate the fit parameters precisely and used to estimate cosmological parameters. Constraints on a flat Λ CDM cosmological model with two free parameters such as the Hubble constant (H_0) and the dark-energy density (Ω_Λ), can be explored with Amati and Yonetoku relations for GRBs.

1.2 Objectives of the research

The prime objective of this study is to model radiation from GRBs and standardize these objects as cosmological standard candles, similar to SNe Type Ia. The standardization of GRBs is based on relations between two or more parameters found from spectral modeling, of which one is strongly dependent on the cosmological model. In this work, we use the Amati and Yonetoku phenomenological correlations of GRB prompt emission to probe cosmological models.

In order to analyze the Yonetoku relation, the $E_{i,p}$ and L_{iso} were computed for all long GRBs with measured redshift from the *Fermi*-GBM and the *Swift*-BAT satellites reported in the catalog, until the end of December 2017. The GBM has large sky coverage and is less sensitive than the BAT. Most GRBs that trigger GBM are also visible to BAT. Moreover, the observed GBM spectral peak energy and flux values are higher than the BAT sample. So, it is interesting to study the correlation of each sample of the GBM and BAT GRBs. Using the coefficients of the correlation obtained from the analyzed samples of GRBs and also combining with the updated SNe Type Ia data, we construct an extended GRB Hubble diagram up to high redshift and constrain cosmological parameters.

Besides, we have presented a time-integrated joint spectral analysis of the GBM and LAT over T_{90} duration for 26 GRBs with known redshift which were detected by the *Fermi*-LAT during 2008–2017 period. We conducted an analysis of the Amati relation for the sample of 25 LGRBs while 1 SGRB appears as an outlier. Subsequently, we use the calibrated fit parameters to construct the extended Hubble diagram and estimate the Hubble constant and dark-energy density in the Λ CDM model using, a) the *Fermi*-LAT/GBM GRBs alone, b) *Fermi*-LAT/GBM

together with another sample of 94 GRBs and c) with the latest SNe Type Ia.

1.3 Summary of the main results

This section recapitulates the main results of this thesis. Having discussed the correlation of GRB energetic and spectral properties, two main phenomenological relations namely the Yonetoku and Amati relations are discussed to probe cosmological parameters and construct the GRB extended Hubble diagram.

1.3.1 Yonetoku relation

- We studied the validity of the Yonetoku relation for the *Fermi*-GBM and *Swift*-BAT samples of GRBs.
- We found the L_{iso} of GBM sample is higher than the BAT sample.
- We constructed the Hubble diagram to redshift 5.46 and constrain the Hubble constant (H_0) and dark-energy density (Ω_Λ) with different samples of GBM and BAT GRBs and combining with the latest SNe Type Ia data.
- The obtained results are consistent with the currently acceptable ranges of H_0 and Ω_Λ but with large errors. However, with the present GBM and BAT samples of GRBs Ω_Λ and H_0 cannot be meaningfully constrained.
- The partial correlation coefficients between $E_{\text{i,p}}$ and L_{iso} by removing the effect of redshift was determined.

1.3.2 Amati relation

- First, we have performed a detailed time-integrated spectral analysis over T_{90} duration of GRBs detected by the *Fermi*-LAT and GBM in 9 years of operation.
- The results of the jointly fitted spectra from these detectors showed that multiple components are required for some GRBs, thus increasing the reliability of the $E_{\text{i,p}}$ and E_{iso} measurements.
- The result of the spectral analysis enabled us to extend the calculation of E_{iso} to 100 MeV.
- The Amati relation for GRBs emitted at > 100 MeV energy range was tested.
- The Amati relation is satisfied by the 25 LGRBs, with fitting parameters similar to previous studies that used data from different satellite instruments, while the only short GRB with known redshift is an outlier.
- We compared the *Fermi* samples of GRBs with Wang et al. (2016) sample of 94 GRBs with updated E_{iso} in the 1 keV–10 MeV energy range. These GRBs were collected from observatories such as *CGRO/BATSE*, *BeppoSAX*, *HETE-2*, *Konus-Wind*, *Suzaku-WAM* and *Swift*-BAT without including the *Fermi*-LAT bursts.

- We extended the GRB Hubble diagram to redshift 8.2, and constrain H_0 and Ω_Λ , with the *Fermi*-LAT/GBM GRBs together with [Wang et al. \(2016\)](#) sample and with the latest SNe Type Ia data.
- The obtained results are consistent with the currently acceptable ranges of those cosmological parameters.
- We further investigated the partial correlation coefficient of the $E_{i,p}$ and E_{iso} by removing the effect of redshift.
- We have also studied the sensitivity of the Amati relation to the initial choice of cosmological parameters (H_0 and Ω_Λ). We explored that normalization of the Amati relation strongly depends on the initial choice of H_0 . On the other hand, the Amati relation parameters are only slightly sensitive to the initial choice of Ω_Λ . The mild dependence on Ω_Λ results from the fact that the luminosity and isotropic emitted energy which depends more strongly on H_0 than Ω_Λ .
- Currently, the GRB sample is small and quality of the Amati relation is poor to make a big impact in the cosmological study with GRBs, but possibilities remain open with future big data sets.

At present, the stability and reliability of the phenomenological Amati and Yonetoku relations are inadequate to make a big impact in the cosmological study with GRBs but possibilities remain open with a future large number of data sets.

1.4 Organization of the thesis

The focus of this study is to bring more information about the phenomenological correlation of GRB prompt emission based on the Yonetoku and Amati relations using observational data mainly from the *Fermi* and *Swift* observatories. These correlations may facilitate to construct standard candles with GRBs to probe a cosmological model.

The structure of this thesis is as follows. In Chapter §2 we provide the background information on GRBs and a brief overview of GRB observatories including both space and ground-based GRB telescopes. We present the history and classification scheme, the types of emission mechanisms of the bursts which allow a better understanding of the physics of GRB prompt and their afterglow emission. Further, we describe the temporal and spectral properties of GRBs and their afterglow emission. Chapter §3 deals with the details of *Fermi* telescopes used for high-energy GRB prompt emission research. We shall focus on the explanation of the observing strategy followed to maximize the prompt emission within T_{90} duration and the data reduction techniques. We also discuss the performance of *Fermi* for GRB studies, their spectral and temporal characteristics. This chapter shows my contribution in the collaboration as “Burst Advocate” on-duty activities. Chapter §4 is entirely devoted to the discussion of cosmological implications of GRBs. In this chapter, we analyze the luminosity and cosmological constraints from GRBs.

Chapter §5 presents an in-depth analysis of the Yonetoku relation for different samples of GRBs from the *Fermi*-GBM and *Swift*-BAT observations. This chapter focuses on the estimation of cosmological parameters and constructing the Hubble diagram using the parameters obtained from the analysis of correlation. Chapter §6 is an extension on the work of Amati relation, in which we render a detailed analysis of the *Fermi* observation of bright GRBs including the GBM, LAT and LLE data. A detailed analysis of Amati relation was employed to constrain the Hubble constant H_0 and dark-energy parameter Ω_Λ in a flat Λ CDM cosmological model. In Chapter §7 we summarize the main results of the thesis and discuss future perspectives for the extension of the present work. Appendix §A contains the derivation of a smoothly-broken power-law model. Appendix §B contains the catalog of the *Fermi*-GBM (Gruber et al., 2014; von Kienlin et al., 2014; Narayana Bhat et al., 2016a) and the *Swift*-BAT (Lien et al., 2016) spectral fitting parameters of GRBs with identified redshift and the reanalysis of W2016 data (Wang et al., 2016). Finally, in Appendix §C, the computed de-correlation energy and their plots for different samples are presented. In this Appendix, we also present the analysis of multivariate normal distribution.



CHAPTER
2

HISTORICAL BACKGROUND AND PHENOMENOLOGY

Contents

2.1	Early observations	10
2.1.1	The Interplanetary Network	11
2.1.2	The Burst and Transient Source Experiment	11
2.1.3	<i>Konus-Wind</i>	13
2.2	Observations in the afterglow era	14
2.2.1	<i>BeppoSAX</i>	14
2.2.2	HETE-2	14
2.2.3	The <i>Swift</i> mission	15
2.3	Observations of high-energy emission	16
2.3.1	<i>Energetic Gamma-Ray Experiment Telescope</i>	16
2.3.2	<i>INTEGRAL</i>	18
2.3.3	<i>AGILE</i>	19
2.3.4	<i>Fermi</i>	20
2.4	GRB alerts in the future from space-based detectors	25
2.5	Ground-based air cherenkov telescopes for GRB detections	25
2.6	GRB phenomenology	29
2.6.1	Prompt emission	29
2.6.2	Spectral models	31
2.6.3	Prompt emission spectra in the keV/MeV–GeV range	33
2.6.4	Fluences and Fluxes	34
2.6.5	Afterglow emission	35
2.6.6	GRB emission mechanism	36
2.7	Summary	38

In this chapter, we describe the earliest, current and future GRB detectors both in space and on the ground. We also present the GRB phenomenology, in particular, the types of emission mechanisms of the bursts, which allow a better understanding of the physics of GRB emission. Further, we describe the temporal and spectral properties of GRBs and their afterglows.

2.1 Early observations

Gamma-ray astronomy is the study of astronomical objects in the limit of very few and energetic photons they radiate. In this astronomical observation of γ -rays, GRBs represent bright transient astrophysical events in the universe. GRB was first discovered on July 2 in 1967 ([Klebesadel et al., 1973](#)). The burst was named as GRB 670702 following Year-Month-Date (YYMMDD) format. It was an unexpected astronomical detection, accidentally triggering Vela military satellites. The motive was to seek the signature of γ -ray radiation from forbidden nuclear weapons in the Earth's atmosphere in order to check that other countries were not breaking the International Test Ban Treaty of 1963. No nuclear test was detected, instead extra-terrestrial, brief and intense bursts of γ -rays were recorded. GRB 670702 showed two peaks over a period of seconds (see its count light curve in Fig. 2.1); however, the result of this GRB was reported six years later in a seminal paper with other fifteen short GRBs (see the description of short GRB in Sec. 2.1.2) detected between 1967 and 1972 ([Klebesadel et al., 1973](#)). The observations of these GRBs were made

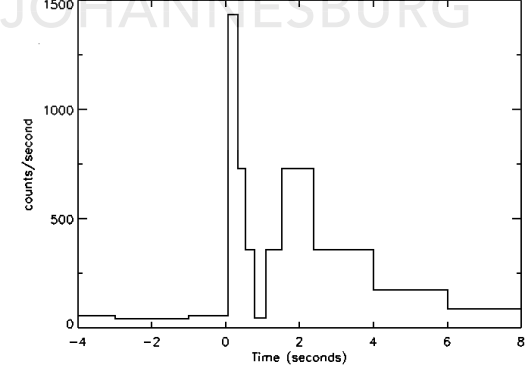


Figure 2.1 GRB 670702 light curve ([Robert & Jerry, 2000](#)).

by CsI scintillation counters of Vela 5 and Vela 6 in the 200 keV–1 MeV and 300 keV–1.5 MeV energy range, respectively. The measured total fluence was in the range between 10^{-5} erg cm $^{-2}$ and 2×10^{-4} erg cm $^{-2}$ ([Klebesadel et al., 1973](#)).

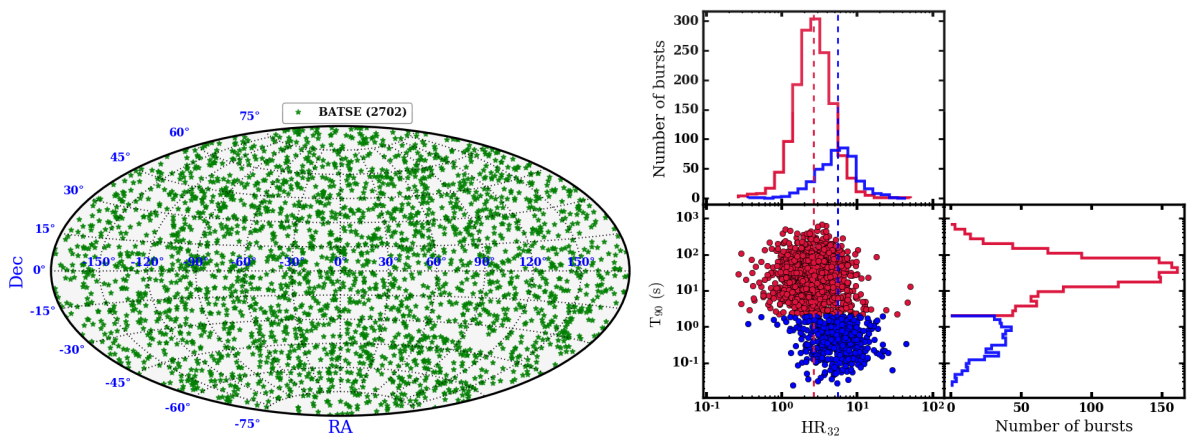
2.1.1 The Interplanetary Network

The count light curves of GRBs observed by Vela showed several “spikes” but there was no way to identify their localization, which originated well outside of our own galaxy. Due to the relatively poor localization capabilities of the burst, it was difficult to follow-up their afterglow counterpart observation with other telescopes.

The 1970s, *French-Soviet program SIGNE* in collaboration with US spacecraft equipped with GRB detectors so-called the *Interplanetary Network* (IPN) was launched to search the direction of GRBs arrivals (Niel et al., 1976). IPN was also used to study the fine time structure and evolution of the energy spectrum of bursts at different time resolution. The timing accuracy of this instrument was ~ 10 ms which allows determining the arrival direction of GRBs with a precision of $\sim 5'$. The experiment of IPN started its golden age by detecting 82 GRBs from 1978 to 1980 (Atteia et al., 1987). About $\sim 79\%$ of the bursts were localized to annuli region, single or double error boxes. This confirmed that the IPN GRBs were isotropically dispersed in the sky without repeated bursts from the same source (i.e., no more than one burst from any source position).

2.1.2 The Burst and Transient Source Experiment

In 1991, a highly sensitive experiment covering 20 keV–2 MeV energy range, the Burst and Transient Source Experiment (BATSE, Fishman et al., 1985), on board the *Compton Gamma Ray Observation* (*CGRO*) provided a better position of the bursts. The position of the GRB was obtained from the relative counting rates of the detectors based on Earth’s occultations. The error distribution of GRB locations was obtained by modeling distribution of the separation between BATSE locations and IPN annuli (Briggs et al., 1999a). The other three experiments on *CGRO*



include: *OSSE* (*Oriented Scintillation Spectrometer Experiment*), *COMPTEL* (*Compton Telescope*) and *EGRET* (*Energetic Gamma Ray Experiment*) covered the energy ranges 100 keV–10 MeV, 1 MeV–30 MeV and 20 MeV–30 GeV, respectively. In order to detect GRB and other transient sources, BATSE used eight identically configured detecting scintillators located at the edges of the spacecraft (Briggs et al., 1999b). Each detector had two NaI(Tl) of a *Large Area Detector* (LAD) used for directional response and sensitivity, and a *Spectroscopy Detector* (SD) used for the coverage of energy and resolution. The combination of these detectors allowed the BATSE to have the ability to localize weak bursts and study their possible spectral features. The detection of 1005 GRBs reported in the third BATSE catalog (Briggs et al., 1996) GRBs are isotropically distributed in the sky. For 2702 GRBs reported by (Briggs et al., 1996; Paciesas et al., 1999), we have shown the distributions of these bursts in the left panel of Fig. 2.2. Following the analysis of burst duration of GRBs, the BATSE collaboration introduced the bimodal burst distribution based on T_{90} . This represents a time at which 5% to 95% of the burst fluence is detected. This led GRBs to classify as long duration burst with $T_{90} \gtrsim 2$ s and short-duration burst with $T_{90} \lesssim 2$ s (Kouveliotou et al., 1993). In the right-hand side of Fig. 2.2, we illustrate the distributions of short GRBs (blue symbols) and long GRBs (crimson symbols). In addition to these two main population of bursts, Howell & Coward (2013) also introduced other sub-population of GRBs based on their redshift and peak flux distributions. Furthermore, new ultra-long duration bursts have been observed with duration up to 100 times greater than typical long bursts (Levan et al., 2014).

One can study the spectral hardness ratio (HR) of the GRBs. For instance, HR_{32} is the ratio of fluence in 100–300 keV energy range over fluence in 50–100 keV energy range. We show the distribution of T_{90} and hardness ratio HR_{32} for short (blue) and long (crimson) GRBs in the right panel of Fig. 2.2. To test the correlation between T_{90} and HR_{32} , we used the Pearson correlation coefficient (Bevington et al., 1993). The results show a low anti-correlation value with - 0.062 for long GRBs and - 0.057 for short GRBs. The median of the HR_{32} of 1488 LGRBs and 464 SGRBs are about 2.63 and 5.53, respectively. Hence, the LGRBs are softer and the SGRBs are harder.

The most significant characteristic of GRB prompt emission is their light curve profiles (see Fig. 2.3). Regardless of some pattern observed among them, the light curve is unique for each GRB. The light curve profiles of the bursts can be classified as smooth (either single or multiple, well-defined peaks), fast rise and exponentially decay with single pulse (i.e., GRB 910711 and GRB 921022B), fast rise and smooth exponential decay with single pulse (i.e., GRB 990316A), fast rise with spike events (i.e., GRB 910503), quasi-exponential decays and distinct (well separated episodes) peaks spanning from time-scales of milliseconds to minutes. A few GRBs show precursors precede to the main emission (i.e., GRB 920221, GRB 921123B, GRB 940210 and GRB 990316A).

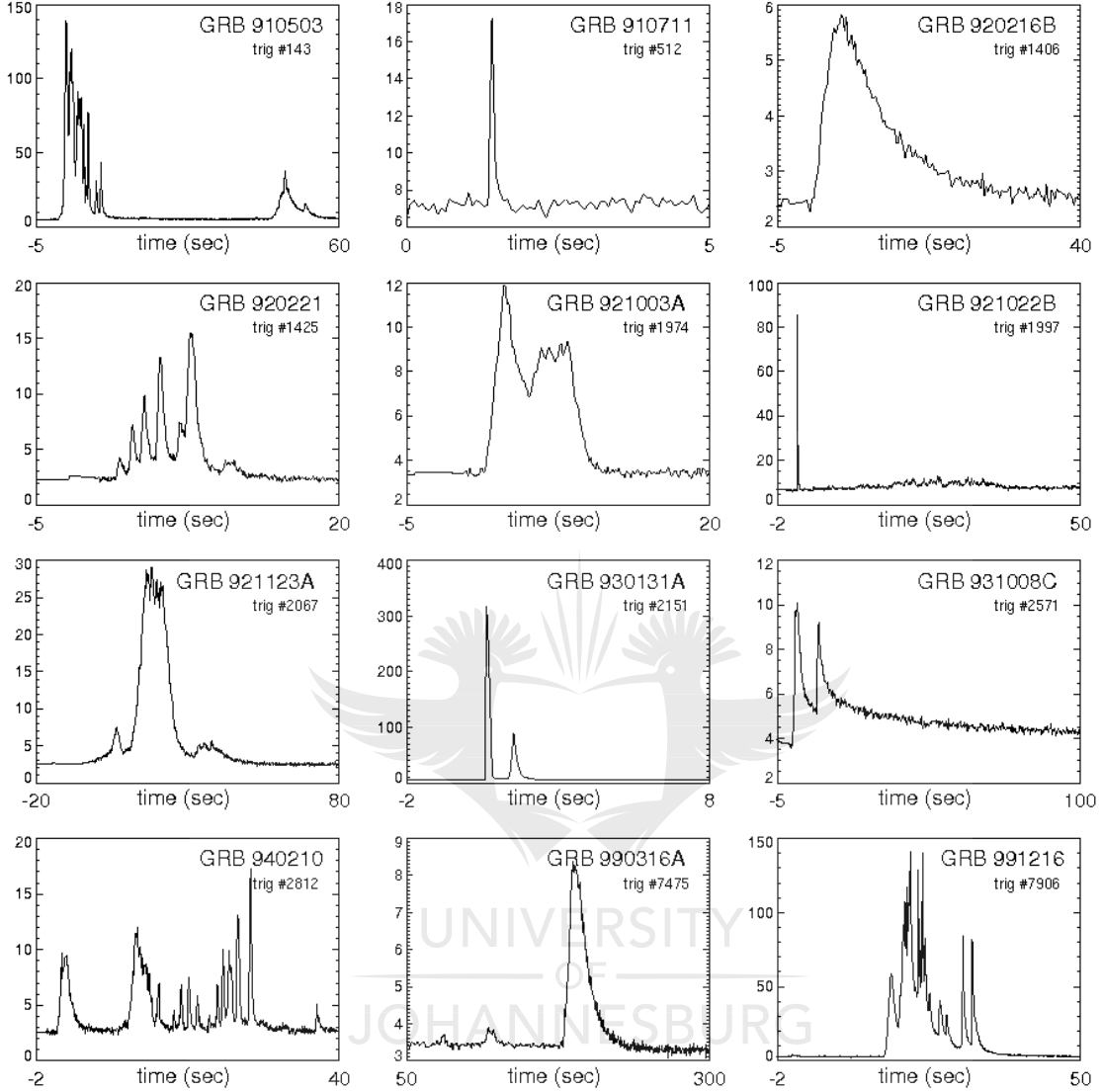


Figure 2.3 Diverse light curves of the GRBs prompt emission detected by BATSE instrument. This sample includes short and long events. <https://gammaray.nsstc.nasa.gov/batse/grb/lightcurve/>

2.1.3 Konus-Wind

The *Konus* instrument of GRB monitor, on board the Wind satellite is the first Russian experiment on a NASA science mission (Terekhov et al., 1998). It was launched in November 1994. *Konus* is a γ -ray spectrometer, which consists of two identical γ -ray sensors S1 and S2. Each of the detectors has 2π sr field of view (FoV), which observes the southern and northern ecliptic hemispheres in all-sky monitoring mode (Swinkin et al., 2016) in the 0.02–20 MeV¹ energy range with a time resolution of 2–256 ms. *Konus* has an advantage over other Earth-orbiting instruments,

¹<http://www.ioffe.ru/LEA/kw/>

for instance, the BATSE GRB monitor, because it has the potential to provide uninterrupted coverage of necessary information on GRBs.

The *Konus-Wind* experiment has made an impressive number of important GRB observations. The GRB spectrometer has observed 150 GRBs. Of these, about 8% of them being SGRBs with measured redshifts. Most of the observed LGRBs with identified redshift were used in the analysis of GRBs phenomenological correlations to study cosmological model ([Tsvetkova et al., 2017](#)).

2.2 Observations in the afterglow era

2.2.1 *BeppoSAX*

The Italian/Dutch X-ray satellite *BeppoSAX* was launched on April 30, 1996 ([Boella et al., 1997](#)) and was dedicated to detect, localize and follow up a few GRBs on very short time scales. The two instruments on *BeppoSAX* satellite, which allowed accurate GRB localization include the *Gamma-Ray Burst Monitor (GRBM, 40–700 keV)* and *Wide Field Cameras (WFC, 2–26 keV)*. The GRBs were localized with a precision of $\sim 3'$. The third one was the *Narrow Field Instruments (NFIs, 0.1–300 keV)* and it included four X-ray focusing telescopes. On February 28, 1997, the first X-ray afterglow for GRB 970228 was observed by *BeppoSAX* ([Costa et al., 1997](#)). The detection of its optical afterglow was also reported by [Groot et al. \(1997\)](#). The spectroscopic redshift of this GRB was about 0.835 ([Bloom et al., 1998](#)).

During its 6 years of observation period from 1996 to 2002, *BeppoSAX* provided the most exciting observations association to GRBs. The key elements of its success were as follows:

- The ability of detectors to locate a position of the event in arcminute in a few hours.
- The ability to discover GRB afterglow emission at multiwavelengths in order to make a breakthrough in setting their distance scale and clarified the cosmological origin of GRBs.
- The discovery of GRBs with measured redshift to use them for cosmological aspects.

2.2.2 *HETE-2*

The High-Energy Transient Explorer 2 satellite (*HETE-2*, [Ricker et al., 2003](#)) was put in equatorial orbit on October 9, 2000. The aim was to quickly localize GRBs with precise coordinates and send the position in real-time to the ground telescopes for afterglow follow up in the optical and radio wavelengths. To accomplish this mission, *HETE-2* carried three main science instruments: the *French Gamma-ray Telescope (FREGATE, 6–400 keV)*, the *Wide-field X-ray Monitor (WXM, 2–25 keV)* and a set of *Soft X-ray Camera (SXC, 0.5–10 keV)*. Compared to previous missions, *HETE-2* had the capability to provide an accurate position of GRBs faster than *BeppoSAX*, since all of its instruments are simultaneously looking into the sky.

FREGATE was the most sensitive instrument with the largest FoV of 4 sr but was unable to localize GRBs with any reasonable precision ([Pizzichini et al., 2004](#)). This instrument had

four sets of NaI crystal scintillators. Each of them was associated with shielding, pulse height analyzers, discriminators, photomultiplier tubes (*PMT*) and digital electronics to detect GRBs. Besides, the composition of these scintillators helped to study the spectro-temporal profiles of GRBs. The *WXM* and *SXC* detectors allowed sky localization of GRBs with about 10' and 20'' precision, respectively (Ricker et al., 2003). *WXM* was the first instrument that quickly provided a refined localization of GRBs on board and sends the position to the ground telescopes for follow-up of the afterglow counterparts. GRB 021211 was first detected by HETE-2 and its early afterglow has been observed (Fox et al., 2003).

From 2001–2006, HETE-2 observed more than 300 GRBs. Of those, about 84 were localized accurately. GRB 030329 was the first LGRB associated with a supernova on the basis of similarities among the spectra of its optical afterglow. The discovery of short GRB 050709 (Fox et al., 2005), whose X-ray afterglow was identified, gives a clue about the mystery of SGRB progenitor by identifying the host galaxy of the burst at redshift $z = 0.16$ (Fox et al., 2005).

2.2.3 The *Swift* mission

The *Swift* mission (Gehrels, 2004) was launched on 20 November 2004. It was designed for the main scientific goal of observing GRB prompt emission and follow-up the afterglow phases. Neil Gehrels had been the principal investigator for *Swift*. After his death in February 2017, *Swift* is renamed as the *Neil Gehrels Swift Observatory*. To optimize its scientific potential, the *Swift* satellite is equipped with three telescopes. These cover from ultraviolet to γ -ray wavebands providing the temporal and spectral information of the events.

A *Swift* observation starts with the Burst Alert Telescope (BAT, Barthelmy et al., 2005), which detects the transient position with an accuracy of 3'. *Swift* slews to the event within seconds and the *X-ray Telescope* (XRT, Burrows et al., 2005) and the *Ultra-violet/Optical Telescope* (UVOT) start to observe. *Swift* has the ability to look at the alteration between the prompt emission and X-ray afterglow emission. The observations by both the XRT and UVOT render a better location of the event with a precision of arcsec.

The BAT (Barthelmy et al., 2005) has a coded imaging aperture of the sky ~ 1.4 sr and is a photon-counting detector, covering 15–150 keV energy range. It has an area of 5200 cm^2 and localizes the burst direction to the precision of 1'–3' within a few seconds after the burst onset. This position can be also uploaded from other satellites through a real-time *Tracking and Data Relay Satellite System* (TDRSS) uplink (Gehrels, 2004). BAT detected more than 1199 GRBs between November 2014 and March 2018 (see the left side panel of Fig. 2.4). This indicates more than 90 GRBs are detected by BAT per year. The diversity and uniform distribution of GRBs observed by BAT (magenta stars) and BATSE (green stars) on the same sky map is shown on the left side of Fig. 2.4.

The XRT (Burrows et al., 2005) is a focusing X-ray telescope with 12 fixed mirrors that focus onto a CCD detector. This instrument covers 0.2–10 keV energy range in the 23' FoV. It

can improve the burst location reported by BAT to within $3''$. UVOT is an Ultra-violet/Optical Telescope which is co-aligned with the XRT, takes images and obtains spectra of GRB afterglows during pointed follow-up observations. UVOT allows broadband UV-visible photometry with low-resolution spectra of energetic GRBs in 170–600 nm bands. These spectra are used to check redshifts and Lyman-alpha cutoffs while the images are used to localize the position in $0.3''$ – $2.5''$ range. The UVOT has a field of view of $17' \times 17'$ with $0.3''$ position accuracy.

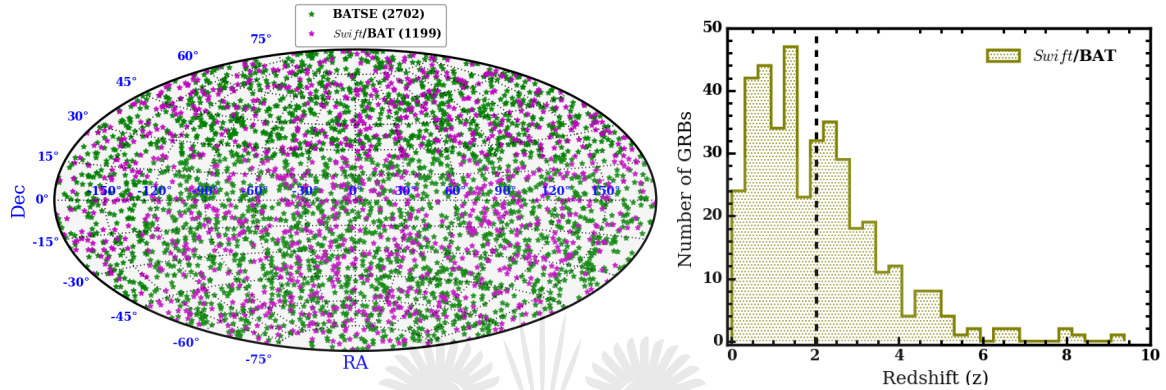


Figure 2.4 *Left panel:* sky distribution of 1199 *Swift*-BAT GRBs detected from November 2014 to March 2018 (magenta stars, Lien et al., 2016) and 2702 *CGRO*/BATSE (magenta stars, Meegan et al., 1996; Paciesas et al., 1999) detected GRBs in Galactic coordinates and Hammer-Aitoff projection. *Right panel:* the redshift distributions of 405 GRBs detected by *Swift*-BAT. The vertical dashed line shows the mean (~ 2.03) of the redshift distributions.

Swift has detected more than 400 GRBs with measured redshift. Of these, more than 35% have the spectroscopic or photometric redshifts from optical fellow ups. The highest photometric redshift, $z \sim 9.4$ is registered for GRB 090429B (Cucchiara et al., 2011). The burst occurred when the universe was 520 million years old. The distributions of these redshifts are shown on the right panel of Fig. 2.4.

2.3 Observations of high-energy emission

2.3.1 Energetic Gamma-Ray Experiment Telescope

The *Energetic Gamma-ray Experiment Telescope* (*EGRET*) was equipped to detect high-energy γ -rays from 20 keV to 30 GeV for the *CGRO*. The instrument had an energy resolution of $\sim 20\%$ with sensitivity higher than earlier γ -ray telescopes. As the main device for measuring energy, it used a large NaI(Tl) *Total Absorption Shower Counter* (TASC) of multilevel spark chamber, triggered by a scintillator anti-coincidence system (Thompson et al., 1993). The spark chamber had a capability of detecting GRBs and would sensitive to γ -rays above 30 MeV with a very high-energy resolution. This provides a large effective area above 1000 cm^2 in the energy range between 100–300 MeV. It allowed achieving an angular resolution of $\sim 0.54^\circ$ above 1 GeV energy.

2.3. OBSERVATIONS OF HIGH-ENERGY EMISSION

It also detected photons via electron-positron pair production and provided its arrival direction ([Thompson et al., 2005](#)). The arrival time of each photon was measured in Universal Coordinated Time (UTC) with an accuracy $> 100 \mu\text{s}$. The *EGRET* pointing direction was altered during each 93-minute orbit and covered more than 30° from the axis of the instrument ([Thompson et al., 1993](#)).

Table 2.1 Main GRB detector of the past, present, and future satellites.

Missions	Operation Periods	Instruments	Energy Range	Localization Accuracy
Vela	1965–1979	multiple satellites	200 keV–1.5 MeV	$10'$
IPN	1978–1980	multiple satellites	20 keV–1 MeV	$5'$
<i>CGRO</i>	1991–2000	BATSE	20 keV–1 MeV	$3\text{--}4^\circ$
		<i>EGRET</i>	20 MeV–30 GeV	
Wind	1994–	<i>Konus</i>	10 keV–20 MeV	$5\text{--}20^\circ$
<i>BeppeSAX</i>	1996–2002	GRBM	40–700 keV	$1\text{--}3'$
		WFC	2–26 keV	
		NFIs	0.1–300 keV	
HETE-2	2000–2006	FREGATE	6–400 keV	$3\text{--}15''$
		WXM	2–25 keV	
		SXC	0.5–10 keV	
INTEGRAL	2002–	SPI/ACS	20 keV–8 MeV	$10\text{--}20'$
		IBIS	15 keV–10 MeV	$<1'$
<i>Swift</i>	2004–	BAT	15–150 keV	$1\text{--}3'$
		XRT	0.2–10 keV	$3''$
		UVOT	170–650 nm	$0.3''$
<i>AGILE</i>	2007–	GRID	30 MeV–50 GeV	$5\text{--}20'$
		SA	15–45 keV	$1\text{--}3'$
<i>Fermi</i>	2008–	LAT	20 MeV– $\gtrsim 300$ GeV	$0.2\text{--}0.5^\circ$
		GBM	8 keV–40 MeV	$\sim 10\text{--}15^\circ$
SVOM	2021–	ECLAIRs	4–120 keV	$>12'$
		GRM	50 keV–5 MeV	

EGRET had a limited effective area, which led to the detection of a few bright GRBs. A long duration GRB 940217 lasted about 5.4×10^3 s ([Hurley et al., 1994](#)), suggest that the prompt

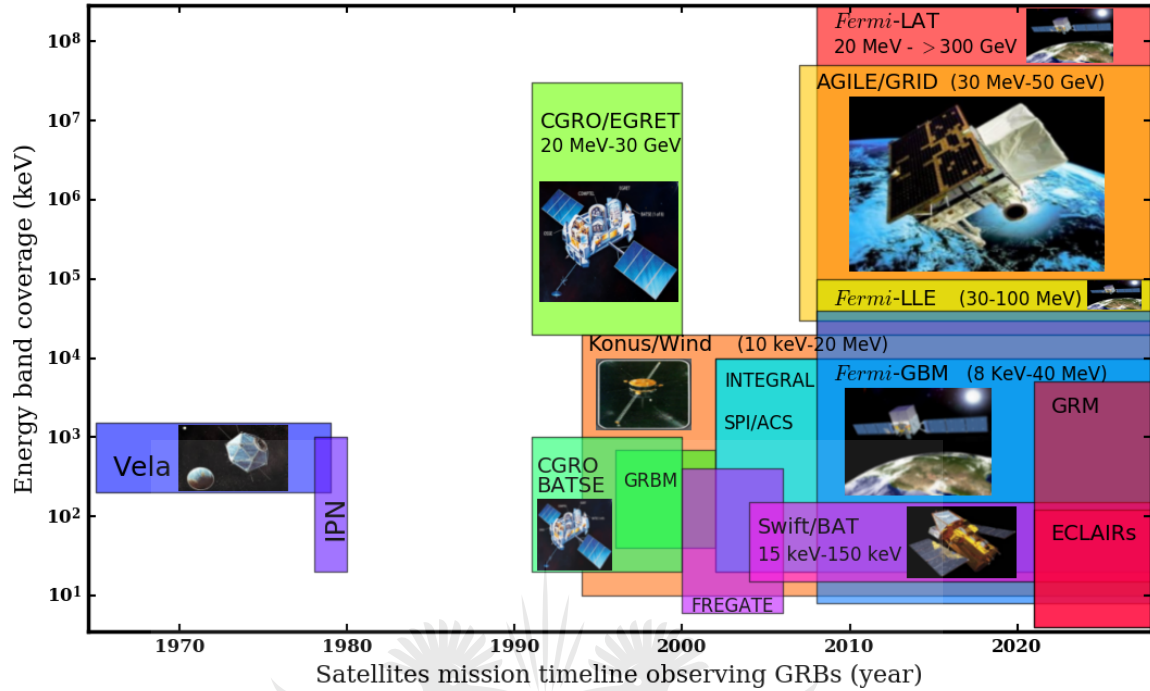


Figure 2.5 History of observational gamma-ray astronomy from Vela satellites in the early 1960s to the future mission SVOM satellite, scheduled for launch in 2021 (see Tab. 2.1).

emission could last longer than the hard X-ray band. The γ -ray photon with the highest energy from the direction of GRB 940217 was 20 GeV. The *EGRET* GRB 990123 is the first GRB whose X-ray and optical emission counterparts were observed and followed by extensive radio observations (Briggs et al., 1999b).

2.3.2 INTEGRAL

The European Space Agency's *INTERnational Gamma-Ray Astrophysics Laboratory (INTEGRAL)*, Winkler et al., 2003) was launched on 17 October 2002. The *INTEGRAL* satellite carries two main γ -ray telescopes: the image recording device (*IBIS*, 15 keV–10 MeV energy range, Ubertini et al., 2003) and the spectrometer (*SPI*, 20 keV–8 MeV energy range, Vedrenne et al., 2003). Besides, another two monitoring science instruments are operating at X-ray band (JEM-X, 3–35 keV) and Optical Monitoring Camera (OMC) in optical Johnson V-band (Mas-Hesse et al., 2003). Such capabilities provide essential information about the physics and nature of events over a broadband wavelength. Overall, it covers an energy range from 3 keV to 10 MeV, where we expected breaks in the power-law distribution in a typical GRB.

The *IBIS* imager provides a fully coded FoV of 9×9 degrees (Produit, 2003). It was designed for high angular resolution, which requires the detector(s) to have a fine pixelation. *IBIS* also used for accurate time measurements. The *SPI* has coaxial Germanium (Ge) detectors with a

characteristic size of 7 cm serving as pixels below a large coded mask. Its angular resolution of 2.5° allows a typical point-like source localization of $10'-20'$. The Anti-coincidence system of *SPI-ACS* consists of 91 Bismuth Germanate (BGO) and covers most of the 4π sr solid angle with a large effective area of 0.3 m^2 . However, it does not include the spectral information, since the energy of an interacting γ -ray photon is not measured. All of the instruments except the optical monitor depend on the coded-aperture imaging to obtain directional information of the observed sources.

The main scientific objective of *INTEGRAL* is to increase our understanding of the most energetic astrophysical events in the universe and sites at which they occur. It is the first γ -ray telescope with a permanent real-time telemetry link and fine imaging capabilities, which permits the accurate localization of GRB in near real-time. Based on the first *INTEGRAL SPI-ACS* GRB catalog (Rau et al., 2005), 388 GRBs are listed in the sample for the first 26.5 months of the mission. This roughly shows us that the detector collects one GRB per two days.

2.3.3 *AGILE*

The small space satellite *Astro-rivelatore Gamma a Immagini LEGgero* (*AGILE*, Tavani et al., 2006) was launched on April 23, 2007. *AGILE* has been devoted to explore the γ -ray universe with a very innovative telescope composed of two main co-aligned imagers: *Gamma Ray Imaging Detector* (*GRID*, 30 MeV–50 GeV energy range) and a hard X-ray monitor, *Super-AGILE* (SA, 15–45 keV band). The third *AGILE* detector is a Mini-calorimeter (*MCAL*) operating in the “burst mode”. *AGILE* has a capability of independently observing GRBs and other transients in the 300 keV–100 MeV band with time resolution better than $2 \mu\text{s}$ (Tavani et al., 2006).

GRID contains a Silicon-Tungsten Tracker, a scintillator CsI(Tl) Calorimeter, and the Anticoincidence system. It was designed to achieve source locations with a precision of $5\text{--}20'$ for an intense source and has very large FoV (~ 2.5 sr), comparable with the *EGRET* (Fishman et al., 1985) performance for sources observed within $10\text{--}20^\circ$ off-axis. The SA (Feroci et al., 2007) is a coded mask imager made of a Silicon detector plane and a thin Tungsten mask positioned 14 cm above the *GRID* instrument. It has an optimal angular resolution of $6'$.

So far, a relatively small number of GRBs have been detected by the large calorimeter of the *EGRET* above MeV energy range. After the operational period of *EGRET*, GRB 080514B (Giuliani et al., 2008) was the first GRB detected by *AGILE* with photon energy up to 100 MeV and lasting somewhat longer than the soft γ -rays. In this burst, a time delay of GeV emission was observed. Initially, the precise position of the burst (RA, DEC) = $(322.82^\circ, 0.71^\circ)$ (see the left panel of Fig. 2.6 indicated by red circle) was estimated by *GRID* before it was localized by SA. Then, the hard X-ray emission was observed by SA that lasted ~ 7 s. The arrival time and energy are shown on the right panel of Fig. 2.6. We also showed the sky distribution of the *MCAL* GRBs in Galactic coordinates and Hammer-Aitoff projection (see the left panel of Fig. 2.6).

AGILE provides important information complementary to many space-based missions including

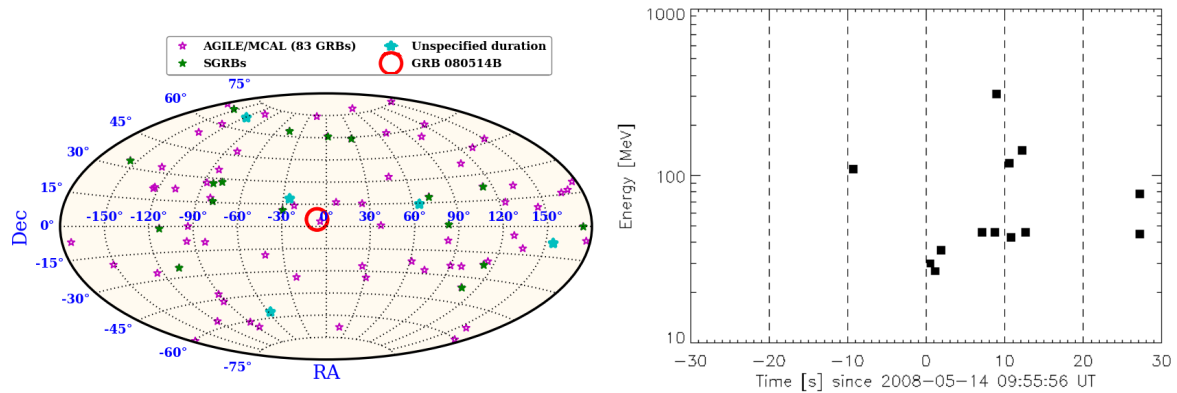


Figure 2.6 *Left panel:* sky distribution of 83 MCAL GRBs (i.e., 17 SGRBs with green stars, 61 LGRBs with magenta stars and 5 unknown GRBs with cyan stars) in Galactic coordinates and using Hammer-Aitoff projection. The data is taken from Galli et al. (2013). *Right panel:* energy of the photons from the direction of GRB 080514B detected by the GRID (Giuliani et al., 2008).

INTEGRAL (Winkler et al., 2003), *Swift* (Gehrels, 2004) and others. It supports the ground-based observations of the radio and optical wavebands. Besides, the main scientific capability of *AGILE* mission includes the improvement of *EGRET* angular resolution in a very large FoV with a good timing capability as well as a good sensitivity for point sources.

2.3.4 *Fermi*

The *Fermi Gamma-ray Space Telescope (FGST)* formerly known as the *Gamma-ray Large Area Space Telescope (GLAST)*, was successfully placed into orbit on 2008 June 11. The mission is a joint international collaboration of NASA with contributions from the United States *Department of Energy* (DOE) and government agencies of Germany, Italy, France, Sweden, and Japan². It is the latest and most sensitive γ -ray observatory in orbit to explore the high-energy part of the electromagnetic spectrum in the sky.

Fermi observatory carries two instruments: the *Large Area Telescope (Fermi-LAT*, hereafter LAT, 20 MeV– \gtrsim 300 GeV band, Atwood et al., 2009) and the *Gamma-ray Burst Monitor (GBM*, 8 keV–40 MeV band, Meegan et al., 2009). These two instruments together allow an unprecedented spectral energy range spanning more than seven decades.

2.3.4.1 Gamma-ray Burst Monitor

The Gamma-ray Burst Monitor (GBM, Meegan et al., 2009) is dedicated to monitoring the hard X-ray and γ -ray bursts, ideally suited to observe transient high-energy astrophysical phenomena such as GRBs, solar flares, Soft Gamma Repeaters (SGRs) and Terrestrial Gamma-ray Flashes (TGFs). The great advantage of GBM is its capacity to observe a large fraction of the sky (i.e., the

²<https://pac.slac.stanford.edu/research/fermi-gamma-ray-space-telescope>

2.3. OBSERVATIONS OF HIGH-ENERGY EMISSION

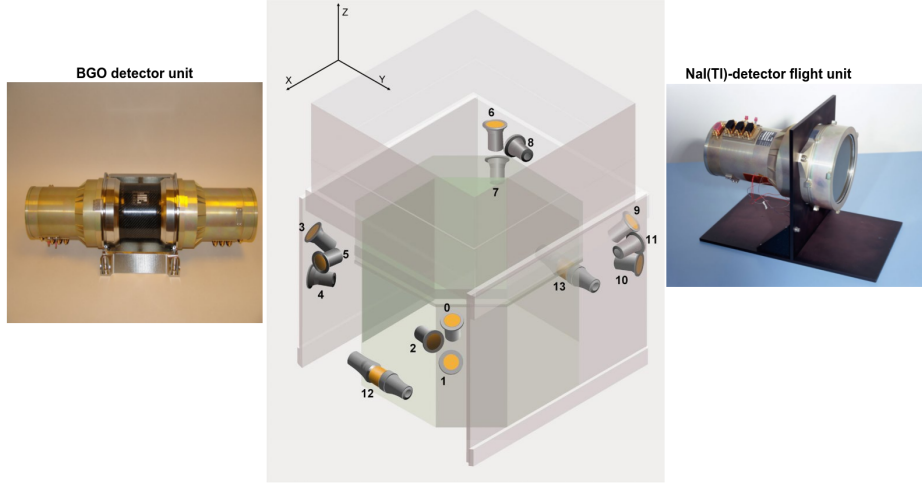


Figure 2.7 Schematics of orientation and location of the GBM detectors (Meegan et al., 2009). Twelve NaI detectors (right panel) are indexed 0–11 (n0–n11) and two BGO detectors (left panel) are denoted by 12 (b0) and 13 (b1) in the figure. The gray box of the middle Figure shows the location of LAT instrument.

part of the sky that is not occulted by the Earth) at any given time, resulting in a FoV of ~ 9.5 sr. It also has a very broad coverage of energy, about four decades. Besides, owing to its large FoV, high uptime, and localization capability, GBM was anticipated to detect the electromagnetic counterpart of gravitational-wave events from the Laser Interferometer Gravitational-wave Observatory (LIGO)/Virgo (Abbott et al., 2017).

The GBM flight hardware composed of 12 thallium activated sodium iodide (NaI(Tl)) and 2 bismuth germanate (BGO) scintillation detectors. The NaI(Tl) covers the ~ 8 keV–1 MeV energy range with a typical effective area of 100 cm^2 between 20 keV–1 MeV energy band as reported by Meegan et al. (2009), where most of the GRB emission takes place. As shown in Fig. 2.7, the NaI(Tl) detectors are oriented in three groups at every four corners of the spacecraft in such a way that the location of GRBs can be obtained from the determined relative counting rates. The NaI detectors have a crystal disk of 12.7 cm diameter and 1.27 cm thickness with a photomultiplier tube (PMT) and the hermetically sealed an aluminum housing (see the right side panel of Fig. 2.7). Each of the two BGO detectors spans ~ 0.20 –40 MeV energy range, with overlap at low energy with the NaI(Tl) detectors and at high-energy with the LAT Low Energy (LLE, 30–100 MeV energy range) (Pelassa et al., 2010). Thus, BGOs provide a bridge for cross-calibration among these three different instruments (i.e., GBM, LLE and LAT). The effective area of the BGO detectors reaches 110 cm^2 in the ~ 0.2 –2 MeV energy range. The two detectors have large cylindrical BGO crystals with 12.7 cm diameter by 12.7 cm thick. Each of the two circular glass side windows is polished with mirror quality and a cylindrical surface is roughened to ensure a diffuse reflection of the induced photon. The BGO detectors are positioned at opposite sides of the spacecraft (see the left panel of Fig. 2.7), so that the observations of the full unocculted sky

is visible to at least one of them and provide spectral information up to the MeV energy range. The localization and triggering of the events are determined from the NaI detectors, while the spectroscopy is performed using both NaI and BGO detectors. This is done by using the relative count rates of detectors at different orientations with respect to the events. The GBM instrument has a dead time per event of nominally $2.6\ \mu\text{s}$. The performance and specifications of GBM are summarized in Tab. 2.2.

Table 2.2 GBM instrument characteristics and performance (Meegan et al., 2009).

Characteristics	Capability
Energy range	$\sim 8\ \text{keV} \text{--} \sim 40\ \text{MeV}$
Field of view	9.5 sr
Spacecraft time accuracy	$\sim 2\ \mu\text{s}$
Average dead time	$\leq 2\ \mu\text{s}/\text{count}$
Energy resolution (0.1–1 MeV)	$\sim 12\%$ at 511 keV
Burst sensitivity (50–300 keV)	$< 0.5\ \text{ph cm}^{-2}\ \text{s}^{-1}$
Alert GRB location error on board	$\sim 15^\circ$
Final GRB ground computed location error (50–300 keV)	$\sim 3^\circ$
GRB trigger rate	$\sim 250/\text{year}$



GBM data set

The GBM persistently records counts in three different types of burst data: TTE, CSPEC and CTIME. The *Time-Tagged Events* (TTE) has 128 PHA (*Pulse Height Analysis*) channels and contains unbinned individual events in time with $2\ \mu\text{s}$ precision. After November 2012, the TTE data recording window from 30 s before and 300 s after trigger time for very GRB detection has been expanded to include more pre-trigger background and longer coverage after-trigger. The CSPEC data has a coarse time resolution of a default time binning of 4.096 s which drops to 1.024 s after a GRB trigger and has, like TTE, 128 full spectral resolution of energy bins. The CTIME has a fine time resolution of 0.256 s and coarse spectral resolution of 8 PHA energy bins which is not suitable for spectroscopy. After detection of a burst, all of these data including the lists of counts, binned counts and the response including the background spectra are telemetered to the ground continuously via the *Tracking and Data Relay Satellite System* (TDRSS) to be processed at the NASA Goddard Space Flight Centre (GSFC) using the Burst Alert Processor (BAP).

2.3.4.2 The LAT instrument

The *Large Area Telescope* (LAT) is the main instrument on board the *Fermi* satellite (Atwood et al., 2009), launched into a near-Earth orbit on 11 June 2008 along with the GBM (8 keV–40 MeV energy range), dedicated to studying transient phenomena. The LAT is detecting photons from \sim 20 MeV to \gtrsim 300 GeV with a wide FoV of about 2.4 sr. The FoV is defined in terms of direction where the effective area is 1/3 of its peak (i.e., \sim 25% of the sky is observable consistently by the LAT) (see Sec. §3.2).

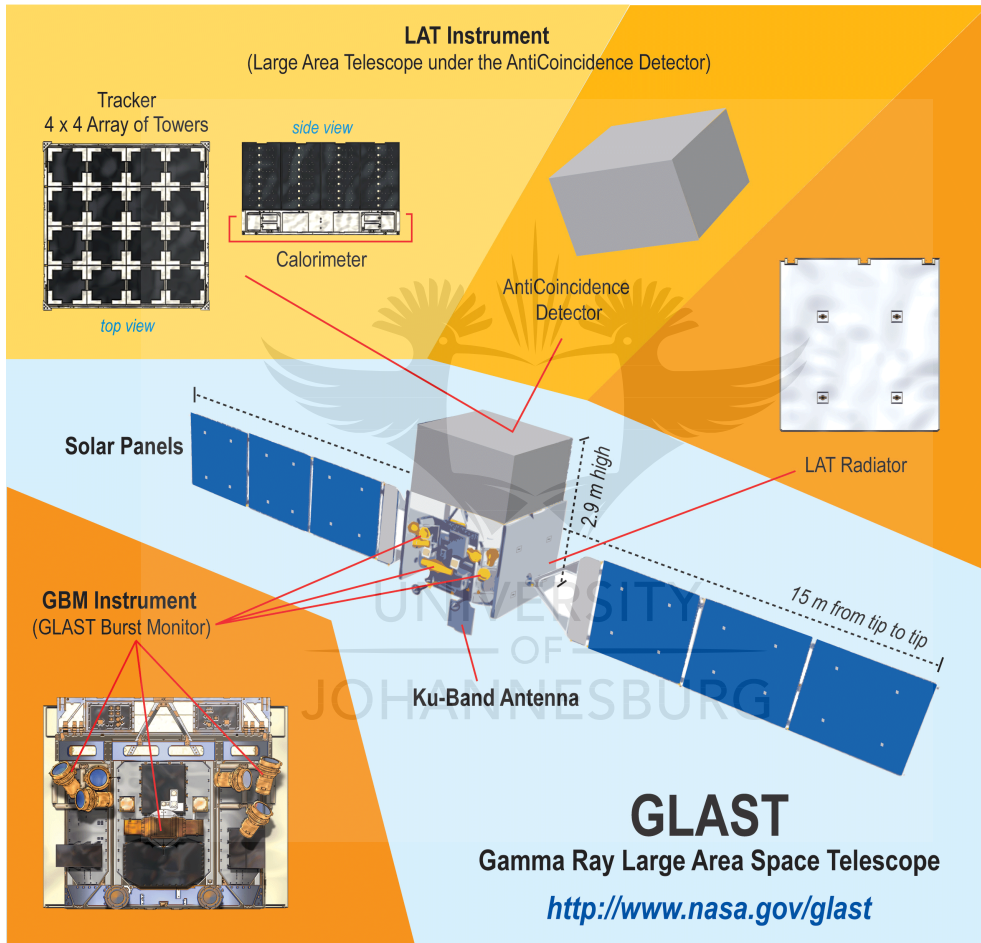


Figure 2.8 The schematic diagram of different part of *Fermi* satellite. (Credit: <http://fermi.sonoma.edu/multimedia/gallery/>)

Since high-energy γ -rays cannot be refracted or reflected; they interact by conversion into e^+e^- pair. Therefore, LAT is a pair-conversion telescope composed of 4×4 array of 16 towers with a precision convert-tracker (see Fig. 2.8). Each tower consists of a tungsten-foil tracker-converter and a silicon-strip particle tracking detector, mated with a hodoscopic cesium-iodide *Calorimeter* (*CAL*). The *CAL* is a total absorption with good energy resolution. The main purpose of *CAL* is to measure energy deposition of the electromagnetic particles shower, which results from e^+e^-

pair conversion. It also estimates fluctuations in shower energy by imaging shower development profiles. Figure 2.8 shows a schematic of different parts of the LAT instrument.

The grid of tracker arrays is covered with a segmented Anti-coincidence Detector (ACD) designed to identify photons from the majority of charged particles, mainly electrons, alphas, and protons (Moiseev et al., 2005). The ACD is required to provide detection efficiency $> 99.97\%$ for a singly charged relativistic particles entering in the LAT FoV, resulting in high-energy interaction in the *CAL*. They can cause the loss of high-energy events above 10 GeV due to “self-veto”³ signal effect in the ACD. To avoid this influence, the ACD is segmented into 89 plastic scintillator tiles and supplemented with fiber ribbons allowing spatial information that can be correlated with the signal from the tracker and *CAL* modules. We summarize the performance and specifications of the LAT instrument in Tab. 2.3.

The main scientific objective of LAT includes:

- Determining the sources of diffuse emission revealed by *EGRET* and their unidentified nature.
- Understanding the energetic characters of GRBs and other transient events.
- Using high-energy γ -ray to explore the cosmic evolution at high redshift and probe the early universe.
- Study the methods of particle acceleration process in celestial sources, particularly in Pulsars, Active Galactic Nuclei (AGNs), Supernova (SN) remnants, and the Sun.

Table 2.3 Parameters of LAT telescope and estimated performance (Atwood et al., 2009).

Characteristics	Capability
Energy range	$\sim 20 \text{ MeV} - \gtrsim 300 \text{ GeV}$
Field of view	2.4 sr
Timing accuracy	$\leq 10 \mu\text{s}$, relative to spacecraft time
Dead time	$\leq 100 \mu\text{s}$ per trigger
Location precision	$< 10'$ GRB location precision on board
Energy resolution	5% around 1 GeV, 10% below 100 MeV and 20% above 10 GeV
Effective area	$\geq 900 \text{ cm}^2$ effective area at normal incident for transients
Angular resolution	$< 1^\circ$ at 1 GeV for a single photon
Sensitivity ($> 100 \text{ MeV}$)	$3 \times 10^{-9} \text{ ph cm}^{-2} \text{ s}^{-1}$

³“self-veto” effect occurs when the energetic photon interactions in the instrument’s *CAL* caused by backsplash.

2.4 GRB alerts in the future from space-based detectors

ECLAIRs telescope on board SVOM

The long-term scientific experimentation needs to improve the accuracy and reliability of GRB localization in near real-time with the appearance of short flashes of γ -rays. It is very important to fully characterize the event and for quick follow-up observations of the GRB afterglow emission with narrow FoV telescopes. ECLAIR is the x- and γ -ray telescope on a future mission for GRB studies called SVOM (Space-based multi-band astronomical Variable Objects Monitor, [Paul et al., 2011](#); [Cordier et al., 2018](#)). It is developed by a collaboration of the Chinese Academy of Sciences (CAS), Chinese National Space Agency (CNSA), the French Space Agency (CNES) and French laboratories. SVOM is scheduled for launch in 2021. The ECLAIRs telescope on board SVOM will trigger in the 4–120 keV energy range and will localize GRB events in its 2 sr FoV. It will also provide accurate localization and fast GRB triggers to other on board telescopes. The ECLAIR is expected to detect about 80 GRBs/year as well as 34% X-ray rich GRBs and high redshift GRBs ([Paul et al., 2011](#)). In particular, the low-energy threshold of SVOM is more convenient for detection of high redshift GRBs.

The SVOM high-energy coverage of the non-imaging GRM (γ -ray spectrometer) will provide information on the light curve and spectral shape of GRBs during the prompt emission in the 15 keV–5 MeV energy band. The camera will localize soft γ -ray transients and X-ray with an accuracy $> 12'$ for 90% of the events at detection ([Cordier et al., 2018](#)). Unlike *Swift*, the SVOM alert processing will not use the NASA Tracking and Data Relay Satellite System. When the ECLAIR's camera detects a transient event on board, immediately the SVOM will slew the narrow field instruments toward the transient position within < 300 s. Then, the X-ray and optical telescopes will obtain the field and detect the afterglow emission ([Cordier et al., 2018](#)). The SVOM will provide spectral measurements of prompt GRB emission with a larger effective area and in a wider energy range with respect to the current *Swift* observatory. It will increase the number of GRBs with measured redshift. This gives good hope to use GRBs as a cosmological probe with good accuracy. Better calibration of the normalization, slope, and dispersion of the GRBs spectral properties and energetics correlation will also be possible with this upcoming mission.

The main GRB detector of the past, active and future satellites are presented in Tab. [2.1](#). We have also illustrated the observational history GRBs from Vela satellites in the early 1960s to the future mission of the SVOM satellite, which is scheduled for launch in 2021 (see Fig. [2.5](#)).

2.5 Ground-based air cherenkov telescopes for GRB detections

The Earth's atmosphere is opaque to photons beyond the optical wavelength. Thus high-energy astrophysics needs space-based observations such as *Fermi*-LAT ([Atwood et al., 2009](#)) to explore

the energy band from ~ 20 MeV to $\gtrsim 300$ GeV. However, the fluence of γ -rays quickly decreases with an increment in energy for which ground-based γ -ray detectors are required. One of the main advantages of ground-based observations with respect to the space-based experiments is the detection area. The space-based experiments could only cover a limited effective area in the order of square meters (see the left panel of Fig. 2.9). If the fluence of γ -rays at very high-energy is small, it requires a large effective area to obtain a suitable rate. Therefore, the ground-based instruments of the Imaging Atmospheric Cherenkov Telescopes (IACT) which have a large effective area (see the right panel of Fig. 2.9) should be employed to get a suitable rate. The Cherenkov radiation effect occurs when charged particles (electrons and positrons) travel through a dielectric medium (i.e., the air in this case) with refractive index $n > 1$ at a speed (v) higher than the group velocity of light in the medium c/n (Watson, 2011).

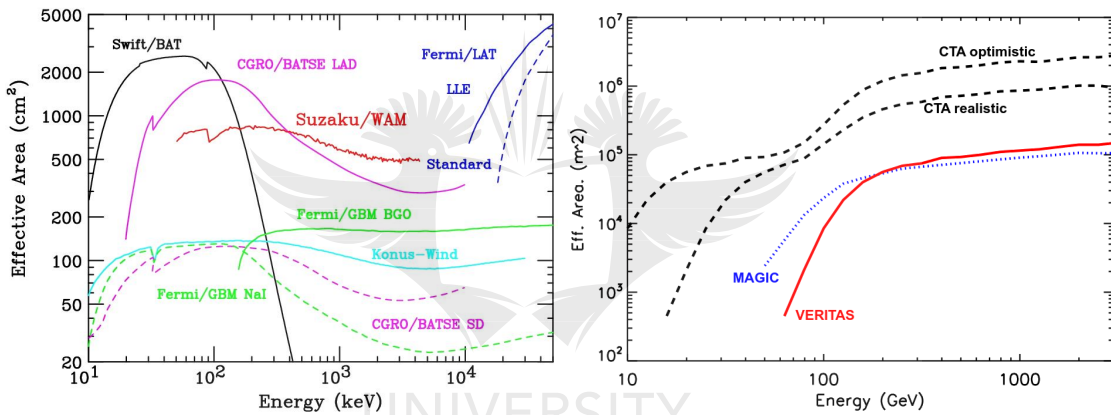


Figure 2.9 *Left panel:* comparison of the effective areas of γ -ray instruments with wide FoV (Yamaoka et al., 2017) between the *Fermi-LAT* (Atwood et al., 2009), *Fermi-GBM* (Meegan et al., 2009), *Swift-BAT* (Barthelmy et al., 2005), *CGRO-BATSE* (Fishman et al., 1985), *Konus-Wind* (Terekhov et al., 1998) and *Suzaku-WAM* (Yamaoka et al., 2009). *Right panel:* comparison of the effective areas of VERITAS, MAGIC, CTA optimistic and CTA realistic (Gilmore et al., 2013).

At present, the main Cherenkov telescope systems in operation are: High-Energy Stereoscopic System telescope (HESS, see §2.5, Hinton et al., 2004), Major Atmospheric Gamma Imaging Cherenkov Telescope (MAGIC⁴) situated at the Roque de Los Muchachos Observatory on island of La Palma and Very Energetic Radiation Imaging Telescope Array System (VERITAS⁵) situated in southern Arizona, United States. The Cherenkov Telescope Array (CTA, Actis et al., 2011; Cherenkov Telescope Array Consortium et al., 2017) is the next generation ground-based instruments and the most sensitive instrument at Very High-Energy (VHE).

⁴<http://www.magic.iac.es/>

⁵<https://veritas.sao.arizona.edu/>

The High-Energy Stereoscopic System telescope

The High-Energy Stereoscopic System (HESS) is a system of IACTs situated in the Khomas Highland in Namibia and has sensitivity to γ -ray photons in the very high-energy (VHE, 100 GeV to a few tens of TeV, [Hinton et al., 2004](#)) range. The HESS observatory is in operation initially with an array of four 13 m diameter IACTs since the end of 2003 (HESS I). The four telescopes are located at a square corner with roughly 120 m side length. The cameras are composed of 960 pixels of a photomultiplier tube (PMT) and a Winston cone light collector of 0.16° angular size providing a total FoV of 5°. On 2012 July 26, one large telescope with 28 m dish (HESS II) was constructed to enhance the array. It is larger and more complex than the other four. The simultaneous operation of all five telescopes improves the sensitivity and energy threshold down to \sim 20 GeV ([Krayzel et al., 2013](#)). From 2003–2009, about 39 GRBs⁶ were observed by HESS with an expected VHE flux ([Aharanian et al., 2009](#)).

The Cherenkov Telescope Array

CTA is the next generation ground-based instrument, which will be used to explore the universe with very high-energy γ -rays in some tens of GeV to beyond 100 TeV ([Actis et al., 2011](#); [Cherenkov Telescope Array Consortium et al., 2017](#)). CTA is complimentary to the *Fermi*-LAT in overlapping energy ranges from 20 GeV to more than 300 GeV. The sensitivity of CTA detectors are characterized by angular resolution, effective detecting area and the rate of residual background; all are functions of energy. CTA will produce a better angular resolution and sensitivity with 5–10 factor improvement compared to the current major facilities like HESS, MAGIC, and VERITAS. To view the full sky, two arrays of IACTs are in the process of being situated on two sites but will be controlled by one single consortium ([Cherenkov Telescope Array Consortium et al., 2017](#)). The South site is situated in the Atacama Desert of Chile and will host ninety-nine telescopes and give a view of the central part of our Galaxy. A second array in the Northern hemisphere is in the process of installation on the Canary Island of La Palma, which will be constituted of about nineteen telescopes. This array will be mainly dedicated to exploring the extra-galactic universe and its connection with the formation and evolution of stars ([Funk et al., 2013](#)).

CTA has three types of instruments, categorized based on the telescope energy range and FoV. The goal of low energy array of CTA will be to detect showers starting from 20 GeV with a FoV about 4–5° while the medium energy array will cover 100 GeV–1 TeV energy range with a FoV of about 6–8°. The high-energy range consists of a large number of telescopes that will detect events above 10 TeV with a FoV of 10°. For overlapping with the CTA and *Fermi*-LAT in time, CTA has the potential for detecting VHE emission from GRBs. Despite, the low detection threshold of CTA, there is an impact due to Extra-galactic Background Light (EBL), which absorbs the emission of

⁶<https://www.lsw.uni-heidelberg.de/projects/hess/HESS/grbs.php>

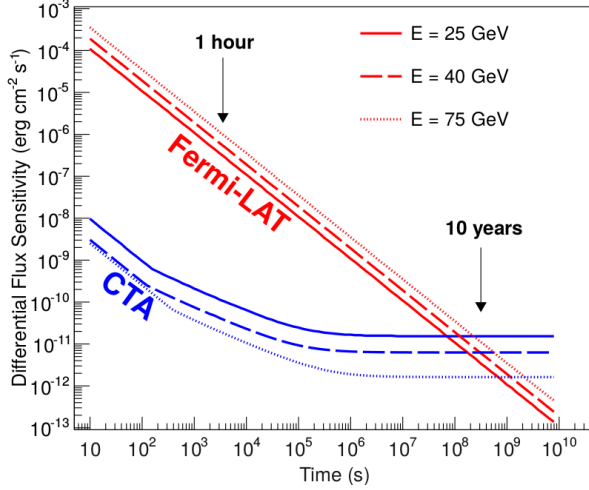


Figure 2.10 The differential sensitivity of CTA and LAT at different energies versus time. Each of the lines shown was generated for a minimum number of 25 events in the 5σ significance of detection (Cherenkov Telescope Array Consortium et al., 2017).

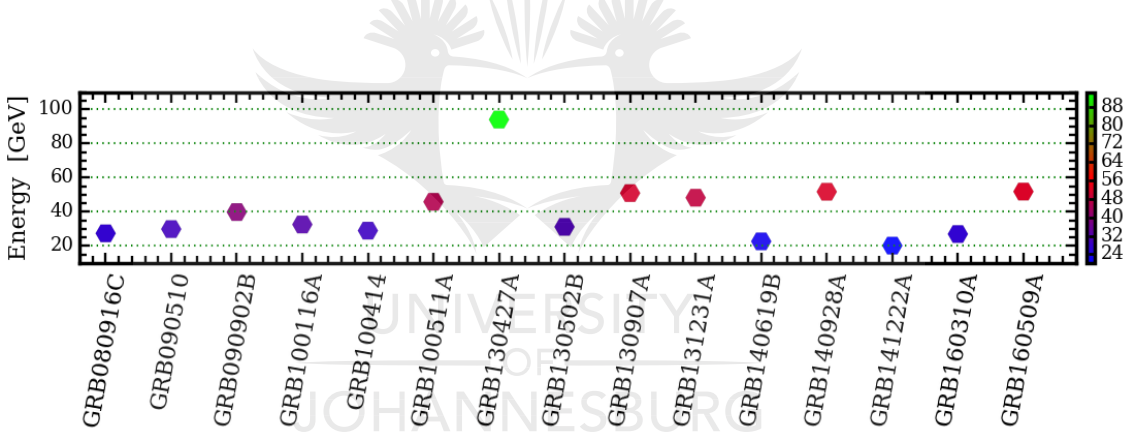


Figure 2.11 The highest energy photons of GRBs detected by *Fermi*-LAT with maximum energy $E_{\max} > 20$ GeV. The color bar represents the E_{\max} of the GRBs.

γ -rays of $E > 10$ GeV due to $\gamma\gamma$ pair production. Fig. 2.10 shows the differential sensitivity of CTA in comparison with LAT at selected energies is a function of event observation time.

GRB detection with CTA will be somewhat difficult since the detection rate is a strong function of the threshold energy and the typical response time. However, the high-energy photons of *Fermi*-LAT GRBs detected above > 20 GeV (see Fig. 2.11) give us hope that GRB detection will be achievable with the CTA. This data indicates that CTA may detect GRBs simultaneously with the LAT with a rate of 1 to 2 GRBs per/year. Assuming a baseline of collecting effective area and background rate with the hopeful instrumental properties, Gilmore et al. (2013) also reported this expected detection rate.

2.6 GRB phenomenology

The two different consecutive episodes of GRB emissions are the high-energy prompt phase and the temporally extended afterglow phase. The GRB prompt emission is a short and intense phase of γ -ray and hard X-ray radiations. The prompt emission phase has a rapid variability, brief duration, thermal and non-thermal spectral appearances. This emission phase is followed by the long-lasting afterglow emission at all electromagnetic wavelengths.

As discussed in Sec. §2.1.2, GRB prompt emission is mainly categorized into long and short, based on their spectra and duration. They have different spectral hardness ratio (HR), which is the ratio of γ -ray fluence at high to low energies, presented in Fig. 2.2 (right panel). This is probably due to the environment and host star differences of the central engine, which led to the hypothesis of the central engine of short and long GRBs (Ghirlanda et al., 2009). There are two scenarios that lead to the formation of a compact central engine, which launches a jet (i.e., defined in Sec. §2.6.6). The first is long-duration GRBs, which are believed to originate from the core collapse of massive stars. These GRBs are longer with smoothly fading afterglow emission that comes from the jet's interactions with the environment. The second scenarios lead to the formation of short-duration GRBs, caused by mergers of compact objects (neutron star-black hole or two neutron stars). The proposed GRB progenitors are the types of celestial objects that can be produced by the accretion disk around the inner engine. The progenitor systems, the nature of the central engine and composition of the jet are still unanswered questions.

2.6.1 Prompt emission

The soft γ -ray or the hard X-ray emission from a GRB in the early time, within T_{90} duration, is known as “prompt emission” while the late emission, which remains active after the prompt emission is known as “afterglow emission”. The prompt emission mostly dominates in γ -rays in the keV–MeV range, while the afterglow emission occurs in X-ray, optical and radio frequencies. The theoretical models of GRBs can be also distinguished by using intrinsic characteristics of the prompt and/or afterglow emission phase. The physical origin and responsible emission mechanisms for such GRBs are still debated issues. However, after the launch of *Swift* (Gehrels, 2004) and the *Fermi* satellites (Atwood et al., 2009), the study of prompt emission of GRBs has been revolutionized. This is due to a new combination of devices in telescopes, updated analysis methods, and new ideas of physical modeling that constrain their radiative processes and jet compositions. The detected GRBs by these telescopes permit to study detailed information about the prompt emission including the temporal and spectral analysis. For cosmological motives, one can use the GRB prompt emission to study the empirical relations such as Amati (Amati et al., 2002), Yonetoku (Yonetoku et al., 2004) and Ghirlanda (Ghirlanda et al., 2004b) relations (see Chapters §5 and §6 for more details).

The high-energy prompt emission observed by *EGRET* has been also detected by the *Fermi*-

LAT (Ackermann et al., 2013a). It often shows with a lower peak flux compared to the prompt emission pulse, however, it can last up to a few hundred seconds with higher total fluence. In extended emission, one can see the spectral lags in which a softer band of the observed pulse is broader than and lagged behind the same observed pulse in a harder spectrum (Gompertz et al., 2014).

One can understand the features of a GRB from the temporal structure of emission by considering the overall timescales of the burst. As discussed in Sec. §2.1.2 the apparent features of the GRB prompt emission temporal profiles show different distinct patterns (Fig. 2.2). There is no identical pattern observed among the bursts (see Sec. §2.1.2). Based on the observed time profile shape of the GRB light curves, it is difficult to classify them rigorously. The duration of GRB emission is traditionally defined by the T_{90} parameter as shown in Fig. 2.12. The detailed quantification of GRB durations differs between different instruments and are usually intuitive. It depends on the energy band of the detector (Zhang et al., 2016). A burst may have a shorter T_{90} if the detector is not sensitive enough (i.e., due to a smaller collecting area) or has a harder energy band. There is also an ambiguous classification in some bursts. For instance, some SGRBs detected by *Swift* telescope indicated that the observed prompt phase is followed by soft extended emission lasting tens of seconds (Norris & Bonnell, 2006).

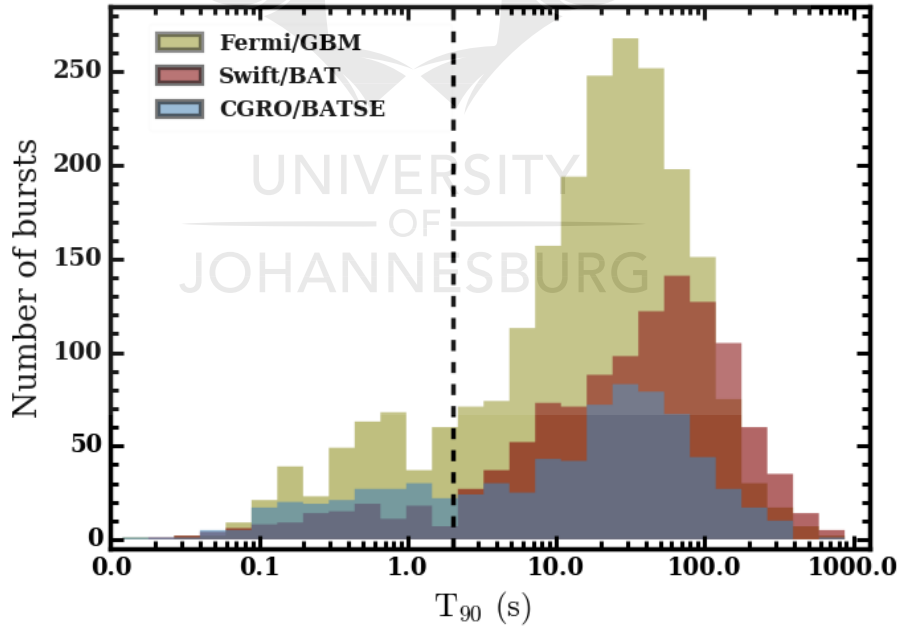


Figure 2.12 The T_{90} distribution for the *Fermi*-GBM (Gruber et al., 2014; von Kienlin et al., 2014; Narayana Bhat et al., 2016b), *Swift*/BAT (Lien et al., 2016) and BATSE (Meegan et al., 1996; Paciesas et al., 1999) GRBs. Their distributions of a statistical data sets are reported in Tab. 2.4. The vertical dashed line shows the value of T_{90} at 2 s.

Using data from the *Fermi* GBM Burst Catalog (Gruber et al., 2014; von Kienlin et al., 2014; Narayana Bhat et al., 2016b), the *Swift* catalog (Lien et al., 2016) and the BATSE catalog (Meegan

Table 2.4 The T_{90} distributions of the GRB prompt emission discovered by *Fermi*-GBM *Swift*-BAT and BATSE instruments until December, 2017.

Detectors	No. of $T_{90} \lesssim 2$ s (Median)	No. of $T_{90} \gtrsim 2$ s (median)	Total T_{90} s (Median)
<i>Fermi</i> /GBM	366 (0.58)	1865 (26.62)	2231 (20.22)
<i>Swift</i> /BAT	112 (0.38)	1058 (47.92)	1170 (38.72)
<i>CGRO</i> /BATSE	194 (0.50)	567 (30.14)	761 (18.24)

et al., 1996; Paciesas et al., 1999), we have shown the distributions of T_{90} in Fig. 2.12. About 10% of the *Swift* GRBs are SGRBs with a median T_{90} of ~ 0.38 s, and approximately 90% LGRBs with median $T_{90} \approx 39$ s. About 25% of GRBs in the BATSE are SGRBs (see Tab. 2.4). The bimodal duration distribution of the prompt emission of GRBs shown in Figure 2.12 indicates that LGRBs are clearly separated from SGRBs as shown by a broken vertical lines.

2.6.2 Spectral models

In this section, we briefly describe the functional forms of different spectral models used in our analysis of GRB data. Modeling and extracting the GRB observation has been performed by using the software package RMFIT⁷ (Spectroscopic Oriented Analysis Routines). Initially, the tool was developed for the purpose of BATSE GRB spectral analysis by the group of gamma-ray astronomy at the University of Alabama. The tool can be used to fit the spectra of GRBs from *Fermi*-LAT/GBM and *Swift*/BAT instruments for a chosen spectral model and observed count rates of the background time intervals that correspond to the Detector Response Matrix (DRM or RSP) from the multi-dimensional response functions. The RSP file is produced by gtrspgen⁸ tool which is used to compute a binned spectrum and exposure-related information. Another tool used to bin the data in time is gtbin⁹. It will produce a compatible PHA (Pulse Height Analyser) file of the transient sources, which can be used by RMFIT. Using the RMFIT tool, we can perform the time-resolved, time-integrated and joint spectral analysis of the GRBs. Alternately, one can also use the X-Ray Spectral Fitting Package (XSPEC)¹⁰ as a spectral analysis tool. Both the RMFIT and XSPEC provide, similar spectral fitting results but RMFIT uses the files with multiple spectra (PHA2) while XSPEC uses a single spectrum (PHA), and anticipates a background file (BAK) provided by the user that is appropriate for the spectrum.

In order to perform the spectral analysis of GRBs, we use different empirical functions, as described next. We denote the spectra, generally written as $dN/(dE dA dt)$ by $N(E)$ or dN/dE .

⁷<https://fermi.gsfc.nasa.gov/ssc/data/analysis/rmfit/>

⁸<https://fermi.gsfc.nasa.gov/ssc/data/analysis/scitools/help/gtrspgen.txt>

⁹<https://fermi.gsfc.nasa.gov/ssc/data/analysis/scitools/help/gtbin.txt>

¹⁰<https://heasarc.gsfc.nasa.gov/xanadu/xspec/>

Band model

The Band function (Band et al., 1993) is an empirical model that is widely used to fit the GRB prompt emission spectra. The Band function is composed of two power-laws with indices α and β joined by an exponential cutoff and amplitude A_{Band} , in units of $\text{cm}^{-2} \text{ s}^{-1} \text{ keV}^{-1}$, as given by

$$N_{\text{Band}}(E) \equiv A_{\text{Band}} \begin{cases} \left(\frac{E}{100 \text{ keV}}\right)^{\alpha} \exp\left[-\frac{E(2+\alpha)}{E_p}\right] & \text{if } E \leq E_b \\ \left(\frac{E}{100 \text{ keV}}\right)^{\beta} \exp(\beta-\alpha) \left[\frac{E_p}{100 \text{ keV}} \frac{\alpha-\beta}{2+\alpha}\right]^{\alpha-\beta} & \text{if } E > E_b, \end{cases} \quad (2.1)$$

where $E_b = E_p(\alpha - \beta)/(2 + \alpha)$ is the break energy, E_p is the spectral peak energy in keV that corresponds to energy at the maximum of the νF_ν spectrum (i.e., the total energy flux per energy band), α and β are the low and high-energy spectral indices, respectively. The peak spectral energy of GRB (when $\beta < -2$ and $\alpha > -2$ is satisfied) is typically distributed from ~ 100 keV to a few MeV. In case of a very steep β , the high-energy part of the model is consistent with an exponential cutoff (Kaneko et al., 2006). The spectral peak energy in the source frame is $E_{i,p} = E_p(1+z)$. At high-energies, a few distinct MeV emission has been detected with *EGRET* such as: GRB 930131 (Bromm & Schaefer, 1999) and GRB 941017 (González et al., 2003). After the advent of the *Fermi* high-energy γ -ray observatory, many GRBs have shown E_p up to MeV energy range.

Comptonized model

The Comptonized (Comp)¹¹ model is a power-law with an exponential cutoff, given by

$$N_{\text{Comp}}(E) \equiv A_{\text{Comp}} \left(\frac{E}{100 \text{ keV}}\right)^\gamma \exp\left[-(2+\gamma)\frac{E}{E_p}\right]. \quad (2.2)$$

It is merely an empirical model which consists of 3 free parameters, namely the amplitude A_{Comp} , the low-energy photon spectral index γ and the peak energy E_p in keV. This model is a subset of more general Band form without a high-energy power-law. The Comp model can also be a good fit for both the *Fermi* GBM and *Swift*-BAT GRB spectra when β of Band model cannot be determined by the data, and the e-folding energy, $E_0 \equiv E_p/(2+\gamma)$ approaches ~ 1 MeV (Kaneko et al., 2006). The model fits well the spectra falling sharply at high-energy. The intrinsic peak energy is given by $E_{i,p} = E_p(1+z)$ in the GRB source frame.

Smoothly-Broken Power-Law

To model the time-integrated and/or time-resolved, background-subtracted photon count spectra, one can use Smoothly Broken Power-Law (SBPL) function. It is a broken power-law characterized

¹¹The Comptonized is an empirical model in which a fraction of the photons in an input seed spectrum is scattered into a power-law component. <https://heasarc.gsfc.nasa.gov/xanadu/xspec/models/simpl.html>

by flexible curvature at the break energy. This model can accommodate spectra with very sharp breaks, as well as with very smooth curvature (Ryde, 1999) and is given as

$$N_{\text{sbpl}}(E) \equiv A_{\text{sbpl}} \left(\frac{E}{100 \text{ keV}} \right)^{\frac{\alpha + \beta}{2}} 10^{(\alpha - \alpha_p)}, \quad (2.3)$$

where

$$\begin{cases} \alpha = \frac{1}{2}\sigma(\beta - \alpha)\ln\left(\frac{e^r + e^{-r}}{2}\right), & \alpha_p = \frac{1}{2}\sigma(\beta - \alpha)\ln\left(\frac{e^{r_p} + e^{-r_p}}{2}\right), \\ r = \frac{\log(E/E_0)}{\sigma}, & r_p = \frac{\log(100 \text{ keV}/E_0)}{\sigma}. \end{cases} \quad (2.4)$$

Here A_{sbpl} is the amplitude, E_0 is the e-folding energy and σ is the break scale (width of the transition region) in decades of energy (see Appendix §A). The value of σ is fixed at 0.3. The peak energy of SBPL model at the νF_ν spectrum can be found as

$$E_p = E_0 \times 10^{\left(\frac{1}{2}\sigma\ln\left[\frac{\alpha+2}{-\beta-2}\right]\right)}, \quad \text{and is valid for } |\frac{\alpha+2}{-\beta-2}| < 1. \quad (2.5)$$

Power-law model

A single PL with 2 free parameters, is given by

$$N_{\text{pl}}(E) \equiv A_{\text{pl}} \left(\frac{E}{100 \text{ keV}} \right)^{\alpha_1}, \quad (2.6)$$

where A_{pl} is the amplitude and α_1 is the photon index.

Blackbody model

The thermal blackbody (BB) function is used to fit the GRB prompt spectra. It can be used to characterize if the emission is consistent with having a thermal character and sometimes performed as an extra-component to constrain a better spectral fit (Ghirlanda et al., 2003; Ryde, 2004). The model is given by

$$N_{\text{bb}}(E) \equiv A_{\text{bb}} \frac{E^2}{\exp(E/kT) - 1}, \quad (2.7)$$

where kT is the thermal temperature and A_{bb} is the amplitude.

2.6.3 Prompt emission spectra in the keV/MeV-GeV range

For the first time, the prompt emission extends to very high-energy components was observed by EGRET (see §2.3.1), represented by GRB 930131 (Sommer et al., 1994) and 940217 (Hurley et al., 1994). The spectra of these bursts were mainly described by the Band function (Band et al., 1993). After EGRET, the Fermi-GBM detected many GRBs, that show a good agreement of the Band model (Gruber et al., 2014). Besides, GRB 100724B (Guiriec et al., 2011), GRB 120323A (Guiriec et al., 2013) and GRB 131014A (Guiriec et al., 2015a) detected by GBM have shown an

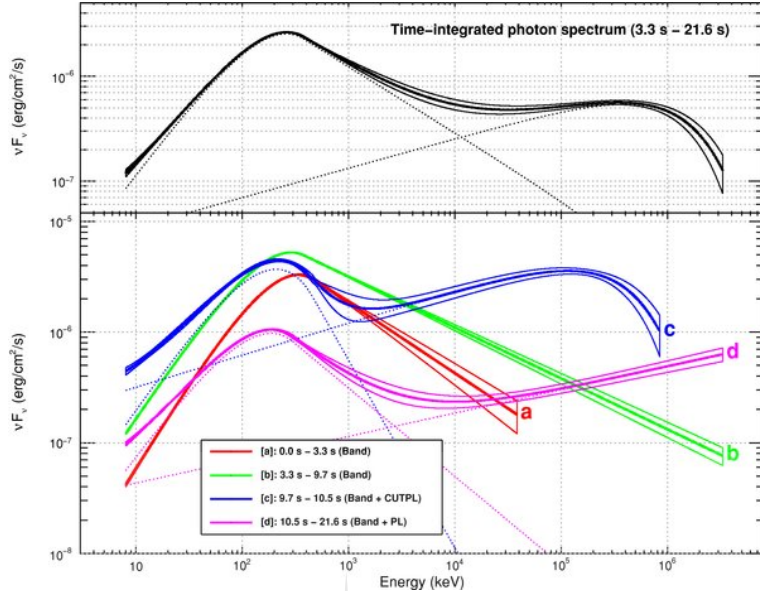


Figure 2.13 The prompt emission spectral of GRB 090926A modeled at different time intervals (bottom panel) as well as for the time-integrated prompt emission (top panel) (Ackermann et al., 2011).

extra thermal components that accounts for the deviations from the Band function. Furthermore, the power-law (PL) component extending to higher and lower energies (i.e., keV to GeV energy range) also observed by the *Fermi*-LAT/GBM (Abdo et al., 2009; Ackermann et al., 2010; Tierney et al., 2013). In Fig. 2.13, the time-resolved spectral fits show different models with additional components. The combined time-integrated spectral analysis of GBM and LAT GRBs are identified in some cases and an extra power-law component is required to improve the quality of the fit (Abdo et al., 2009; Ackermann et al., 2010; Tierney et al., 2013; Dirirsa et al., 2017a).

2.6.4 Fluences and Fluxes

The fluence is the total radiant energy collected from the GRBs per unit area over the duration of the event (i.e., T_{90}). It is computed by integrating its energy flux over time and the energy range of the detector (i.e., the total energy collected per unit time and per unit area). The fluence measured between energies E_{\min} and E_{\max} is given by

$$S = T_{90} \int_{E_{\min}}^{E_{\max}} E \frac{dN}{dE} dE. \quad (2.8)$$

The energy flux of a burst is defined

$$F = \int_{E_{\min}}^{E_{\max}} E \frac{dN}{dE} dE. \quad (2.9)$$

The energy flux of GBM (see the right panel of Fig. 2.14) between 10 and 1000 keV obtained from the fit of Band model while the energy flux of *Swift*-BAT in the energy range 15–150 keV is fitted

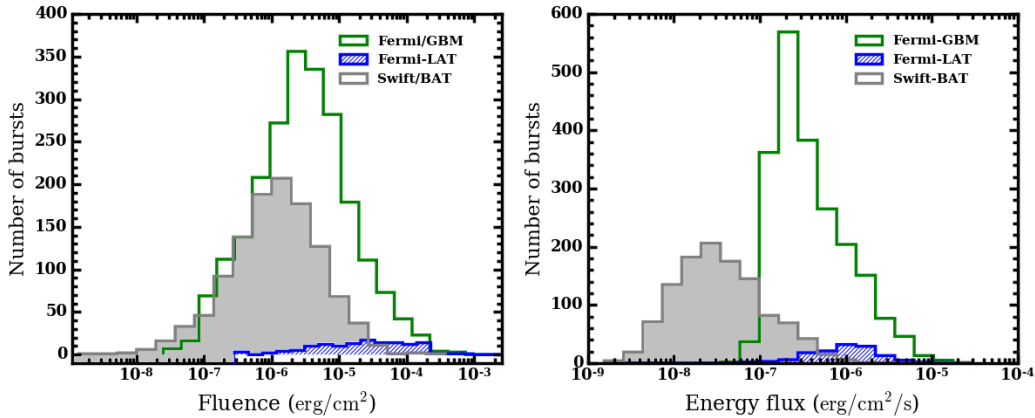


Figure 2.14 *Left panel:* distribution of the fluences of 2231 GBM (10–1 MeV, Gruber et al., 2014; von Kienlin et al., 2014; Narayana Bhat et al., 2016a), 135 LAT (from Fermi.gsfc.nasa.gov, 2017) and 1154 BAT (15–150 keV, Lien et al., 2016) GRBs collected from the catalog until December 2017. *Right panel:* the energy fluxes of 2115 GBM (10–1 MeV), 132 LAT and 1154 BAT (15–150 keV).

by power-law. These distributions could be used to identify the bright GRBs. The GBM bursts with an energy flux distribution peaking at a significantly higher value than the BAT energy flux. The left panel of Fig. 2.14 shows the distribution of fluence profiles of GBM, LAT and BAT detected bursts. GBM and LAT bursts have higher fluence than BAT bursts. It was found that the fluences and energy fluxes of LAT are similar with those detected by the GBM bursts.

2.6.5 Afterglow emission

From a phenomenological point of view, the afterglow emission follows the prompt γ -ray burst. It can be observed in multiple frequencies, covering from X-rays to radio wavelengths and can last from minutes to months after the GRB event (Zhang et al., 2006). The emissions after T_{90} are assumed to be the afterglow. The afterglow emission can provide the information being developed in the jet-following the flaring activities. The first X-ray afterglow associated with GRB was detected by BeppoSAX for long GRB 970228 (Costa et al., 1997). For the same GRB, the detection of optical counterpart was reported by Groot et al. (1998). The GRB radio afterglow happened during the same year for another burst GRB 970508 (Frail et al., 1997). This burst had an unusually bright optical afterglow counterpart that led to the measurement of its spectrum. Using them with a few absorption lines, the redshift, $z = 0.8$ of GRB was measured for the first time. The *Swift* is an ideal instrument for quick localization of GRBs and rapid follow-up observation and consequently redshift measurement (Gehrels et al., 2009). *Swift* has been detected many short GRBs. It is the first instrument which has provided a precise localization of short GRB 050509B (Gehrels et al., 2005) and detected its afterglow emission. The accurate position of burst led to determine redshift either using an optical counterpart or a companion

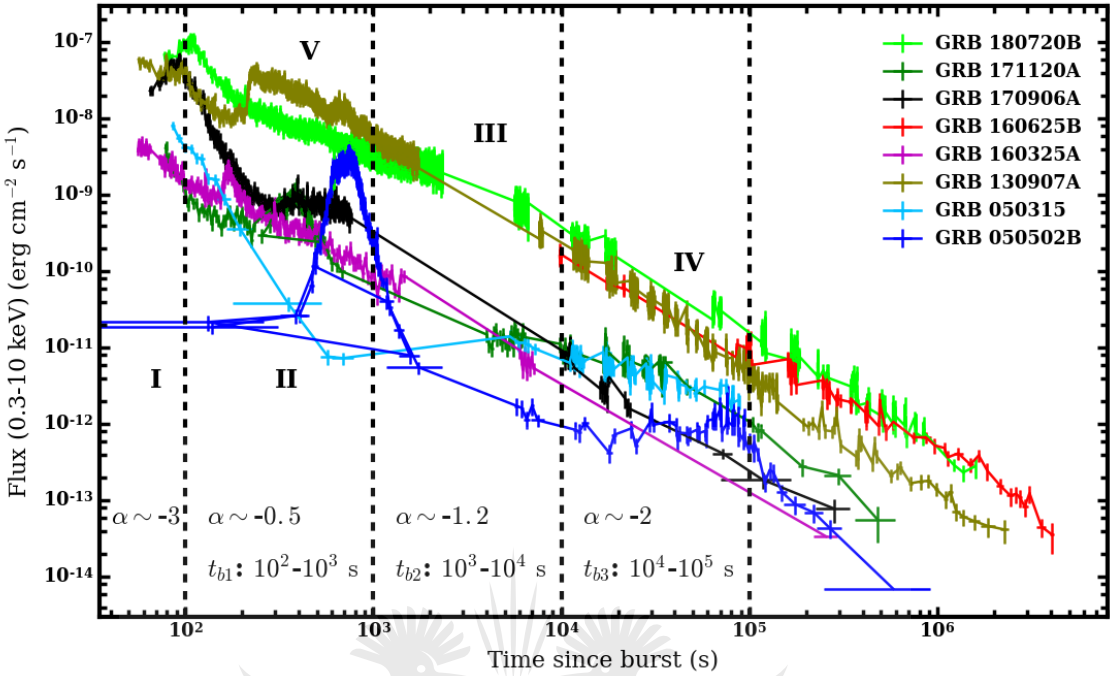


Figure 2.15 The *Swift*-XRT light curves for which their prompt emission were simultaneously detected by *Fermi*-LAT, except GRB 050315 and 050502B (from the *Swift*-XRT GRB light curve repository [Swift-XRT, 2018](#)). We used the segmented indices (α) of the power-law as defined by [Zhang et al. \(2006\)](#).

host galaxies. The most distant GRB known today is GRB 090429B, whose photometric redshift is $z \approx 9.4$ ([Cucchiara et al., 2011](#)).

Following the tentatively synthetic cartoon of the *Swift* X-ray light curves with different segments drawn by [Zhang et al. \(2006\)](#), the data of the x-ray afterglow for GRBs simultaneity detected by both *Fermi*-LAT and Swift (GRB 050315 and 050502B detected only by *Swift*) are shown in Fig. 2.15. It is segmented into four flaring components based on the indices (α) of the power-law (i.e., $F \propto t^\alpha$). The first segment (phase I, an initial steep decay $\alpha \sim -3$) cover the duration of hundred seconds from the trigger time. The rest of the three transition time components are designated as t_{b1} (phase II, shallow decay with $\alpha \sim -0.5$), t_{b2} (phase III, normal decay with a typical $\alpha \sim -1.2$) and t_{b3} (phase IV, late steeper decay with $\alpha \sim -2$), respectively. About 46% of the *Fermi*-LAT GRBs are followed by an afterglow detected by *Swift* instruments.

2.6.6 GRB emission mechanism

The theoretical models for GRBs should be able to explain the whole process of the prompt and afterglow emission with respect to the observed characteristics of the burst light curves and spectral energy distribution ([Fishman & Meegan, 1995](#)) but not yet fully developed. Many processes have been proposed to get a better picture of the GRB emission mechanism. These

processes include out-flow dynamics, and the mechanisms accountable for the acceleration of particle, radiation and magnetic field generation. These are also not completely solved problems, but many studies have tried to answer some of these questions.

The correlation related to the GRB prompt emission can enable discrimination among the most reasonable theoretical models explaining the mechanism responsible for the emission and their physical interpretations. One of the models used to describe such phenomenon is the “fireball” model (Rees & Meszaros, 1992; Cavallo & Rees, 1978; Mészáros, 1998) in which the central engines powered by extraordinary events of the merger product of binary neutron stars or collapsing star (see Fig. 2.16). This launches a highly relativistic two oppositely jetted plasma blobs with an opening angle of $\theta \sim 3\text{--}30^\circ$. However, we can only observe a small fraction of the jet in the line of sight as it travels with very high bulk Lorentz factor¹². This ultra-relativistic jet consists of photons, e^+e^- pairs and baryons (Rees & Meszaros, 1992; Cavallo & Rees, 1978). Blobs of material thrown out from the central engine due to the accelerated kinetic energy of the relativistically expanding shell of the blast-wave are believed to produce a flash of extremely energetic γ -rays (i.e., the prompt emission). This kind of emission could be explained by internal shocks and possibly produce a bright GRB with energies of the order of 10^{48} to 10^{54} erg, assuming isotropic emission. The released energy may lead to the formation of a fireball containing the γ -ray photons.

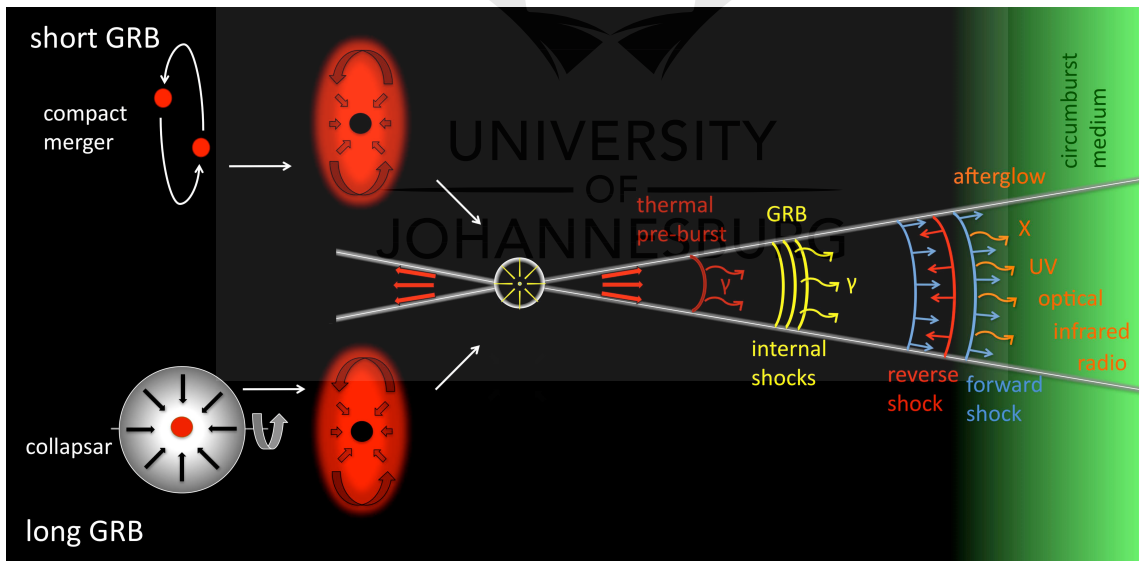


Figure 2.16 Schematic fireball model of GRBs, and emission regions of a collapsing star and compact merger (Gomboc, 2012).

Interaction of the jet with its surrounding material (external forward shock) can generate the multi-wavelength afterglow emission as synchrotron radiation (Rees & Meszaros, 1992). An

¹²The bulk Lorentz coefficient, $\gamma = 1/\sqrt{1-(v/c)^2}$. Here c and v are the speed of light and the relative velocity between inertial reference frames, respectively.

external reverse shock is also produced in the GRB ejecta that propagates toward the central engine (see Fig. 2.16). However, problems of the standard fireball model arose after more complex features of the light curves were discovered by *Swift*, requiring more detailed modeling (Gehrels, 2004; Nousek et al., 2006).

The discovery of the correlations between physical parameters of the prompt emission has been used as a possible discriminator of models. This phenomenological correlation could also encourage the understanding of the mechanism accountable for the prompt phase.

2.7 Summary

GRBs were discovered in 1967 and many space-borne detectors have detected GRBs. Currently *Swift*, *Fermi*, INTEGRAL and others are detecting GRBs on a regular basis. In the future, SVOM will be detecting GRBs and ground-based telescopes such as CTA will detect VHE gamma rays. GRB prompt emission is characterized by rapid variable emission lasting for $\gtrsim 2$ s for long GRBs and $\lesssim 2$ s for short GRBs. Prompt gamma-ray emission is typically modeled with mathematical functions, Band, SBPL, Compton, etc. GRB afterglow emissions are characterized by smoothly-decaying light curves across different energy bands. The physical origin of the prompt emission is not fully known yet but there are promising theories such as synchrotron radiation. Afterglow emissions are better understood and external shock models of GRB ejecta interacting with a surrounding medium can explain many observed properties. Study of correlation among observed emission properties may give clues to the physical understanding of the prompt emission.

UNIVERSITY
OF
JOHANNESBURG

THE *Fermi* GAMMA-RAY SPACE TELESCOPE

Contents

3.1	<i>Fermi</i> mission overview	39
3.2	Source model and instrument response functions	40
3.2.1	LAT event classifications	42
3.3	Maximum likelihood analysis of the LAT data	45
3.3.1	The unbinned maximum likelihood analysis	45
3.3.2	The binned likelihood analysis	47
3.4	On orbit and ground processing	49
3.4.1	On orbit processing	49
3.4.2	Ground processing	50
3.4.3	GRB detection	50
3.5	Detection of new LAT GRBs	51
3.6	The Gamma-ray Burst Monitor performance	53
3.6.1	GBM spectral analysis	53
3.6.2	LAT and GBM joint spectral analysis	55
3.7	Summary	57

3.1 *Fermi* mission overview

The *Fermi Gamma-ray Space Telescope (FGST)* has opened a wide window on the high-energy universe. It was launched on June 11, 2008, with an anticipated mission lifetime of $\gtrsim 10$ years. With a large leap in all key capabilities, *Fermi* data is enabling researchers to answer many questions covering a wide range of topics, including the origin of cosmic rays, GRBs, supermassive black-hole systems and searching for signals of new physics. *Fermi* can independently change

its position of observations to detect GRBs during and after the low-energy γ -ray emission and quickly alert the GRB science community. The *Fermi* spacecraft consists two instruments: the LAT (20 MeV – >300 GeV energy range, Atwood et al., 2009) and the GBM (an energy range extending from 40 MeV down to 8 keV, Meegan et al., 2009). Fig. 3.1 shows the spectral energy coverage of GBM and LAT detectors including the LAT Low Energy (LLE) event selection energy range (Pelassa et al., 2010). The lists of counts in these detectors could allow us to select the same temporal binning of the data to perform joint spectral fits to binned one-dimensional spectra. The LAT is the main scientific telescope of FGST, which represents a significant improvement

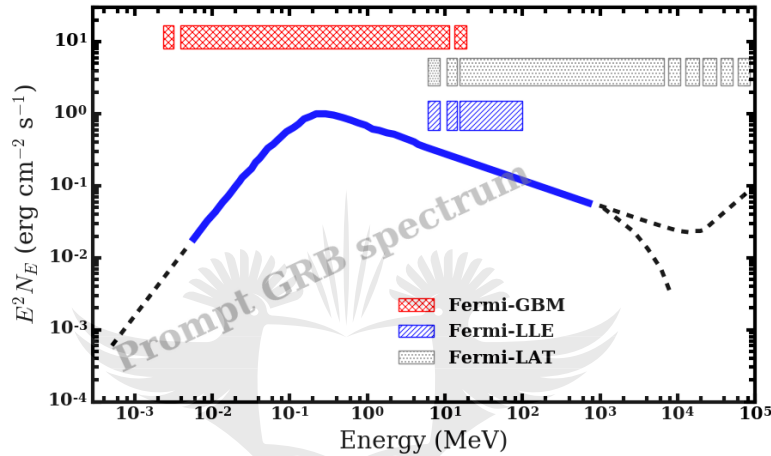


Figure 3.1 The spectral energy coverage of GBM, LLE, and LAT.

in sensitivity and resolution compared with the high energy instrument *EGRET* onboard the *CGRO*. The major scientific aims of the LAT include, I) study the high-energy behavior of γ -ray radiation of transient events in the 8 keV to $\gtrsim 300$ GeV energy range, II) distinguish discrete sources from diffuse γ -ray emission and the nature of undefined high-energy sources observed by *EGRET*, III) explore the high energy part of the GRB spectra, IV) understand the process of particle acceleration that produces high energy emission, V) search for the signatures of dark matter above ~ 1 GeV in the Galactic diffuse emission and VI) probe the extragalactic background light (EBL) in the optical-UV band, where absorption breaks are anticipated for sources (Gilmore et al., 2009). In Fig. 2.9, a comparison of the effective area of the LAT and other instruments is illustrated.

3.2 Source model and instrument response functions

The LAT events are simulated based on the instrument response functions (IRFs¹, Davis, 2001), the source usually falls within a specific Region of Interest (RoI) as a circle around a sky position

¹IRFs are the instruments response functions that describe the response of a detector to an incoming flux of particles

3.2. SOURCE MODEL AND INSTRUMENT RESPONSE FUNCTIONS

in (RA, DEC i.e., Right Ascension, Declination in degrees) and a background model. The total source model $S(E, \hat{q})$ (in units of $\text{cm}^{-2} \text{ s}^{-1} \text{ keV}^{-1} \text{ sr}^{-1}$) is the sum of contributions of spectrum from individual sources with index j of the point-like sources (S_j), the galactic diffuse emission (S_G) and the extragalactic and/or isotropic diffuse emission (S_{eg}). Therefore

$$S(E, \hat{q}) = \sum_j S_j(E) \delta(\hat{q} - \hat{q}_j) + S_G(E, \hat{q}) + S_{\text{eg}}(E, \hat{q}), \quad (3.1)$$

where $S_j(E)$ is the measured energy spectrum that is determined by using the source spectral models² and \hat{q}_j is its location in the sky. Note that the $S_j(E)$ have dimensions of $dN/dEdtdA$ while S_G and S_{eg} have dimensions of $dN/dEdtdAd\Omega$. Here, Ω is the angular size of the sources. The entire components as well as the spectral models of the sources are defined in the XML² (short for eXtensible Markup Language) file. In this file, we can also define the source region (RA, DEC radius in degrees) and its lower and upper energy intervals.

The source model used in Eq. (3.1) can be folded with the IRFs, to obtain the predicted photon counts in the measured energy E' , direction \hat{q}' at the detector and photon arriving time t . The probability distribution of the detected photons as a function of reconstructed energy E' in units of photon flux $\text{cm}^{-2} \text{ s}^{-1} \text{ keV}^{-1} \text{ sr}^{-1}$ is given by

$$M(E', \hat{q}', t) = \int_{\text{RoI}} dE d\hat{q} S(E, \hat{q}, t) R(E', \hat{q}'; E, \hat{q}, t). \quad (3.2)$$

Here, $S(E, \hat{q}, t)$ is the predicted counts density given in Eq. 3.1 and the integral is the convolution over the IRF, $R(E', \hat{q}'; E, \hat{q}, t)$. The integral performed over the sky region, which covers all the sources contributing to the RoI, thus the exposure function of energy. In the standard LAT data analysis, we consider the RoI within $8\text{--}15^\circ$ and the steady total sources, i.e., $S(E, \hat{q}, t) \rightarrow S(E, \hat{q})$. The number of photons predicted from a given source can be computed as

$$N_{\text{pred}} = \int dE' d\hat{q}' dt M(E', \hat{q}', t). \quad (3.3)$$

In Eq. (3.1), a function $R(E', \hat{q}'; E, \hat{q}, t)$ represent a high-level model of the total IRFs that typically composed of three components,

$$R(E', \hat{q}'; E, \hat{q}, t) = A(E, \hat{q}, t) P(\hat{q}'; E, \hat{q}, t) D(E'; E, \hat{q}, t), \quad (3.4)$$

where $A(E, \hat{q}, t)$ is the effective area of the LAT cross-section for detection efficiency of the arrival photons with (E, \hat{q}) at time t , $P(\hat{q}'; E, \hat{q}, t)$ is the Point Spread Function (PSF) that a photon with true energy E and arrival direction \hat{q} has a construction direction \hat{q}' , and $D(E'; E, \hat{q}, t)$ is the energy dispersion, which measures the probability density of an event energy E' for a photon with E , arrival direction \hat{q} and t . It is defined in terms of the fractional difference between E' and E , $\sigma E'/E = (E' - E)/E$. For Pass 8 data, the energy dispersion correction can reduce systematic errors at all energies but can affect the spectral fits of the sources below 300 MeV. The correction

²https://fermi.gsfc.nasa.gov/ssc/data/analysis/scitools/source_models.html

is more significant below 100 MeV where the induced fractional change in the count spectrum can easily exceed statistical errors. This increases the effective area, which allows the analysis of LAT data below 100 MeV. It is strongly recommended to take into account the energy dispersion in the case of a binned maximum likelihood analysis.

Since the LAT pointing is not fixed in the sky coordinate of the true direction \hat{q} , so each component should depend on time. The LAT acceptance (A_{ac}) is defined as the integral of the effective area over the solid angle Ω given by

$$A_{\text{ac}} = \int_{\Omega} A(\hat{q} = 0, E) d\Omega. \quad (3.5)$$

At a given energy, the FoV is defined as the ratio between the acceptance $A_{\text{ac}}(E)$ (i.e., the effective area integrated over the solid angle) and the on-axis effective area (A_{peak}) at normal incident ($\hat{q} = 0$) of the steady arrival time $t = 0$, i.e.,

$$FoV = \frac{A_{\text{ac}}}{A_{\text{peak}}}. \quad (3.6)$$

The LAT can request autonomous re-pointing of the spacecraft and alter the pointing. The pointing precision is below 2° (target of $< 0.5^{\circ}$) in 68% confidence level.

The LAT IRFs have been subsequently updated with different versions called “Passes” that take into account the effects measured in flight and different reconstruction algorithms. The first data set, which released in 2009 was Pass 6 ([Atwood et al., 2009](#)). Then, the instrument was affected by background events so-called “ghosts”, the new events Pass through the LAT trigger window. It piles-up and creates an accidental coincidence effect with good count detectors by leaving residual electronic signals in the subsystems of LAT detector. The problems of these events were properly accounted in the Monte-Carlo simulation and then another updated version of Pass 6 data was released, but it was still affected by a loss of efficiency. In August 2011, the subsequent sets of IRFs of Pass 7 ([Ackermann et al., 2012](#)) data set was released. The overall analysis and the event reconstruction methods were not modified, but the study of point-like sources based on the event system was re-corrected on simulated data sets. In the reconstructed simulation, the effect of ghost signals was included ([Ackermann et al., 2012](#)). It was the period when the LAT collaboration has started to think about the improvement of the instrumental simulation, rebuild the events reconstruction and the classification of the algorithm entirely. The most recent Pass 8 ([Atwood et al., 2013](#)) data set was released on June 24, 2015, after years of dedicated efforts intended to separate the ghosts coincidence residual signals from the good photons. It has increased the effective area over a wide range of energy compared to the previous IRF called reprocessed version of Pass 7 ([Bregeon et al., 2013](#)) data algorithm shown in Fig. 3.2.

3.2.1 LAT event classifications

Besides the event reconstruction process, the LAT data is defined in different event classes based on their γ -ray efficiency, individual event topologies and the quality of their reconstruction.

3.2. SOURCE MODEL AND INSTRUMENT RESPONSE FUNCTIONS

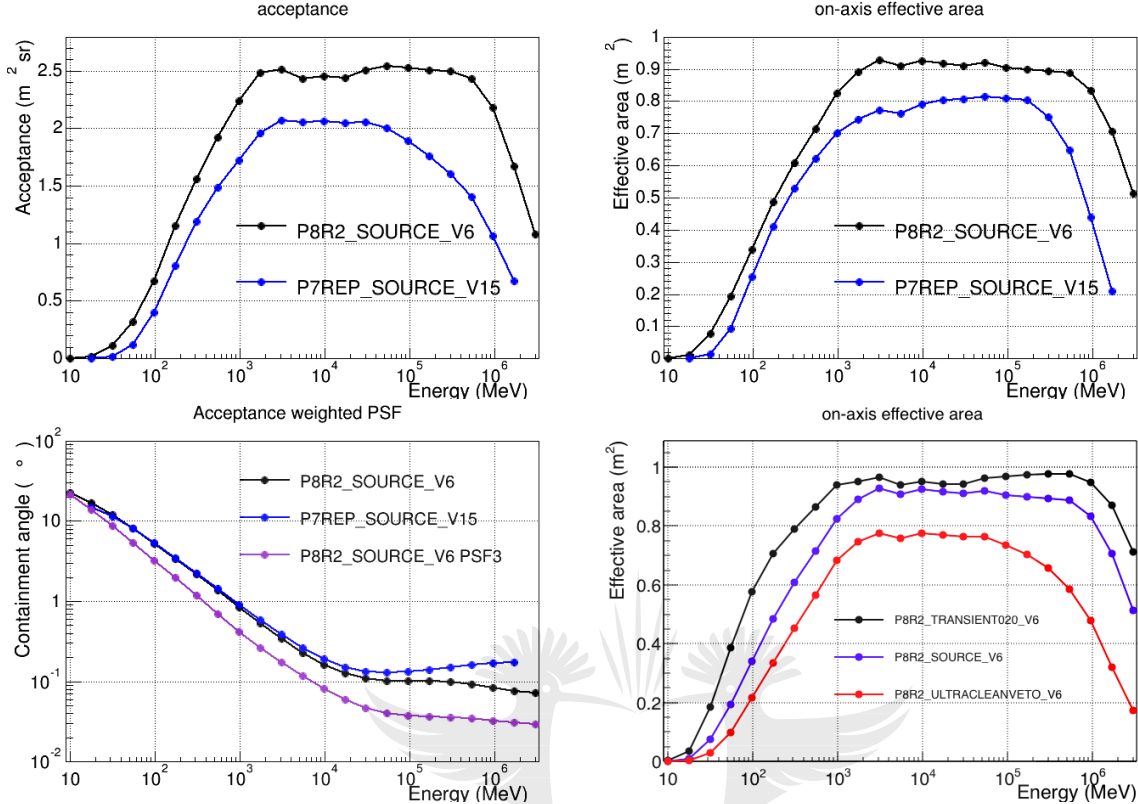


Figure 3.2 The top two panels and the bottom left panel plots show the performance comparison of the P7REP_SOURCE_V15 with P8R2_SOURCE_V6 event classes. *Top left panel:* comparison of the effective area integrated in the FoV (acceptance) between Pass 7 and Pass 8 SOURCE events classes. *Top right panel:* comparison of the effective area between Pass 7 and Pass 8 SOURCE events classes. *Bottom left panel:* comparison of the angular resolution between Pass 7 and Pass 8 SOURCE event classes. *Bottom right panel:* the on-axis comparison of the effective area as a function of energy for three distinct Pass 8 SOURCE classes of event. From the source: http://www.slac.stanford.edu/exp/glast/groups/canda/lat_Performance.htm

These event classes are characterized by their own set of IRFs. The most challenging task of all the event reconstruction analysis is background rejection. This is due to a very low photon to cosmic-ray (charged particle) ratio in the incoming data and the large FoV covered by the LAT. Thus, the background reduction analysis has been built, which is used to optimize the specific data analysis, depending on Monte-Carlo simulation, the backgrounds in orbit, and the LAT performance. A wide range of LAT observation and different levels of background residual analysis (misclassified cosmic-rays) and signal contamination leads to the definition of various event selections³.

- TRANSIENT class: this class is the loosest selection criteria designed for short duration sources such as GRB prompt emission and solar flares. In this class, high purity events

³https://fermi.gsfc.nasa.gov/ssc/data/analysis/documentation/Cicerone/Cicerone_Data/LAT_DP.html

are not expected since the time selection benefits from the increased event statistics while maintaining a large background fraction and wide point spread function (PSF). In Pass 8 data set (i.e., Release 2 Version 6, known as P8R2_V6) the background contamination is calibrated from the isotropic diffuse γ -ray background emission of the power-law best fit (hereafter B10). Based on this background rate, the TRANSIENT class can be categorized into different sub-classes such as TRANSIENT020 ($2\times$ than the B10 reference spectrum) and TRANSIENT010 ($1\times$ the B10 reference spectrum). With a less restrictive fiducial cut on projected track length through the calorimeter, these classes are corresponding to the superset of TRANSIENT020E and TRANSIENT010E, respectively.

- SOURCE class: this event class has a fraction of background rate of $\lesssim 1$ Hz in the LAT FoV and photons with a larger PSF. It provides better sensitivity for point source analysis and is reasonably extended from medium to long time scales.
- CLEAN class: above 3000 MeV, this class has lower background contamination than the SOURCE class that reduced to a level of about ~ 0.1 Hz across the LAT FoV. It is somewhat sensitive to hard spectrum sources at high Galactic latitudes (i.e., $|b| > 10^\circ$) and more preferred for the diffused emission of γ -ray analysis.
- ULTRACLEAN class: this class has a lower residual contamination, about $\sim 40\%$ than that of the CLEAN class around 100 MeV but the same above 10 GeV. It is the tightest class at the expense of lower effective areas detection to study the extragalactic γ -ray emission at a minimized charged cosmic-ray background contamination.
- ULTRACLEANVETO class: this class is the cleanest and most restrictive selection of Pass 8 event. In the energy range of 100 MeV–10 GeV, the background rate is less than the background rate of SOURCE class, which has an additional cut to further reduce residual background. This results in very high cosmic-ray rejection and is recommended to study for charge cosmic-ray induced systematic. Additionally, it is used to study the diffuse emission that requires a low level of charged cosmic-ray contamination.

The LAT photon FITS⁴ files contain information, which are necessary for the analysis of science data using the CLEAN, SOURCE, ULTRACLEAN and ULTRACLEANVETO event classes. It includes the event position, the arrival time in MET (i.e., Mission Elapsed Time, since 01, January 2001), the energy and their quality of reconstruction. There is also an extended file consisting of the same columns as the photon data file with additional photons, which are in the TRANSIENT classes in the typical data analysis. We also have the spacecraft file (hereafter “FT2”) that contains the spacecraft orientation and information on the position, binned in 30 s (some intervals may be shorter at the end of a file) for data analysis. All of these data are obtained from the data server (FSSC) currently distributing Pass 8 data for analysis⁵. The LAT data files are publicly accessible

⁴FITS (*Flexible Image Transport System*) is the data format used for analyzing, transporting and archiving scientific data files (hereafter “FT1”). https://fits.gsfc.nasa.gov/fits_primer.html

⁵<https://fermi.gsfc.nasa.gov/cgi-bin/ssc/LAT/LATDataQuery.cgi>

at the FSSC⁶ (*Fermi Science Support Centre*).

3.3 Maximum likelihood analysis of the LAT data

The likelihood \mathcal{L} is the probability of obtaining a set of data given a model. It is an estimate of how likely a model can reproduce observational data. The *Fermi*-LAT instrument has been observing hundreds of millions of counts, but for the most scientific purpose, we will be interested typically in a small subset of few hundreds or a few thousands of counts. From the *Fermi* data analysis, we require the maximum likelihood estimate (MLE) to determine the parameters of the statistical model for the given source in which the observed data supports the statistical hypothesis. This method was predominant to the analysis of high energy γ -ray data from the *EGRET* instrument to estimate the value of parameters, which maximize the likelihood (Mattox et al., 1996; Cash, 1979). The MLE estimation is accomplished by two methods, such as “unbinned” and “binned” likelihood analysis.

3.3.1 The unbinned maximum likelihood analysis

An unbinned Maximum Likelihood Analysis (MLA) is performed by using the reconstructed direction and energy of each event and the assumed sky model folded through the instrument response functions (IRFs). For a small number of counts with a short timescale, the standard unbinned likelihood analysis is the preferred method to be used for LAT spectral analysis.

Data preparation with the *Fermi* Science Tools

The *Fermi* Science Support Center (FSSC) provides a set of basic tools, called the Science Tools, necessary to perform unbinned and binned MLA of both the LAT and GBM data at a high level. In order to prepare the data for the analysis, a user needs the FT1 photon file and the FT2 spacecraft data file, which are publicly⁷ available in the *Fermi* database since August 2009. To start the analysis of these data sets, we use gtselect⁸ tool to make cuts on energy range and the time interval required for the analysis. In order to analyze the Pass 8 data, we can consider energy $\gtrsim 30$ MeV by enabling energy dispersion (i.e., finite energy resolution) correction for the spectral analysis of data below 100 MeV (see Sect. §3.2). Currently, the Science Tools only support the energy dispersion in the case of a binned MLA. Besides, gtselect tool takes into account the region of interest (RoI), zenith angle (θ_z), instrument coordinates (RA, DEC), an event type (new in Pass 8) when the selection cuts performed on event data files. It is strongly recommended to define a large region encompassing all sources contributing to RoI. In the standard LAT data analysis, we select our RoI within a size of 8–15° with the zenith angles $\theta_z \lesssim 110^\circ$, which is the

⁶<http://fermi.gsfc.nasa.gov/ssc/data/access>

⁷<https://fermi.gsfc.nasa.gov/ssc/data/access/>

⁸<https://fermi.gsfc.nasa.gov/ssc/data/analysis/scitools/help/gtselect.txt>

angle between the incoming photon direction and the direction perpendicular to the Earth's surface. At high zenith angles $\theta_z > 110^\circ$ the terrestrial albedo contaminates the γ -ray data due to the cosmic-rays and Earth's atmosphere interaction within the RoI. For this purpose, a cut on the zenith angle is recommended to eliminate all the events which are not within a maximum zenith angle. Then, the likelihood tools use this information to analyze data.

The next step is to apply `gtmktime`⁹ tool, which makes cuts based on the spacecraft variables (pointing and livetime history) contained in the FT2 spacecraft data file and update the *Good Time Intervals* (GTIs). A GTI is a time range when the data file containing information about the spacecraft pointing as a function of time could be considered valid. This tool is also designed to exclude times when some event negatively affects the quality of the LAT data or the periods where the RoI is outside the FoV. Furthermore, it is used to exclude periods in which the spacecraft is transiting the South Atlantic Anomaly (SAA) region.

Fitting procedure

We have defined the exposure function in Eq. (3.2) that the likelihood can be performed to calculate the expected numbers of events from a given source using Eq. (3.3). To compute the exposure time (livetime) of the LAT, which is the time that the detector spent observing a given position of the sky, we use the `gtltcube`¹⁰ tool. This tool calculates the integrated livetime as a function of the sky position and of the angle between this direction and the instrument z -axis(i.e., commonly referred to as off-axis angle). It makes a new file called a *livetime (exposure) cube* relying on the FT1 file, FT2 file, the cosine of the desired inclination angle and the bin size in degrees per pixel. Then, based on the input event file, FT2 files, IRFs, longitude and latitude values (n_{long} , n_{lat}), energy bins and the *livetime cube*, the `gtexpmap`¹¹ tool used to create an exposure map needed to determine the expected number of photons. Eq. (3.3) in the RoI associated with the diffuse constituents of the spectral source model. Each component of the source model is computed for an individual photon at each step of the likelihood maximization. After the source model is generated, *livetime cube*, the `gtdiffrsp`¹² tool can be run to compute the integral over solid angle of a diffuse emission model convolved with the IRFs, which allows to save time during fitting of the maximum likelihood analysis. To compute this diffuse emission response, the tool requires the event file, FT2 file, XML source model file, the initial values of the Right Ascension and Declination (RA, DEC). In the standard data analysis with a predefined diffuse response, we can skip this step in our analysis.

Since the source XML model file contains several sources, to constrain their model parameters we use the `gtlike`¹³ tool in unbinned maximum likelihood analysis. Apart from the source XML

⁹<https://fermi.gsfc.nasa.gov/ssc/data/analysis/scitools/help/gtmktime.txt>

¹⁰<https://fermi.gsfc.nasa.gov/ssc/data/analysis/scitools/help/gtltcube.txt>

¹¹<https://fermi.gsfc.nasa.gov/ssc/data/analysis/scitools/help/gtexpmap.txt>

¹²<https://fermi.gsfc.nasa.gov/ssc/data/analysis/scitools/help/gtdiffrsp.txt>

¹³<https://fermi.gsfc.nasa.gov/ssc/data/analysis/scitools/help/gtlike.txt>

3.3. MAXIMUM LIKELIHOOD ANALYSIS OF THE LAT DATA

model file, event file, FT2 file and IRFs; this tool uses the files created by `gtselect`, `gtltcube` and `gtexpmap`. In conjunction with those processes, we also use `iso_P8R2_SOURCE_V6_v0614` as an isotropic model file. Then, the created new source model fit provides information about the flux, spectral indices and errors. The unbinned likelihood analysis was also used to compute the statistical probability of the model significance and the spectral behavior of the sources. The logarithm of the likelihood for individual photon events of index i is given by

$$\log \mathcal{L} = \sum_i \log M(E'_i, \hat{q}'_i, t_i) - N_{\text{pred}}. \quad (3.7)$$

The detection significance of the source is determined by using the maximum likelihood analysis with a Test Statistic (TS) defined as

$$TS = 2(\log \mathcal{L}_{\max,1} - \log \mathcal{L}_{\max,0}). \quad (3.8)$$

where $\mathcal{L}_{\max,0}$ is the maximum likelihood value for a model of the null hypothesis, i.e., a model that does not include the GRB and $\mathcal{L}_{\max,1}$ is the maximum likelihood value for a model including the GRBs. In the limit of a large number of statistics, the [Wilks \(1938\)](#) theorem states that the TS value is distributed asymptotically as a χ^2_m with m number of parameters quantifying for an extra source. The detection significance of the given source is roughly proportional to the square root of the TS .

3.3.2 The binned likelihood analysis

This analysis is used for long timescale or high source count data such as in the Galactic plane that consume time in the standard unbinned maximum likelihood analysis. Binned likelihood analysis is the favoured method for the LAT spectral analysis since the events in each bin is described by a Poisson distribution. For the given data set, one can bin them in the dimension of measured energy E' and apparent direction \hat{q}' . For the binned data the number of photons predicted from the contribution of point-like and diffuse emission indexed i lying in that energy bin j given the model:

$$\theta_j = \sum_i \theta_{ij}, \quad (3.9)$$

where θ_{ij} is give as

$$\theta_{ij} = \int_j dE' d\hat{q}' \int_{SR} dE d\hat{q} S_i(E, \hat{q}) R(E', \hat{q}'; E, \hat{q}, t). \quad (3.10)$$

Here $\int_j dE' d\hat{q}'$ shows the integral over the j th bin while the time integral is over the duration of the events observation. The observed number of photons in each bin is described by a Poisson distribution. The probability of Poisson likelihood to observe the detected photons in each bin n_j is given by

$$\mathcal{L} = \prod_{j=1}^{n_j} \frac{\theta_j^{n_j} e^{-\theta_j}}{n_j!} = \prod_j e^{-\theta_j} \prod_j \frac{\theta_j^{n_j}}{n_j!}, \quad (3.11)$$

¹⁴<https://fermi.gsfc.nasa.gov/ssc/data/access/lat/BackgroundModels.html>

where

$$\prod_j e^{-\theta_j} = e^{-N_{\text{pred}}}. \quad (3.12)$$

The logarithm of Eq. (3.11) is

$$\log \mathcal{L} = \sum_j n_j \log \theta_j - N_{\text{pred}}. \quad (3.13)$$

If the bin sizes approach to infinitesimally small value such that, $n_j = 0$ or 1 then, we are left with a product running over the number of photons which is unbinned likelihood (Sec. §3.3.1).

The binned likelihood analysis consists of a sequence of accessible data to simulate them. The analysis starts by binning data in time, energy and space into counts cube created using the *CCUBE* algorithm option of the *gtbin* tool, which is the data cube with the count stacking maps generated in projected sky coordinates using different energy bins. The *gtbin* allows selecting linear or logarithmic energy binning to make the spectra in a PHA or FITS file. It also provides the possibility to make light curves from the FT1 event file. The *gtexpcube2*¹⁵ tool then allows to make an exposure map for different energies. It is the first indicator of a usable data set for the livetime cube that was provided by *gtltcube*. The tool that convolves the IRFs and the XML file, which contains the spectral and spatial shape of each source in the model is *gtsrcmaps*¹⁶. The spectral shapes can be taken from a set of models, such as Comp (Eq. 2.2), SBPL (Eq. 2.3), PL (Eq. 2.6.2) and Broken Power-Law (BPL). The BPL function is given by

$$N_{\text{bpl}}(E) \equiv A_{\text{bpl}} \begin{cases} (E/E_b)^{\gamma_1} & \text{if } E < E_b \\ (E/E_b)^{\gamma_2} & \text{if } E \leq E_b, \end{cases} \quad (3.14)$$

where A_{bpl} is the amplitude, γ_1 and γ_2 are the indices before and after the break point for the energy E_b in keV, respectively. Additionally, the *gtsrcmaps* tool requires the spacecraft FT2 file and the binned exposure map created by the *gtexpcube2*. Finally, the fitting of spectrum is performed with *gtlike* tool using the binned likelihood analysis method. However, this method needs a high computing time.

In both unbinned and binned MLA method, a useful tool to compute the probabilities of photons associated to each event rely on an input source model, as opposed to other sources such as the Galactic or extragalactic diffuse emission, called the *gtsrcprob*¹⁷. This tool requires the FT2 file, the IRFs and the source XML model file. Afterwards, we use *gtdiffrsp* tool to run on this analysis in the case of the diffuse emission is excluded from the model.

¹⁵<https://fermi.gsfc.nasa.gov/ssc/data/analysis/scitools/help/gtexpcube2.txt>

¹⁶<https://fermi.gsfc.nasa.gov/ssc/data/analysis/scitools/help/gtsrcmaps.txt>

¹⁷<https://fermi.gsfc.nasa.gov/ssc/data/analysis/scitools/help/gtsrcprob.txt>

3.4 On orbit and ground processing

3.4.1 On orbit processing

The *Fermi* spacecraft orbits around the Earth at an altitude of ~ 565 km with an inclination of 26° (see Fig. 3.3 indicated by the dash lines) with respect to the equator. It operates typically in the survey mode, allowing a scan of the entire γ -ray sky every three hours (i.e., two orbits) that is oriented to point the LAT upward at all time. So the earth does not block the view. In this way, an observatory is partially protected from the cosmic-ray signal by the Earth's magnetosphere. The rocking causes the satellite pointing in which the normal to the front of the instrument (i.e., z-axis) to alternate orbits of $+35^\circ$ from the zenith direction towards the Northern and -35° from the zenith on the Southern hemispheres orbit (Atwood et al., 2009). This mode optimizes the

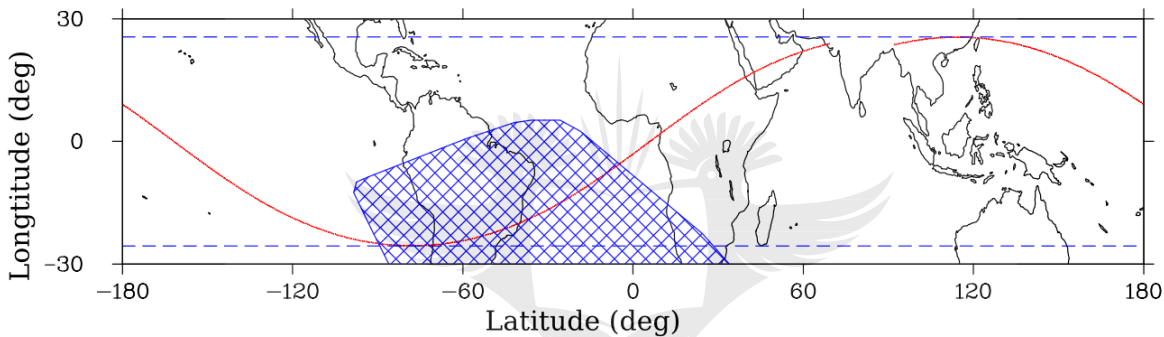


Figure 3.3 The *Fermi* spacecraft orbit: The blue hatched polygon band is representing the South Atlantic Anomaly (SAA) boundary, in which the detectors are turned off, the solid red curve is the path of the spacecraft over one orbit path from West to East and the horizontal dashed blue lines show the maximum of the inclination of $\pm 26^\circ$ (Fitzpatrick et al., 2012).

sky coverage of the LAT and maintains near-uniform exposure. Then, the instrument operates constantly and monitors the γ -ray sky over time. The onboard SAA polygon (see Fig. 3.3) for GBM has been updated on the *Fermi* spacecraft to reduce the number of GRB false detections near the SAA since 2010. The pointing variations also complicate the background in GBM due to the changing geomagnetic conditions (Fitzpatrick et al., 2012). The LAT does not operate when passing through the SAA, where the Van Allen signal belt approaches the Earth's surface at an elevation of ~ 200 km and the Earth's magnetic field is so high that it could saturate the radiations. The *Fermi* observatory can be pointed as well either by issuing commands from the ground or autonomously in the incident of a GRB. To compute the spacecraft position for different pointing and survey mode strategies, the simulator tool gtorbsim¹⁸ has been implemented based on the code already provided by FSSC for planning and scheduling system by the so-called *Timeline Assembler Keyword Oriented* (TAKO), but it does not have the capabilities of scheduling. The simulator tool can determine the time at which the spacecraft enters or exits the SAA.

¹⁸<https://fermi.gsfc.nasa.gov/ssc/data/analysis/scitools/help/gtorbsim.txt>

3.4.2 Ground processing

Each of the *Fermi* instruments (GBM and LAT) produce a series of real-time and ground-generated messages about transients and GRBs in an automated way. The initial position is produced by the Ground-Auto location and Flight Software algorithms on-board. One of the main goals of GBM is to provide information in order to allow re-pointing of the satellite in case the burst is not in the LAT FoV. When a burst trigger occurs, the onboard software determines the direction using the relative count rate in various NaI detectors. After two seconds, the LAT starts to observe the burst. The direction of the burst is determined by using the NaI detectors relative rates by comparing with the relative rates for each of 1634 directions ($\sim 5^\circ$ resolution) that are in the spacecraft coordinates (i.e., the right ascension and declination) (Meegan et al., 2009). Then, the trigger data (TRIGDAT) that contains all of the information about the rate of background, onboard position and burst intensity taken by GBM are transferred to the ground that helps the ground-based telescopes to follow up the GRB.

GCN circulars

The localization of GRBs detected by the BATSE instrument was rapidly distributed to the scientific community via the BATSE coordinates distribution network (BACODINE, Barthelmy et al., 1995). Thereafter, it was renamed as the Gamma-Ray Burst Coordinates Network (GCN)¹⁹. This system must provide the coordinates of the GRB (i.e., RA, DEC), hence when the GRBs are detected by various spacecraft telescopes, the obtained position is quickly received and distributed by the GCN circulars. However, in the *Fermi*-GBM, after real-time data arrives on-ground, a Burst Advocate (BA)²⁰ of the GBM duty scientist should review the results obtained by the automated processing. This also includes computation of the GRB duration, refining the localizations and classifications, analysis of the fluence, peak flux, and spectral parameters. Then, the BA submits the GCN circulars for follow-up observations at other wavelengths to the ground-based and space-based optical, radio, and X-ray observatories. The early afterglow follow-up strategy leads to redshift determination for a large fraction of GRBs and identification of GRB host-galaxies. This would prove essential for the establishment of cosmological distances of GRBs.

3.4.3 GRB detection

It is useful to produce a refined ground location of the LAT detected bursts as soon as possible after more data is delivered. This requires human intervention (Human in the Loop) to find an optimized location by using the gtfindsr²¹ tool. This tool determines the location of the point source by using a maximum likelihood analysis (see Sec. §3.3). For every detection, the ground-based telescopes receive a notification via a GCN within 10 s through the TDRSS satellite

¹⁹<https://gcn.gsfc.nasa.gov/>

²⁰BA is a person responsible to quickly react in case of GRB detections and anything related.

²¹<https://fermi.gsfc.nasa.gov/ssc/data/analysis/scitools/help/gtfindsr.txt>

network. There are two ways of distributing circulars to the GRB community. The first is the real-time distribution of GRB positions detected by various spacecraft (*Swift*, *INTEGRAL*, *IPN*, etc.). The second one is the distribution of follow-up observation which is sent by the GBM and LAT team members.

The LAT likelihood detection is required to perform a Likelihood Ratio Test (LRT) between a model containing all the background sources with a point source and a model containing only the background sources. The LAT GRB is considered as likelihood detection if the number of high energy photons with probability $> 90\%$ coming from the position of bursts greater than two and their *Test Statistic* (*TS*, see Eq. 3.8) more than 25 (i.e., 5σ). The *TS* values between 20 and 25, provide a marginal detection of the GRBs. The LAT Low-Energy (LLE, Pelassa et al., 2010) class is produced to be used for the study of GRBs in energy between 30 and 100 MeV. The

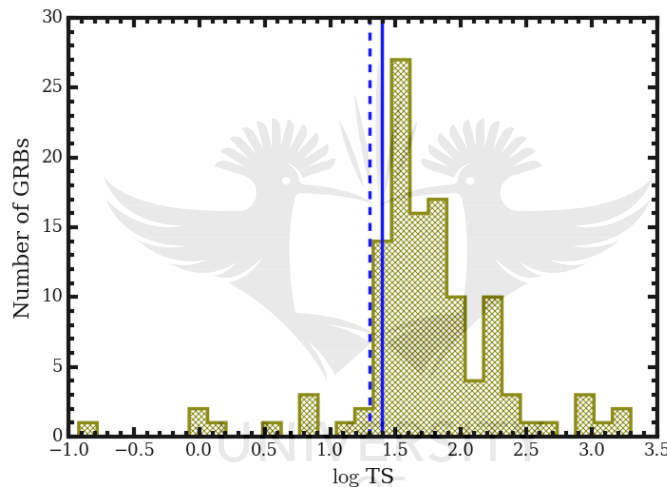


Figure 3.4 The test statistic distribution of 134 LAT GRBs (from Fermi.gsfc.nasa.gov, 2017).

detection of an LLE GRB is made on data accumulated -500 s and 500 s before and after the trigger, respectively. Using the data off-pulse intervals one can construct a background model by interpolating over the on-pulse interval. Then, it is claimed an LLE detection if the signal in the on-pulse time interval is $> 4.7\sigma$ above the expected background level and the significance $> 4\sigma$ is claimed as a marginal detection. In Fig. 3.4, the vertical broken line indicates the marginal detection with $TS = 20$ while the vertical line shows the threshold detection at $TS = 25$.

3.5 Detection of new LAT GRBs

The *Fermi*-LAT and GBM are both able to localize GRBs onboard and in real-time. This enables the announcement of detections and localizations to be distributed to the broader GRB community in less than a minute. These duties are performed by an assigned BA, who performs a standard likelihood analysis to identify significant signals and localization of the detected bursts in a

timely manner. Once LAT data arrives on the ground (~ 8 hours after the trigger), a few different automated processes run through the data to search for transient or flaring events on different time scales, with results monitored by BA. The automated pipelines relevant to the search for excess emission in GRB data are the internal BA tool and the LAT Transient Factory (LTF, [Vianello et al., 2015](#)).

The LAT BA Tool has been designed by the *Fermi* group to provide automated analysis of LAT data using the gtGRB package for a particular burst location and Mission Elapsed Time (MET). The code initially developed for the likelihood followup of the *Fermi* All-sky Variability Analysis (FAVA, [Ackermann et al., 2013b](#)) observed events to search for high-energy emission from GRBs detected by GBM over a various time- and energy-scales. The tool is very interactive to run the analysis. The LTF tool is a new GRB-detection scheme made it possible to overcome the large GBM systematic error on the localization by searching the LAT data on various timescales and in a larger FoV. This increases the number of LAT-detected burst rate of the order of about 50% of the reported GRBs in GCNs. The LAT has detected high-energy γ - ray emission from > 130 GRBs ([Bissaldi et al., 2017](#)), including 10 short GRBs.

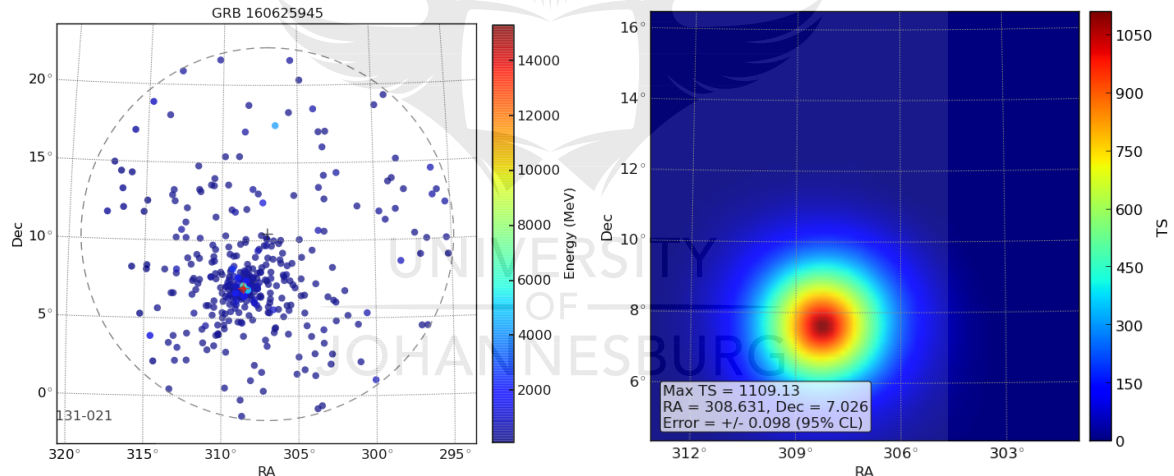


Figure 3.5 *Left panel:* the energy distribution of GRB 160625B with respect to the best localization of $(\text{RA}, \text{DEC}) = (308.56^\circ, 6.93^\circ)$. The color bar indicates the photon energy in MeV. *Right panel:* the TS map of GRB 160625B. The color bar denotes the TS at a given location. (Credit: Flare Advocate (FA) *Fermi* tool)

In case a bright LAT GRB is detected, a BA can use results from the LTF and BA tool to determine if further manual analysis needs to be done. Both tools have similarities and are good for cross-checking. Sometimes it is obvious that a candidate is not real. However, in most cases, BA needs to proceed with manual analysis to check the detection of the GRB and refine its localization. The manual analysis searches for excess emissions by performing a likelihood fit and generating a TS map over different timescales. A source with $TS > 25$ ($\sim 5\sigma$) above the expected background is considered as a detection.

For an interesting bright GRB detected by LAT, the *Fermi* collaboration publishes the results, where the main author would be the BA. For instance, while I was acting as a BA duty, four bright GRBs were detected for which I am the author of their GCN circulars. Among these, GRB 160625B (Dirirsa & Fermi-LAT Collaboration, 2016; Dirirsa et al., 2016) is an extremely bright GRB with three distinct γ -ray emission episodes, which was followed by a bright prompt optical flash. This is an unusual event when the GRB is still active and bright. More than 300 photons were detected above 100 MeV with probability $> 90\%$ (see the left panel of Fig. 3.5). The highest-energy photon is a 15 GeV event which was observed at 345 s after GBM trigger time. A preliminary result of this analysis was published by Dirirsa & Fermi-LAT Collaboration (2016). The right panel of Fig. 3.5 depicts the *TS* map of GRB 160625B with more than 33σ significance that obtained from the BA tool. The other six LAT GRBs were detected when I was on a BA duty includes GRB 181231A (Dirirsa & Ohno, 2018), GRB 180210A (Dirirsa & Bissaldi, 2018), GRB 170206A (Dirirsa et al., 2017b), and GRB 160623A (Vianello et al., 2016). Additionally, I have contributed analysis to other five new bright LAT GRBs such as GRB 190731A (Ohno et al., 2019), GRB 190511A (Axelsson et al., 2019), GRB 160816A (Racusin et al., 2016), GRB 160521B (Axelsson et al., 2016) and GRB 160509A (Longo et al., 2016).

3.6 The Gamma-ray Burst Monitor performance

One of the main goals of the LAT instrument is to support GBM in observing GRBs by providing high-energy measurements (i.e., 30 MeV– $\gtrsim 300$ GeV energy range, Atwood et al., 2009). In addition, GBM provides the location of GRBs by using the signals from the low-energy detectors (i.e., NaI, 8 keV–1 MeV energy range) within several degrees (see Fig. 2.7). This information may be used to re-point the LAT towards an interesting energetic GRB that occurred outside its FoV. This re-pointing would be requested if the GBM burst exceeds a specified threshold peak flux or fluence. Furthermore, it provides a rapid GRB position for ground or space-based telescopes for fast follow-up observations and for further improvements in localization using the *Swift*. The low-energy detectors of GBM are overlapping in energy with the detectable energy range of the *Swift*-BAT (i.e., 15–150 keV band) instrument. So, the GBM sample is valuable for *Swift*-BAT science by providing important characteristics of prompt emission. The GBM high-energy detectors (i.e., BGO, 200 keV–40 MeV band) provides good sensitivity, overlapping with the LAT low-energy analysis (Pelassa et al., 2010) at the bottom end of the gamma-ray energy range, and with the LAT at the high-end (Atwood et al., 2009).

3.6.1 GBM spectral analysis

In this section, we describe the GBM spectral analysis. GBM data are obtained from multiple configurations (see Sec. §2.3.4.1): TTE, CTIME and CSPEC. These data can be downloaded from the

Fermi GSFC Data Center²² or directly using the gtburst²³, which is a python *Graphical User Interface* used to analyse GRBs.

We have implemented the criteria in [Guiriec et al. \(2011\)](#) for GBM detector selection of the *Fermi* data, as discussed below. We used the RMFIT package to simultaneously fit the spectral data of GBM NaI detectors that have source incidence smaller than 50° . In order to subtract the background in GBM data, we defined two-time intervals before and after the GRB prompt emission for every energy channel. We fitted a second-order polynomial function to a user-defined background and have interpolated this fit across the whole GRB prompt phase. We have also used the standard 128 energy bins of the CSPEC data-type, for NaI using the channels from 8 keV to 900 keV by cutting out the overflow high energy channels as well as the Iodine K-edge from 30 to 40 keV ([Meegan et al., 2009](#)). For the GBM BGO detectors, we have used data from 220 keV to 40 MeV and from 210 keV to 40 MeV, respectively for detectors b0 and b1. In general we used b0 together with NaI 1–6 detectors and b1 together with NaI 7–12 detectors, in case there was no overlap.

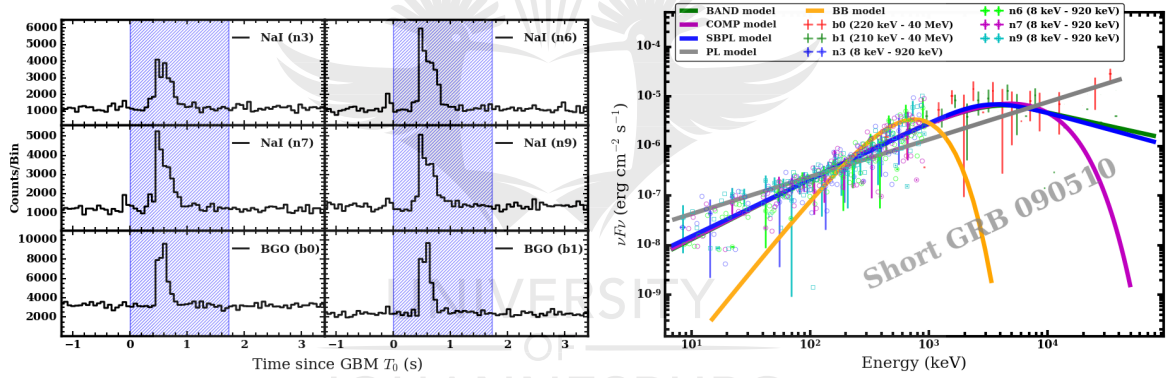


Figure 3.6 *Left panel:* the light curves of short GRB 090510 for different GBM detectors. The hatched band indicates the interval $T_{90} = T_{05} - T_{95}$ (s) from the GBM trigger T_0 . *Right panel:* the Band, SBPL, Comp, PL and BB spectral models performed to fit the spectra of short GRB 090510.

Here we used the short GRB 090510 to summarize the spectral features of the GBM data detected in the T_{90} interval. The GBM light curves of NaI (n3, n6, n7 and n9) and BGO (b0 and b1) detectors are shown on the left panel of Fig. 3.6. The time-integrated spectral analysis is performed using the RMFIT over $T_{90} = 1.74$ s from the GBM trigger time. The SBPL model gives a reasonable fit (see Tab. 3.1). In particular, we show the comparison of the spectral profile corresponding to the Comp model, SBPL model, Band model, PL model and the BB model considered for GRB 090510 as depicted in Fig. 3.6. The fit statistics used for spectral analysis was the Castor statistic (C-stat), which is a variant of the log-likelihood introduced by [Cash \(1979\)](#).

²²<https://fermi.gsfc.nasa.gov/ssc/data/access/>

²³<https://fermi.gsfc.nasa.gov/ssc/data/analysis/scitools/gtburst.html>

Table 3.1 The result of T_{90} time-integrated spectral analysis.

GRB Name	Model	$T_{05}-T_{95}$ (s)	E_p/E_0 (keV)	α, α_1, γ	β	kT (keV)	C-Stat/dof ^(*)
GRB 090510	Band	0.00–1.74	4382 ± 430	-0.77 ± 0.03	-2.5 ± 0.2		879.7/706
	Comp		4816 ± 293	-0.79 ± 0.03			895.2/707
	SBPL		3002 ± 468	-0.85 ± 0.03	-2.7 ± 0.2		871.8/706
	PL			-1.25 ± 0.01			1302.8/708
	BB					193.6 ± 6.4	1568.2/708

Notes: α and β are the lower and higher photon indices for the Band and SBPL functions, respectively. γ is the photon index of the Comp model while α_1 is that of the PL. E_0 is the SBPL e-folding energy and E_p is the Band or Comp peak energy. kT is the BB temperature. The C-Stat/dof^(*) is the ratio of the C-stat resulting from the fit and the associated degrees of freedom (dof).

It is the modification of Cash-statistic²⁴ combined with the χ^2 statistic, thus it can be used to estimate the goodness of a fit. The capability of each function to better represent the GBM GRB spectral shape is clearly visible. The three models are similar at low energies below ~ 500 keV, but they differ in the high energy tail of GBM BGO spectra. The Comp model (magenta curve) excessively higher estimate the spectral break energy due to the lack of a power-law higher energy component. Besides, the Band model (green curve) tends to be softer at low energies and harder at higher energies than the SBPL (blue curve). The spectral energy of the BB model is shown in an orange curved line.

3.6.2 LAT and GBM joint spectral analysis

In this sub-section, we discuss the information needed to perform spectral analysis of a GRB prompt emission using both the GBM and LAT data and fitting those data using the spectral fitting package RMFIT. We also present the methodology needed to do a combined LAT and GBM (BGO and NaI) analysis. The method of GBM spectral analysis is presented in Sec. §3.6.1. For the analysis of LAT data, we have selected Pass 8 Transient class events (Transient20E)²⁵ within a 10° radius of interest. The data is binned in 30 logarithmic energy steps between 30 MeV and 300 GeV. Since we have considered energies below 100 MeV, the gtlike tool was used to perform a binned maximum-likelihood analysis that includes a correction for the energy dispersion effect. We derived the observed spectrum and the detector response matrix using the *Fermi* Science Tools gtrspgen and gtbin, respectively. To produce a background spectrum file, the background estimation tool gtbkg²⁶ was used.

²⁴<https://heasarc.nasa.gov/docs/xanadu/xspec/xspec11/manual/node57.html>

²⁵https://fermi.gsfc.nasa.gov/ssc/data/analysis/documentation/Cicerone/Cicerone_Data/LAT_DP.html

²⁶<https://fermi.gsfc.nasa.gov/ssc/data/analysis/scitools/help/gtbkg.txt>

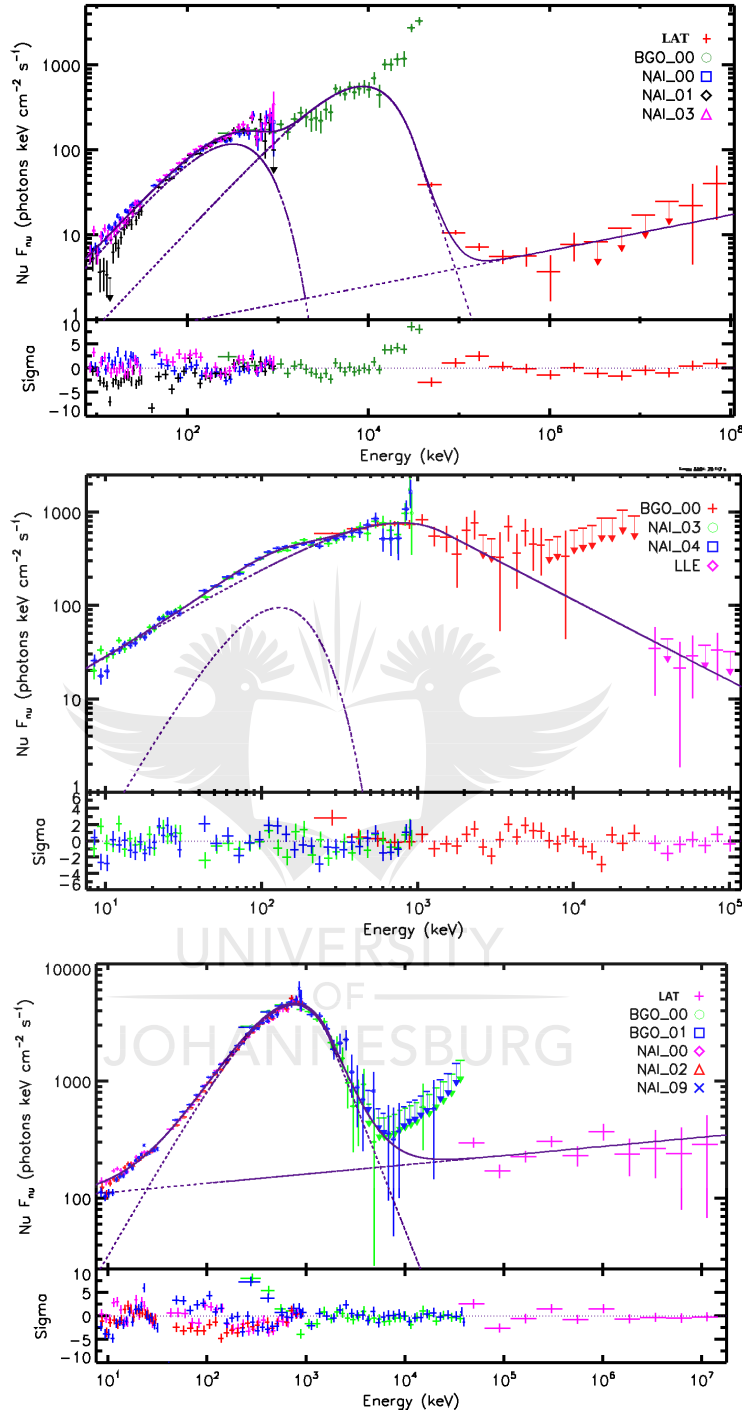


Figure 3.7 Top panel: the νF_ν joint spectral fitting of GBM and LAT data of GRB 160509A. Top middle panel: the νF_ν joint spectral fit of GBM and LLE data of GRB 150403A. Bottom panel: the νF_ν joint spectral fitting of GBM and LAT data of GRB 090902B. The lower panels show the residual of the spectral fit. The fit results are summarized in Tab. 3.2.

Table 3.2 GRB 160509A, GRB 150403A and GRB 090902B as jointly measured by GBM and LAT (or LLE) and results from the spectral model fits of time-integrated flux within T_{90} .

GRB Name	Model	$T_{05} - T_{95}$ (s)	α, γ	β	E_p, E_0 (keV)	kT (keV)	α_1	C-Stat/dof
GRB 160509A	Band+Comp+PL	7.68-379.4	-0.87 ± 0.08	-5.16 ± 0.49	8591.5 ± 68.3			
			-0.79 ± 0.04		317.1 ± 16.6		-1.76 ± 0.10	1741.9/474
GRB 150403A	Band+BB	3.33-25.6	-1.02 ± 0.02	-2.95 ± 0.10	793.6 ± 52.6	33.30 ± 1.58		524.8/358
GRB 090902B	Band+PL	0-22	-0.53 ± 0.01	-4.14 ± 0.28	760.7 ± 7.7		-1.92 ± 0.01	1320.6/601

3.7 Summary

We have briefly presented the *Fermi* mission overview based on the source model, event classification, instrumental response functions and the type of data processing. We have also discussed data preparation, using the suite of *Fermi* science tools, which is relevant to the GRB spectral analysis. Besides, the maximum likelihood method used to compute the probability of obtaining an input model for γ -ray sources and their associated spectra is discussed. Furthermore, we presented my contributions to the LAT Burst Advocate shift of detecting new LAT GRBs. The description of the GBM spectral analysis, as well as the combined LAT and GBM time-integrated spectral analysis, was reviewed, with examples.



GAMMA-RAY BURST COSMOLOGY

Contents

4.1	Introduction	59
	4.1.1 Connection between Supernovae and GRBs	61
4.2	Cosmological parameters	61
	4.2.1 Distance measures in cosmology	64
	4.2.2 Distance modulus	65
4.3	Lambda-Cold Dark Matter model	66
4.4	Using GRBs as standard candles	68
	4.4.1 Amati relation	69
	4.4.2 Yonetoku relation	71
	4.4.3 Decorrelation energy	72
4.5	Extended Hubble diagram	73
	4.5.1 Construction of the Hubble diagram from the Amati relation	73
	4.5.2 Construction of the Hubble diagram from the Yonetoku relation	75
4.6	Constraints on the dark-energy and the Hubble constant	75
4.7	Evolution of the Amati relation with redshift	76
4.8	Summary	78

4.1 Introduction

In this chapter, we review the cosmological implications of GRBs. Cosmology is the study of the universe, which strives to make sense of the large-scale nature of objects as a whole around us using scientific techniques. The extreme brightness of GRBs with isotropic luminosities up to 10^{54} erg s⁻¹ enables them to be detectable up to very high redshift of $z \sim 9.4$ (GRB 090429B, Cucchiara

et al., 2011), which is the most distant known GRB to date. The photons from this burst took approximately 13.2 billion years to reach us and irradiated the extragalactic objects along our line of sight up to the first stars, after the Big Bang (see the left panel of Fig. 4.1). Therefore, GRB allows studying the cosmic star formation rate and their evolution in the early universe, which could have been difficult in the past. Therefore, GRBs could be remarkable cosmological tools to explore the high-redshift universe. The furthest astrophysical object detected to date with a

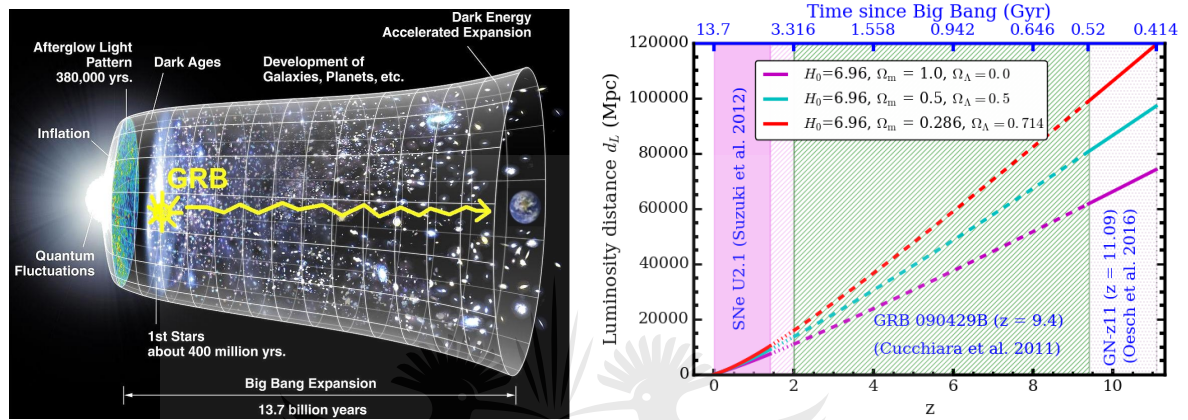


Figure 4.1 *Left panel:* photons from a GRB and its afterglow travel on its way to us through the surrounding burst medium, host galaxy medium, and other intervening absorbers. GRBs may probe the properties and environment of the first stars and galaxies in the universe (<http://www.armaghplanet.com/blog/the-big-bounce-theory-what-is-it.html>). *Right panel:* the luminosity distance, d_L , of different astrophysical objects in Λ CDM cosmology with standard parameters vs. redshift. The upper x -axis shows the time (Gyr) since Big Bang.

spectroscopic redshift of $z = 11.09$ was Galaxy GN-z11 (see the right panel of Fig. 4.1) that has been reported recently by Oesch et al. (2016).

GRBs could be used as standard candles, like SNe Type Ia to use them for cosmology (Amati et al., 2002; Ghirlanda et al., 2004b; Yonetoku et al., 2004; Amati, 2006b; Amati et al., 2008) (See Chapters §5 and §6 for the detailed analysis of constraining cosmological parameters). But SNe Type Ia can only be observed at $z < 2$. They are believed to be the result of the explosion of a carbon-oxygen white dwarf in a binary as it goes over the mass of the Chandrasekhar limit of $1.4 M_\odot$ and explodes (Jones et al., 2013). Empirically, GRBs are brighter than all SNe at the maximum light of the absolute magnitude and characterized by their absence of Hydrogen emission lines in the spectra. Thus, they could be treated as useful tools to determine distances in cosmology.

The accelerating expansion of the universe is discovered by two independent groups of researchers (Riess et al., 1998; Perlmutter et al., 1999; Perlmutter & Schmidt, 2003), which is attributed to the mysterious energy with negative pressure the so-called “Dark-Energy”. The latest observations confirm that more than 70% of the constituent of the universe is currently

dominated by dark-energy (Planck Collaboration et al., 2018; Riess et al., 2018), but its nature remains a big challenge. Furthermore, observational results from different independent sources such as the Cosmic Microwave Background (CMB, Spergel et al., 2003; Hinshaw et al., 2013; Bennett et al., 2013), the Hubble parameters (Jimenez et al., 2003) and the Baryon Acoustic Oscillations (BAO, Eisenstein et al., 2005) also strongly supported the hypothesis that the current universe appears to be spatially flat and the expansion is accelerating. The early universe from the period when the CMB was emitted at $z \sim 1100$ to the epoch when the first stars were formed about $z \sim 20$, so-called the dark age is still poorly understood (Barkana & Loeb, 2001). So, GRBs are a promising tool to explore the cosmic expansion at higher redshift beyond the observation of SNe Ia.

4.1.1 Connection between Supernovae and GRBs

Observations have proved that Supernovae Type II b/c can be associated with long GRBs (Zeh et al., 2004). For instance, SN 1998bw was observed in the error-box of GRB 980425 and indicated that the two events of the explosion are associated (Galama et al., 1999). There are also spectroscopically confirmed GRB-connected SNe such as GRB 030329/SN 2003dh (Hjorth et al., 2003; Stanek et al., 2003), GRB 031203/SN 2003lw (Malesani et al., 2004) and GRB 060218/SN 2006aj (Mazzali et al., 2006). The total energy released from a GRB is comparable to that of the energy emitted during a core-collapse supernova (i.e., the supernovae caused when the deaths of massive stars collapse their cores). However, there is an important difference between the two types of events. In GRB, the energy is emitted in a few tens of seconds. But in a supernova, the energy emission takes a few months (Gomboc, 2012).

4.2 Cosmological parameters

The key equations of cosmology are the two Friedmann-Lemaître-Robertson-Walker (FLRW) equations (see for e.g., Friedmann, 1922; Carroll, 2001; Frieman et al., 2008) that are obtained from the modified standard Einstein's field equation with cosmological constant (Λ), which defines how the dark-energy in the universe drives its expansion. The field equations of General Relativity applied to the FLRW metric are given by

$$\begin{aligned} H^2 \equiv \left(\frac{\dot{a}}{a}\right)^2 &= \frac{8\pi G}{3}\rho + \frac{\Lambda}{3} - \frac{k}{a^2}, \\ H^2 + \dot{H} \equiv \frac{\ddot{a}}{a} &= -\frac{4\pi G}{3}(\rho + 3p) + \frac{\Lambda}{3}, \end{aligned} \quad (4.1)$$

where $\dot{a} = da/dt$ is the derivative of a with respect to time, $a = 1/(1+z)$ is the scale factor, $H = \dot{a}/a$ is the Hubble parameter, G is the gravitational constant, $k = 0$ or ± 1 , ρ and p are the matter density and pressure, respectively. These two FLRW equations allow to describe different components, radiation, matter and dark-energy, all involve in the expanding universe differently

(see Fig. 4.2). To find the continuity equation which holds all components of the cosmological fluid with a non-cosmological constant, we differentiate Eq. (4.1) as

$$\dot{\rho} + 3\frac{\dot{a}}{a}(\rho + p) = 0. \quad (4.2)$$

The terms in Eq. (4.2) contribute to the change in the component density as the universe is stretching. The term $(\rho + p)$ is corresponding to the dilution in the density as the size of the universe has expanded. The p term is corresponding to the dissipated energy due to the work done by pressure as the universe expands. In cosmology, each density constituent of the universe is sometimes described by the pressure and density, so-called the equation of state $w = p/\rho$. Then, Eq. (4.2) can be written as

$$\frac{d\rho}{\rho} = -3(1+w)\frac{da}{a}. \quad (4.3)$$

This equation has a solution with a power-law dependence on the scale factor

$$\rho = \rho_0 \left(\frac{a}{a_0} \right)^{-3(w+1)}, \quad (4.4)$$

where $a_0 = 1$ is a common value used at the current time, which will be determined as the change in the scale factor when its reference value at the fixed instant of time t is chosen. The term ρ_0 is the density at the current epoch. The evolution of the density in terms of a can be determined with the equation of state function $w = p/\rho$. Non-relativistic matter has $w \equiv w_m \simeq 0$, where matter is considered collisionless in the large-scale structure, then the dark matter density evolves as $\rho_m \propto a^{-3}$. For photons (radiation) $w \equiv w_r = 1/3$, or ultra-relativistic particles (implying $\rho_r \propto a^{-4}$). For the cosmological constant at $w \equiv w_{de} = -1$, implying $\rho_\Lambda \propto a^0 = \text{constant}$. Since the $(\rho + 3p)$ term in the second part of Eq. (4.1), the gravity of a component that satisfies $p < -\rho/3$, with non-cosmological constant, $w < -1/3$ is repulsive. Then, we find the main property of dark-energy (i.e., $\ddot{a} > 0$), which cause the expansion of our current universe to accelerate.

Considering a flat universe ($k = 0$) with cosmological constant $\Lambda = 0$, we can obtain the critical energy density from Eq. (4.1), $\rho_{cr} = 3H^2/8\pi G$. Critical density changes over time as the Hubble parameter evolves. Then, the density parameter for the comparison of different cosmological models is defined as,

$$\Omega = \frac{\rho}{\rho_{cr}} = \frac{8\pi G}{3H^2}\rho, \quad (4.5)$$

where Ω is representing the constituent density parameter which decides the fate of the universe. Hence, $\Omega > 1$ implies a closed universe, $\Omega < 1$ an open universe and $\Omega = 1$ a flat universe. We can rewrite the FLRW Eq. (4.1) for the sum of the density parameters from all individual components i.e.,

$$\Omega_r + \Omega_m + \Omega_\Lambda - \Omega_k = 1, \quad (4.6)$$

where radiation density parameter $\Omega_r = 8\pi G \rho_r / 3H^2$, the matter density parameter $\Omega_m = 8\pi G \rho_m / 3H^2$, the cosmological constant $\Omega_\Lambda = \Lambda / 3H^2$ and $\Omega_k = k/(Ha)^2$ is a constant characterizing the

curvature. Using Eq. (4.4), one can determine the density in terms of scale factor $a = 1/(1+z)$ for radiation, matter and cosmological constant as

$$\begin{aligned}\rho_r &= \rho_{r0}a^{-4} = \rho_{r0}(1+z)^4, \\ \rho_m &= \rho_{m0}a^{-3} = \rho_{m0}(1+z)^3, \\ \rho_\Lambda &= \rho_{de0}a^{-3(w_{de}+1)} = \rho_{de0}(1+z)^{3(w_{de}+1)},\end{aligned}\quad (4.7)$$

where $\rho_{r0} \simeq 4.6 \times 10^{-31} \text{ kg m}^{-3}$, $\rho_{m0} \simeq 2.4 \times 10^{-27} \text{ kg m}^{-3}$ and $\rho_\Lambda \simeq 7 \times 10^{-27} \text{ kg m}^{-3}$ are the present energy density of radiation, matter and dark-energy, respectively (Read, 2014). In the left panel of Fig. 4.2, the hatched maroon color represents dark-energy parameter $w_{de} = -1 \pm 0.2$ (Debono & Smoot, 2016). Considering the expansion rate $H = \dot{a}/a_0$ for flat universe and non cosmological constant Eq. (4.1) can be written as

$$\left(\frac{1}{a_0} \frac{da}{dt}\right)^2 = \frac{8\pi G}{3}(\rho_r + \rho_m + \rho_{de}), \quad (4.8)$$

where $\rho = \rho_r + \rho_m + \rho_{de}$. Using Eqs. (4.5) and (4.7), the FLRW Eq. (4.8) can be expressed in terms of the current cosmological parameters as

$$\begin{aligned}\frac{1}{a_0} \frac{da}{dt} &= H_0 \sqrt{\Omega_{r0}(1+z)^4 + \Omega_{m0}(1+z)^3 + \Omega_{\Lambda0}}, \\ &= H_0 E(z),\end{aligned}\quad (4.9)$$

where

$$E(z) = \sqrt{\Omega_{r0}(1+z)^4 + \Omega_{m0}(1+z)^3 + \Omega_{\Lambda0}}, \quad (4.10)$$

is a function proportional to $\dot{a}/a(t)$ and H_0 is the rate of expansion today. Here, the total

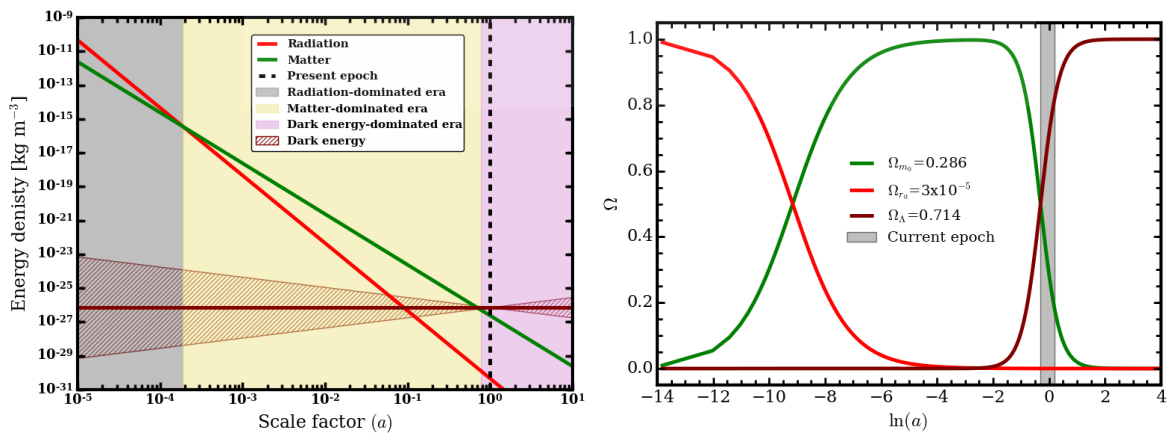


Figure 4.2 *Left panel:* the density evolution of the main constituents of the universe with the scale factor. The hatched band in maroon color represents $w_{de} = -1 \pm 0.2$. *Right panel:* the energy density of each cosmic component illustrated with different line colors, as labeled in the legend. A vertical shaded region corresponds to the current epoch.

constituent density of the universe is $\Omega_{r0} + \Omega_{m0} + \Omega_{\Lambda0} = 1$. Then, the critical density as a function of z is

$$\rho_{cr} = \frac{3}{8\pi G} \frac{\dot{a}^2}{a^2} = \frac{3H_0^2}{8\pi G} E^2(z) = \rho_{c0} E^2(z). \quad (4.11)$$

We can use this value to describe the density parameters of the universe following Eq. (4.1),

$$\Omega_i = \frac{\rho_i}{\rho_{cr}} = \Omega_{i0} \frac{(1+z)^{n_i}}{E^2(z)}, \quad (4.12)$$

where a zero subscript refers present-day values and $n_i = 3(1+w_i)$. Here, w_i is the equation of state for each density component of the universe that contributing to the evolution of expansion.

Now we integrate Eq. (4.9) for the universe to expand from 0 to $a = 1/(1+z)$

$$t(a) = \int_0^t dt = \frac{1}{H_0} \int_0^a \frac{da}{\sqrt{\Omega_{r0}a^{-4} + \Omega_{m0}a^{-3} + \Omega_{\Lambda0}}}. \quad (4.13)$$

This gives the age-scale relationship of the universe. In the left panel of Fig. 4.2 we have shown the density evolution of the constituents of the universe with different powers of a ; their relative importance also changes over time. For instance, at the current time, the energy density due to radiation is much lower than the energy density of matter and the energy density of the dark-energy. The behavior of the energy density due to dark-energy does not vary with scale factor and is exceeded by the energy densities in radiation and matter at the early time. As shown in the right panel in Fig. 4.2 (maroon curved line), the dark-energy is, only just at the present epoch, starting to dominate the energy density of the universe.

4.2.1 Distance measures in cosmology

In cosmology, the commonly used distance measurement from the observer to the source at redshift z is the comoving distance, which is given by

$$d_C = \frac{c}{H_0} \int_0^z \frac{dz'}{E(z')}, \quad (4.14)$$

where $c = 3 \times 10^{10}$ cm/s is the speed of light. The transverse comoving distance d_M that correspond to along the line of sight of d_C (e.g., Hogg, 1999) is given by

$$d_M = \begin{cases} \frac{c}{H_0 \sqrt{|\Omega_k|}} \sin\left(\sqrt{|\Omega_k|} d_C(z) \frac{H_0}{c}\right) & \text{for } \Omega_k < 0 \text{ (open universe),} \\ d_C(z) & \text{for } \Omega_k = 0 \text{ (flat universe),} \\ \frac{c}{H_0 \sqrt{\Omega_k}} \sinh\left(\sqrt{\Omega_k} d_C(z) \frac{H_0}{c}\right) & \text{for } \Omega_k > 0 \text{ (closed universe).} \end{cases} \quad (4.15)$$

The d_L is related to the transverse comoving distance d_M of Eq. (4.15) by

$$d_L = (1+z)d_M(z). \quad (4.16)$$

In the analysis of the GRB phenomenological observables, to compute the peak luminosity and the isotropic radiated energy in the spatially flat universe ($\Omega_k = 0$), we use the d_L given by

$$d_L = (1+z) \frac{c}{H_0} \int_0^z \frac{dz'}{E(z')}.$$
 (4.17)

This result motivates the strong connection between cosmology and GRB science. An essential

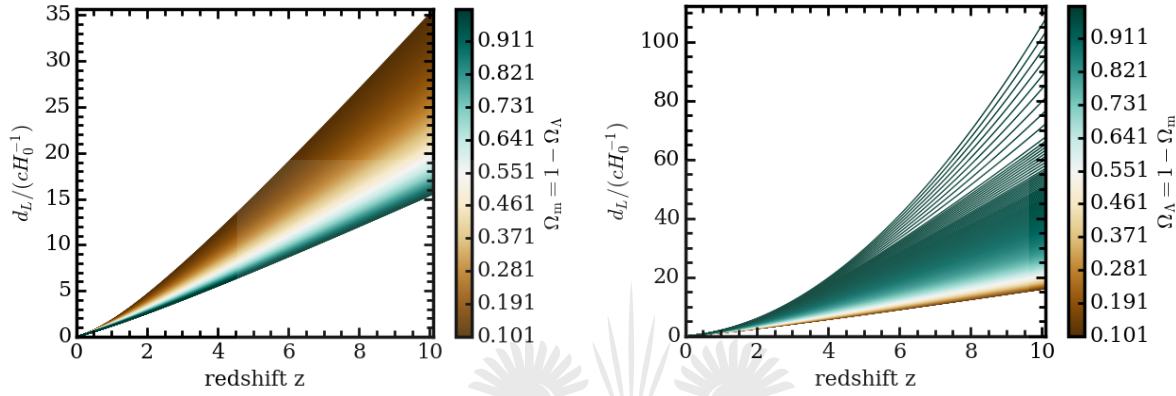


Figure 4.3 *Left panel:* the distribution of d_L for different values of the dark matter parameters. *Right panel:* the distribution of d_L with different values of the dark-energy parameters, assuming a flat universe.

constituent here is the fact that the d_L can be expressed in terms of the cosmological parameters, as a series of density parameters $\Omega_\Lambda = 1 - \Omega_m$ and $\Omega_m = 1 - \Omega_\Lambda$, i.e., assuming the total density parameters $\Omega = 1$ (see Fig. 4.3). The left panel of Fig. 4.3 shows the d_L at high redshift is strongly sensitive to the density of dark matter, $\Omega_m \lesssim 0.5$. The value of the d_L/cH_0^{-1} is mainly depends on Ω_Λ at lower redshift, i.e., d_L/cH_0^{-1} exhibits an exponential increase as $\Omega_\Lambda \gtrsim 0.5$ which is also reflected in the right panel of Fig. 4.3. This indicates that high-redshift objects such as GRBs could be useful to study the evolution of dark matter and could provide precise constraints on the cosmic expansion history.

4.2.2 Distance modulus

The equation commonly used to determine the d_L to astrophysical objects in the universe is

$$F = \frac{L}{4\pi d_L^2},$$
 (4.18)

where P is the observed flux of the source and L (in units of erg/s) is the luminosity used to determine the rate at which the source releases energy. Astronomers have been measuring the brightness (i.e., the absolute magnitude, M) of the astrophysical objects using the apparent magnitude, m (Hogg, 1999). The apparent (measured) magnitude is defined in terms of the

logarithmic observed flux (F) of Eq. (4.18) as

$$m = -2.5 \log \frac{F}{F_0}, \quad (4.19)$$

where F_0 is a normalization constant. Similarly, the absolute magnitude M is given in terms of the logarithmic L of the object as

$$M = -2.5 \log \frac{L}{L_0}, \quad (4.20)$$

where L_0 is a luminosity normalization constant. Both the F_0 and L_0 are defined so that the measured and intrinsic magnitude agree for an object at 10 pc (~ 32.62 light years) away. This difference, $m - M$ is called the distance modulus. Therefore,

$$\mu \equiv m - M = 2.5 \log \frac{L}{F} + C, \quad (4.21)$$

where C is the constant. From Eq. (4.18), we get $d_L^2 4\pi = L/F$ in units of pc 2 . Replacing this term in Eq. (4.21), we get the distance modulus

$$\mu = 5 \log \frac{d_L}{10 \text{ pc}}. \quad (4.22)$$

Since we are dealing with distant astrophysical objects, it is more useful to use an equivalent equation with a unit of 1 Mpc. Therefore, Eq. (4.22) can be expressed as

$$\mu = 5 \log \frac{d_L}{\text{Mpc}} + 25. \quad (4.23)$$

The distance modulus of source depends on the d_L (i.e., the larger d_L will have a greater μ). The distance modulus (Eq. 4.23) can be equated for d_L , and it becomes

$$d_L = 10^{1/5(\mu - 25)} \text{ Mpc}. \quad (4.24)$$

So, this equation indicates that if a source's m and M are known, we can easily determine the distance of the object. The distance of the source can also be determined from Eq. (4.18) if the source's flux and its luminosity are known. In general, Eq. (4.24) is independent of cosmological parameters.

4.3 Lambda-Cold Dark Matter model

The Lambda-Cold Dark Matter model (Λ CDM) is based on cosmological constants in a flat universe. The current cosmological picture of the universe is characterized by the Λ CDM model, which depends on the dark-energy and cold dark matter¹ components. According to the Hubble Space Telescope (HST) cluster Supernova Survey project of “Union 2.1” (hereafter SNe U2.1,

¹Cold dark matter is a form of matter needed to quantify the observed gravitational effects in large-scale structures, which interacts weakly with electromagnetic radiation.

Suzuki et al., 2012), these two components describe roughly 95% of the energy constituent of the universe.

The dark-energy has constraint on large-scales. The main evidence for its existence comes from the estimation of the distance modulus of SNe Type Ia (Riess et al., 1998; Perlmutter et al., 1999; Perlmutter & Schmidt, 2003). Dark-energy is characterized by a repulsive gravity (acting as a negative pressure field) uniformly distributed in the universe. Dark-energy could be associated with a cosmological constant (Λ). However, the estimated value of the dark-energy is off by 120 orders of magnitude from predictions of theoretical particle physics (Carroll, 2001; Frieman et al., 2008).

The realization of the Λ CDM model depends on an accumulation of large-scale observations. SNe Type Ia is one of the measurements that agree with the parameters of the Λ CDM paradigm. At present, the preferred results for constituents of the universe are estimated from the data of the Wilkinson Microwave Anisotropy Probe (WMAP) observations of nine years (Hinshaw et al., 2013), joint to the constraints from SNe U2.1 (Suzuki et al., 2012), the radiation of Cosmic Microwave Background (CMB) (Spergel et al., 2003; Hinshaw et al., 2013; Bennett et al., 2013) and Baryon Acoustic Oscillations (BAO) (Eisenstein et al., 2005) found the values $\Omega_\Lambda = 0.729 \pm 0.014$ and Hubble constant $H_0 = 69.33 \pm 0.88 \text{ km s}^{-1} \text{ Mpc}^{-1}$. For a flat Λ CDM universe, the HST survey project of SNe U2.1 alone constrains the dark-energy density, $\Omega_\Lambda = 0.705^{+0.040}_{-0.043}$ at 1σ confidence level, including systematic error (Suzuki et al., 2012). The left panel of Fig. 4.4 shows confidence intervals on Ω_m and Ω_Λ from the SNe, BAO and CMB data samples.

SNe U2.1 sample has 833 sources drawn from 19 data sets. Of these, a compilation of 580 data points passes strict selection cuts and is available for use in the supernova cosmology project link². Combining this sample with the GRB sample may constrain the cosmological parameters. The right panel of Fig. 4.4 shows the Hubble diagram of SNe U2.1 sample that covers the redshift from $z = 0.015$ to $z = 1.414$. This diagram has been used to demonstrate the expansion of the universe. The curved line indicates the best-fit using the Λ CDM model.

Supernovae Type Ia can be standardized to use as cosmological standard candles and provide constraints on the cosmological parameters at redshift $z < 2$ (Perlmutter et al., 1999; Riess et al., 1998; Perlmutter & Schmidt, 2003). In the meanwhile, SNe Type Ia at maximum brightness appears to be better standard candles in the near-infrared, requiring little or even without correction for the light-curve shape (Kosciunas et al., 2004; Wood-Vasey et al., 2008). However, it is necessary to use more distant objects to constrain these parameters. GRBs and SNe data together can potentially be used as a powerful tool for distance measurement and to probe the Hubble diagram at high redshifts.

²<http://supernova.lbl.gov/union/>

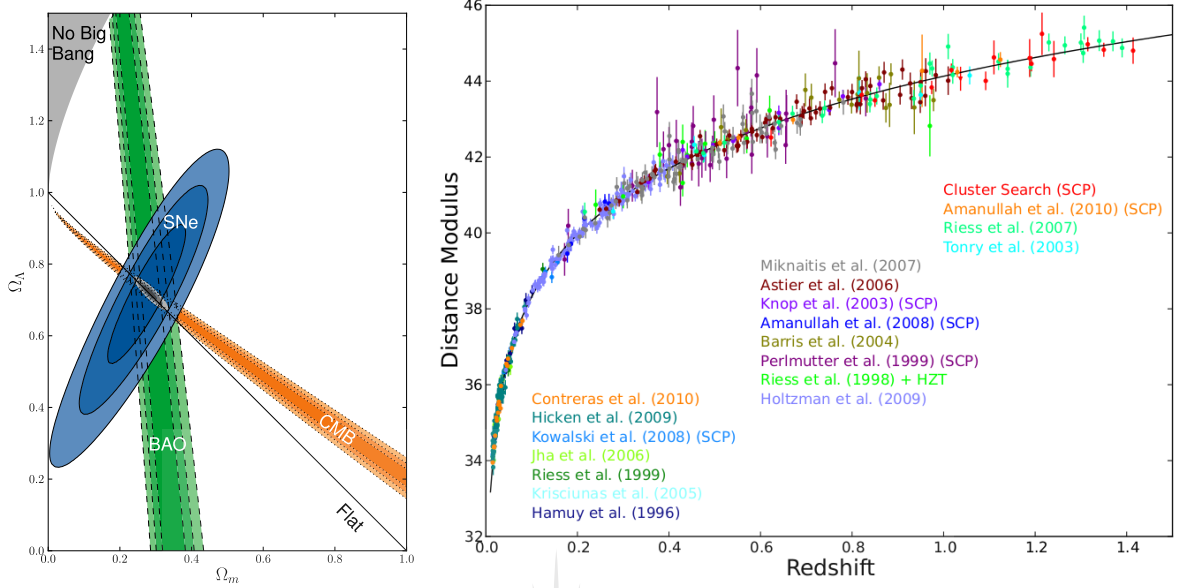


Figure 4.4 *Left panel:* the Λ CDM model: 1σ , 2σ and 3σ confidence levels in the $(\Omega_m, \Omega_\Lambda)$ plane from SNe U2.1 combined with the constraints from BAO and CMB. *Right panel:* Hubble diagram of the SNe U2.1 sample. The solid line represents the best-fit cosmology for a flat Λ CDM universe from the SNe U2.1 data (Suzuki et al., 2012).

4.4 Using GRBs as standard candles

GRBs are recognized as being powerful cosmological tools in the universe (Ghirlanda et al., 2004a) because they are detected at redshift up to $z \sim 9.4$ (Cucchiara et al., 2011). They are also very bright (i.e., with isotropic peak luminosities up to $\sim 10^{54}$ erg/s) and energetic (i.e., with an isotropic radiated energy up to $(5.35 \pm 0.17) \times 10^{54}$ erg (Dirirsa et al., 2017a)). Thus, these sources may be interesting for cosmological studies, to provide measurements of the dark-energy and the Hubble constant. In order to probe the characteristics of these parameters, the relation between distance and redshift is very important. Over the past decades, SNe Type Ia have emerged as one of the most reliable ways for making distance measurements under the standard candle assumption, but they can only probe the universe at low redshifts, $z < 2$. In order to study the evolution of dark-energy and Hubble constant at higher redshift range, high-redshift standard candles are required. GRBs could be complementary probes of dark-energy and the Hubble constant at these high redshifts.

The detection of GRB afterglow emission and the redshift measurements after the *BeppoSAX* spacecraft (Boella et al., 1997) introduced an interesting property of GRBs in cosmological aspect. Long-duration GRBs may serve as standard candles to constrain cosmological parameters by probing the Hubble diagram well beyond the range of redshift currently accessible using SNe Type Ia. The standardization of GRBs is based on phenomenological relations between two or

more parameters found from spectral modeling (see §2.6.2), of which one is strongly dependent on the cosmological model. In this section, we will describe some empirical relations of the intrinsic properties of GRB prompt emission and its implication to cosmology.

4.4.1 Amati relation

The investigation of a correlation between the cosmological source-frame energy $E_{i,p}$ at which the prompt gamma-ray spectral energy distribution νF_ν peaks, and the isotropic-equivalent bolometric energy E_{iso} emitted during the prompt phase in the Amati work (Amati et al., 2002) has been characterized by LGRBs. After this finding, many researchers have widely discussed the results on reliability of the so-called Amati relation (i.e., $E_{\text{iso}} - E_{i,p}$). A strong correlation between $E_{\text{iso}} - E_{i,p}$ based on a sample of *BeppoSAX* (Boella et al., 1997) LGRBs with known redshift was confirmed with the only exception of the peculiar sub-energetic GRB 980425. Then, the relation was quickly proposed as a tool to estimate GRB redshifts and constrain the cosmological parameters.

For GRBs having the redshift and measured spectrum, the isotropic radiated energy released in the cosmological source frame is defined as

$$E_{\text{iso}} = \frac{4\pi d_L^2}{1+z} S_{\text{bolo}}(E_1, E_2, z), \quad (4.25)$$

where $S_{\text{bolo}}(E_1, E_2, z)$ is the bolometric fluence in units of [erg cm⁻²] integrated over the energy range from $E_1 = 1$ keV to $E_2 = 10^4$ keV, assuming an ideal detectors that can detect radiation at all wavelength range,

$$S_{\text{bolo}}(E_1, E_2, z) = T_{90} \int_{E_1/(1+z)}^{E_2/(1+z)} EN(E)dE, \quad (4.26)$$

with $N(E)$ describe the spectral model (see Sec. §2.6.2) and d_L is the d_L ³ obtained from Eq. (4.17) and we have

$$d_L = (1+z) \frac{c}{H_0} \int_0^z \frac{dz'}{\sqrt{(1-\Omega_\Lambda)(1+z')^3 + \Omega_\Lambda}}, \quad (4.27)$$

assuming a flat universe and $\Omega_\Lambda = 1 - \Omega_m$. Fig. 4.5 shows the first Amati relation plot for 12 LGRBs fitted by a PL: $E_p \propto E_{\text{iso}}^{0.52 \pm 0.06}$, where E_p is the spectral peak energy in keV. Amati (2006a) updated 12 LGRBs data with sub-energetic bursts (GRB 980425 and GRB 031203) and for the two short GRB 050709 and GRB 051221 (see the right panel of Fig. 4.5). The short and sub-energetic GRBs are clearly seen as outliers, which do not meet the Amati relation. Hence, for short GRBs the E_{iso} values are very low with respect to their intrinsic peak energy $E_{i,p}$. Amati (2006a) also extended data to 41 GRBs and X-ray flashes (XRFs, i.e., particularly soft bursts GRB 020903 and GRB 050416) with known redshift collected from different detectors including BATSE (Fishman et al., 1985), *BeppoSAX* (Boella et al., 1997), HETE-2 (Ricker et al., 2003), Konus-Wind (Terekhov

³Hereafter throughout the thesis, I assume widely accepted Λ CDM cosmological model: the dark-energy density $\Omega_\Lambda = 0.714$, the total density of baryonic and dark matter $\Omega_m = 0.286$ and the Hubble parameter $H_0 = 69.6$ km s⁻¹ Mpc⁻¹ (Planck Collaboration et al., 2018; Riess et al., 2018), unless otherwise specified.

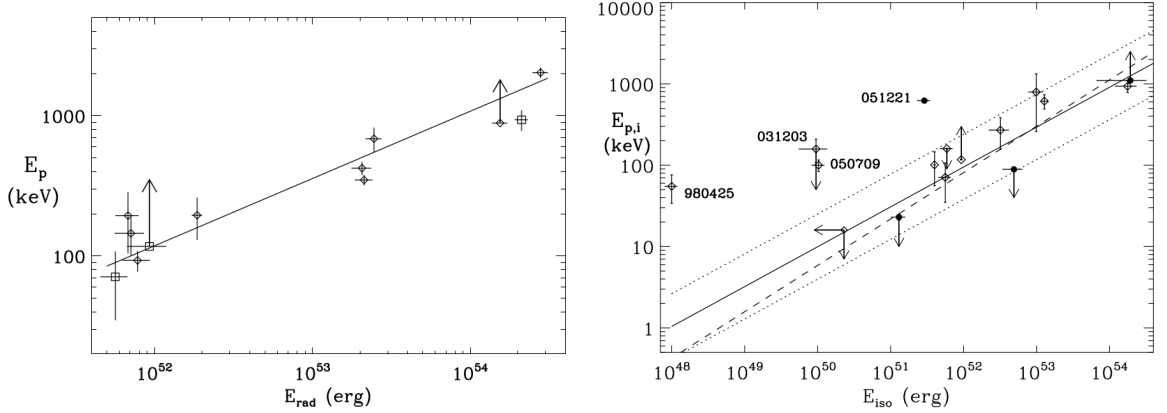


Figure 4.5 *Left panel:* the Amati relation for 12 LGRBs (Amati et al., 2002). *Right panel:* 12 LGRB data updated with sub-energetic bursts (GRB 980425 and GRB 031203) and the two short GRB 050709 and GRB 051221 (Amati, 2006a).

et al., 1998) and *Swift* (Gehrels, 2004) (see Chapter §2 for more details about the detectors). The relation was updated to $E_{i,p} \propto E_{\text{iso}}^{0.57 \pm 0.02}$ with Spearman’s rank correlation coefficient ρ_{sp} (Spearman, 1904) about 0.89 which is highly correlated (Amati, 2006a). Later, Amati et al. (2008) (hereafter, A2008) extended data to 70 GRBs including XRFs with known redshift.

In general, the phenomenological Amati relation (Amati et al., 2002) between the E_{iso} and $E_{i,p}$ is of the form

$$E_{\text{iso}} \propto \left(\frac{E_{i,p}}{E_0} \right)^m E_{0,\text{iso}}, \quad (4.28)$$

where $E_{0,\text{iso}} = 10^{52}$ erg, E_0 is reference energy and m is PL fitting index. Following Wang et al. (2016) and Demianski et al. (2017) we can define a linearized Amati relation with amplitude k as

$$y = mx + k, \quad (4.29)$$

where $y \equiv \log(E_{\text{iso}}/E_{0,\text{iso}})$ and $x \equiv \log(E_{i,p}/E_0)$. The reference energy E_0 allows us to calculate the so-called “decorrelation” value of x as $x_{\text{dec}} = -C_{km}/\sigma_m^2$ (see Eq. 4.40). Here, C_{km} is the covariance of the parameters k and m , and σ_m is the error on m . The error on the distance dependent quantity y in Eq. (4.29) is estimated as (Wang et al., 2016; Demianski et al., 2017)

$$\sigma_y = \sqrt{\sigma_k^2 + m^2 \sigma_x^2 + \sigma_m^2 x^2 + \sigma_{\text{ext}}^2}, \quad (4.30)$$

where σ_{ext} is the scatter due to the presence of unknown variables that influence the correlation to be tested. The systematic uncertainty σ_{x_i} and σ_{y_i} are errors on the x and y data, respectively. In order to characterize the dependence of $E_{i,p}$ - E_{iso} extrinsic scatter on cosmology, we can also use the maximum likelihood statistical method as discussed by D’Agostini (2005). We apply the log likelihood function $-\ln \mathcal{L}(m, k, \sigma_{\text{ext}}) \equiv L(m, k, \sigma_{\text{ext}})$ to fit the $x = \log(E_{i,p}/E_{0,\text{dec}})$ and

$y = \log(E_{\text{iso}}/E_{0,\text{iso}})$ data with Eq. (4.29). The functional form is given by

$$L(m, k, \sigma_{\text{ext}}) = \frac{1}{2} \sum_i^N \ln(\sigma_{\text{ext}}^2 + \sigma_{y_i}^2 + m^2 \sigma_{x_i}^2) + \frac{1}{2} \sum_i^N \frac{(y_i - mx_i - k)^2}{(\sigma_{\text{ext}}^2 + \sigma_{y_i}^2 + m^2 \sigma_{x_i}^2)}. \quad (4.31)$$

To determine uncertainties of a fit parameter q_i , as in Demianski & Piedipalumbo (2011), we evaluate a marginalized likelihood function $\mathcal{L}_i(q_i)$ by integrating over the other parameters. Then, the median value for the parameter $q_{i,\text{med}}$ is found from the integral

$$\int_{q_{i,\text{min}}}^{q_{i,\text{med}}} \mathcal{L}_i(q_i) dq_i = \frac{1}{2} \int_{q_{i,\text{min}}}^{q_{i,\text{max}}} \mathcal{L}_i(q_i) dq_i, \quad (4.32)$$

where $q_{i,\text{min}}$ and $q_{i,\text{max}}$ are the minimum and maximum values of the parameter, respectively. The 1σ or 68.27% confidence interval $(q_{i,l}, q_{i,h})$ of the parameters are then found by solving the integral (D'Agostini, 2005)

$$\begin{aligned} \int_{q_{i,l}}^{q_{i,\text{med}}} \mathcal{L}_i(q_i) dq_i &= \frac{1}{2}(1-\eta) \int_{q_{i,\text{min}}}^{q_{i,\text{max}}} \mathcal{L}_i(q_i) dq_i, \\ \int_{q_{i,\text{med}}}^{q_{i,h}} \mathcal{L}_i(q_i) dq_i &= \frac{1}{2}(1-\eta) \int_{q_{i,\text{min}}}^{q_{i,\text{max}}} \mathcal{L}_i(q_i) dq_i \end{aligned} \quad (4.33)$$

where $\eta = 0.6827$. Hence, we can calculate the mean of the upper and lower uncertainties for each parameter.

4.4.2 Yonetoku relation

Yonetoku et al. (2004) discovered a positive correlation between the energy at which the vF_v spectrum peaks in the cosmological rest frame and the isotropic peak luminosity (L_{iso}) of GRBs prompts emission observed by BATSE (Fishman et al., 1985) and BeppoSAX (Boella et al., 1997). The peak L_{iso} is defined with 1-s time window during which the flux is maximum as,

$$L_{\text{iso}} = 4\pi d_L^2 P_{\text{bolo}}(E_1, E_2, z), \quad (4.34)$$

where $P_{\text{bolo}}(E_1, E_2, z)$ is the bolometric peak flux P_{bolo} in units of [$\text{erg cm}^{-2} \text{s}^{-1}$] over an energy range $E_1 = 1 \text{ keV}$ and $E_2 = 10^4 \text{ keV}$ is defined as

$$P_{\text{bolo}}(E_1, E_2, z) = \int_{E_1/1+z}^{E_2/1+z} EN(E) dE. \quad (4.35)$$

The phenomenological correlation $L_{\text{iso}} - E_{i,p}$, the so called Yonetoku relation (Yonetoku et al., 2004) can be defined by using a PL model as

$$L_{\text{iso}} \propto \left(\frac{E_{i,p}}{E_0} \right)^m L_{0,\text{iso}}, \quad (4.36)$$

where E_0 is a reference energy and $L_{0,\text{iso}} = 10^{52} \text{ erg s}^{-1}$. The Yonetoku relation of Eq. (4.36) could be linearized in the form

$$y = mx + k ; y \equiv \log \frac{L_{\text{iso}}}{L_{0,\text{iso}}}, x \equiv \log \frac{E_{i,p}}{E_0}. \quad (4.37)$$

To estimate the fitting parameters and its error, we use a likelihood method similar to Eqs. (4.31) and (4.33), respectively.

In this analysis, I have only considered the Amati and the Yonetoku relations which show high degrees of correlation. Besides these correlations, many empirical GRB luminosity relations have been suggested as distance indicators and possible cosmological implications such as

- $E_\gamma - E_{i,p}$: A tight correlation between the source frame ($E_{i,p}$) and the collimation corrected emitted energy (E_γ) as explored by [Ghirlanda et al. \(2004b\)](#), and is so-called the Ghirlanda relation. Through geometric corrections, the emitted energy of the jet $E_\gamma = (1 - \cos\theta)E_{\text{iso}}$ where θ is the half angle of the GRB jet. They found that $E_{i,p} \propto (E_\gamma)^{0.7}$ keV.
- $L_{\text{iso}} - \tau_{\text{lag}}$: [Norris et al. \(2000\)](#) analyzed correlation between isotropic luminosity (L_{iso}) and spectral lag (τ_{lag})⁴ for six GRBs with known redshift and found that $L_{\text{iso}}/10^{53} \text{ erg s}^{-1} \propto (\tau_{\text{lag}}/0.01 \text{ s})^{-1.14}$. The existence of this correlation has been studied by various authors using arbitrary observer-frame energy ranges of various instruments ([Norris, 2002](#); [Hakkila et al., 2008](#); [Ukwatta et al., 2012](#)). Based on a sample of 43 *Swift*-BAT long GRBs with known redshift, [Ukwatta et al. \(2012\)](#) found a higher degree of correlation. Most GRB pulses have correlated properties, i.e., short-lag pulses have shorter durations and more luminous than long-lag pulses ([Ukwatta et al., 2012](#)).
- $L_{\text{iso}} - V$: A correlation between the isotropic luminosity (L_{iso}) and variability (V) has been described by [Fenimore & Ramirez-Ruiz \(2000\)](#) and found $L_{\text{iso}} \propto V^{3.3}$. Here, V is the variability light curve of the GRBs. It is calculated by taking the difference between the observed light curve and its smoothed version ([Reichart et al., 2001](#)).
- $E_p - E_{\text{iso}} - t_b$: A close correlations of isotropic energy (E_{iso}), peak energy (E_p) and the break time of optical afterglow light curves t_b was derived by [Liang & Zhang \(2005\)](#), the so-called Liang-Zhang relation. $E_{\text{iso}}/10^{52} \text{ erg} \propto (E_p/100 \text{ keV})^{1.94 \pm 0.17} (t_b/1 \text{ day})^{-1.24 \pm 0.23}$. These three parameters are directly obtained from the observed statistics of GRB prompt emission and afterglow.
- $L \propto E_{i,p}^\rho$: The correlation between the instantaneous luminosity and the spectral peak energy to some power ρ within a burst. The relation is referred to as the Golenetskii correlation (GC, [Golenetskii et al., 1983](#)). This correlation holds important clues to the physics of GRBs and is thought to have the potential to determine redshifts of bursts.

4.4.3 Decorrelation energy

The decorrelation parameter is defined as the narrowest point at which the error of x become small (i.e., x_{dec}). The reference energy E_0 allows us to calculate the value of this decorrelation

⁴Spectral lag is the difference in time of arrival of low- and high-energy photons.

energy. In order to get the uncertainty of y , we can use the error propagation method

$$\begin{aligned}\sigma_y &= \left(\left(\frac{\partial y}{\partial k} \right)^2 \sigma_k^2 + \left(\frac{\partial y}{\partial m} \right)^2 \sigma_m^2 + 2 \left(\frac{\partial y}{\partial k} \right) \left(\frac{\partial y}{\partial m} \right) C_{km} \right)^{1/2}, \\ &= (\sigma_k^2 + x^2 \sigma_m^2 + 2x C_{km})^{1/2},\end{aligned}\quad (4.38)$$

where $C_{km} = \text{cov}[k, m]$ is the covariance of the parameters k and m , and σ_m is the error on m . The values of these parameters can be obtained after data is analyzed by using the optimization of curve fitting. For computation of the decorrelation parameter (x_{dec}), the following result immediately follows by differentiating Eq. (4.38) with respect to x (i.e., $\partial\sigma_y/\partial x = 0$),

$$2x\sigma_m^2 + 2C_{km} = 0. \quad (4.39)$$

This is true if :

$$x \equiv x_{\text{dec}} = -\frac{C_{km}}{\sigma_m^2}. \quad (4.40)$$

The error on y is the smallest at $x = x_{\text{dec}}$. By using the reference energy $E_0 = 100$ keV, Eqs. (4.29) or (4.37) and (4.40), yields

$$\log \frac{E_{i,p}}{100 \text{ keV}} = -\frac{C_{km}}{\sigma_m^2}. \quad (4.41)$$

At $E_{i,p} \equiv E_{0,\text{dec}}$, one can obtain the following decorrelation energy

$$\begin{aligned}E_{0,\text{dec}} &= 10^{\left(2 - \frac{C_{km}}{\sigma_m^2}\right)} \text{ keV}, \\ &= 10^{x_{\text{dec}}} 100 \text{ keV}.\end{aligned}\quad (4.42)$$

The butterfly band can be sketched from the lower and upper boundaries obtained from σ_y , then, we have

$$y = k + mx \pm \sigma_y. \quad (4.43)$$

For example, the *Fermi*-GBM sample obtained from the Comp spectral model, which was used in the analysis of the Yonetoku relation (see App. C.1), we can compute C_{km} , σ_m , x_{dec} and $E_{0,\text{dec}}$ reported in App. Tab. C.1.1. It is obvious that the decorrelation peak energy is much higher than $E_0 = 100$ keV, i.e., see Fig. 4.6 (blue line). When we use $E_{0,\text{dec}}$ in the fit of the Yonetoku relation as shown in Fig. 4.6 (green line), the parameters correlation between m and k decrease.

4.5 Extended Hubble diagram

4.5.1 Construction of the Hubble diagram from the Amati relation

To construct the Hubble diagram, we use parameters obtained from fitting the linearized Amati relation (Eq. 4.29). In particular, we can invert the relation in Eq. (4.25) to obtain the d_L as

$$d_L = \left[\frac{1+z}{4\pi} \frac{E_{0,\text{iso}}}{S_{\text{bolo}}} 10^k \left(\frac{E_{i,p}}{E_{0,\text{dec}}} \right)^m \right]^{1/2}. \quad (4.44)$$

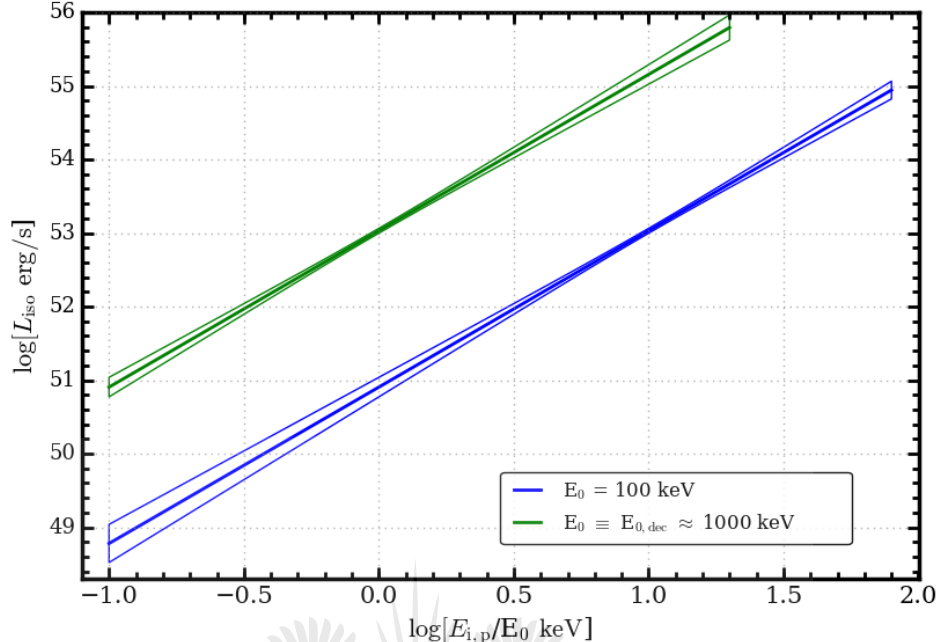


Figure 4.6 The Yonetoku relation using the reference energy of $E_0 = 100$ keV (blue line) and the decorrelation energy of $E_{0,\text{dec}} = 1000$ keV (green line). The butterfly is the $\sigma_{L_{\text{iso}}}$ contour of the L_{iso} analysis.

We then use this d_L for each GRB to construct the GRB Hubble diagram. Using Eqs. (4.23) and (4.44), the distance modulus can be written as

$$\mu = \frac{5}{2} \log \left[\frac{1+z}{4\pi} \frac{E_{0,\text{iso}}}{S_{\text{bolo}}} \left(\frac{E_{i,p}}{E_{0,\text{dec}}} \right)^m \right] + \frac{5}{2} k - 5 \log(\text{Mpc}) + 25. \quad (4.45)$$

Here, the distance modulus uses all the fitting parameters obtained from the Amati relation. The variance of the distance modulus μ (Eq. 4.45) could be obtained by using the error propagation method as

$$\begin{aligned} \sigma_\mu^2 &= \left(\frac{\partial \mu}{\partial \log E_{\text{iso}}} \right)^2 \sigma_{\log E_{\text{iso}}}^2 + \left(\frac{\partial \mu}{\partial S_{\text{bolo}}} \right)^2 \sigma_{S_{\text{bolo}}}^2, \\ &= \left(\frac{5}{2} \sigma_{\log E_{\text{iso}}} \right)^2 + \left(\frac{5}{2} \frac{\sigma_{S_{\text{bolo}}}}{\ln 10 S_{\text{bolo}}} \right)^2, \end{aligned} \quad (4.46)$$

where $\sigma_{\log E_{\text{iso}}}$ is the propagated uncertainties on E_{iso} computed from Eq. (4.30) and yields

$$\sigma_{\log E_{\text{iso}}}^2 = \left(\sigma_m \log \frac{E_{i,p}}{E_{0,\text{dec}}} \right)^2 + \left(\frac{m}{\ln 10} \frac{\sigma_{E_{i,p}}}{E_{i,p}} \right)^2 + \sigma_k^2 + \sigma_{\text{ext}}^2. \quad (4.47)$$

Following the values of the distance modulus obtained from Eq. (4.45) and its uncertainties in Eq. (4.46), one can plot the Hubble diagram of the calibration obtained from the Amati relation.

4.5.2 Construction of the Hubble diagram from the Yonetoku relation

The d_L in Eq. (4.17) can be expressed in terms of the L_{iso} (Eq. 4.34) and P_{bolo} (Eq. 4.35) as

$$d_L^2 = \frac{L_{0,\text{iso}} 10^k}{4\pi P_{\text{bolo}}} \left(\frac{E_{i,p}}{E_{0,\text{dec}}} \right)^m. \quad (4.48)$$

Replacing these terms in Eq. (4.23), we get distance modulus related to the Yonetoku relation as

$$\mu = \frac{5}{2} \log \left[\frac{L_{0,\text{iso}}}{4\pi P_{\text{bolo}}} \left(\frac{E_{i,p}}{E_{0,\text{dec}}} \right)^m \right] + \frac{5}{2} k - 5 \log(\text{Mpc}) + 25. \quad (4.49)$$

The variance σ_μ^2 of the distance modulus μ is computed by using error propagation technique as

$$\begin{aligned} \sigma_\mu^2 &= \left(\frac{\partial \mu}{\partial \log L_{\text{iso}}} \right)^2 \sigma_{\log L_{\text{iso}}}^2 + \left(\frac{\partial \mu}{\partial P_{\text{bolo}}} \right)^2 \sigma_{P_{\text{bolo}}}^2, \\ &= \left(\frac{5}{2} \sigma_{\log L_{\text{iso}}} \right)^2 + \left(\frac{5}{2} \frac{\sigma_{P_{\text{bolo}}}}{\ln 10 P_{\text{bolo}}} \right)^2, \end{aligned} \quad (4.50)$$

where

$$\sigma_{\log L_{\text{iso}}}^2 \equiv \sigma_y^2 = \left(\sigma_m \log \frac{E_{i,p}}{E_{0,\text{dec}}} \right)^2 + \left(\frac{m}{\ln 10} \frac{\sigma_{E_{i,p}}}{E_{i,p}} \right)^2 + \sigma_k^2 + \sigma_{\text{ext}}^2. \quad (4.51)$$

This is obtained by considering the extrinsic parameter that corresponding standard deviation of Eq. (4.30). One can plot the Hubble diagram (Eq. 4.49) with its uncertainty (Eq. 4.50) for GRB prompt emission by using the coefficients obtained from the Yonetoku relation.

4.6 Constraints on the dark-energy and the Hubble constant

We can constrain the parameters of a flat Λ CDM cosmological model using GRB data or GRB data with SNe U2.1 sample. The distance modulus of the GRBs depends on the distance (i.e., the larger distance will have a greater μ) and the coefficients of Amati et al. (2002) and Yonetoku et al. (2004) relations found from data fitting. Dai et al. (2004) proposed a method to constrain cosmological parameters using GRBs and applied it to a sample containing 12 GRBs relying on the correlation between E_p in the local observer frame and the beaming-corrected gamma-ray energy, E_γ . The cosmological parameters can be determined by minimization of the χ^2 expression given by

$$\chi^2(H_0, \Omega_\Lambda) = \sum_{i=0}^N \frac{(\mu(z) - \mu^{\text{th}}(z; H_0, \Omega_\Lambda))^2}{\sigma_{\mu(z)}^2}, \quad (4.52)$$

where $\Omega_\Lambda = 1 - \Omega_m$, z is the measured redshift for GRB, $\mu(z)$ is the observed modulus distance obtained from Eqs. (4.45) and (4.49) for the Amati and the Yonetoku relations, respectively. The $\sigma_{\mu(z)}$ is the uncertainty of the observed distance modulus obtained from equation Eqs. (4.46) and (4.50) for the Amati and the Yonetoku relations, respectively. In Eq. (4.52), $\mu^{\text{th}}(z, H_0, \Omega_\Lambda)$ is defined as the theoretical value of the distance modulus that could be determined for the FLRW cosmology (Friedmann, 1922; Carroll, 2001) with Ω_Λ and H_0 . Hence, it follows from the expression in Eq. (4.17), we obtain $\mu^{\text{th}}(z, H_0, \Omega_\Lambda) = 5 \log(d_L(H_0, \Omega_\Lambda)/\text{Mpc}) + 25$.

4.7 Evolution of the Amati relation with redshift

In this section we present possible redshift evolution of the $E_{\text{iso}} - E_{\text{i,p}}$ correlation. Most of the results obtained in this section have been published in [Dirirsa & Razzaque \(2015\)](#).

The data samples are taken from [Amati et al. \(2008\)](#), hereafter A2008 and [Ghirlanda et al. \(2008\)](#), hereafter G2008 which consists of 68 and 74 long GRBs, respectively. Among these, X-Ray Flash (XRF), GRB 050416A and GRB 020903 are not considered because their rest-frame T_{90} duration is smaller than 2 s. All of the bursts used in this study were triggered by the BATSE ([Fishman et al., 1985](#)), BeppoSAX ([Boella et al., 1997](#)), HETE-2 ([Ricker et al., 2003](#)), Konus-Wind ([Terekhov et al., 1998](#)) and *Swift* ([Gehrels, 2004](#)) satellites which provide the estimates of spectral parameters. The redshift samples span from redshift $z = 0.0331$ up to $z = 6.29$. In order to find the

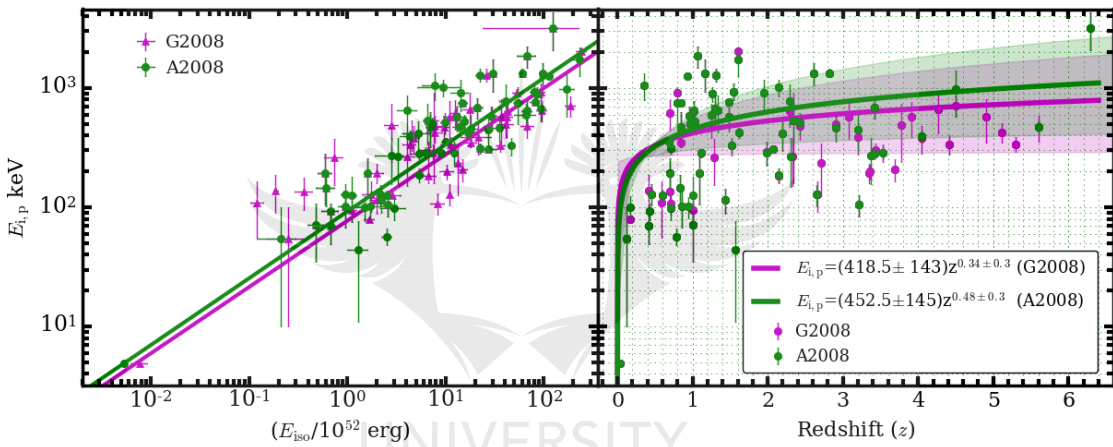


Figure 4.7 *Left panel:* the Amati relation for 68 GRBs. Data taken from [Amati et al. \(2008\)](#) and 74 GRBs from [Ghirlanda et al. \(2008\)](#) fitted by a power-law. *Right panel:* the distribution of the $E_{\text{i,p}}$ with respect to the redshift.

evolution of the Amati relation parameters with redshift, we divide both the A2008 and G2008 samples into four bins of redshift from low values to high values (see Tab. 4.1). Then, the analysis of $E_{\text{i,p}} - E_{\text{iso}}$ correlation has been done for each binned data and fitted with the Amati relation in the form $k(E_{\text{iso}}/10^{52} \text{ erg})^m$, where k and m are the amplitude and index of the fitting model, respectively.

In the left panel of Fig. 4.7 we have shown the Amati relation for the full samples of A2008 and G2008 fitted by power-laws. With a sample of A2008, we obtained the power-law best-fit (green line) parameters $k = 92.16 \pm 6.2$ and $m = 0.56 \pm 0.02$ with Spearman's rank correlation coefficient $\rho_{\text{sp}} = 0.859$ (see Fig. 4.7). The dispersion of data around the power-law fit is very large with a reduced $\chi^2_{\text{red}} = 6.4$. This large dispersion may be caused by unknown systematic uncertainty related to the physical origin of the Amati relation. The magenta line shows the best-fit power-law to the G2008 sample. We obtain a correlation coefficient $\rho_{\text{sp}} = 0.842$ with the

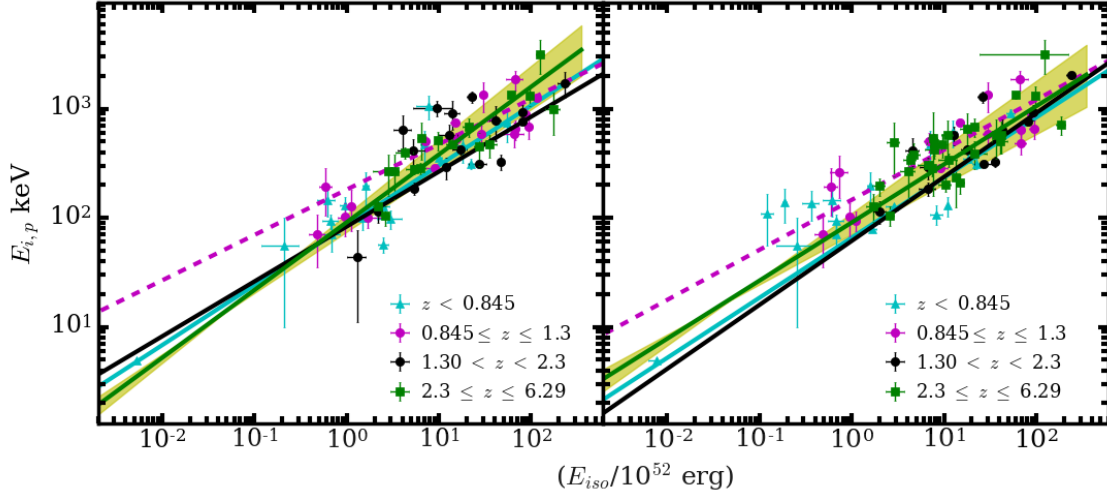


Figure 4.8 *Left panel:* the correlation of $E_{i,p}$ and E_{iso} for different redshift bins for the A2008 sample which consists of 68 LGRBs. *Right panel:* the correlation of $E_{i,p}$ and E_{iso} for the redshift binned into four groups for the G2008 sample containing 74 GRBs. For both samples, the results of the best-fit parameters are reported in Tab. 4.1.

best-fit parameters $k = 77.06 \pm 7.80$ and $m = 0.56 \pm 0.03$. This relation shows a discrepancy of index about 0.07 to the one found by Heussaff et al. (2013) from a sample of *Fermi* and *Swift* with 43 GRBs fitted by $E_{i,p} = 118 \times (E_{iso}/10^{52} \text{ erg})^{0.486}$. The right panel of Fig. 4.7, depicts the distribution of $E_{i,p}$ with respect to the redshift of the bursts, which are modeled by a least-square curve fit. Those GRBs with low redshift are more populated around the low value of intrinsic peak energy.

The fitting indices of A2008 (0.56 ± 0.02) and G2008 (0.556 ± 0.028) are compatible except the normalization parameter. To investigate any variation of the Amati relation with redshift, we arranged the GRBs based on their redshift distribution and binned them into four redshift bins. Each bin of the A2008 sample contains 17 GRBs, but the number of GRBs in the G2008 sample is not equally divided hence the binning is done by fixing the intervals of the GRB redshift. Then, each of the binned data is fitted with the simple power-law used for the Amati relation (see Fig. 4.8). A power-law fit to the binned A2008 sample provided different values of indices from $m \sim 0.42$ to ~ 0.62 . Each of the bins of the G2008 sample also shows very large variations in indices from $m \sim 0.46$ to $m \sim 0.59$ but no evolution with redshift as shown in the second panel of Fig. 4.9. The correlation in the data varies from bin to bin, with some bins having a very strong correlation (i.e., ρ_{sp}).

We identify that there is no systematic trend of redshift dependence on the fitting parameters k and m in the correlation analysis tested for different redshift intervals (see Fig. 4.9). It is also worth investigating if any evolution with redshift can affect the $E_{i,p}$ - E_{iso} correlation defined by this sample. For the high redshift span of $2.3 \leq z \leq 6.29$ and $2.3 \leq z \leq 6.29$, A2008 and G2008

Table 4.1 The best-fit parameters of the $E_{\text{iso}} - E_{i,p}$ correlation fits to the samples of A2008 and G2008 for different redshift bins. The Spearman rank correlation coefficient ([Spearman, 1904](#)) is done with ρ_{sp} and χ^2_{red} , which is the reduced χ^2 .

Sample	k	m	χ^2_{red}	ρ_{sp}	Redshift Interval	Number of GRBs
A2008	85.3 ± 6.9	0.55 ± 0.02	5.7	0.776	$z < 0.845$	17
	181.4 ± 41.8	0.42 ± 0.06	6.2	0.858	$0.845 \leq z \leq 1.3$	17
	83.2 ± 29.3	0.50 ± 0.10	6.7	0.776	$1.30 < z < 2.3$	17
	91.1 ± 16.5	0.62 ± 0.06	2.7	0.901	$2.3 \leq z \leq 6.29$	17
	92.16 ± 6.2	0.56 ± 0.02	6.44	0.859	$0.0331 \leq z \leq 6.29$	68
G2008	65.8 ± 6.8	0.55 ± 0.04	6.0	0.641	$z < 0.845$	18
	146.1 ± 45.2	0.46 ± 0.09	10.0	0.771	$0.845 \leq z \leq 1.3$	15
	61.4 ± 24.96	0.59 ± 0.10	6.8	0.758	$1.30 < z < 2.3$	13
	90.6 ± 19.96	0.53 ± 0.07	3.9	0.743	$2.3 \leq z \leq 6.29$	28
	77.06 ± 7.80	0.56 ± 0.03	7.14	0.842	$0.0331 \leq z \leq 6.29$	74

samples of GRBs are well fitted by a power-law.

4.8 Summary

From the current evidence of cosmological observations of SNe Type Ia and the cosmic microwave background radiation measured in the large-scale structure, we know that the expansion of the universe is accelerating. Hence, the energy density is dominated by a mysterious component referred to as dark-energy, which makes up $\sim 70\%$ of our universe. The matter density is about 23% of the constituent of the universe's energy budget. These energy components drive the expansion of our current universe. The equations of the cosmological densities constituent of the universe (Eq. 4.7) and the FLRW equation (4.1) that defines how the energy in the universe drives its expansion are presented. We have also discussed theoretical and analytical methods to use GRBs as a promising tool to explore the cosmic expansion at higher redshift by filling the gap between SNe Ia and CMB. Using GRBs as cosmological probes to measure distances in the early universe will enable us to understand the universe's mysterious expansion over time. We have recognized that long-duration GRBs hold considerable promise in the analysis of the Amati relation as probes of the high-redshift universe.

We have also explored the evolution of redshift with the Amati relation by using the samples of GRBs that were collected from the previous work presented by A2008 and G2008. The correlation between E_{iso} and $E_{i,p}$ for both samples with the best-fit power-law index 0.56 ± 0.02 (68 GRBs data) and 0.556 ± 0.028 (74 GRBs data) are scrutinized. We have also divided the GRB samples into redshift bins and have compared the slope of the $E_{i,p}$ correlation for each redshift bin. No evolution of the Amati relation parameters (i.e., m and k) with redshift has been investigated.

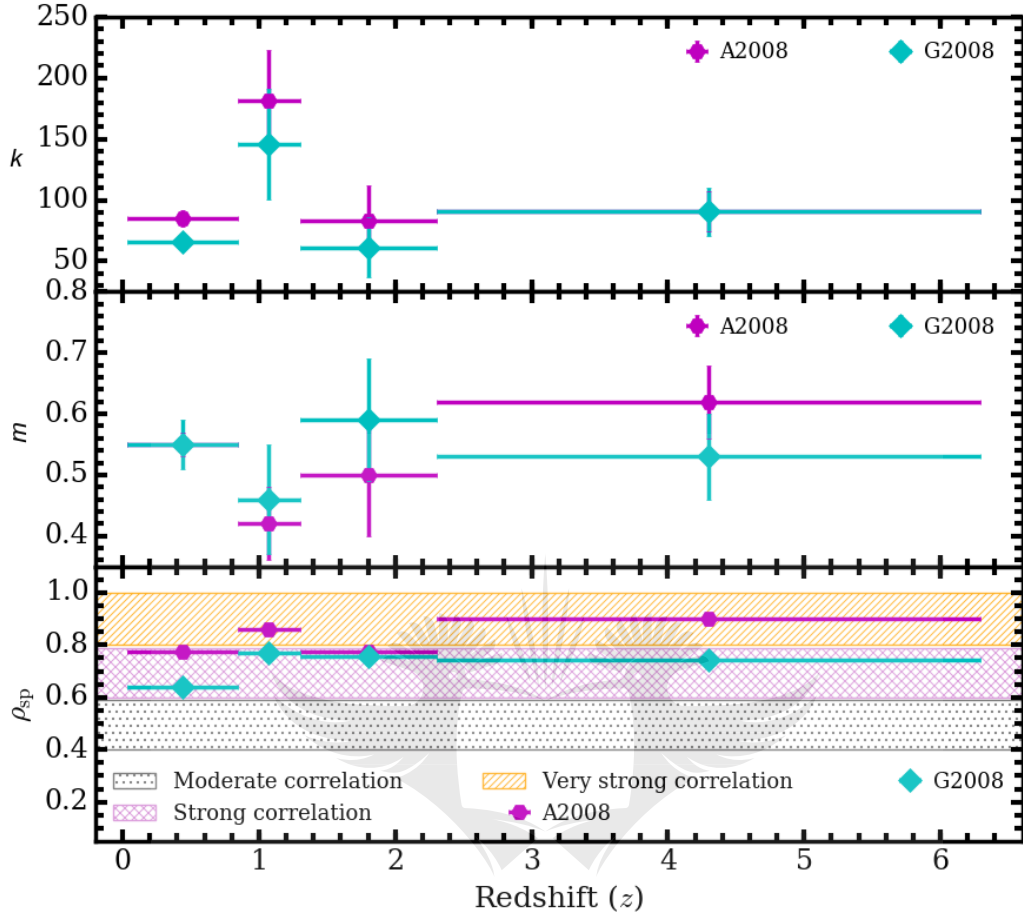


Figure 4.9 The best-fit parameters for each of the binning for the A2008 and G2008 samples with their Spearman's rank correlation coefficient ρ_{sp} (first panel). The result of parameters for each bin of the A2008 sample obtained from the PL fit (magenta hexagon symbols) and G2008 sample (cyan diamond symbols).

The results in this chapter, together with those derived in Eqs. (4.45), (4.49) and (4.52), provide a framework for possible future estimation of the cosmological parameters and construct the extended Hubble diagram of the GRBs up to high redshift in the analysis of the Amati and the Yonetoku relations, as will be presented in Chapters §5 and §6.

YONETOKU RELATION FOR *Fermi*-GBM AND *Swift*-BAT GRBS

Contents

5.1	Introduction	82
5.2	Observational data from <i>Fermi</i> -GBM and <i>Swift</i> -BAT	83
5.3	Intrinsic peak energy and isotropic luminosity calculations	85
5.4	Samples of GRBs	86
5.4.1	Common GRBs (GBM and BAT)	86
5.4.2	GBM GRBs fitted with Comp and Band models	87
5.4.3	The combined sample of GBM and BAT GRBs of the best-fit model	89
5.5	The Yonetoku relation between $E_{i,p}$ and L_{iso}	92
5.5.1	Fitted model	92
5.5.2	Partial correlation analysis	93
5.5.3	Likelihood analysis of $E_{i,p}$ and L_{iso}	93
5.6	Constraints on cosmological parameters and the extended Hubble diagram	96
5.6.1	Constraints on dark-energy and Hubble parameters	96
5.6.2	The extended Hubble diagram	98
5.7	Summary	99

The plan of this chapter is the following: in the next Sec. §5.1 we briefly review the Yonetoku relation (Yonetoku et al., 2004). In Sec. §5.2 we present the observational spectral energy coverage of the *Fermi*-GBM and the *Swift*-BAT instruments and the distribution of GRBs in the sky. We also discuss the sample selection methods. In Sec. §5.3 we describe the fitting model of the Yonetoku relation. In Sec. §5.4 we discuss different samples of GRBs for the analysis of correlation and present a comparison of the samples of GBM and BAT GRBs. In Sec. §5.5 we describe numerical fitting methods, present results of the calibration parameters and determine the partial correlation coefficients. In Sec. §5.6 we performed the Yonetoku relation fits different

samples and we determine the cosmological model parameters using the parametrized Yonetoku relation. Finally, results are summarized and discussed in Sec. §5.7.

5.1 Introduction

In this chapter, we study a GRB empirical relation between the intrinsic peak energy $E_{\text{i,p}}$ in the νF_ν spectrum and the isotropic peak luminosity L_{iso} in the cosmological source frame using the [Yonetoku et al. \(2004\)](#) relation [see Sec. §4.4.2 for a description of this relation]. Our sample comprises all long GRBs with measured redshift from observations of *Fermi*-GBM ([Gruber et al., 2014](#); [von Kienlin et al., 2014](#); [Narayana Bhat et al., 2016a](#)) and *Swift*-BAT ([Lien et al., 2016](#)), until December 2017. For all of the selected events, we derive, where possible, the $E_{\text{i,p}}$ and the L_{iso} . In order to compute these observables, we consider a one-second (T_{peak}) time-integrated spectral analysis, that is a time when the light curve of a GRB prompt emission peaks and this time is measured from the GRB trigger time. Since, the GBM has high sky coverage and is less sensitive than the BAT, the GRBs that trigger GBM are visible to the BAT. The GRB spectral energy coverage of the GBM and BAT are shown on the left panel of Fig. 5.1. The BAT spectral peak energy is lower compared to that of the GBM. Since most GRBs have E_p above the energy range (15-150 keV) of the BAT on *Swift*, obtaining accurate E_p values of *Swift* bursts has been difficult. This may lead to finding different spectral peak energy for the same burst detected by GBM and BAT.

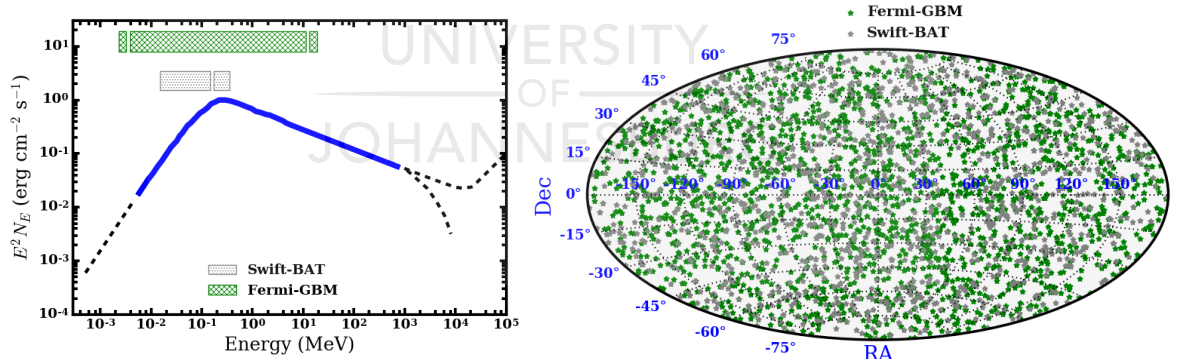


Figure 5.1 *Left panel:* GRB spectral energy coverage of the GBM and BAT. *Right panel:* GRBs detected by the *Fermi*-GBM (green symbols, [Gruber et al., 2014](#); [von Kienlin et al., 2014](#); [Narayana Bhat et al., 2016a](#)) and *Swift*-BAT (gray symbols, [Lien et al., 2016](#)) are isotropically distributed in the sky.

Following the finding of the Yonetoku relation, many efforts have been made by several independent authors ([Ghirlanda et al., 2012b](#); [Nava et al., 2009](#)) to investigate whether this relation has a physical origin or it is due to an instrumental selection effect (or bias) ([Dainotti & Amati, 2018](#)). This bias usually arises when the observational sample is not representative

of the correct, underlying bursts that may affect correlation. There is a debate on the physical interpretation of the GRB correlation. A lack of sufficient GRBs with known redshift and the limited energy spectrum provided by previous telescopes are also main issues against the validation of this correlation. While there is still no unique interpretation of the coefficients of the Yonetoku relation, the discovery of small dispersion/outliers with a tighter correlation around the power-law best-fit line is promising. Despite this discussion, the $E_{\text{i,p}}-L_{\text{iso}}$ correlation has been proposed as a possible mechanism to construct a GRB Hubble diagram and constrain the cosmological parameters (Ghirlanda et al., 2006; Schaefer & Collazzi, 2007). We note that a significant correlation among the spectral parameters of the GRB emission has relevant implications to understand the theory of prompt emission and use them as standard candles for the study of cosmology.

5.2 Observational data from *Fermi*-GBM and *Swift*-BAT

Up until 2017 December, the *Swift*-BAT (15–150 keV energy range, see the left panel of Fig. 5.1) has detected 1192 GRBs, of which about 35% have measured redshifts. The *Fermi*-GBM (8 keV–40 MeV energy range) has also detected a significant number of GRBs (i.e., 2232 GRBs). The sky map of BAT GRBs (gray stars) and GBM GRBs (green stars) are shown in the right panel of Fig. 5.1. Both instruments have been observing the GRBs at the rates that reflect their relative sky exposures, with the BAT detecting ∼92 per/year compared to ∼240 for GBM. Of the GBM-detected GRBs, only ∼5% have measured redshift. Since the energy band of the BAT is narrow (15–150 keV), the E_{p} is sometimes outside of the energy band. So, we cannot precisely characterize the E_{p} of the vF_v spectrum. For bursts with soft spectra (i.e., low power-law index), tend to have E_{p} below the energy threshold in the BAT energy range. Otherwise, a simple power-law (PL) is an acceptable spectral fit for most of the GRBs detected by BAT, which do not provide a E_{p} . In our analysis, we do not include bursts for which a simple PL is an acceptable fit and no E_{p} . This reduces the number of GRBs with measured redshift to use for the analysis of the $E_{\text{i,p}}-L_{\text{iso}}$ correlation. Using the sample of BAT GRBs for which the Comp model is the best-fit and the GBM sample, we can calibrate the best-fit parameters of the Yonetoku relation.

All GRBs used in this study have been detected either with the *Swift*-BAT or *Fermi*-GBM or with both instruments. The GRBs detected by GBM have a larger energy flux (i.e., $\sim 8.6 \times 10^{-8}$ – 1.2×10^{-5} erg cm $^{-2}$ s $^{-1}$ computed in 10–1000 keV energy range) than the ones detected by BAT (i.e., from $\sim 1.5 \times 10^{-9}$ – 2.4×10^{-6} erg cm $^{-2}$ s $^{-1}$ computed in 15–50 keV energy range, see the left panel of Fig. 5.2). In order to use a quality data set, we include the bursts in the sample for which their spectra fitting parameter are constrained from the spectral models such as the Band function (Band et al., 1993), smoothly broken power-law (SBPL, Ryde, 1999) and power-law with an exponential cutoff (Comp, Eq. 2.2) (see Sec. §2.6.2). We do not consider GRBs when the spectral-fit parameters are not listed in the catalog. We compute the L_{iso} as in Eq. (5.2) for each of

the GRBs of *Swift*¹ sample. The computation is performed by using the parameters obtained from the spectral-fit integrated over T_{peak} of the GRB spectrum. The uncertainty for each parameter has been estimated at 90% confidence level. For 394 *Swift*-BAT GRBs (see the right panel of Fig. 5.2) with measured redshift, we identified acceptable spectral fitting parameters obtained from the Comp model (see Eq. 2.2) and PL model (see Eq. 2.6). Since the value of E_p is not available for BAT GRBs fitted with PL model, we consider the GRBs constrained by Comp model only. Accordingly, an acceptable sample of the BAT consisting of 38 GRBs (hereafter, S_{Comp}) is identified for the analysis of the Yonetoku relation (see Tab. B.1).

We have also analyzed the L_{iso} as in Eq. (5.2) for 116 GRBs detected by GBM. The computation of this analysis is obtained using parameters from the spectral fit integrated over the time range of the peak flux of the burst. The L_{iso} of these GRBs are shown in the right panel of Fig. 5.2. The spectra of GBM GRBs can be modeled by the SBPL, Band, Comp and PL functions. Among these GRBs, we have identified 76 GRBs (hereafter, $F_{\text{best-model}}$) that have the spectral peak energy or break energy with a best-fit model. The parameters obtained from the spectral fitting models are given in Tab. B.2. This selection later provides us with 12 GRBs, which are commonly detected by both GBM and BAT instruments (see Fig. 5.3).

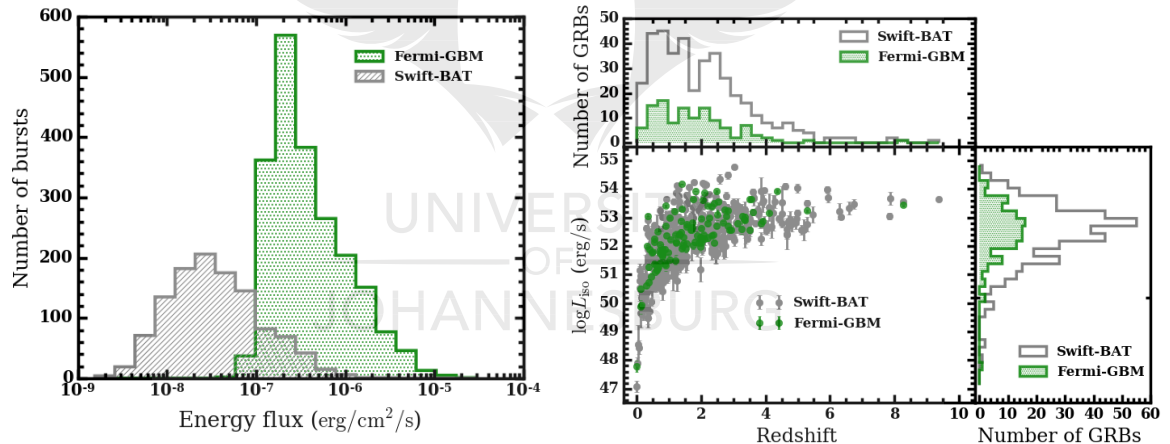


Figure 5.2 *Left panel:* the energy flux histograms of GBM (green hatched, 2115 GRBs) and BAT (gray hatched, 1154 GRBs) data collected until December 2017. *Right panel:* the L_{iso} distribution of GBM (green symbols) and *Swift* (gray symbols) computed in the 1 keV–10 MeV energy range extrapolated based on the best-fit model over the time range of the peak flux of the bursts with respect to their redshifts. The L_{iso} and redshift distributions for GBM (green dotted histogram) and for BAT (gray histogram).

In order to study the effect of spectral fitting models on the Yonetoku relation, we identified the GBM GRB sample containing 90 GRBs modeled by Comp (F_{Comp} , see Tab. B.3) and 46 GRBs modeled by a Band function (F_{Band} , see Tab. B.4). We have also combined the $F_{\text{best-model}}$ sample

¹<https://swift.gsfc.nasa.gov/results/batgrbcat/>

with S_{Comp} excluding the commonly detected 12 GRBs. In this case, we have identified the total sample includes 102 GRBs (hereafter, $FS_{\text{best-model}}$).

5.3 Intrinsic peak energy and isotropic luminosity calculations

In this section we discuss the correlation between L_{iso} and $E_{\text{i,p}}$ for different GRB samples presented in §5.2 which are resulted from the BAT and GBM instruments. After measuring the redshift of a GRB, one can correct for cosmological effects and infer its rest frame photon peak energy obtained from the Band function, spectral profile as

$$E_{\text{i,p}} = E_{\text{p}}(1+z). \quad (5.1)$$

For the cases, the lower spectra index of the Band function $\alpha > -2$ and the upper index $\beta < -2$, the E_{p} is the peak energy in keV of the vF_v spectrum and $E_b = E_{\text{p}}(\alpha - \beta)/(2 + \alpha)$ is the break energy in keV. The peak energy of the vF_v spectrum of the GRBs fitted by Comp model is also designated by E_{p} . For the GRB spectrum fitted by the SBPL model (Eq. 2.3), the peak energy is defined as, $E_{\text{p}} = E_0 \times 10^{(1/2\sigma \ln[(\alpha+2)/(-\beta-2)])}$, which is valid only for $|(\alpha+2)/(-\beta-2)| < 1$. Here, E_0 is the e-folding energy and σ is the break scale in decades of energy fixed at 0.3.

The L_{iso} is defined as

$$L_{\text{iso}} = 4\pi d_L^2 F_{\text{bolo}}(E_1, E_2, z), \quad (5.2)$$

where L_{iso} is 1-second peak luminosity, in units of [erg s^{-1}], and $F_{\text{bolo}}(E_1, E_2, z)$ is a measured bolometric flux in units [$\text{erg cm}^{-2} \text{ s}^{-1}$] integrated over the energy range from $E_1 = 1 \text{ keV}$ to $E_2 = 10^4 \text{ keV}$ and is given as

$$F_{\text{bolo}}(E_1, E_2, z) = \kappa \int_{E_1/(1+z)}^{E_2/(1+z)} EN(E) dE. \quad (5.3)$$

Here, the factor $\kappa = 1.6 \times 10^{-9}$ is defined to make the keV to erg conversion and $N(E)$ is the 1-second time-integrated spectrum of the acceptable fitting models (i.e., Band, Comp, SBPL, etc.). The L_{iso} is computed using the parameters obtained from the fitting model. The uncertainty, $\sigma_{L_{\text{iso}}}$ of the luminosity fitted by the Comp model could be evaluated following the error prorogation method

$$\sigma_{L_{\text{iso}}}^2(A_{\text{Comp}}, \gamma, E_{\text{p}}) = \left(\frac{\partial L_{\text{iso}}}{\partial A_{\text{Comp}}} \right)^2 \sigma_{A_{\text{Comp}}}^2 + \left(\frac{\partial L_{\text{iso}}}{\partial \gamma} \right)^2 \sigma_{\gamma}^2 + \left(\frac{\partial L_{\text{iso}}}{\partial E_{\text{p}}} \right)^2 \sigma_{E_{\text{p}}}^2, \quad (5.4)$$

where $\sigma_{A_{\text{Comp}}}$, σ_{γ} and $\sigma_{E_{\text{p}}}$ are the errors on parameters A_{Comp} , γ and E_{p} , respectively. Similarly, the uncertainty of the L_{iso} of the GRBs fitted with the Band and SBPL functions can be defined as

$$\sigma_{L_{\text{iso}}}^2(A_{\text{Band/sbpl}}, \alpha, \beta, E_{\text{p}}) = \left(\frac{\partial L_{\text{iso}}}{\partial A_{\text{Band/sbpl}}} \right)^2 \sigma_{A_{\text{Band/sbpl}}}^2 + \left(\frac{\partial L_{\text{iso}}}{\partial \alpha} \right)^2 \sigma_{\alpha}^2 + \left(\frac{\partial L_{\text{iso}}}{\partial \beta} \right)^2 \sigma_{\beta}^2 + \left(\frac{\partial L_{\text{iso}}}{\partial E_{\text{p}}} \right)^2 \sigma_{E_{\text{p}}}^2. \quad (5.5)$$

Here, $\sigma_{A_{\text{Band/sbpl}}}$, σ_{α} , σ_{β} and $\sigma_{E_{\text{p}}}$ are the errors on the $A_{\text{Band/sbpl}}$, α , β and E_{p} , respectively.

5.4 Samples of GRBs

Our main motivation is to check the validity and stability of the Yonetoku relation (Yonetoku et al., 2004), using the samples of GRBs from the BAT and GBM instruments. The calibrated parameters obtained from these correlations can be used to construct the extended Hubble diagram to probe the cosmological expansion history. We can also use these parameters to probe the dark-energy density and Hubble constant.

5.4.1 Common GRBs (GBM and BAT)

The *Swift*-BAT and *Fermi*-GBM have detected 30 GRBs in common in each year². Additional GRBs could also be detected by the *Swift* instrument when the *Swift*-XRT points at *Fermi*-LAT observed GRBs. According to the data selection for the best-fit spectral model presented in the previous section, we identified 12 GRBs simultaneously detected by both GBM and BAT instruments. Fig. 5.3 compares the $E_{i,p}$ (left panel) and L_{iso} (right panel) measured with these instruments.

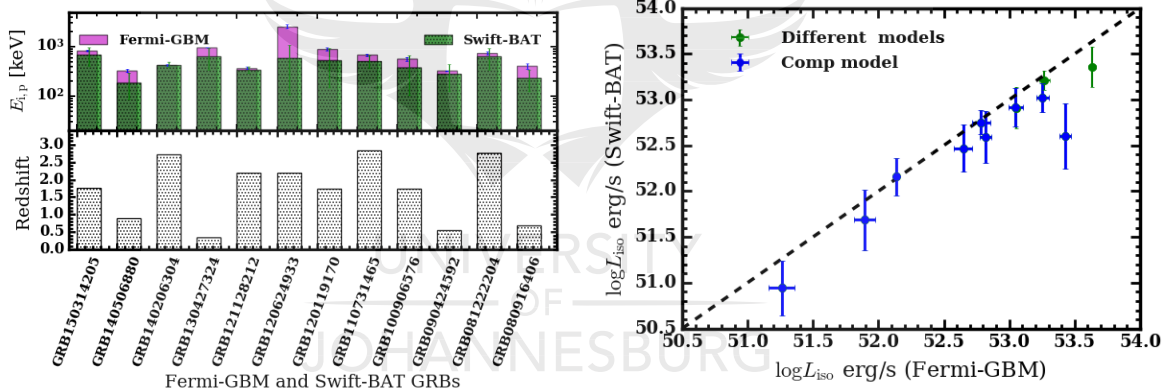


Figure 5.3 *Left panel:* comparison of $E_{i,p}$ measured by the GBM and BAT for 12 GRBs detected in common. *Right panel:* the correlation between L_{iso} of GBM and BAT sample. Blue symbols correspond to the BAT and GBM GRBs fitted with the same Comp spectral model while the green symbols indicate the fit with different spectral models. The dashed line indicates the equality of L_{iso} measured with the GBM and BAT.

As shown in the right panel of Fig. 5.3, we see that the two measurements agree in the majority of GRBs when the same Comp model is used by the two instruments (blue symbols) and different models (green symbols). We note that these two quantities are correlated with a wide dispersion of the observational data. However, there is a deviation between the two values, the GBM measures slightly larger L_{iso} as demonstrated by the location of the majority of the blue and green symbols below the black dashed line. However, adding the BAT data into the

²<https://fermi.gsfc.nasa.gov/ssc/observations/types/grbs/>

GBM during the Yonetoku relation analysis does not significantly change the values. For most GRBs, the measured $E_{i,p}$ by GBM are also higher than the BAT as shown in the left panel of Fig. 5.3. This indicates that the GRB, which has a higher $E_{i,p}$ energy are also characterized by high luminosity, i.e., the GBM bursts are biased towards higher flux.

5.4.2 GBM GRBs fitted with Comp and Band models

This section presents Comp and Band spectral models fitted to the GBM data. It is of interest to investigate the difference in the values of the L_{iso} and $E_{i,p}$ between the Comp and Band models, since they are the two main suitable functions used to study the GRB prompt spectra. In Fig. 5.4 we show the relative deviation between the bolometric flux modeled with Comp ($S_{bolo}^{Comp,43}$) and Band ($S_{bolo}^{Band,43}$), including the redshift of 43 GRBs. Apart from a few cases, the bolometric

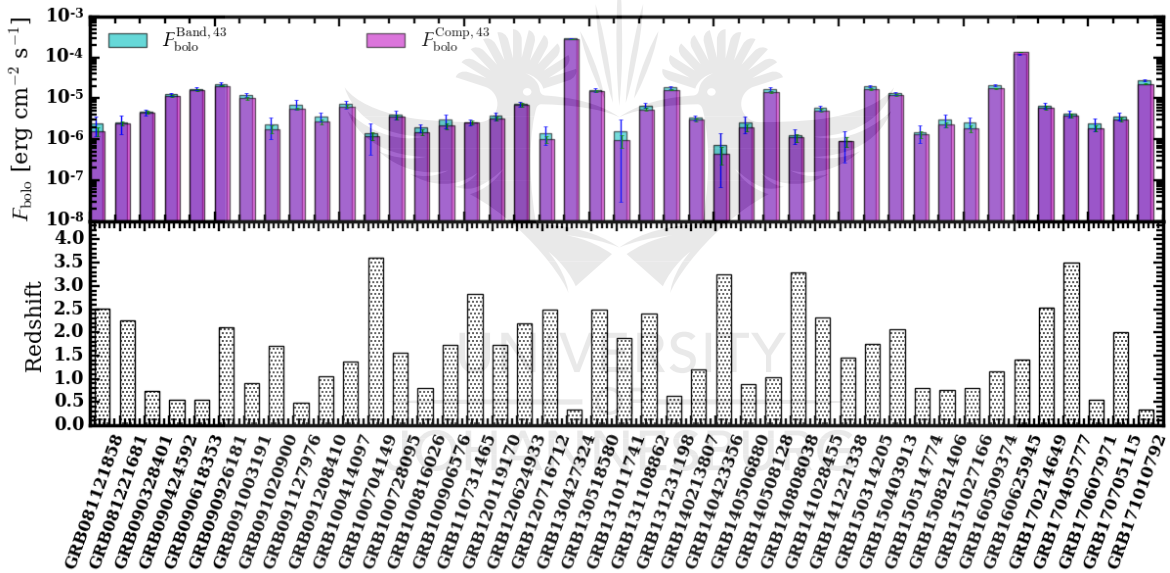


Figure 5.4 Top panel: distribution of the bolometric flux F_{bolo} as the GBM GRB spectrum modeled by both Comp (blue histogram) and Band (green histogram) models. Bottom panel: redshift of 43 GRBs.

flux of the two models are in agreement. The difference between the correlation of luminosities of $L_{iso}^{Band,43}$ and $L_{iso}^{Comp,43}$ (see left panel of Fig. 5.5) and the difference between intrinsic peak energies of $E_{i,p}^{Band,43}$ and $E_{i,p}^{Comp,43}$ (see right panel of Fig. 5.5) can have a significant effect in the model-dependent studies of the Yonetoku relation. In both models, a slight difference is observed. The obtained result shows that the $L_{iso}^{Band,43}$ and $E_{i,p}^{Comp,43}$ have higher numerical values as demonstrated by the dashed lines in Fig. 5.5. This may possibly lead to a bias in the analysis of the Yonetoku relation and it would represent a good line of research for future investigation.

Following Goldstein et al. (2012), we determine the change of the relative deviation in L_{iso}

$$\Delta L_{\text{iso}} = \frac{|L_{\text{iso}}^{\text{Comp},43} - L_{\text{iso}}^{\text{Band},43}|}{\sigma_{L_{\text{iso}}^{\text{Comp},43}} + \sigma_{L_{\text{iso}}^{\text{Band},43}}}, \quad (5.6)$$

and $E_{i,p}$

$$\Delta E_{i,p} = \frac{|E_{i,p}^{\text{Comp},43} - E_{i,p}^{\text{Band},43}|}{\sigma_{E_{i,p}^{\text{Comp},43}} + \sigma_{E_{i,p}^{\text{Band},43}}}, \quad (5.7)$$

between the two models. If the variation between the isotropic luminosity or intrinsic energy

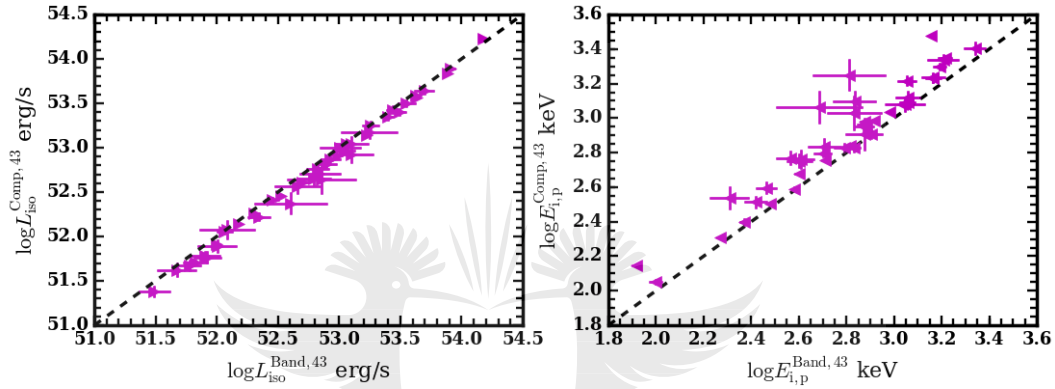


Figure 5.5 *Left panel:* the correlation between L_{iso} of GBM Comp and Band samples. *Right panel:* the correlation between $E_{i,p}$ of GBM Comp and Band samples. The dashed line denotes the equality of L_{iso} and $E_{i,p}$ measured with GBM Comp and Band function.

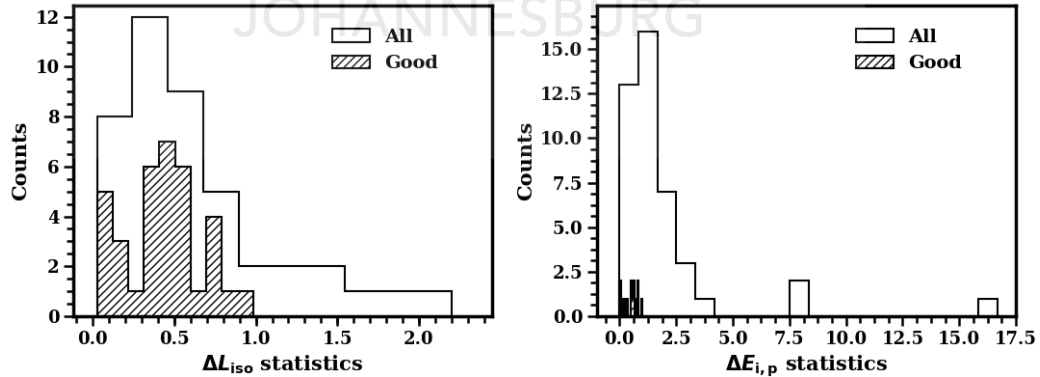


Figure 5.6 *Left panel:* distribution of the L_{iso} statistic for the Comp and Band models. A value less than 1 indicates the L_{iso} values are inside errors. *Right panel:* distribution of the $E_{i,p}$ statistic for the Comp and Band models. A value < 1 indicates the $E_{i,p}$ values are inside errors.

values is precisely matched with the sum of their errors, then ΔL_{iso} and $\Delta E_{i,p}$ values have a result of unity. A value of $\Delta L_{\text{iso}} < 1$ or $\Delta E_{i,p} < 1$ show that the value is within errors, otherwise

they are not inside errors of each other. In the left panel of Fig. 5.6, we showed the distribution of Comp and Band L_{iso} values. About 81% of the values are found to be within the combined errors. On the other hand, the right-hand side of Fig. 5.6 shows the distribution of the $E_{\text{i,p}}$, and roughly 33% of the Comp and Band $E_{\text{i,p}}$ values are inside the joint errors.

5.4.3 The combined sample of GBM and BAT GRBs of the best-fit model

We have combined the samples of GBM and BAT detectors and constructed a uniform database of GRBs with known redshift to use for the correlation analysis. The parameters obtained from the best-fit model of the sample result in the best estimate of the observed properties of GRBs. In Tab. 5.1, the values of $E_{\text{i,p}}$ and L_{iso} computed using the parameters of the best-fit model for both GBM and BAT samples are reported. The error on the $E_{\text{i,p}}$ is computed from the spectral fit uncertainty of the observed peak energy, while the error on L_{iso} is determined using the error propagation method discussed in §5.3. It is important to mention that the pivot energy of the Comp model for the BAT and GBM GRB spectral analysis are held fixed at 50 keV and 100 keV, respectively as reported in the BAT catalog (Lien et al., 2016) and GBM catalog (Gruber et al., 2014; von Kienlin et al., 2014; Narayana Bhat et al., 2016a). It normalizes the model to the energy interval under inspection and supports reduce cross-correlation of other parameters. Depending on these values, the L_{iso} is computed for each of the GRBs.

Table 5.1 The $E_{\text{i,p}}$ and L_{iso} of the *Fermi*-GBM sample of 76 GRBs in the cosmological rest frame which are computed using the best-fit model with their redshift. Also calculated are distance modulus μ .

GRB Name	Model	z	$E_{\text{i,p}}$ (keV)	$F_{\text{bolo}} (10^{-5}$ erg cm $^{-2}$ s $^{-1}$)	L_{iso} (10 52 erg s $^{-1}$)	$\mu \pm \sigma_\mu$	References for Redshift
GRB 171010792	Band	0.3285	397.9 ± 16.0	2.74 ± 0.19	0.99 ± 0.07	41.8 ± 1.4	Kankare et al. (2017)
GRB 170903534	Comp	0.886	342.5 ± 99.3	0.06 ± 0.02	0.25 ± 0.08	45.6 ± 1.5	de Ugarte Postigo et al. (2017d)
GRB 170705115	Comp	2.01	625.6 ± 37.7	0.31 ± 0.03	9.27 ± 0.98	44.9 ± 1.4	de Ugarte Postigo et al. (2017c)
GRB 170607971	Comp	0.557	344.3 ± 57.4	0.188 ± 0.03	0.24 ± 0.04	44.4 ± 1.4	de Ugarte Postigo et al. (2017b)
GRB 170405777	Comp	3.51	1719.6 ± 126.8	0.37 ± 0.04	43.70 ± 4.76	46.4 ± 1.4	de Ugarte Postigo et al. (2017a)
GRB 170214649	Band	2.53	1606.9 ± 262.0	0.67 ± 0.13	35.6 ± 6.72	45.7 ± 1.5	Kruehler et al. (2017)
GRB 161129300	Comp	0.645	448.4 ± 93.7	0.09 ± 0.02	0.16 ± 0.04	45.7 ± 1.5	Cano et al. (2016)
GRB 161117066	Comp	1.549	187.3 ± 14.4	0.08 ± 0.02	1.21 ± 0.37	44.4 ± 1.5	Malesani et al. (2016)
GRB 161014522	Comp	2.823	754.8 ± 84.6	0.07 ± 0.02	5.08 ± 1.28	46.8 ± 1.4	de Ugarte Postigo et al. (2016)
GRB 160629930	Comp	3.332	1035.8 ± 126.8	0.08 ± 0.02	8.68 ± 1.79	47.2 ± 1.4	Castro-Tirado et al. (2016)
GRB 160625945	Band	1.406	1428.5 ± 36.6	12.0 ± 0.44	150.0 ± 5.55	42.3 ± 1.4	Xu et al. (2016)
GRB 160509374	Band	1.17	749.3 ± 33.1	2.12 ± 0.15	16.8 ± 1.16	43.1 ± 1.4	Tanvir et al. (2016)
GRB 151027166	Comp	0.81	575.3 ± 78.6	0.18 ± 0.03	0.58 ± 0.10	45.3 ± 1.4	Perley et al. (2015)
GRB 150821406	Comp	0.755	685.6 ± 83.3	0.22 ± 0.03	0.6 ± 0.09	45.4 ± 1.4	D'Elia et al. (2015)
GRB 150514774	Comp	0.807	112.3 ± 4.7	0.13 ± 0.03	0.42 ± 0.09	42.9 ± 1.6	de Ugarte Postigo et al. (2015c)
GRB 150403913	Band	2.06	1558.3 ± 105.8	1.32 ± 0.12	42.4 ± 3.88	44.9 ± 1.4	Pugliese et al. (2015)
GRB 150314205	Band	1.758	822.0 ± 27.6	1.98 ± 0.14	43.2 ± 3.12	43.4 ± 1.4	de Ugarte Postigo et al. (2015b)

Continued on next page

CHAPTER 5. YONETOKU RELATION FOR *FERMI*-GBM AND *SWIFT*-BAT GRBS

Table 5.1 – Continued from previous page

GRB 150301818	Comp	1.5169	433.8 ± 66.9	0.05 ± 0.01	0.81 ± 0.22	46.2 ± 1.4	de Ugarte Postigo et al. (2015a)
GRB 141225959	Comp	0.915	484.1 ± 88.1	0.05 ± 0.02	0.21 ± 0.10	46.5 ± 1.5	Gorosabel et al. (2014b)
GRB 141221338	Comp	1.452	804.6 ± 197.7	0.09 ± 0.02	1.19 ± 0.34	46.7 ± 1.5	Perley et al. (2014)
GRB 141220252	Comp	1.3195	497.8 ± 26.6	0.22 ± 0.03	2.3 ± 0.27	44.9 ± 1.4	de Ugarte Postigo et al. (2014c)
GRB 141028455	Band	2.33	1460.5 ± 116.6	0.58 ± 0.07	25.1 ± 3.07	45.7 ± 1.4	Xu et al. (2014)
GRB 141004973	Comp	0.573	220.8 ± 40.0	0.09 ± 0.02	0.12 ± 0.03	44.5 ± 1.5	de Ugarte Postigo et al. (2014b)
GRB 140907672	Comp	1.21	249.9 ± 30.2	0.04 ± 0.01	0.32 ± 0.12	45.7 ± 1.5	Castro-Tirado et al. (2014b)
GRB 140808038	Comp	3.29	675.0 ± 46.4	0.11 ± 0.02	11.1 ± 2.32	46.2 ± 1.4	Gorosabel et al. (2014a)
GRB 140703026	Comp	3.14	1125.5 ± 191.5	0.07 ± 0.02	6.15 ± 1.68	47.5 ± 1.5	Castro-Tirado et al. (2014a)
GRB 140620219	Comp	2.04	281.2 ± 36.4	0.05 ± 0.02	1.68 ± 0.62	45.5 ± 1.5	Kasliwal et al. (2014)
GRB 140606133	Comp	0.384	1169.6 ± 303.4	0.35 ± 0.07	0.18 ± 0.04	45.8 ± 1.5	Singer et al. (2015)
GRB 140512814	Comp	0.725	1000.1 ± 136.3	0.30 ± 0.04	0.73 ± 0.11	45.7 ± 1.4	de Ugarte Postigo et al. (2014a)
GRB 140508128	Band	1.027	762.9 ± 38.5	1.69 ± 0.15	9.72 ± 0.89	43.4 ± 1.4	Atteia et al. (2017)
GRB 140506880	Comp	0.889	325.9 ± 27.3	0.20 ± 0.04	0.79 ± 0.15	44.3 ± 1.4	Fynbo et al. (2014)
GRB 140423356	Comp	3.26	1066.7 ± 277.8	0.04 ± 0.02	4.33 ± 1.96	47.9 ± 1.5	Tanvir et al. (2014)
GRB 140304557	Comp	5.283	1855.2 ± 674.1	0.04 ± 0.02	12.2 ± 5.92	49.0 ± 1.6	Jeong et al. (2014)
GRB 140213807	Comp	1.2076	203.9 ± 6.0	0.30 ± 0.03	2.56 ± 0.22	43.05 ± 1.5	Schulze et al. (2014)
GRB 140206304	SBPL	2.73	419.5 ± 15.2	0.29 ± 0.03	18.6 ± 1.81	44.3 ± 1.4	Malesani et al. (2014)
GRB 131231198	Band	0.642	513.4 ± 18.2	1.85 ± 0.12	3.33 ± 0.22	42.6 ± 1.4	Cucchiara (2014)
GRB 131108862	Band	2.4	1130.8 ± 109.0	0.67 ± 0.09	31.2 ± 4.36	45.1 ± 1.4	de Ugarte Postigo et al. (2013c)
GRB 131105087	Comp	1.69	1209.1 ± 173.9	0.19 ± 0.03	3.67 ± 0.58	46.6 ± 1.4	Xu et al. (2013)
GRB 131011741	Comp	1.874	1155.5 ± 279.4	0.09 ± 0.03	2.36 ± 0.78	47.3 ± 1.5	Rau et al. (2013)
GRB 130518580	Band	2.488	1635.8 ± 116.5	1.6 ± 0.14	81.6 ± 7.2	44.8 ± 1.4	Sanchez-Ramirez et al. (2013)
GRB 130427324	Band	0.3399	961.5 ± 8.0	28.9 ± 0.45	11.4 ± 0.18	40.7 ± 1.4	Levan et al. (2013)
GRB 121128212	Comp	2.2	369.6 ± 19.2	0.16 ± 0.03	6.08 ± 1.08	44.7 ± 1.4	Tanvir et al. (2012b)
GRB 120907017	Comp	0.97	263.8 ± 62.6	0.05 ± 0.02	0.22 ± 0.11	45.6 ± 1.6	Sanchez-Ramirez et al. (2012)
GRB 120716712	Comp	2.48	588.2 ± 58.0	0.10 ± 0.02	5.11 ± 0.97	46.0 ± 1.4	Greiner et al. (2012)
GRB 120711115	SBPL	1.41	3070.7 ± 119.3	1.6 ± 0.23	20.2 ± 2.85	45.8 ± 1.5	Tanvir et al. (2012a)
GRB 120624933	Comp	2.1974	2548.4 ± 239.6	0.71 ± 0.08	26.8 ± 2.97	46.4 ± 1.5	de Ugarte Postigo et al. (2013a)
GRB 120326056	Comp	1.798	217.3 ± 19.5	0.06 ± 0.01	1.37 ± 0.34	44.9 ± 1.5	Tello et al. (2012)
GRB 120119170	Comp	1.728	895.8 ± 69.3	0.32 ± 0.03	6.61 ± 0.69	45.5 ± 1.4	Cucchiara & Prochaska (2012)
GRB 110731465	Comp	2.83	675.3 ± 44.0	0.26 ± 0.03	17.9 ± 2.05	45.2 ± 1.4	Tanvir et al. (2011)
GRB 110213220	Comp	1.4607	226.8 ± 17.7	0.14 ± 0.03	1.98 ± 0.36	44.0 ± 1.5	Milne & Cenko (2011)
GRB 100906576	Comp	1.727	564.4 ± 57.0	0.21 ± 0.04	4.45 ± 0.77	45.1 ± 1.4	Tanvir et al. (2010b)
GRB 100816026	Comp	0.8049	250.7 ± 12.5	0.15 ± 0.02	0.47 ± 0.07	44.1 ± 1.4	Tanvir et al. (2010a)
GRB 100728439	Comp	2.106	381.7 ± 63.6	0.05 ± 0.02	1.83 ± 0.63	46.0 ± 1.5	Flores et al. (2010)
GRB 100728095	Comp	1.567	1311.7 ± 123.3	0.36 ± 0.05	5.82 ± 0.90	46.0 ± 1.4	Kruehler et al. (2010)
GRB 100704149	Comp	3.6	1198.9 ± 134.0	0.12 ± 0.03	15.1 ± 3.21	47.0 ± 1.4	Campana & Grupe (2010)
GRB 100615083	Comp	1.398	215.7 ± 19.3	0.07 ± 0.02	0.81 ± 0.22	44.8 ± 1.5	Kruehler et al. (2013)
GRB 100414097	Comp	1.368	1237.2 ± 76.8	0.64 ± 0.06	7.48 ± 0.65	45.3 ± 1.4	Cucchiara (2010)
GRB 091208410	Comp	1.0633	394.5 ± 33.5	0.27 ± 0.03	1.67 ± 0.20	44.3 ± 1.4	Wiersema et al. (2009)
GRB 091127976	SBPL	0.49	83.7 ± 1.9	0.70 ± 0.03	0.65 ± 0.03	40.6 ± 1.6	Cucchiara et al. (2009e)
GRB 091020900	Comp	1.71	1779.7 ± 417.3	0.18 ± 0.04	3.63 ± 0.79	47.3 ± 1.5	Xu et al. (2009)
GRB 091003191	Band	0.8969	746.5 ± 51.4	1.22 ± 0.15	5.0 ± 0.63	43.7 ± 1.4	Cucchiara et al. (2009b)
GRB 090926181	Band	2.1062	1077.3 ± 33.7	2.26 ± 0.15	76.7 ± 4.99	43.7 ± 1.4	Malesani et al. (2009)

Continued on next page

5.4. SAMPLES OF GRBS

Table 5.1 – Continued from previous page

GRB 090618353	Comp	0.54	689.2 ± 31.0	1.56 ± 0.09	1.84 ± 0.11	43.3 ± 1.4	Cenko et al. (2009c)
GRB 090424592	Comp	0.544	321.0 ± 7.0	1.15 ± 0.04	1.38 ± 0.05	42.4 ± 1.4	Chornock et al. (2009c)
GRB 090328401	Comp	0.736	804.2 ± 51.6	0.45 ± 0.04	1.14 ± 0.103	44.9 ± 1.4	Cenko et al. (2009b)
GRB 090323002	Comp	3.57	1809.6 ± 124.4	0.36 ± 0.04	43.8 ± 5.06	46.5 ± 1.4	Chornock et al. (2009a)
GRB 090113778	Comp	1.7493	554.4 ± 83.1	0.05 ± 0.02	1.04 ± 0.33	46.7 ± 1.4	Krühler et al. (2012)
GRB 090102122	Comp	1.547	962.1 ± 56.7	0.31 ± 0.04	4.92 ± 0.60	45.6 ± 1.4	Cenko et al. (2009a)
GRB 081222204	Comp	2.77	746.1 ± 55.4	0.17 ± 0.02	11.2 ± 1.47	45.9 ± 1.4	Cucchiara et al. (2008c)
GRB 081221681	Comp	2.26	388.3 ± 12.3	0.25 ± 0.03	9.88 ± 1.12	44.4 ± 1.4	Salvaterra et al. (2012)
GRB 081121858	Band	2.512	683.3 ± 159.5	0.24 ± 0.12	12.6 ± 6.44	45.3 ± 1.5	Berger & Rauch (2008)
GRB 081008832	Comp	1.97	485.4 ± 112.0	0.03 ± 0.02	0.94 ± 0.445	46.9 ± 1.5	Cucchiara et al. (2008b)
GRB 080916406	Comp	0.69	403.8 ± 47.1	0.09 ± 0.02	0.18 ± 0.05	45.6 ± 1.4	Fynbo et al. (2008)
GRB 080916009	Comp	4.35	2809.4 ± 297.3	0.429 ± 0.06	83.9 ± 11.4	47.1 ± 1.5	Greiner et al. (2009)
GRB 080810549	Comp	3.36	2729.2 ± 1047.4	0.10 ± 0.03	10.5 ± 3.6	48.6 ± 1.7	Holland & Page (2008)
GRB 080804972	Comp	2.20	551.8 ± 64.4	0.05 ± 0.02	1.96 ± 0.64	46.6 ± 1.4	Cucchiara et al. (2008a)

Notes. The bolometric flux F_{bolo} and $E_{\text{i,p}} = E_{\text{p}}(1+z)$ for the Band or Comp or SBPL spectral fits, with peak energy E_{p} .

Table 5.2 The $E_{\text{i,p}}$ and L_{iso} of the *Swift*-BAT sample of 38 long GRBs in the cosmological rest frame which are computed using the best-fit model with their redshift. The distance modulus μ is also shown.

GRB Name	Model	z	$E_{\text{i,p}}$ (keV)	$F_{\text{bolo}} (10^{-5}$ erg cm $^{-2}$ s $^{-1}$)	L_{iso} (10^{52} erg s $^{-1}$)	$\mu \pm \sigma_\mu$	References for Redshift
GRB 170705A	Comp	2.01	485.5 ± 264.6	0.22 ± 0.14	6.52 ± 4.17	46.2 ± 2.0	de Ugarte Postigo et al. (2017c)
GRB 150314A	Comp	1.758	686.4 ± 282.0	1.04 ± 0.68	22.7 ± 14.8	45.5 ± 1.7	de Ugarte Postigo et al. (2015b)
GRB 140506A	Comp	0.889	189.6 ± 104.0	0.12 ± 0.14	0.49 ± 0.553	44.1 ± 2.2	Fynbo et al. (2014)
GRB 140206A	Comp	2.73	431.3 ± 56.4	0.25 ± 0.07	16.2 ± 4.5	45.7 ± 1.0	Malesani et al. (2014)
GRB 130427A	Comp	0.3399	626.3 ± 285.6	20.8 ± 14.4	8.16 ± 5.7	42.0 ± 1.8	Levan et al. (2013)
GRB 130420A	Comp	1.297	133.1 ± 35.7	0.03 ± 0.03	0.32 ± 0.317	44.5 ± 1.7	de Ugarte Postigo et al. (2013b)
GRB 121128A	Comp	2.2	344.7 ± 51.8	0.15 ± 0.05	5.68 ± 1.98	45.6 ± 1.1	Tanvir et al. (2012b)
GRB 120811C	Comp	2.671	220.5 ± 48.6	0.04 ± 0.03	2.27 ± 1.86	45.8 ± 1.4	Fynbo et al. (2012)
GRB 120729A	Comp	0.8	117.0 ± 31.5	0.03 ± 0.03	0.08 ± 0.08	44.3 ± 1.7	Tanvir & Ball (2012)
GRB 120712A	Comp	4.1745	515.9 ± 288.9	0.03 ± 0.04	4.68 ± 6.79	48.6 ± 2.5	Xu et al. (2012)
GRB 120624B	Comp	2.1974	594.3 ± 486.2	0.11 ± 0.14	4.01 ± 5.1	47.6 ± 2.9	de Ugarte Postigo et al. (2013a)
GRB 120119A	Comp	1.728	539.0 ± 390.2	0.19 ± 0.17	3.90 ± 3.56	46.6 ± 2.5	Cucchiara & Prochaska (2012)
GRB 110731A	Comp	2.83	517.8 ± 152.2	0.15 ± 0.07	10.50 ± 4.59	46.8 ± 1.3	Tanvir et al. (2011)
GRB 110715A	Comp	0.8224	277.0 ± 59.5	0.79 ± 0.20	2.62 ± 0.68	43.1 ± 1.1	Piranomonte et al. (2011)
GRB 110503A	Comp	1.613	340.2 ± 83.6	0.44 ± 0.25	7.67 ± 4.36	44.38 ± 1.3	de Ugarte Postigo et al. (2011)
GRB 100906A	Comp	1.727	377.3 ± 272.2	0.14 ± 0.11	2.96 ± 2.34	45.9 ± 2.4	Tanvir et al. (2010b)
GRB 100814A	Comp	1.44	380.4 ± 143.8	0.05 ± 0.05	0.66 ± 0.68	47.1 ± 1.8	O'Meara et al. (2010)
GRB 100621A	Comp	0.542	139.8 ± 22.5	0.14 ± 0.05	0.17 ± 0.06	43.0 ± 1.2	Milvang-Jensen et al. (2010)
GRB 091029	Comp	2.752	199.5 ± 68.7	0.02 ± 0.02	0.99 ± 1.43	46.5 ± 2.1	Chornock et al. (2009d)
GRB 090424	Comp	0.544	283.2 ± 157.6	1.20 ± 0.72	1.45 ± 0.87	42.7 ± 2.0	Chornock et al. (2009c)

Continued on next page

Table 5.2 – Continued from previous page

GRB 081222	Comp	2.77	626.9 ± 291.4	0.12 ± 0.08	8.22 ± 5.02	47.5 ± 1.8	Cucchiara et al. (2008c)
GRB 080916A	Comp	0.6887	233.5 ± 108.8	0.04 ± 0.04	0.09 ± 0.09	45.8 ± 2.0	Fynbo et al. (2008)
GRB 080413B	Comp	1.1014	234.0 ± 85.3	0.22 ± 0.12	1.53 ± 0.80	44.0 ± 1.5	Vreeswijk et al. (2008)
GRB 071010B	Comp	0.947	133.4 ± 18.2	0.07 ± 0.03	0.34 ± 0.16	43.6 ± 1.2	Cenko et al. (2007)
GRB 070508	Comp	0.82	388.6 ± 129.4	0.52 ± 0.24	1.7 ± 0.79	44.6 ± 1.4	Jakobsson et al. (2007)
GRB 061222A	Comp	2.088	697.4 ± 351.7	0.18 ± 0.14	6.05 ± 4.79	47.4 ± 2.0	Perley et al. (2009)
GRB 060927	Comp	5.4636	841.5 ± 391.8	0.04 ± 0.04	13.0 ± 12.1	49.7 ± 2.0	Ruiz-Velasco et al. (2007)
GRB 060908	Comp	1.8836	354.7 ± 254.1	0.04 ± 0.06	1.06 ± 1.51	47.1 ± 2.8	Fynbo et al. (2009)
GRB 060719	Comp	1.532	138.8 ± 30.5	0.02 ± 0.02	0.28 ± 0.38	45.2 ± 1.9	Krühler et al. (2012)
GRB 060306	Comp	1.559	285.4 ± 148.3	0.07 ± 0.06	1.18 ± 0.92	45.8 ± 2.0	Jakobsson et al. (2012)
GRB 060206	Comp	4.0559	413.4 ± 138.1	0.03 ± 0.02	4.79 ± 3.39	47.9 ± 1.5	Fynbo et al. (2006)
GRB 060117	Comp	4.6	565.1 ± 74.5	0.57 ± 0.15	126.0 ± 33.3	45.6 ± 1.0	de Ugarte Postigo et al. (2006)
GRB 060111A	Comp	2.32	285.5 ± 150.9	0.02 ± 0.02	0.76 ± 0.93	47.4 ± 2.2	Host Lyman-alpha (2006)
GRB 050922C	Comp	2.1995	468.7 ± 343.1	0.11 ± 0.09	3.98 ± 3.50	46.9 ± 2.5	Jakobsson et al. (2005)
GRB 050502B	Comp	5.2	457.0 ± 132.4	0.01 ± 0.02	3.78 ± 4.96	49.1 ± 1.9	Afonso et al. (2011)
GRB 050401	Comp	2.8983	420.9 ± 157.0	0.15 ± 0.16	11.2 ± 11.6	46.2 ± 1.8	Fynbo et al. (2005)
GRB 050318	Comp	1.4436	164.3 ± 39.8	0.03 ± 0.02	0.39 ± 0.32	45.2 ± 1.5	Berger & Mulchaey (2005)
GRB 050219A	Comp	0.2115	134.6 ± 70.2	0.04 ± 0.05	0.006 ± 0.007	44.2 ± 2.3	Hunt et al. (2014)

5.5 The Yonetoku relation between $E_{\text{i,p}}$ and L_{iso}

In this section, we provide a brief overview of the fitting model and the Markov Chain Monte Carlo maximum likelihood estimation method. We also study the derivation of the partial correlation analysis used in the Yonetoku relation.

5.5.1 Fitted model

The Yonetoku et al. (2004) relation of L_{iso} and $E_{\text{i,p}}$ can be described by a simple power-law as

$$L_{\text{iso}} \propto \left(\frac{E_{\text{i,p}}}{E_{0,\text{dec}}} \right)^m, \quad (5.8)$$

where $E_{0,\text{dec}}$ is a reference energy defined in Eq. (4.42). The power-law relation of Eq. (5.8) can be linearized in the form

$$y = mx + k, \quad (5.9)$$

where the following expression of the L_{iso} – $E_{\text{i,p}}$ plane should be given by

$$\begin{cases} y \equiv \log L_{\text{iso}}, \\ x \equiv \log \frac{E_{\text{i,p}}}{E_{0,\text{dec}}}. \end{cases} \quad (5.10)$$

For each GRB in the samples, we have computed the prompt rest-frame peak energy as in Eq. (5.1) and the L_{iso} using Eq. (5.2) in the 1 keV–10 MeV energy range. In such a way that Eqs. (5.1) and (5.2) take the linearized form of Eq. (5.9), which provides conditions under which each data point in the sample can be considered in the maximization of the likelihood function.

5.5.2 Partial correlation analysis

In order to study the strength of the correlation between L_{iso} and $E_{i,p}$, we use the Pearson linear correlation coefficient, denoted with $\rho_{p_{E_{i,p},L_{\text{iso}}}}$ (Bevington et al., 1993) and Spearman's rank correlation coefficient with $\rho_{sp_{E_{i,p},L_{\text{iso}}}}$ (Spearman, 1904). The latter is equal to Pearson correlation coefficient between the rank values of two main variables $L_{\text{iso}}(z)$ and $E_{i,p}$. However, using these correlation coefficients will affect the values since the redshift (z) variable is numerically related to both $L_{\text{iso}}(z)$ and $E_{i,p}$. Besides, we point out that many other relevant correlations with respect to these variables were studied by Petrosian et al. (2015); Dainotti & Amati (2018). The descriptions of the peak luminosity undergoes a strong redshift evolution, $L_p \propto (1+z)^{2.0-2.3}$ (Petrosian et al., 2015). Therefore, the z -dependence need to be taken into account when computing the strength of correlation between the main variables. The partial correlation coefficient gauges the degree of relationship between $E_{i,p}$ and L_{iso} while removing the effect of redshift as

$$\rho_{E_{i,p},L_{\text{iso}},z} = \frac{\rho_{p_{E_{i,p},L_{\text{iso}}}} - (\rho_{p_{E_{i,p},z}})(\rho_{p_{L_{\text{iso}},z}})}{\sqrt{1 - \rho_{p_{E_{i,p},z}}^2} \sqrt{1 - \rho_{p_{L_{\text{iso}},z}}^2}}. \quad (5.11)$$

Here, $\rho_{p_{E_{i,p},L_{\text{iso}}}}$ is the Pearson correlation coefficient of the two main parameters, $E_{i,p}$ and L_{iso} defined as

$$\rho_{p_{E_{i,p},L_{\text{iso}}}} = \frac{n \sum E_{i,p} L_{\text{iso}} - \sum E_{i,p} \sum L_{\text{iso}}}{\sqrt{(n \sum E_{i,p}^2 - (\sum E_{i,p})^2)(n \sum L_{\text{iso}}^2 - (\sum L_{\text{iso}})^2)}}, \quad (5.12)$$

where $\rho_{p_{E_{i,p},z}}$ is the Pearson correlation coefficient between $E_{i,p}$ and z , given by

$$\rho_{p_{E_{i,p},z}} = \frac{n \sum E_{i,p} z - \sum E_{i,p} \sum z}{\sqrt{(n \sum E_{i,p}^2 - (\sum E_{i,p})^2)(n \sum z^2 - (\sum z)^2)}}, \quad (5.13)$$

and $\rho_{p_{L_{\text{iso}},z}}$ is the Pearson correlation coefficient between L_{iso} and z , given by

$$\rho_{p_{L_{\text{iso}},z}} = \frac{n \sum L_{\text{iso}} z - \sum L_{\text{iso}} \sum z}{\sqrt{(n \sum L_{\text{iso}}^2 - (\sum L_{\text{iso}})^2)(n \sum z^2 - (\sum z)^2)}}, \quad (5.14)$$

where n is the number of GRBs in the sample. We have also performed the Pearson correlation coefficient analysis between these two main variables. The obtained results show that the $E_{i,p}$ and L_{iso} are strongly correlated even after removing the effect of z . The results are reported in Tab. 5.3.

5.5.3 Likelihood analysis of $E_{i,p}$ and L_{iso}

The analysis of likelihood function given in Eq. (4.31) considers the variables in Eq. (5.9) and their errors including the extrinsic systematics σ_{ext} on y , due to unknown physical parameter. We maximize the function given in Eq. (4.31) to obtain the best-fit values of the parameters of the Yonetoku relation.

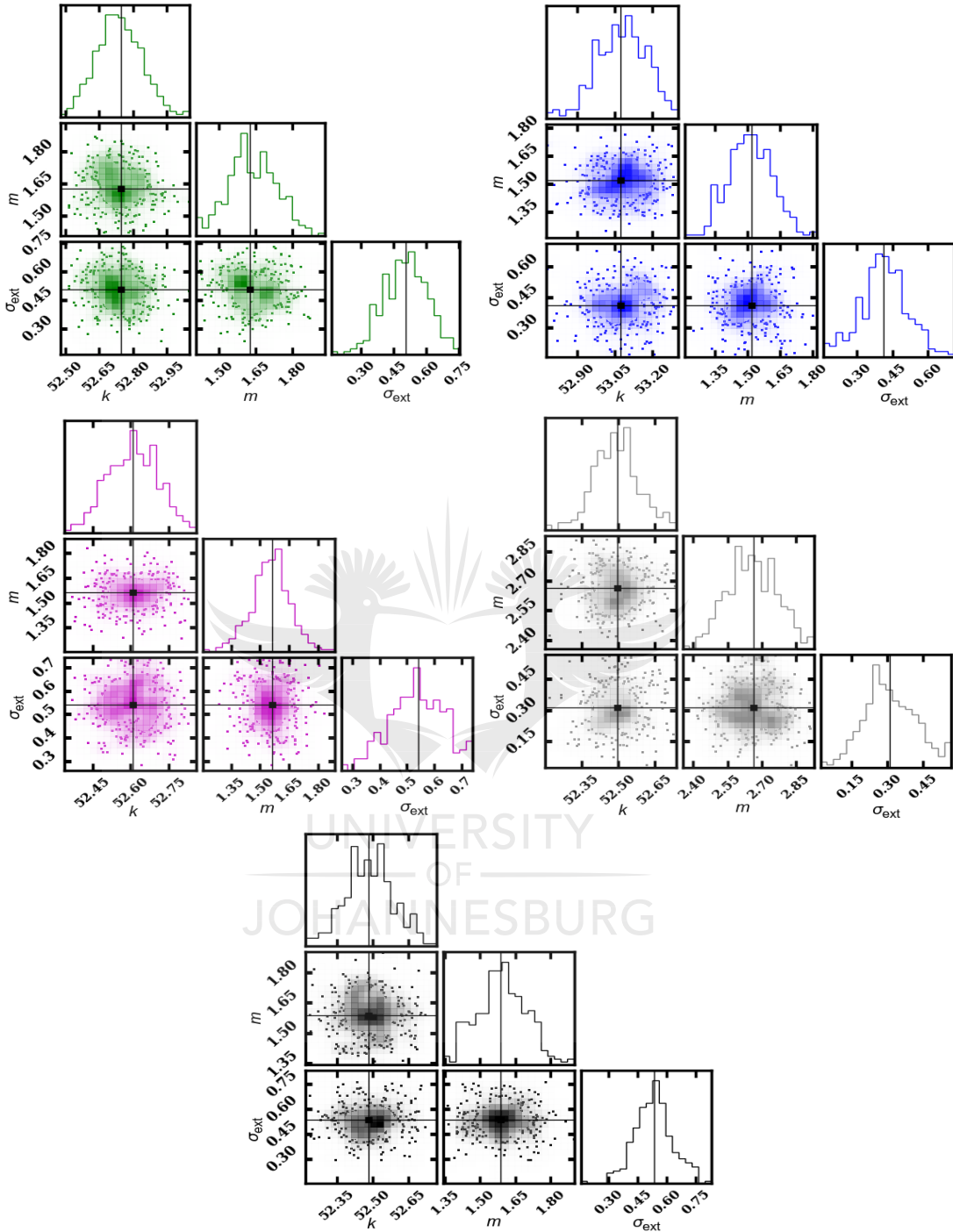


Figure 5.7 Distributions of the fitting parameters of the Yonetoku relation estimated using MCMC method for different GRB samples. k , m and σ_{ext} are the coefficients of the Yonetoku relation defined in Eq.(5.9) during the MCMC sampling run. *Top left panel*: the estimated parameters of the observational F_{Comp} sample (green). *Top right panel*: the estimated parameters for F_{Band} sample (blue). *Middle left panel*: the estimated parameters for $F_{\text{best-model}}$ sample (magenta). *Middle right panel*: the estimated parameters for S_{Comp} (gray). *Bottom panel*: the estimated parameters for $FS_{\text{best-model}}$ sample of 76 GRBs. The parameter of the highest likelihood found during the run is indicated by the cross lines.

Table 5.3 The best-fit parameters of the $E_{i,p}$ – L_{iso} correlation for five categories of GRB samples. The $\rho_{p_{E_{i,p},L_{\text{iso}},z}}$, $\rho_{p_{E_{i,p},L_{\text{iso}}}}$, $\rho_{p_{L_{\text{iso}},z}}$ and $\rho_{p_{E_{i,p},z}}$ are the Pearson correlation coefficients defined in Eqs. (5.11), (5.12), (5.13) and (5.14), respectively.

LGRB Samples	No. of GRBs	$\rho_{p_{E_{i,p},L_{\text{iso}}}}$	$\rho_{p_{E_{i,p},L_{\text{iso}},z}}$	$\rho_{p_{L_{\text{iso}},z}}$	$\rho_{p_{E_{i,p},z}}$	$E_{0,\text{dec}}$ (keV)	m	k	σ_{ext}
F_{Comp}	90	0.71	0.63	0.56	0.42	1000	1.6 ± 0.3	52.7 ± 0.1	0.5 ± 0.1
F_{Band}	46	0.76	0.70	0.66	0.44	900	1.5 ± 0.4	53.1 ± 0.1	0.4 ± 0.1
$F_{\text{best-model}}$	76	0.67	0.52	0.64	0.51	700	1.6 ± 0.4	52.6 ± 0.1	0.5 ± 0.1
S_{Comp}	38	0.83	0.75	0.60	0.55	350	2.7 ± 0.7	52.5 ± 0.2	0.3 ± 0.2
$FS_{\text{best-model}}$	102	0.70	0.63	0.60	0.40	550	1.6 ± 0.3	52.5 ± 0.1	0.5 ± 0.1

The uncertainty can be derived using Eq. (4.33). We can also estimate the best-fit parameters by employing Markov Chain Monte Carlo (MCMC) Maximum likelihood estimation method as advocated for fitting a model to data (Hogg et al., 2010). A brief introduction to the MCMC technique and implementation of estimating the fitting parameters are described in details in the work by Hogg et al. (2010). We calibrate the Yonetoku relation and compute the maximum likelihood via Eq. (4.31) by using the MCMC and without performing the MCMC. The obtained fitting parameters of these two methods are consistent with each other. For all different samples that discussed in §5.2, the MCMC method was implemented to estimate the best-fit parameters. Fig. 5.7 shows the best-fit parameters obtained from this method. These results, including the estimated errors using Eq. (4.33) are reported in Tab. 5.3 for our different samples. We also plotted the Yonetoku relation in Fig. 5.8 by using the best-fit parameters listed in this table for the *Fermi*-GBM sample fitted by Comp (F_{Comp}), GBM band (F_{Band}), the GBM sample obtained from the best-fit model ($F_{\text{best-model}}$), the *Swift*-BAT sample obtained from the best-fit Comp model (S_{Comp}) and the joint GBM and BAT samples for the best-fit spectra ($FS_{\text{best-model}}$).

We see that the normalization parameter of the L_{iso} – $E_{i,p}$ correlation for the F_{Comp} sample is somewhat larger than the one computed for the F_{Band} sample, while the slope parameter show no significant difference. This is consistent with the results of Lin et al. (2016). The best-fit index (i.e., 2.69 ± 0.65) for the S_{Comp} sample is steeper than the indices of the other samples reported in Tab. 5.3. The best-fit parameters of the L_{iso} – $E_{i,p}$ correlations reported in Tab. 5.3 are also consistent with the result of Schaefer & Collazzi (2007) (i.e., $m = 1.68$) and Lin et al. (2016) (i.e., $m = 1.65 \pm 0.25$, $k = 52.52 \pm 0.08$, $\sigma_{\text{ext}} = 0.45 \pm 0.05$ and the $\rho_{\text{sp}} = 0.70$ for Band spectrum). The slope of the Yonetoku relation of a BAT sample is also consistent with the result of Zitouni et al. (2014). At low luminosities, we find a mild shift of population away from the best-fit of the Yonetoku relation in the direction of higher $E_{i,p}$ (see Fig. 5.8). This indicates that the correlation line has a steeper (harder) slope at the specified luminosity range. For a sample of S_{Comp} the partial correlation coefficient $\rho_{p_{E_{i,p},L_{\text{iso}},z}} = 0.75$. The degree of this correlation is higher than the other samples.

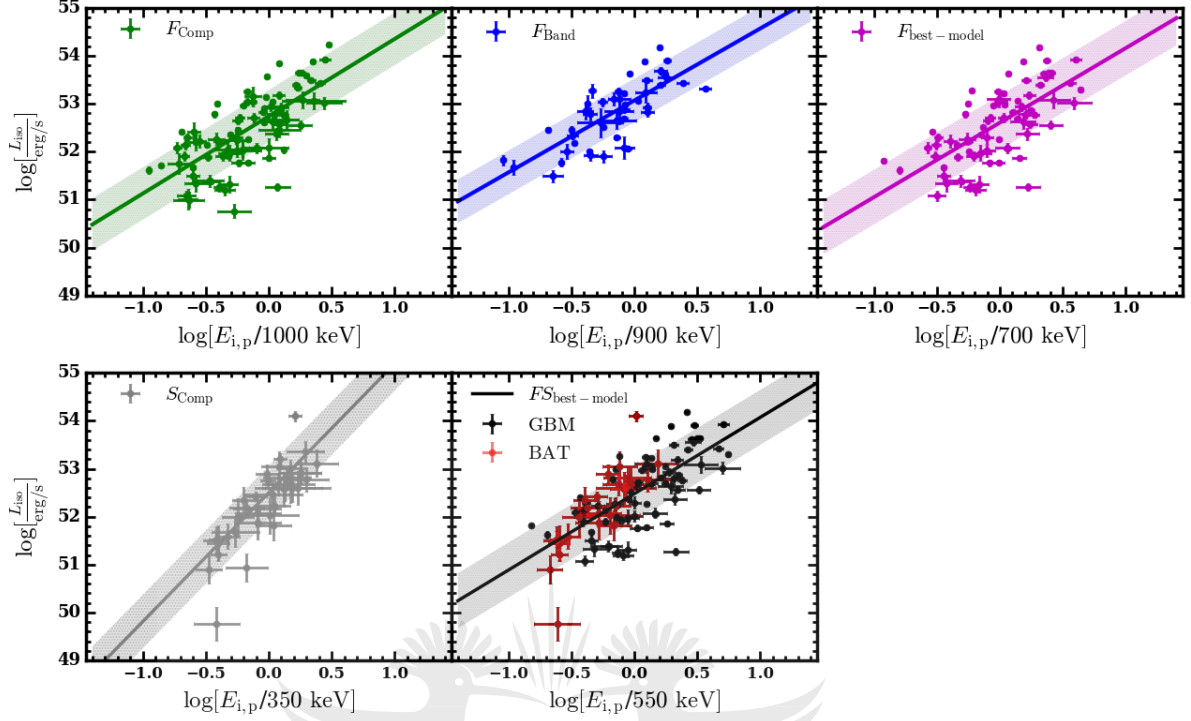


Figure 5.8 The correlation between L_{iso} and $E_{i,p}$ and the best-fit curves of the Yonetoku relation. *Top left panel*: the measured parameters of the observational F_{Comp} sample (green). *Top middle panel*: the measured parameters for F_{Band} sample (blue). *Top right panel*: the measured parameters for $F_{\text{best-model}}$ sample (magenta). *Bottom left panel*: the measured parameters for S_{Comp} (gray). *Bottom right panel*: the joint 78 GBM sample of GRBs (black points with error bars) and 26 BAT sample of GRBs (red points with error bars) with the best-fit model, which are not simultaneously detected by the GBM ($FS_{\text{best-model}}$).

5.6 Constraints on cosmological parameters and the extended Hubble diagram

5.6.1 Constraints on dark-energy and Hubble parameters

We have performed a χ^2 analysis to constrain cosmological parameters using LGRBs and applied it to different samples (see Sec. §5.2) depending on the coefficients of the $E_{i,p}$ – L_{iso} relation. Then, we consider all possible values of the cosmological parameter with $\Omega_\Lambda \in (0.0, 0.85)$ and $H_0 \in (30, 90) \text{ km s}^{-1} \text{ Mpc}^{-1}$ to plot the likelihood contours in the (Ω_Λ, H_0) plane of 1σ and 2σ confidence levels as shown in Fig. 5.9. The measured values of H_0 in 1σ confidence level for different samples are reported in Tab. 5.4. Comparing the contours of the GBM samples in Fig. 5.9 with BAT S_{Comp} , the shape of the likelihood contour of S_{Comp} stands vertically with high dispersion because the likelihood minimization of the χ^2 that used to constrain the cosmological parameters strongly depends on the errors of the coefficients of the Yonetoku relation. Thus, the

5.6. CONSTRAINTS ON COSMOLOGICAL PARAMETERS AND THE EXTENDED HUBBLE DIAGRAM

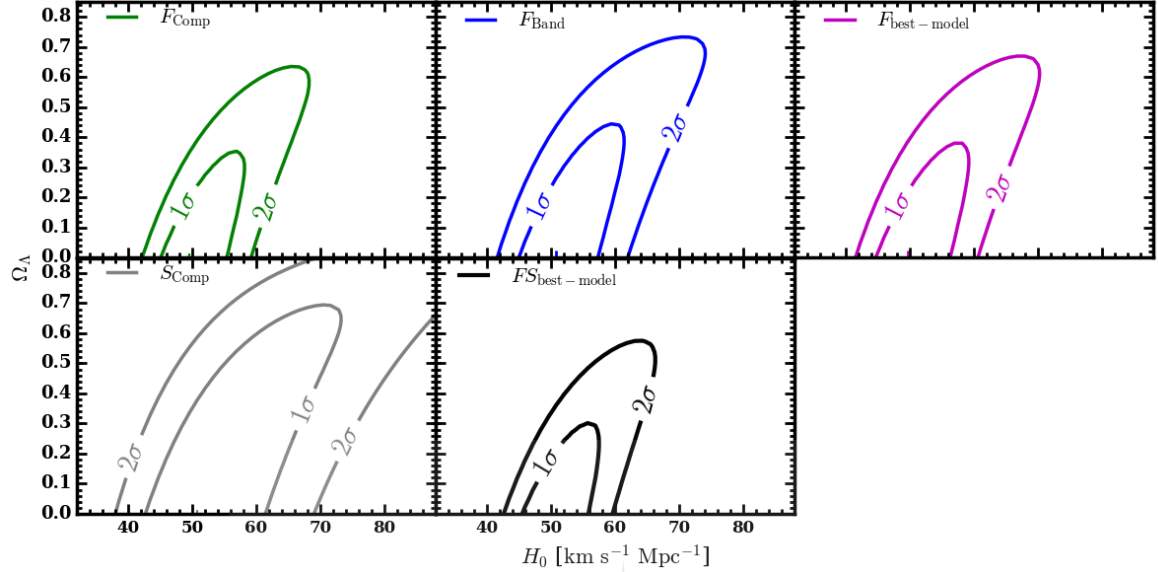


Figure 5.9 Constraints on the cosmological parameters from the fitting of the Yonetoku relation for different samples of LGRBs. *Top left panel:* the Ω_Λ and H_0 obtained for the observational F_{Comp} sample (green). *Top middle panel:* the Ω_Λ and H_0 obtained with the observational F_{Band} sample (blue). *Top right panel:* the Ω_Λ and H_0 obtained from the observational $F_{\text{best-model}}$ sample (magenta). *Bottom left panel:* the Ω_Λ and H_0 obtained with the observational S_{Comp} sample (gray). *Bottom right panel:* the $\Omega_\Lambda - H_0$ obtained from the observational $FS_{\text{best-model}}$ sample (black). The 1σ and 2σ confidence levels of the pair of cosmological parameters determined by following $\Delta\chi^2 \equiv \chi^2 - \chi^2_{\min} \leq 2.30$ and 6.18 , respectively. The plus sign indicates the best-fit location, which found within range.

Table 5.4 Constraints on H_0 and $\Omega_\Lambda \in (0.0, 0.85)$ in 1σ confidence level in the flat universe.

Samples	F_{Comp}	F_{Band}	$F_{\text{best-model}}$	S_{Comp}	$FS_{\text{best-model}}$
$H_0 [\text{km s}^{-1} \text{Mpc}^{-1}]$	$49.59^{+9.80}_{-5.09}$	$50.82^{+10.88}_{-5.82}$	$49.59^{+9.71}_{-5.00}$	$50.82^{+22.83}_{-8.17}$	$50.82^{+6.89}_{-5.49}$

corresponding errors of normalization $\sigma_k = 0.18$ and the slope $\sigma_m = 0.65$.

The combination of GRBs and SNe Type Ia data can potentially be used as a probe of the Hubble diagram. In our analysis we used the recent 580 SNe U2.1 sample (Suzuki et al., 2012) that covers the redshift from 0.015 to 1.414. Fig. 5.10 present the likelihood contours of SNe U2.1 with a measured value of $H_0 = 69.992^{+0.539}_{-0.526} \text{ km s}^{-1} \text{ Mpc}^{-1}$ and $\Omega_\Lambda = 0.723^{+0.029}_{-0.032}$ and the likelihood contours of $FS_{\text{best-model}} + \text{SNe U2.1}$ sample with a measured value of $H_0 = 69.908^{+0.533}_{-0.517} \text{ km s}^{-1} \text{ Mpc}^{-1}$ and $\Omega_\Lambda = 0.715^{+0.029}_{-0.030}$ in 1σ confidence intervals. Thus values are determined by using $\Delta\chi^2 \equiv \chi^2 - \chi^2_{\min} \leq 2.3$. The best-fitting value in 1σ confidence level is consistent with the Planck values (Planck Collaboration et al., 2018; Riess et al., 2018). However, the errors on parameters are rather large that may arise due to the large extrinsic systematics scattering associated with the simulated sample.

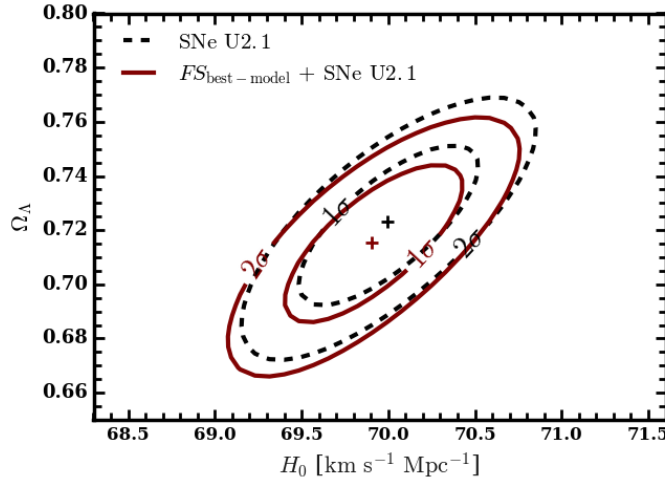


Figure 5.10 Contours of likelihood in the (H_0, Ω_Λ) plane for SNe U2.1 (black color) and SNe U2.1 with $FS_{\text{best-model}}$ (maroon color) samples in 1σ and 2σ confidence levels. The plus signs show the location of the best-fit.

5.6.2 The extended Hubble diagram

After we derive the luminosity distances (Eq. 4.48) as a function of z , we used the modulus distance (Eq. 4.49) related to the Yonetoku relation from the $FS_{\text{best-model}}$ sample of GRBs. Then,

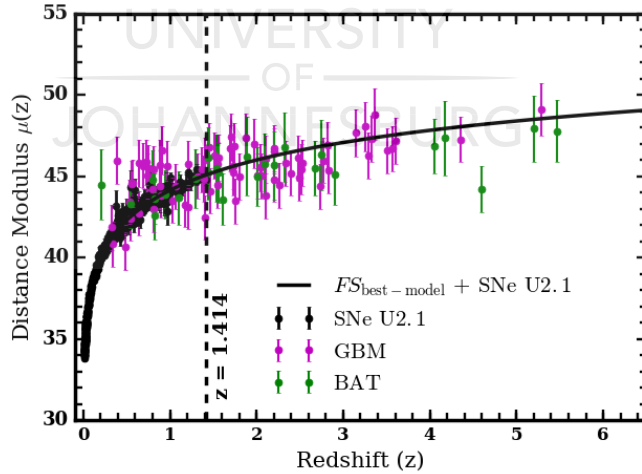


Figure 5.11 Combined SNe and GRB Hubble diagram for the $FS_{\text{best-model}} + \text{SNe U2.1}$ sample. The black curved line is plotted using the estimated cosmological parameters $H_0 = 69.908 \text{ km s}^{-1} \text{ Mpc}^{-1}$ and $\Omega_\Lambda = 0.715$ obtained from the joint $FS_{\text{best-model}} + \text{SNe U2.1}$ data. The vertical broken line is plotted at the maximum redshift $z = 1.414$ of the SNe U2.1 data.

the best-fit parameters (see Tab. 5.3) obtained from the relation are substituted into Eq. (4.49)

and becomes

$$\mu = 2.5 \log \left[\frac{1}{4\pi F_{\text{bolo}}} \left(\frac{E_{i,p}}{550} \right)^{1.6} \right] - 5 \log(\text{Mpc}) + 156.2. \quad (5.15)$$

Hence, it follows from a distance modulus error Eq. (4.50) that

$$\sigma_{\mu}^2 = \left(\frac{5}{2} \sigma_{\log L_{\text{iso}}} \right)^2 + \left(1.086 \frac{\sigma_{F_{\text{bolo}}}}{F_{\text{bolo}}} \right)^2, \quad (5.16)$$

where the uncertainty of the isotropic peak luminosity in Eq. (4.51) gives

$$\sigma_{\log L_{\text{iso}}} = \left((1.51 \log(E_{i,p}/550))^2 + (1.74(\sigma_{E_{i,p}}/E_{i,p}))^2 + 0.04 \right)^{1/2}.$$

We plot a Hubble diagram of $FS_{\text{best-model}}$ GRB sample relying on Eqs. (5.15) and (5.16), combining with the data of 580 SNe U2.1 in Fig. 5.11. The curved line is plotted by using the parameters H_0 and Ω_{Λ} obtained from the minimization of χ^2 method of Eq. 4.52.

5.7 Summary

The *Swift*-BAT and *Fermi*-GBM data allow an increasing number of useful GRBs with known redshift, providing increased accuracy in the estimate of cosmological parameters. At present, there are more than 400 GRBs with known redshift³, but the E_p has not been measured for all GRBs. In this work, we discussed the $L_{\text{iso}}-E_{i,p}$ correlation for different samples of LGRBs with measured redshift detected by *Fermi*-GBM and *Swift*-BAT until December 2017. Our analysis is based on GRB T_{peak} time-integrated at one-second peak flux. Since the spectra of GBM GRBs are in a wide energy range, it can usually be described by the Band function, which is a smoothly broken power-law with break energy and a Comp or SBPL model, which provide a break or peak energy to compute the $E_{i,p}$. For the BAT GRBs, we only consider the best-fit spectra of the Comp model that was reported in the catalog since it can provide a firm E_p observable. Using the parameters obtained from the fit of these models, we computed the $E_{i,p}$ and L_{iso} to study the Yonetoku relation. Using the parameters of the best-fit relation, we constrain the cosmological parameters and plotted the extended Hubble diagram. The best-fit of the Yonetoku relation for $FS_{\text{best-model}}$ sample can be expressed as

$$\frac{L_{\text{iso}}}{\text{erg s}^{-1}} = 10^{52.48 \pm 0.10} \left(\frac{E_{i,p}}{550 \text{ keV}} \right)^{1.60 \pm 0.29}.$$

Extending the validity of the Yonetoku relation for the studied GBM and BAT samples of GRB prompt emission, we found that the L_{iso} of GBM sample is higher than the BAT sample. Thus instrumental biases contribute to shaping the distribution of GRBs in the $L_{\text{iso}}-E_{i,p}$ plane, however, they cannot be fully responsible for the observed correlation, which therefore must also have a physical origin. A strong correlation between the GRBs in the $E_{i,p}-L_{\text{iso}}$ plane was also observed,

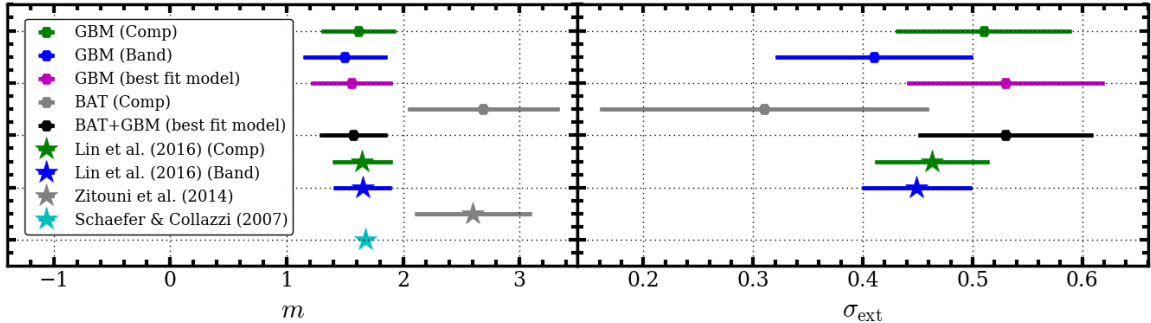


Figure 5.12 Comparison of the coefficients of the Yonetoku relation of our current work with the previous work done by Schaefer & Collazzi (2007); Zitouni et al. (2014); Lin et al. (2016).

while the correlation for the S_{Comp} sample is especially high. Finally, we summarize that the phenomenological correlation of $E_{i,p}$ and L_{iso} showed a strong correlation so that GRB study could be used as a potential cosmological probe. Fig. 5.12 summarizes the indices and extrinsic parameters obtained from the best-fit values of the Yonetoku relation for different analysis. Thus, our results are consistent with the previous work of Schaefer & Collazzi (2007); Tsutsui et al. (2009); Zitouni et al. (2014); Lin et al. (2016). We also extended the SNe Hubble diagram up to a redshift of $z = 5.4636$ with GRBs where the d_L is more sensitive to dark-energy properties and evolution. However, with the present GBM and BAT samples of GRBs Ω_Λ and H_0 cannot be meaningfully constrained.

UNIVERSITY
OF
JOHANNESBURG

³https://swift.gsfc.nasa.gov/results/batgrbcatalog/summary_cflux/summary_general_info/GRBlist_redshift_BAT.txt

AMATI RELATION FOR *Fermi*-LAT GRBS

Contents

6.1	Introduction	102
6.2	Data sets	103
6.2.1	GRB samples	103
6.2.2	<i>Fermi</i> data preparation	104
6.3	Spectral analysis	105
6.3.1	Spectral fitting	105
6.3.2	Isotropic energy calculation	106
6.4	Amati relation between E_{iso} and $E_{i,p}$	109
6.4.1	Fitted model	109
6.4.2	Likelihood analysis	111
6.5	The Hubble diagram and constraints on cosmological parameters	114
6.5.1	Sensitivity on the initial choice of cosmological parameters	116
6.5.2	Joint fits with SNe U2.1 data	117
6.6	Discussion and Summary	119

This chapter is organized as follows: in Sec. §6.1 we briefly discuss the phenomenological Amati relation; in Sec. §6.2 we discuss the sample selection and data analysis criteria; in Section §6.3 we perform time-integrated spectral analysis over T_{90} duration, calculate E_{iso} and $E_{i,p}$ for the selected GRBs; in Sec. §6.4 we perform Amati relation fits to our data and to other joint GRB samples. We carry out a cosmological analysis using our parametrized Amati relation in Sec. §6.5; and finally we discuss our results in Sec. §6.6. Most of the results obtained in this chapter have been accepted for publication in Dirirsa et al. (2019).

6.1 Introduction

The Amati relation is between the source-frame energy, $E_{i,p}$, at which the prompt gamma-ray spectral energy distribution νF_ν peaks, and the isotropic-equivalent bolometric energy E_{iso} emitted during the prompt phase, as mentioned in Sec. §4.4.1. We performed spectral analysis of 26 GRBs with a known redshift that are detected by the *Fermi*-LAT during its nine years of operations from July 2008 to September 2017, thus extending the computation of E_{iso} to the 100 MeV range. Multiple components are also required to fit the spectra of a number of GRBs. Using these data, we have tested the Amati relation. Subsequently, we applied the Amati relation to constrain the Hubble constant H_0 and dark-energy parameter Ω_Λ in a flat universe Λ CDM cosmological model.

In order to analyze the Amati relation, we used a sample of GRBs detected by the GRB Monitor (GBM, 200 keV–40 MeV energy range, [Meegan et al., 2009](#)) and the (LAT, 30 MeV to over 300 GeV band, [Atwood et al., 2009](#)) onboard the *Fermi* Observatory. Together, they record GRBs over a broad energy range spans more than 7 energy decades from 10 keV to 300 GeV (see Sec. §3.1). Observation of GRBs with *Fermi* has enabled us to characterize the broad-band prompt emission, revealing a spectral diversity and the presence of multiple spectral components ([Ackermann et al., 2013a](#)). An overview of the possible physical interpretations of these features can be found in [Gehrels & Razzaque \(2013\)](#).

We selected bright GRBs detected simultaneously with *Fermi* GBM and LAT and for which the redshift is known. We used the latest Pass 8 *Fermi*-LAT data selection and binned maximum likelihood analysis presented in Sec. §3.3.2. This forms a uniform sample of 25 LGRBs and 1 SGRB with exceptional energy coverage to constrain the energy E_p of the peak of the νF_ν spectrum using joint GBM-LAT spectral fitting. On the contrary, for instance, the BAT instrument onboard the *Swift* satellite often misses E_p due to its limited energy (15–150 keV) coverage. Detection by LAT, including LAT Low Energy (LLE) data selection in the ∼30–100 MeV range ([Pelassa et al., 2010](#)), also allows modeling multiple spectral components, if required by data. The GBM, LLE and LAT PASS 8 data have been used to calculate E_{iso} from keV energies up to 100 MeV. Overall, we precisely calculate E_{iso} and $E_{i,p}$ values for each GRB in our sample and their associated errors in view of fitting the Amati relation. Such a sample based on detectors on the same satellite is assumed more reliable than the data collected from different instruments for the search of phenomenological correlations.

In addition to the bright *Fermi* GRB sample, we reanalyze the GRB sample that [Wang et al. \(2016\)](#) used to fit the Amati relation. We compare and contrast our fits to the Amati relation with fits for this sample as well as from other work ([Heussaff et al., 2013](#); [Demianski et al., 2017](#)). We also perform fits to joint samples of GRBs and GRBs in different redshift bins to explore the redshift evolution of cosmological parameters. Finally, we use a simple analysis to explore possibilities of constraining H_0 and Ω_Λ with our *Fermi* GRB sample and with various combinations of data, including the recent SNe Type Ia sample ([Suzuki et al., 2012](#)).

6.2 Data sets

This section is providing an overview of the *Fermi* GRB sample with measured redshift used with an emphasis on the joint time-integrated spectral analysis including the GBM, LLE and LAT data.

6.2.1 GRB samples

From the launch of *Fermi* on 11 June 2008 until September 2017, about 32 GRBs were detected with identified redshift z , including the marginally detected GRB 091208B (Ackermann et al., 2013a) by *Fermi*-LAT. Of these, the GBM did not trigger on GRB 081203A and GRB 130907A. Also for the GRB 160623A, GRB 130702A and GRB 120711A we could not find sufficient LAT photons within the GBM T90 duration to perform a time-integrated joint spectral analysis of the LAT and GBM data. By excluding these six GRBs, we conduct our analysis only for the *Fermi* GRB sample of 25 LGRBs and 1 SGRB with well-constrained spectral properties. This covers from GRB 080916C to GRB 170405A, as listed in Tab. 6.1. The spectroscopic or photometric redshifts

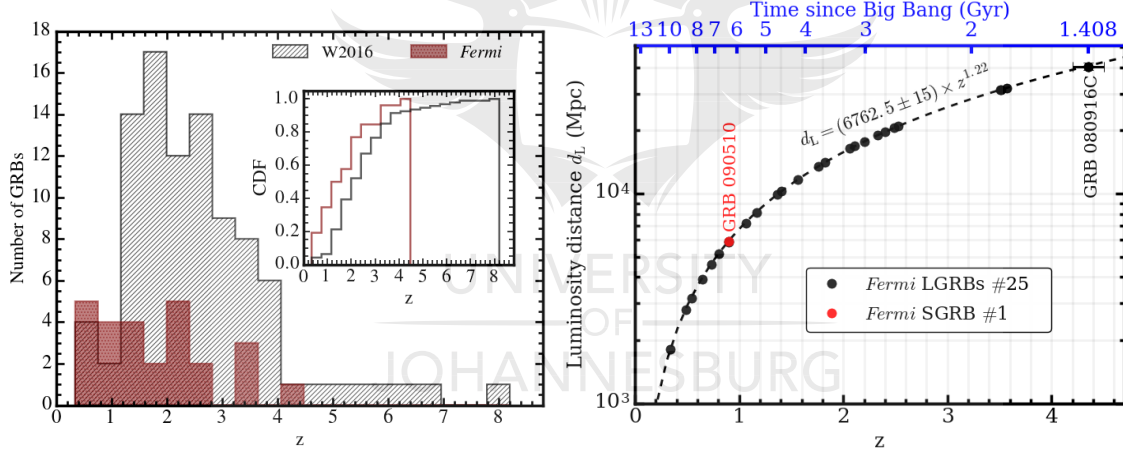


Figure 6.1 *Left panel:* redshift distribution for our sample of 26 (25 long and 1 short) *Fermi* GRBs (maroon histogram) and the W2016 sample of 94 GRBs (gray histogram). The cumulative distribution function (CDF) of the *Fermi* (median: $z = 1.66$, mean: $z = 1.79$) and W2016 (median: $z = 2.30$, mean: $z = 2.57$) samples are indicated in the inset with maroon and gray lines, respectively. *Right panel:* the luminosity distance d_L of 26 *Fermi* GRBs in Λ CDM cosmology with standard parameters vs. redshift. The upper x -axis shows the time (Gyr) since the Big Bang.

of these GRBs have been obtained from various GCN notices and published papers, as noted in Tab. 6.2. In addition to the *Fermi* GRB sample, we also use a sample of 94 GRBs from Wang et al. (2016), hereafter W2016, for comparisons. These 94 GRBs have been selected from 151 GRBs analyzed by Wang et al. (2016), and which are not in our *Fermi* GRB sample or counted twice. We update the relevant GRB parameters of the W2016 sample using the latest cosmological model (see App. B.5). In particular, unless otherwise stated, we have adopted Λ CDM cosmology

with standard parameters (Riess et al., 2018; Planck Collaboration et al., 2018), the dark-energy density, $\Omega_\Lambda = 0.714$, total density of baryonic and dark matter, $\Omega_m = 0.286$, the Hubble parameter $H_0 = 69.6 \text{ km s}^{-1} \text{ Mpc}^{-1}$ and a spatially flat universe.

In Fig. 6.1 we show the redshift distribution of our *Fermi* GRB sample and that of W2016. Unlike the redshift of GRBs peaking at ≈ 1.5 for the W2016 sample, *Fermi* GRBs are rather uniformly distributed in redshift and are comparatively closer. This could be due to a selection effect and to the smaller size of the *Fermi* sample. The bottom panel of Fig. 6.1 shows the luminosity distances of *Fermi* GRBs with standard parameters of the Λ CDM cosmology. The closest one is GRB 130427A at $z = 0.3399$.

6.2.2 *Fermi* data preparation

We have implemented the criteria in Guiriec et al. (2011) for GBM detector selection for *Fermi* data, as discussed below. We used the RMFIT to simultaneously fit the spectral data of GBM NaI detectors that have incidence angle smaller than 50° . In order to subtract background in GBM data, we fitted a second-order polynomial to data collected from two-time intervals selected before and after the prompt emission. Then, this background model has been interpolated across the source selection time interval (see Sec. §3.6.1). We have also used the standard 128 energy bins of the CSPEC data-type, for NaI using the channels from 8 keV to 900 keV by cutting out the overflow of high-energy channels, as well as the Iodine K-edge from ~ 30 to ~ 40 keV (Meegan et al., 2009). For the GBM BGO detectors, we have used data from ~ 220 keV to ~ 40 MeV and from ~ 210 keV to ~ 40 MeV, respectively, for detectors b0 and b1 (Yu et al., 2016). We use 2 BGO detectors when the source angle is less than 100° for both and in addition, NaI detectors from both the 0–5 and 6–11 groups are triggered. The detectors selected for each GRB are listed in Table 6.1.

For the analysis of LAT data, we have selected the Pass 8 Transient event class (Transient20E) within a 10° region of interest (RoI). The data is binned in 30 logarithmic energy steps between 30 MeV–300 GeV. Since we have considered energies below 100 MeV, the gtlike tool was used to perform a binned maximum-likelihood analysis that includes a correction for the energy dispersion effect. It is strongly recommended by the *Fermi* group to take into account the energy dispersion in the case of a binned maximum-likelihood analysis as discussed in Sec. §3.2. We derive the detector response matrix and the observed spectrum using the *Fermi* Science Tools gtrspgen and gtbin, respectively. To produce a background spectrum file, the background estimation tool gtbkg was used.

Table 6.1 *Fermi* sample of 25 LGRBs and 1 SGRB with selected detectors and results from the spectral model fits of Time-integrated Flux within T_{90} .

GRB Name	Detectors	Model	$T_{05} - T_{95}$ (s)	α, γ	β	E_p, E_0 (keV)	kT (keV)	α_1	C-Stat/dof ^(*)
GRB 170405A	n6+n7+n9+nb+b1+LAT	Band	7.36-86.08	-0.84 ± 0.01	-2.44 ± 0.02	315.8 ± 7.78			1544.1/588
GRB 170214A	n0+n1+n3+b0+LAT	SBPL+BB	12.54-135.49	-1.17 ± 0.02	-2.51 ± 0.01	507.7 ± 34.9	41.99 ± 1.28		1253.7/368
GRB 160625B	n7+n9+b1+LAT	Band+BB+PL	188.45-650.54	-0.40 ± 0.06	-2.70 ± 0.02	642.92 ± 15.48	27.94 ± 1.09	-2.16 ± 0.04	1462.9/354
GRB 160509A	n0+n1+n3+b0+LAT	Band+CPL+PL	7.68-379.4	-0.87 ± 0.08	-5.16 ± 0.49	8591.48 ± 68.27			
				-0.79 ± 0.04		317.14 ± 16.60		-1.76 ± 0.10	1741.9/474
GRB 150514A	n3+n6+n7+b0+LAT	Band	0.00-10.8	-1.45 ± 0.08	-2.33 ± 0.05	76.28 ± 8.26			590.57/472
GRB 150403A	n3+n4+b0+LLE	Band+BB	3.33-25.60	-1.02 ± 0.02	-2.95 ± 0.10	793.63 ± 52.55	33.30 ± 1.58		524.75/358
GRB 150314A	n0+nna+n1+n9+b1+LAT	Band	0.6-11.29	-0.63 ± 0.01	-3.02 ± 0.10	357.38 ± 4.78			1333.0/588
GRB 141028A	n6+n7+n9+b1+LAT	Band	6.66-38.16	-0.91 ± 0.02	-2.37 ± 0.02	396.45 ± 15.29			691.79/473
GRB 131231A	n0+n3+n7+b0+LAT	Band	13.31-44.31	-1.23 ± 0.01	-2.65 ± 0.03	225.17 ± 3.02			1665.0/476
GRB 131108A	n0+n3+n6+n7+b0+b1+LAT	SBPL	0.32 - 19.32	-0.99 ± 0.02	-2.23 ± 0.01	205.32 ± 6.91			950.58/716
GRB 130518A	n3+n6+n7+b0+b1+LAT	Band	9.9-57.9	-0.89 ± 0.01	-2.71 ± 0.03	458.85 ± 9.22			1357.1/592
GRB 130427A	n6+n9+na+b1+LAT	Band+PL	11.23-142.34	-1.41 ± 0.01	-2.27 ± 0.01	219.61 ± 4.38		-1.22 ± 0.21	2105.1/488
GRB 120624B	n1+n2+na+b0+b1+LAT	SBPL	-258.05-13.31	-1.04 ± 0.01	-2.78 ± 0.04	352.9 ± 11.4			2015.7/588
GRB 110721A	n6+n7+n9+b1+n11+LAT	Band+BB	0.45 - 24.9	-1.24 ± 0.01	-2.89 ± 0.06	1923.0 ± 189.0	34.05 ± 1.58		770.32/586
GRB 109028A	n0+n1+n2+n5+b0+LAT	Band	13.25-178.75	-0.52 ± 0.02	-2.63 ± 0.04	310.7 ± 7.06			3075.3/595
GRB 100414A	n7+n9+n11+b1+LAT	Band	2.0 - 28.4	-0.50 ± 0.02	-2.91 ± 0.06	578.89 ± 11.69			750.82/469
GRB 091208B	n10+n9+b1+LAT	Band	0.26 - 15.26	-1.29 ± 0.07	-2.53 ± 0.12	98.22 ± 9.74			422.09/351
GRB 091127	n6+n7+n9+b1+LAT	SBPL	0.00-7.80	-1.42 ± 0.05	-2.33 ± 0.02	33.10 ± 2.38			731.85/479
GRB 091003A	n0+n3+n6+b0+b1+LAT	Band	1.09 - 22.19	-1.08 ± 0.01	-2.79 ± 0.05	452.21 ± 17.44			674.54/600
GRB 090926A	n6+n7+n8+b1+LAT	Band+PL	2.05-22.05	-0.66 ± 0.03	-2.34 ± 0.02	279.60 ± 4.51		-1.82 ± 0.03	918.19/476
GRB 090902B	n0+n2+n9+b0+b1+LAT	Band+PL	0.22	-0.53 ± 0.01	-4.14 ± 0.28	760.66 ± 7.69		-1.92 ± 0.01	1320.6/601
GRB 090510	n3+n6+n7+n9+b0+b1+LAT	Band+PL	0.002-1.744	-0.63 ± 0.08	-2.57 ± 0.08	3805.0 ± 385.0		-1.60 ± 0.03	756.57/717
GRB 090424	n7+n8+nb+b1+LAT	Band	0.448-14.720	-0.83 ± 0.02	-2.49 ± 0.04	153.4 ± 2.91			857.75/474
GRB 090328	n7+n8+b1+LAT	Band	4.67-61.67	-1.04 ± 0.02	-2.37 ± 0.04	703.75 ± 47.16			769.08/360
GRB 090323	n6+n7+n9+n11+b1+LAT	SBPL	-1.0 - 173	-1.29 ± 0.01	-2.50 ± 0.02	399.44 ± 17.17			1558.6/597
GRB 080916C	n3+n4+b0+LAT	Band+BB	0 - 66	-1.27 ± 0.03	-2.28 ± 0.03	1297.0 ± 222.0	46.78 ± 1.93		536.28/362

Notes: α and β are the lower and higher photon indices for the Band and SBPL functions, respectively. γ is the photon index of the Comp model, while α_1 is that of the PL. E_0 is the SBPL e-folding energy and E_p is the Band or Comp peak energy. kT is the BB temperature. The C-Stat/dof^(*) is the ratio of the C-stat resulting from the fit and the associated degrees of freedom (dof). The row marked in bold represents a value of short GRB 090510.

6.3 Spectral analysis

6.3.1 Spectral fitting

We have performed a spectral analysis over the T_{90} duration, namely using the time-integrated data. Subsequently, we have run RMFIT with the following phenomenological models which are widely used: the Band function (as in Eq. 2.1, Band et al., 1993), SBPL (as in Eq. 2.3, Ryde, 1999), and Comp (see, e.g., Kaneko et al., 2006, defined in Eq. 2.2), which is an exponentially cut-off power-law. We have also studied spectral deviation from these models in the form of Band or SBPL combined with single power-law (PL) and/or blackbody (BB) components. The details of the functional forms of these models are described in Sec. §2.6.2. Like the Cash-statistic, the C-stat is suitable for the analysis of counts that are Poisson distributed¹. It has been proposed to mimic a χ^2 statistic and to provide straightforward goodness of fit in the large sample limit. Assuming that the C-stat is χ^2 distributed in the low count regime only provides an approximate judgment of the fit quality. Like the Cash-statistic, the C-stat can also be used to perform hypothesis testing

¹<https://heasarc.nasa.gov/docs/xanadu/xspec/xspec11/manual/node57.html>

between two nested models. Following the Wilks' theorem (Wilks, 1938), and again assuming that the large sample limit is reached, we decide that a new spectral component (BB or PL, which both have two parameters) is required by the data in addition to the main component (Band, SBPL, or Comp, chosen from the model with the lowest C-stat value) if they cause a decrease in C-stat that is larger than 25 (i.e. approximately 5σ for a χ^2 with 2 degrees of freedom) (Axelsson et al., 2012). We use the same criterion to compare the Band+BB and Band+BB+PL models, or the Band+CPL and Band+Comp+PL models. The spectral parameters obtained from the best-fit models along with the C-stat values (see Sec. §3.6.1) are presented in Tab. 6.1. Often the brighter GRBs require more complex models such as SBPL + BB, Band + BB, Band + Comp + PL; etc., for fitting their spectra. Fig. 6.2 shows the νF_ν energy spectrum using the best-fit spectral models for each GRB in Tab. 6.1. The top left panel shows the spectra fitted with Band or Band + BB and the top right panel shows the spectra fitted with SBPL or SBPL + BB. The bottom left panel shows GRB 160625B spectrum fitted with Band + BB + PL and GRB 160509A spectrum fitted with Band + Comp + PL. The bottom right panel shows the spectra of GRB 130427A, and GRB 090902B, both fitted with Band + PL. The shaded regions correspond to the 1σ confidence intervals of the models.

6.3.2 Isotropic energy calculation

It has been empirically established that the most important intrinsic parameters (not directly observables), like the total radiated energy, is derived from more than one observed parameters. For GRBs with reliable redshift and measured spectrum we can compute the isotropic radiated energy E_{iso} (Eq. 4.25) at a luminosity distance d_L (Eq. 4.27) as

$$E_{\text{iso}} = \frac{4\pi d_L^2}{1+z} S_{\text{bolo}}, \quad (6.1)$$

where

$$S_{\text{bolo}} = T_{90} \int_{E_{\min}/(1+z)}^{E_{\max}/(1+z)} EN_i(E) dE, \quad (6.2)$$

is the bolometric fluence integrated over the minimum photon energy $E_{\min} = 1$ keV and the maximum photon energy $E_{\max} = 10^4$ keV or 10^5 keV. Here, $N_i(E)$ represents the best-fit spectral model discussed previously. The luminosity distance used to compute the E_{iso} is strongly depends on the cosmological model. The results of S_{bolo} and E_{iso} are reported in Tab. 6.2. The values of $S_{\text{bolo}}^*(\text{F10})$ and $E_{\text{iso}}^*(\text{F10})$ correspond to the energy interval $1\text{--}10^4$ keV, while the values of $S_{\text{bolo}}^*(\text{F100})$ and $E_{\text{iso}}^*(\text{F100})$ correspond to the energy interval $1\text{--}10^5$ keV. The intrinsic peak energies of the νF_ν spectra are reported as $E_{i,p}$ in Tab. 6.2. In all cases, $E_{i,p} = E_p(1+z)$.

We have used Monte Carlo simulations to estimate the value of S_{bolo} and the error on it. In particular, we assume the parameters of the spectral models follow a multivariate Gaussian function (see App. C.3). Using the RMFIT, the GRB spectral fitting provides a normalization covariance matrix (i.e., the correlation coefficient matrix, ρ_{ij} between two variables i and j)

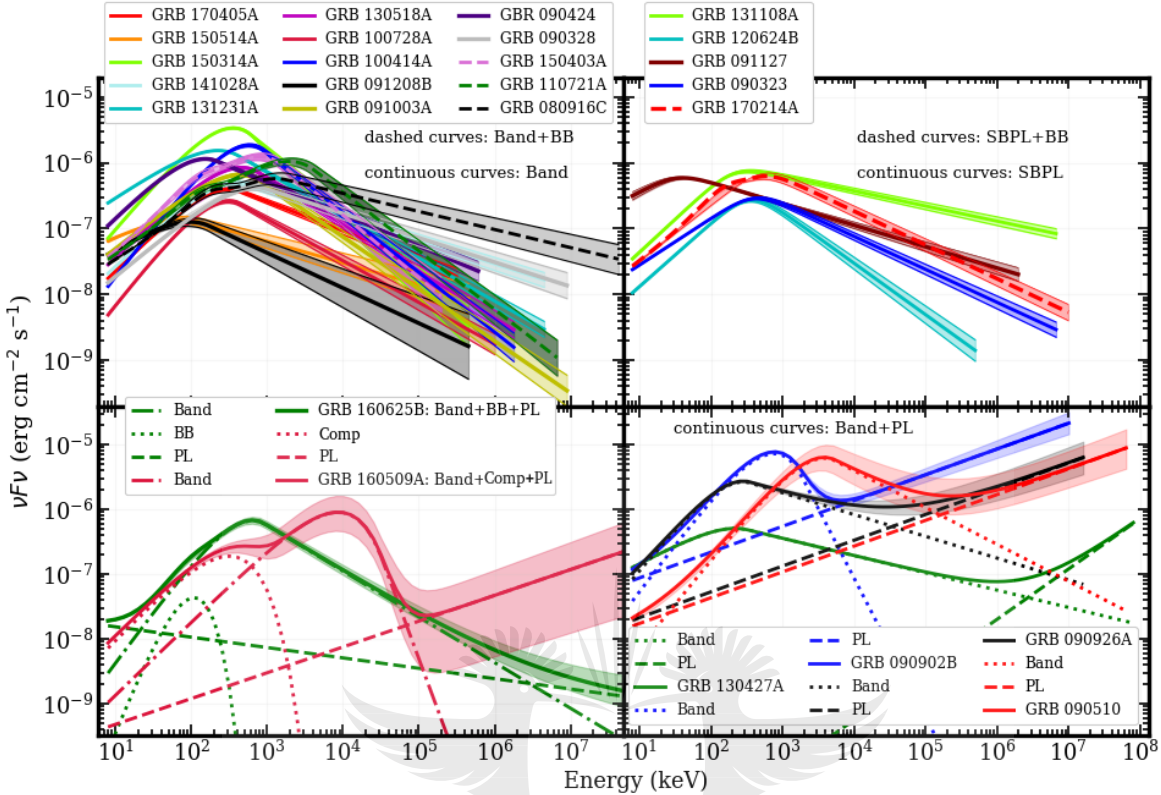


Figure 6.2 νF_ν spectra of *Fermi*-LAT/GBM GRBs with known redshift resulting from the time-integrated spectral analysis over the T_{90} duration. The top left panel shows the Band or Band + BB model fits, while the top right panel shows SBPL or SBPL + BB model fits. The bottom panels show more complex models along with their components. The 1σ confidence regions of the models are shown with shades of the same color as the model lines.

defined in App. C.5) as a form of symmetric array given in App. (C.6). Then, the covariance matrix in terms of the correlation is given in App. (C.7). Performing these covariance matrix obtained from the spectral fit, we generate 10,000 sets of random values for each of the parameters to calculate S_{bolo} (see Eq. 6.2). We select 68.27% confidence intervals from the resulting distribution of S_{bolo} values to evaluate its error. Thus, the value of E_{iso} (Eq. 4.25) and its error can be computed from the obtained values. In Fig. 6.3, we show an example of the output of this simulation with the parameters obtained from the Band spectral fitting model of GRB 150514A. In each of the panels, the distribution was built from 10,000 spectra and in the bottom two panels, we used them to compute 68.27% error confidence intervals around the maximum probability value. Similarity, we computed the S_{bolo} and its errors for the other 25 GRBs, which are listed in Tab. 6.2.

Figure 6.4 shows the distributions of bolometric fluence, isotropically radiated energy and peak energy of the νF_ν spectra of *Fermi* GRBs and those in the W2016 sample. There are small differences between the bolometric fluence S_{bolo}^* (F10) and S_{bolo}^* (F100) for the *Fermi* sample (green

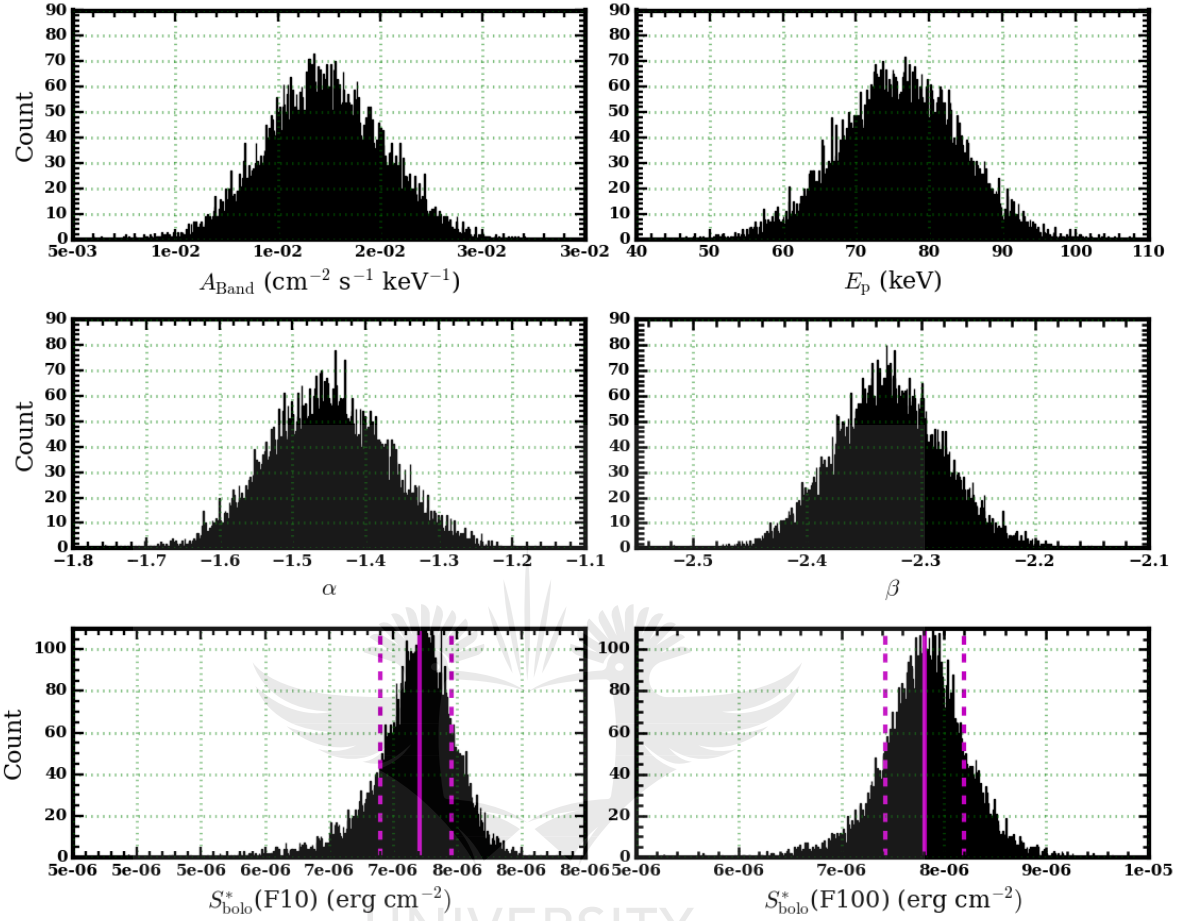


Figure 6.3 The top four panels show the distribution of the parameters from the simulated 10,000 spectra that obtained from the best-fit Band model of GRB 150514A. $S_{\text{bolo}}^*(\text{F10})$ and $S_{\text{bolo}}^*(\text{F100})$ are the bolometric fluences corresponding to the energy interval $1-10^4$ keV and $1-10^5$ keV, respectively. The results are presented in Tab. 6.2. The mean values represented as the solid vertical magenta lines and the 68.27% errors as the vertical broken magenta lines.

and red histograms, respectively, in the top-left panel), but both distributions peak at a higher fluence than the W2016 sample (gray histogram). The difference between F10 and F100 is due to high-energy emission in the *Fermi*-LAT range, often requiring additional spectral component(s). On the other hand, the difference between the *Fermi* and W2016 samples indicates that the GRBs detected by *Fermi*-LAT are more fluent. Similar conclusions can be drawn for the isotropic energy distributions (top-right panel), although the difference between the *Fermi* and W2016 samples is less dramatic. The distributions of the E_p (bottom-left panel) and $E_{i,p}$ (bottom-right panel), also indicate higher values for the *Fermi* sample compared to W2016.

Table 6.2 Intrinsic Peak Energy, $E_{\text{i,p}}$, and Isotropic radiated Energy, E_{iso} , for the *Fermi* GRB sample.

GRB Name	z	$E_{\text{i,p}}$ (keV)	$E_{\text{iso}}^*(\text{F10})$ (10^{52} erg)	$S_{\text{bolo}}^*(\text{F10})$ (10^{-5} erg cm $^{-2}$)	$\mu \pm \sigma_{\mu}^{\dagger}$	$E_{\text{iso}}^*(\text{F100})$ (10^{52} erg)	$S_{\text{bolo}}^*(\text{F100})$ (10^{-5} erg cm $^{-2}$)	$\mu \pm \sigma_{\mu}^{\ddagger}$	References for Redshift
GRB 170405A	3.51	1424.42 \pm 35.24	240.00 \pm 2.41	9.24 \pm 0.09	46.22 \pm 1.27	293.00 \pm 4.87	11.28 \pm 0.19	46.19 \pm 1.20	de Ugarte Postigo et al. (2017a)
GRB 170214A	2.53	2119.788 \pm 119.06	338.00 \pm 4.36	22.40 \pm 0.29	45.49 \pm 1.30	425.00 \pm 6.10	28.22 \pm 0.40	45.47 \pm 1.21	Kruhler et al. (2017)
GRB 160625B	1.406	1546.86 \pm 37.25	435.01 \pm 6.06	83.54 \pm 1.16	43.25 \pm 1.27	494.13 \pm 7.34	94.87 \pm 1.42	43.31 \pm 1.20	Xu et al. (2016)
GRB 160509A	1.17	19334.10 \pm 652.25	182.68 \pm 4.97	49.91 \pm 1.36	46.89 \pm 1.67	364.81 \pm 13.81	99.73 \pm 3.79	46.57 \pm 1.26	Tanvir et al. (2016)
GRB 150514A	0.807	137.84 \pm 14.93	1.26 \pm 0.05	0.71 \pm 0.03	45.05 \pm 1.45	1.37 \pm 0.07	0.78 \pm 0.04	44.92 \pm 1.23	de Ugarte Postigo et al. (2015c)
GRB 150403A	2.06	2428.51 \pm 160.80	85.20 \pm 1.81	8.10 \pm 0.17	46.61 \pm 1.31	95.30 \pm 2.72	9.06 \pm 0.27	46.73 \pm 1.21	Pugliese et al. (2015)
GRB 150314A	1.758	985.66 \pm 13.20	72.70 \pm 0.96	9.20 \pm 0.12	45.22 \pm 1.26	76.00 \pm 1.72	9.61 \pm 0.22	45.33 \pm 1.20	de Ugarte Postigo et al. (2015b)
GRB 141028A	2.33	1320.18 \pm 50.90	64.00 \pm 0.74	4.89 \pm 0.06	46.48 \pm 1.27	79.80 \pm 1.24	6.10 \pm 0.09	46.42 \pm 1.20	Xu et al. (2014)
GRB 131231A	0.6439	370.15 \pm 4.97	19.20 \pm 0.13	17.42 \pm 0.12	42.73 \pm 1.31	20.10 \pm 0.20	18.23 \pm 0.18	42.74 \pm 1.21	Cucchiara (2014)
GRB 131108A	2.40	1163.20 \pm 28.54	66.80 \pm 0.65	4.85 \pm 0.05	46.35 \pm 1.26	89.90 \pm 1.19	6.53 \pm 0.09	46.20 \pm 1.20	de Ugarte Postigo et al. (2013c)
GRB 130518A	2.49	1601.40 \pm 32.19	167.00 \pm 1.53	11.40 \pm 0.11	45.86 \pm 1.27	189.00 \pm 2.48	12.92 \pm 0.17	45.92 \pm 1.21	Sanchez-Ramirez et al. (2013)
GRB 130427A	0.3399	294.25 \pm 5.86	9.29 \pm 0.06	31.72 \pm 0.20	41.56 \pm 1.33	10.65 \pm 0.12	36.34 \pm 0.39	41.46 \pm 1.21	Levan et al. (2013)
GRB 120624B	2.2	1214.47 \pm 26.24	242.00 \pm 2.95	20.49 \pm 0.25	44.78 \pm 1.26	267.00 \pm 4.65	22.63 \pm 0.39	44.85 \pm 1.20	de Ugarte Postigo et al. (2013a)
GRB 110721A	3.512	8675.78 \pm 852.66	160.0 \pm 2.33	6.14 \pm 0.09	48.94 \pm 1.50	243.00 \pm 9.35	9.35 \pm 0.34	48.85 \pm 1.24	Berger (2011)
GRB 100728A	1.567	797.62 \pm 18.05	75.00 \pm 1.06	11.74 \pm 0.17	44.61 \pm 1.26	82.50 \pm 1.74	12.92 \pm 0.27	44.64 \pm 1.20	Kruhler et al. (2010)
GRB 100414A	1.368	1370.82 \pm 27.68	58.70 \pm 0.77	11.88 \pm 0.16	45.19 \pm 1.27	63.50 \pm 1.24	12.86 \pm 0.25	45.30 \pm 1.20	Cucchiara (2010)
GRB 091208B	1.063	202.63 \pm 20.10	2.26 \pm 0.12	0.75 \pm 0.04	45.63 \pm 1.39	2.37 \pm 0.17	0.78 \pm 0.06	45.59 \pm 1.23	Wiersema et al. (2009)
GRB 091127	0.49	60.32 \pm 1.93	1.41 \pm 0.02	2.25 \pm 0.04	42.55 \pm 1.61	1.52 \pm 0.03	2.42 \pm 0.05	42.36 \pm 1.25	Cucchiara et al. (2009c)
GRB 091003A	0.8969	857.81 \pm 33.08	9.58 \pm 0.16	4.43 \pm 0.08	45.43 \pm 1.26	10.20 \pm 0.21	4.70 \pm 0.10	45.51 \pm 1.20	Cucchiara et al. (2009b)
GRB 090926A	2.1062	868.63 \pm 13.85	196.00 \pm 1.39	17.90 \pm 0.13	44.47 \pm 1.26	246.00 \pm 3.26	22.43 \pm 0.30	44.37 \pm 1.20	Malesani et al. (2009)
GRB 090902B	1.822	2146.57 \pm 21.71	329.00 \pm 1.87	39.05 \pm 0.22	44.66 \pm 1.29	349.00 \pm 3.85	41.45 \pm 0.40	44.83 \pm 1.21	Cucchiara et al. (2009a)
GRB 090510	0.903	7227.15 \pm 731.88	4.15 \pm 0.18	1.89 \pm 0.08	-	7.19 \pm 0.34	3.28 \pm 0.16	-	Rau et al. (2009)
GRB 090424	0.544	236.91 \pm 4.55	4.45 \pm 0.07	5.72 \pm 0.09	43.30 \pm 1.36	4.77 \pm 0.12	6.13 \pm 0.15	43.25 \pm 1.21	Chornock et al. (2009c)
GRB 090328	0.736	1221.71 \pm 81.87	11.60 \pm 0.29	7.99 \pm 0.20	45.14 \pm 1.27	14.20 \pm 0.45	9.82 \pm 0.31	45.10 \pm 1.21	Cenko et al. (2009b)
GRB 090323	3.57	2060.09 \pm 138.07	430.00 \pm 10.40	15.76 \pm 0.39	46.12 \pm 1.29	535.00 \pm 17.20	19.64 \pm 0.62	46.10 \pm 1.21	Chornock et al. (2009b)
GRB 080916C	4.35 \pm 0.15	6953.87 \pm 1188.77	380.00 \pm 8.61	10.40 \pm 0.24	48.28 \pm 1.47	605.00 \pm 24.80	16.54 \pm 0.68	48.11 \pm 1.25	Greiner et al. (2009)

Notes. The bolometric fluence $S_{\text{bolo}}^*(\text{F10})$ and isotropic energy $E_{\text{iso}}^*(\text{F10})$ are computed for the energy range 1-10⁴ keV using Eqs. (6.2) and (6.1). $S_{\text{bolo}}^*(\text{F100})$ and $E_{\text{iso}}^*(\text{F100})$ are computed for the energy range 1-10⁵ keV. $E_{\text{i,p}} = (1+z)E_{\text{p}}$ for the Band or Comp or SBPL spectral fits, with peak energy E_{p} .

6.4 Amati relation between E_{iso} and $E_{\text{i,p}}$

This section provides a brief review of the fitting model used in the Amati relation, which was originally derived under a given set of cosmological parameters. We also discuss a likelihood analysis to extract the best-fit values of the parameters including the extrinsic systematic σ_{ext} on E_{iso} , which is treated as an unknown parameter.

6.4.1 Fitted model

As outlined in Sec. §4.4.1, the PL form of the Amati relation (Amati et al., 2002) between E_{iso} and $E_{\text{i,p}}$ is given by

$$E_{\text{iso}} \propto \left(\frac{E_{\text{i,p}}}{E_0} \right)^m E_{0,\text{iso}}, \quad (6.3)$$

where E_0 and $E_{0,\text{iso}}$ are reference energies. This phenomenological relation might be used to make GRBs standard candles and use them for cosmology. A linearized Amati relation (Wang

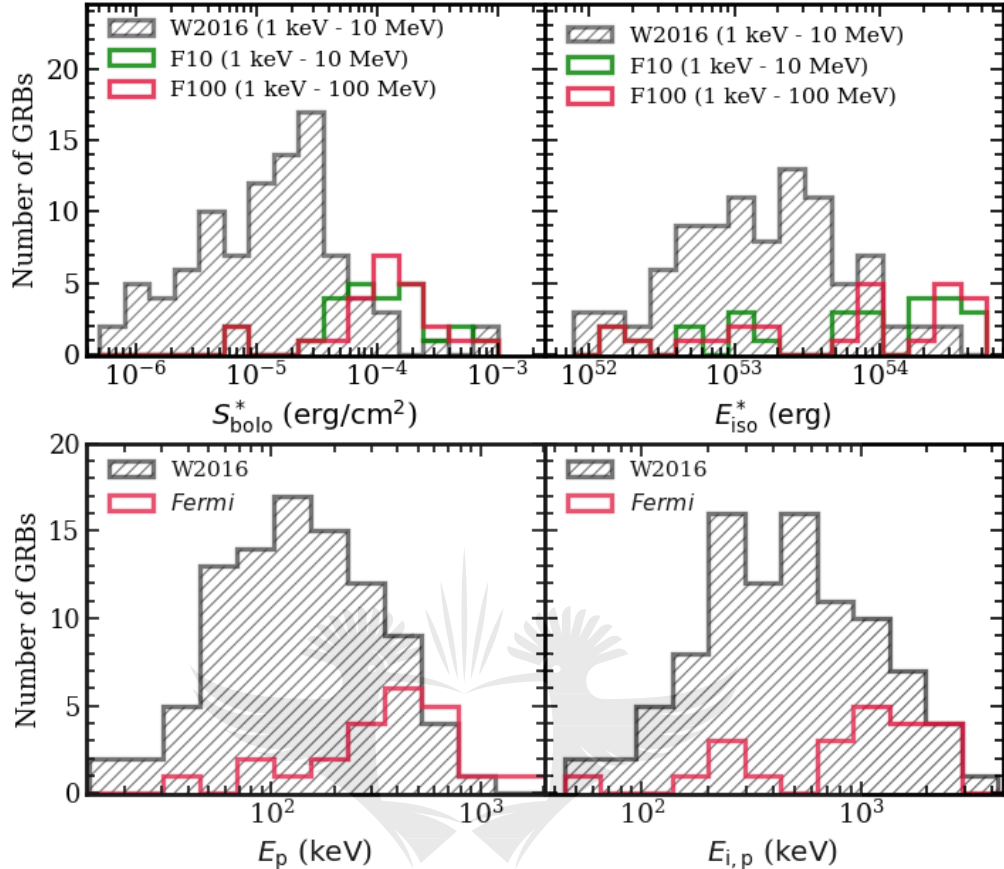


Figure 6.4 *Top panels:* distributions of bolometric fluence and isotropic energy of *Fermi* (F10, S_{bolo} and E_{iso} computed in the 1 keV–10 MeV energy range and F100, the same computed in the 1 keV–100 MeV energy range) and of W2016 samples. *Bottom panels:* distributions of the observed peak energy (left) and of intrinsic peak energy (right) for the *Fermi* and W2016 bursts.

et al., 2016; Demianski et al., 2017) can be written as

$$y = mx + k, \quad (6.4)$$

where

$$\begin{cases} y \equiv \log \frac{E_{\text{iso}}}{E_{0,\text{iso}}}, \\ x \equiv \log \frac{E_{i,p}}{E_0}. \end{cases} \quad (6.5)$$

However, in the work of Amati et al. (2008), the value of $y = \log(E_{i,p}/1\text{keV})$, thus the extrinsic scatter σ_{ext} does not contain the error that involve with the cosmological models. We use only LGRBs for Amati relations fits. A preliminary fit to the E_{iso}^* and $E_{i,p}$ data for the *Fermi* sample in Tab. 6.2 with $E_{0,\text{iso}} = 10^{52}$ erg and $E_0 = 100$ keV allows us to calculate the so-called “decorrelation”² value (see §4.4.3) of x at which the error on y is the smallest. This value can be

²https://fermi.gsfc.nasa.gov/ssc/data/analysis/scitools/python_tutorial.html

obtained from a simple error propagation in equation (6.4) as $x_{\text{dec}} = -C_{\text{km}}/\sigma_m^2$, where C_{km} is the co-variance of the parameters k and m , and σ_m is the error on m . The error on the value of y is the smallest at $x = x_{\text{dec}}$ as presented in Eq. (4.40). Setting E_0 at the decorrelation energy in the following analysis also ensures that the final value of the covariance C_{km} vanishes, which will allow us to discuss the results on the parameters m and k independently. Subsequently, we use the following decorrelation energy

$$E_{0,\text{dec}} = 10^{x_{\text{dec}}} 100 \text{ keV} \approx 950 \text{ keV}, \quad (6.6)$$

for our analysis of E_{iso}^* (F10). The value of $E_{0,\text{dec}}$ for E_{iso}^* (F100) data is also 950 keV. For the W2016 sample in Tab. B.5, however, this energy is 450 keV. We also calculate the decorrelation energy for the combined *Fermi* and W2016 data sets. Furthermore, the values of $E_{0,\text{dec}}$ for the analysis of high redshift samples of GRBs listed in Tab. 6.3.

6.4.2 Likelihood analysis

We have performed a likelihood analysis to extract not only the best-fit values of the parameters m and k in Eq. (6.4) but also the extrinsic uncertainty σ_{ext} on y , which is treated as an unknown parameter. This may account for hidden parameters related to the physical origin of the Amati relation. Following D'Agostini (2005) we apply the log likelihood function $-\ln \mathcal{L}(m, k, \sigma_{\text{ext}}) = L(m, k, \sigma_{\text{ext}})$ to fit the $x = \log(E_{\text{i,p}}/E_{0,\text{dec}})$ and $y = \log(E_{\text{iso}}/E_{0,\text{iso}})$ data with Eq. (6.4). The functional form is given in Eq. (4.31). We minimize function given in this equation to find the best-fit values of the parameters m , k and σ_{ext} . The obtained values are listed in Tab. 6.3 for the *Fermi* and W2016 samples, and for the combination of the two. To compute the errors of a fit parameter, as in Demianski & Piedipalumbo (2011), we evaluate the marginalized likelihood function in 4.31 by integrating over other parameters. The 68.27% confidence interval of the parameter is then found by solving the integral (D'Agostini, 2005) given in Eq. (4.33).

Fig. 6.5 shows the Amati relation plotted against the *Fermi* and W2016 data samples. As for comparisons of our fit parameters with those by other recent studies, Wang et al. (2016) found $m = 1.48 \pm 0.09$ and $\sigma_{\text{ext}} = 0.34 \pm 0.01$ from 151 GRBs. Similarly, Demianski & Piedipalumbo (2011) found $m = 1.52$ and $\sigma_{\text{ext}} = 0.41$ by analyzing 109 GRBs. The results of our fit to the linearized Amati relation are shown in Figs. 6.5 and 6.6, and are listed in Tab. 6.3. The shaded region in Figs. 6.5 and 6.6 shows the $\pm 1\sigma_y$ uncertainties on the Amati relation. We have fitted data from the 25 *Fermi* LGRBs (F10 and F100 samples in the top left and right panels of Fig. 6.5, respectively), the W2016 sample of 94 GRBs (bottom left panel of Fig. 6.5) and a combination of the F10 and W2016 samples (bottom right panel of Fig. 6.5). Interestingly, the values of the parameters m , k and σ_{ext} for the F10 and F100 samples are comparable (see Tab. 6.3). In particular, similar results are obtained for the slope parameter m and for the extrinsic error σ_{ext} . However, there is a noticeable difference for the parameter k between the F10 or F100 sample and the W2016 or F10+W2016 sample. This difference can be accounted for when considering the value of the

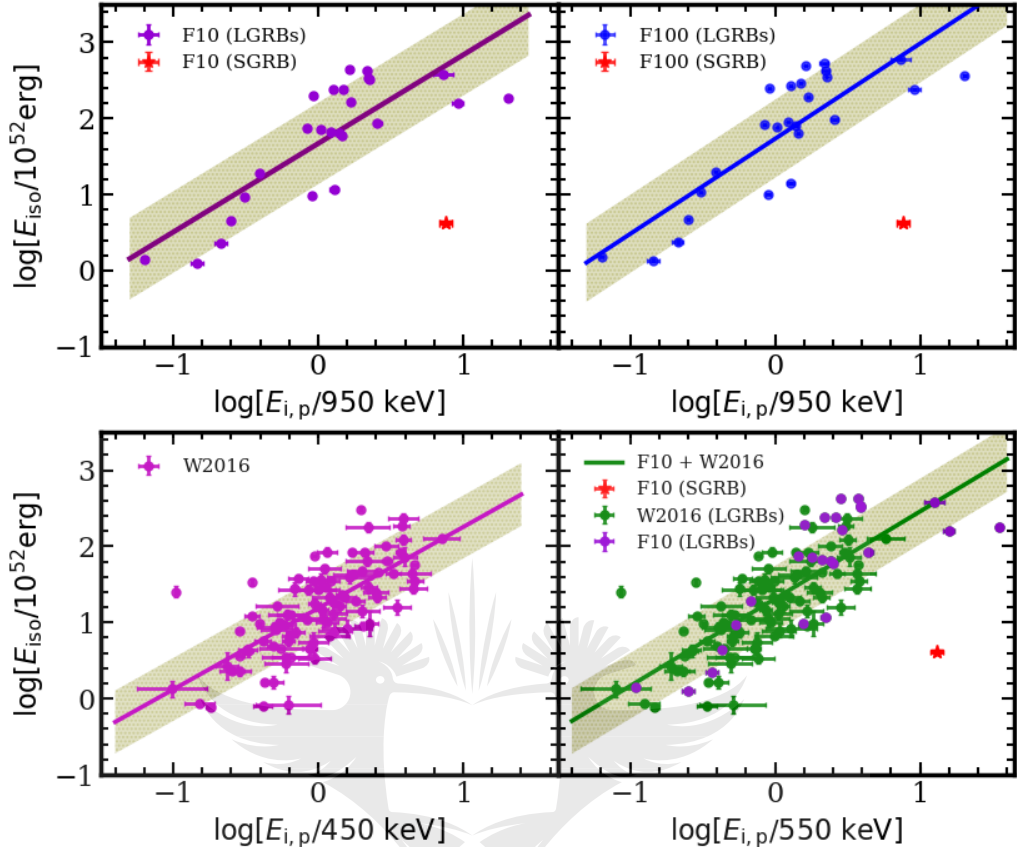


Figure 6.5 Amati relation fits (solid lines) to different data samples in the $\log E_{\text{iso}} - \log E_{i,p}$ plane. The shaded regions correspond to 1σ scatter. *Top left panel:* *Fermi* 25 LGRBs with E_{iso}^* (F10) computed in the 1 keV–10 MeV energy range. *Top right panel:* *Fermi* 25 LGRBs with E_{iso}^* (F100) computed in the 1 keV–100 MeV energy range. *Bottom left panel:* 94 LGRBs in the W2016 sample. *Bottom right panel:* joint fit to the *Fermi* F10 and W2016 data reported in Tab. 6.3.

Table 6.3 The best-fit parameters of the Amati relation fits to the full samples of GRBs and GRBs with redshift $z > 1.414$. $\rho_{E_{i,p}, E_{\text{iso}}, z}$ is the partial correlation coefficient (see Eq. 5.11).

Full LGRB Samples	No. of GRBs	$\rho_{E_{i,p}, E_{\text{iso}}, z}$	$E_{0,\text{dec}}$ (keV)	m	k	σ_{ext}
F10	25	0.65	950	1.16 ± 0.37	1.67 ± 0.16	0.47 ± 0.12
F100	25	0.70	950	1.25 ± 0.33	1.73 ± 0.18	0.45 ± 0.13
W2016	94	0.71	450	1.07 ± 0.20	1.19 ± 0.08	0.38 ± 0.06
F10+W2016	119	0.77	550	1.15 ± 0.16	1.31 ± 0.07	0.41 ± 0.05
$z > 1.414$ Samples						
F10	14	0.10	1500	0.40 ± 0.63	2.19 ± 0.13	0.26 ± 0.09
W2016	84	0.71	500	1.02 ± 0.17	1.22 ± 0.07	0.37 ± 0.05
F10+W2016	98	0.77	550	1.13 ± 0.17	1.37 ± 0.08	0.38 ± 0.05

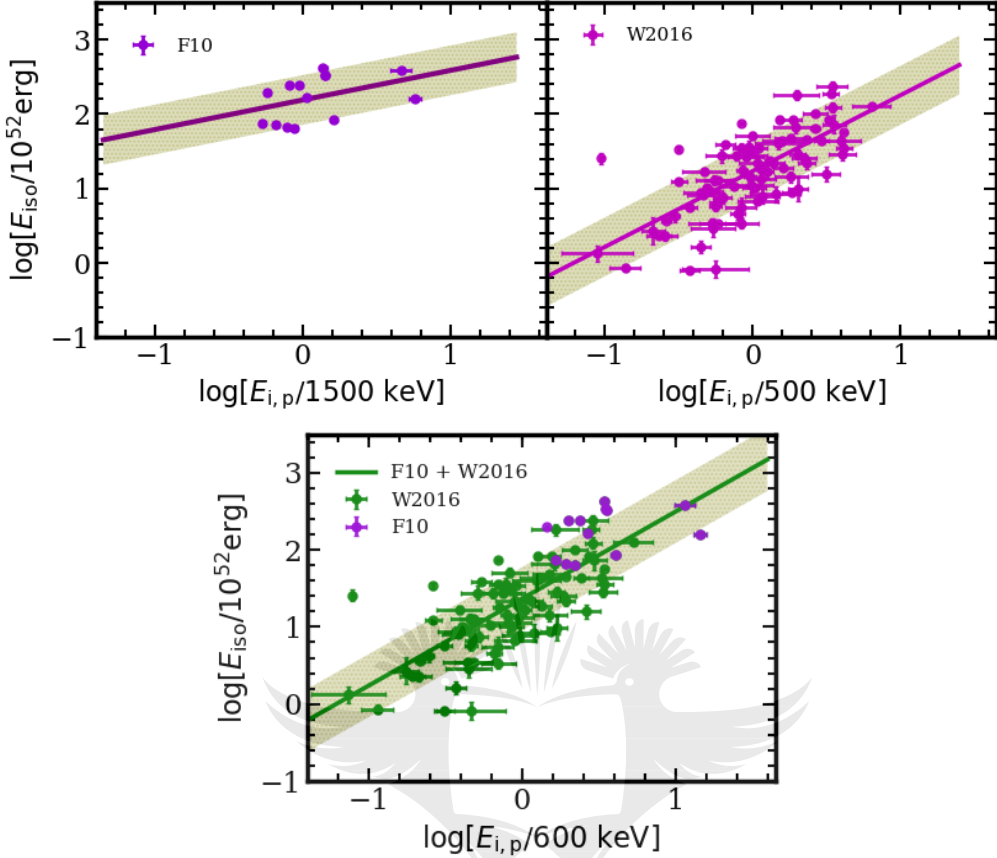


Figure 6.6 Amati relation fits (solid lines) to different data samples with redshift > 1.414 in the $\log E_{\text{iso}} - \log E_{\text{i,p}}$ plane. The sample descriptions are the same as in Fig. 6.5.

extrinsic parameter σ_{ext} . Tab. 6.3 also lists the decorrelation energy $E_{0,\text{dec}}$ for each sample and their combination, as well as partial correlation coefficient between $E_{\text{i,p}}$ and E_{iso} . Analysis for the full data set provides a partial correlation coefficient (ρ) of 0.65 and 0.70 for samples F10 and F100, respectively, which are highly significant.

We have also studied the Amati relation for GRBs with redshift $z > 1.414$, i.e., beyond the measured redshift of the supernovae data sample SNe U2.1 used for cosmology (Suzuki et al., 2012). This redshift cut leaves 14 *Fermi* LGRBs and 85 W2016 LGRBs for analysis. The results of the fits are shown in Fig. 6.6 and are listed in Tab. 6.3. Mainly, the *Fermi* GRBs have high E_{iso} and $E_{\text{i,p}}$ values than the W2016 sample as shown in the bottom panel of Fig. 6.6. The reduced F10 sample itself does not provide significant constraints on the fit parameter m and the corresponding partial correlation coefficient is also not significant. On the other hand, the combination of the reduced F10 and W2016 samples gives the parameter values similar to those obtained from fitting all LGRBs. The partial correlation coefficient is also very high in this case. The reduced W2016 sample itself gives similar results as the full W2016 sample.

6.5 The Hubble diagram and constraints on cosmological parameters

Once the parameters are obtained by fitting the linearized Amati relation (Sec. §6.4), we can use the LGRBs as cosmological probes. In particular, we can invert the relation in Eq. (6.1) to obtain the luminosity distance d_L (Eq. 4.44) and determine the distance modulus as a function of the redshift, $\mu(z) = 5 \log(d_L/\text{Mpc}) + 25$. Using Eqs. 4.46 and 4.47, we can estimate the measurement error on μ given by,

$$\sigma_\mu(z) = \left[\frac{25}{4} \left\{ \left(\sigma_m \log \frac{E_{i,p}}{E_{0,\text{dec}}} \right)^2 + \left(\frac{m}{\ln 10} \frac{\sigma_{E_{i,p}}}{E_{i,p}} \right)^2 + \sigma_k^2 + \sigma_{\text{ext}}^2 \right\} + \left(\frac{5}{2 \ln 10} \frac{\sigma_{S_{\text{bolo}}}}{S_{\text{bolo}}} \right)^2 \right]^{1/2}.$$

We use the Amati relation parameters from Tab. 6.3 in Eq. (4.30) to calculate the uncertainty of the distance modulus. The best-fit density parameter Ω_Λ and Hubble parameter H_0 are estimated by the minimization of the χ^2 expression given in Eq. 4.52.

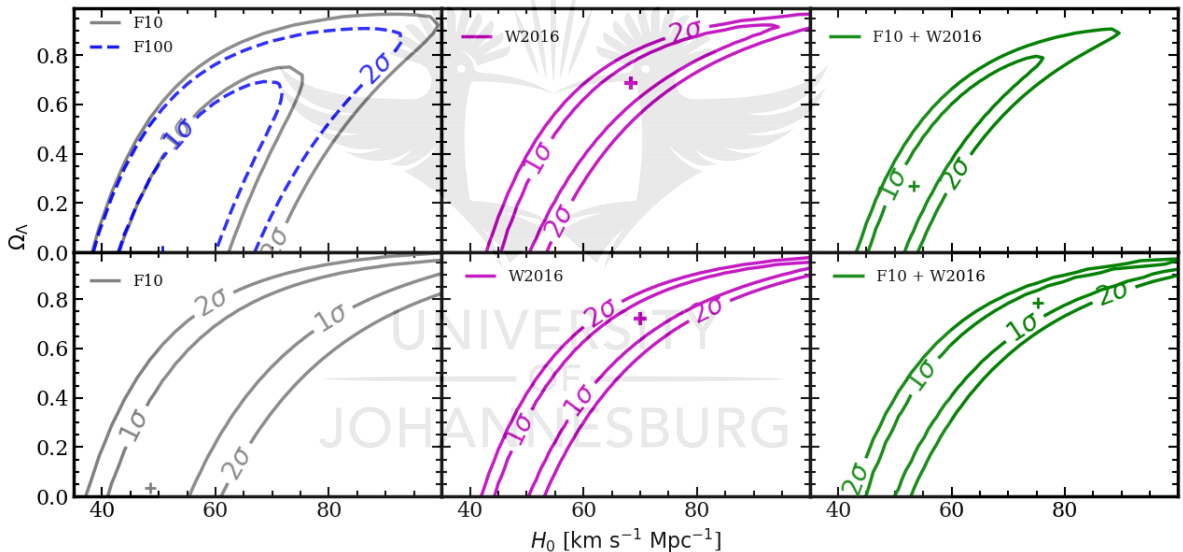


Figure 6.7 Constraints on the cosmological parameters H_0 and Ω_Λ from the Amati relation for different samples of LGRBs. The top and bottom panels correspond to the samples with all redshifts and with redshifts > 1.414 , respectively. The 1σ and 2σ confidence level contours are determined by following $\Delta\chi^2 \equiv \chi^2 - \chi^2_{\min} \leq 2.30$ and 6.18 , respectively. The plus sign indicates the best-fit location.

The results from our analysis are listed in Tab. 6.4, giving the best-fit values of H_0 and Ω_Λ when it is possible to constrain those parameters. Fig. 6.7 shows 1σ and 2σ contours in the $H_0 - \Omega_\Lambda$ plane for different sample selections. We note that F10 and F100 samples by themselves cannot constrain Ω_Λ (Fig. 6.7 top left panel). The size of the W2016 sample is larger and corresponds to a wider range in redshift (see the top panel of Fig. 6.1). Since the Ω_Λ parameter determines the evolution of the luminosity distance with redshift (see Eq. 4.27), this sample provides better

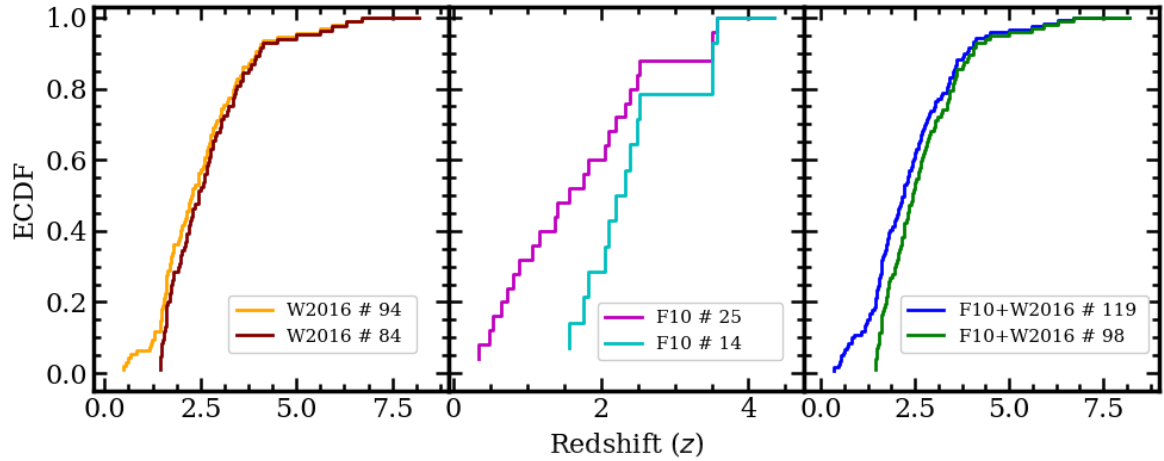


Figure 6.8 *Left panel:* the empirical cumulative distribution functions (ECDF) of the W2016 full sample and W2016 ($z > 1.414$) are indicated in the inset with orange and maroon lines, respectively (K-S Test: $D = 0.11$, p-value = 0.67). *Middle panel:* ECDF plot showing expression differences for F10 full sample comparing the F10 ($z > 1.414$) sample (K-S Test: $D = 0.44$, p-value = 0.04). *Right panel:* the ECDF of the F10+W2016 full sample and F10+W2016 ($z > 1.414$) are indicated in the inset with blue and green lines, respectively (K-S Test: $D = 0.28$, p-value = 0.23).

results and best-fit values of H_0 and Ω_Λ (Fig. 6.7 top middle panel) consistent with the current best-fit values from Planck (Planck Collaboration et al., 2018; Riess et al., 2018). The combined F10 + W2016 sample moves the best-fit point in the H_0 – Ω_Λ plane (Fig. 6.7 top right panel) away from the point for the W2016 sample alone, but still consistent within 1σ error. The bottom panels of Fig. 6.7 shows 1σ and 2σ contours in the H_0 – Ω_Λ plane for the same samples as in the top panels but only for $z > 1.414$. The combined F10 + W2016 sample (bottom right panel) in this case provides the best-fit point consistent with the Planck values (Planck Collaboration et al., 2018; Riess et al., 2018) but the F10 + W2016 full sample do not provide any sufficient constraint.

The Kolmogorov-Smirnov (K-S) test was applied to the empirical cumulative distribution functions (ECDF) in order to estimate the probability (p-value) that the full samples of *Fermi* and W2016 and the high redshift ($z > 1.414$) of these samples are drawn from the same distribution. The test statistic (D) is the maximum value of the absolute differences between the ECDF of the full sample and the ECDF of the sample with $z > 1.414$ for every value of z . As D value approach to zero the more likely it is that the two samples were drawn from the same distribution. Shown in Fig. 6.8 are the ECDF of the full samples of *Fermi* and W2016 and their high redshift ($z > 1.414$) samples. As can be seen from the left and right panels, the two distributions agree with one another to a reasonable extent. From the K-S test, we derived a p-value = 0.67 for the W2017 full sample and $z > 1.414$, which is large enough that the two samples cannot be distinguished with any statistical significance. The two populations shown in the right panel of Fig. 6.8 has a p-value = 0.23. This indicates that there is no significant difference between the samples. The two

populations shown in the middle panel of Fig. 6.8 has p-value = 0.04, which is not large enough that the two samples can be distinguished with any statistical significance.

Table 6.4 Constraints on (H_0, Ω_Λ) for a flat universe from the Amati relation, and reduced χ^2/dof of the fits.

Reference (All Samples)	$H_0 [\text{km s}^{-1} \text{Mpc}^{-1}]$	Ω_Λ	χ^2/dof
F10	51^{+25}_{-8}	-	-
F100	48^{+21}_{-8}	-	-
W2016	68^{+26}_{-23}	$0.69^{+0.2}_{-0.7}$	87.2/92
F10 + W2016	53^{+23}_{-8}	$0.27^{+0.53}_{-0.27}$	111.0/117
SNe U2.1	$70^{+0.6}_{-0.5}$	0.72 ± 0.03	562.3/578
F10 + SNe U2.1	$70^{+0.6}_{-0.5}$	0.72 ± 0.03	580.4/603
F10 + W2016 + SNe U2.1	70 ± 0.5	0.72 ± 0.03	667.6/697
Sample with $z > 1.414$			
F10	48^{+51}_{-8}	$0.03^{+0.95}_{-0.03}$	9.1/12
W2016	70^{+30}_{-26}	$0.72^{+0.2}_{-0.7}$	78.4/82
F10 + W2016	75^{+24}_{-31}	$0.78^{+0.17}_{-0.78}$	89.4/96
F10 + SNe U2.1	$70^{+0.5}_{-0.6}$	0.72 ± 0.03	578.2/592
F10 + W2016 + SNe U2.1	70 ± 0.5	0.72 ± 0.03	648.8/676

6.5.1 Sensitivity on the initial choice of cosmological parameters

Since the calculation of E_{iso} requires assuming standard values of the cosmological parameters (see Eqs. 6.1, and 4.27), the choice of these initial values may bias the Amati relation. To address this issue of circular logic, we reanalyzed the data using initial values different than the default case with $H_0 = 69.6 \text{ km s}^{-1} \text{ Mpc}^{-1}$ and $\Omega_\Lambda = 0.714$, and we tested the stability of our results. In this analysis, we have used the F10 sample of 25 *Fermi* GRBs as an example.

The results of our reanalysis are shown in Figs. 6.9 and 6.10. First, in Fig. 6.9 we fix $\Omega_\Lambda = 0.714$ at its default value and vary H_0 to take values of $100 \text{ km s}^{-1} \text{ Mpc}^{-1}$ (blue lines) and $50 \text{ km s}^{-1} \text{ Mpc}^{-1}$ (green lines). Next, in Fig. 6.10 we fix $H_0 = 69.6 \text{ km s}^{-1} \text{ Mpc}^{-1}$ at its default value and vary Ω_Λ to take values of 0.80 (blue lines) and 0.60 (green lines). The default case with $H_0 = 69.6 \text{ km s}^{-1} \text{ Mpc}^{-1}$ and $\Omega_\Lambda = 0.714$ is shown as gray lines in both Figs. 6.9 and 6.10.

We find that the normalization parameter k of the Amati relation is rather sensitive to the initial choice of H_0 , while the slope parameter m and the unknown systematic parameter σ_{ext} are virtually insensitive to this choice (see the left panel of Fig. 6.9). Therefore the Amati relation in the $E_{\text{i,p}} - E_{\text{iso}}$ plane just scales linearly with H_0 with the same slope (Fig. 6.9 middle panel). The resulting 1σ contours in $\Omega_\Lambda - H_0$ plane also shifts to the higher values of H_0 with increasing initial values (Fig. 6.9 right panel). On the other hand, the Amati relation parameters and σ_{ext} are only mildly sensitive to the initial choice of Ω_Λ (Fig. 6.10 left panel). As a result, the shape of

6.5. THE HUBBLE DIAGRAM AND CONSTRAINTS ON COSMOLOGICAL PARAMETERS

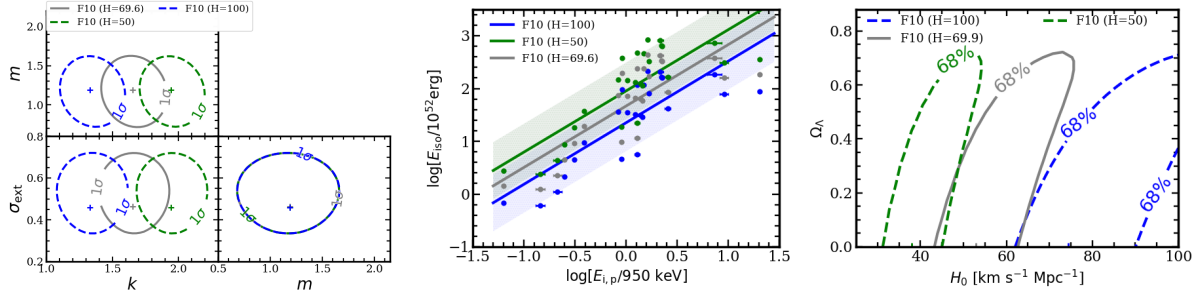


Figure 6.9 Results from the sensitivity study of the Amati relation and cosmological parameters on the initial choice of H_0 and Ω_Λ to calculate E_{iso} . The gray lines correspond to initial $H_0 = 69.6 \text{ km s}^{-1} \text{ Mpc}^{-1}$ (default case). The blue and green lines correspond to initial values of $H_0 = 100$ and $50 \text{ km s}^{-1} \text{ Mpc}^{-1}$, respectively. The initial value of $\Omega_\Lambda = 0.714$ (default case) is the same for all cases.

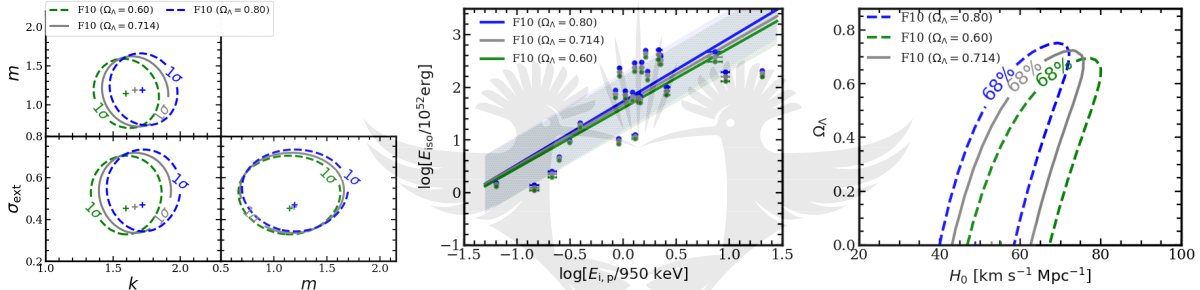


Figure 6.10 Results from the sensitivity study of the Amati relation and cosmological parameters on the initial choice of H_0 and Ω_Λ to calculate E_{iso} . The gray lines correspond to initial $\Omega_\Lambda = 0.714$ (default case). The blue and green lines correspond to initial values of $\Omega_\Lambda = 0.8$ and 0.6 , respectively. The initial value of $H_0 = 69.6 \text{ km s}^{-1} \text{ Mpc}^{-1}$ (default case) is the same for all cases.

the Amati relation in the $E_{i,p}$ - E_{iso} plane is basically unchanged (Fig. 6.10 middle panel) and the 1σ contours in Ω_Λ - H_0 plane shifts mildly (Fig. 6.10 right panel).

6.5.2 Joint fits with SNe U2.1 data

We have jointly analyzed GRBs in our samples together with the recent 580 SNe U2.1 sample from Suzuki et al. (2012) that spans a redshift range from 0.015 to 1.414. For this combined dataset we simply estimate the best-fit parameters as the sum of both samples, i.e., $\chi^2_{\text{total}} = \chi^2_{\text{GRBs}} + \chi^2_{\text{SNe}}$. The results of this joint analysis are shown in Figs. 6.11 and 6.12, and are also listed in Tab. 6.4. The constrained values of H_0 and Ω_Λ for the joint samples of F10 + SNe U2.1 and F10 + W2016 + SNe U2.1 are consistent with those estimated for the SNe U2.1 data alone and are in agreement with the values obtained by Wang et al. (2016); Demianski et al. (2017). The 1σ and 2σ contours in the H_0 - Ω_Λ plane, however, become much tighter (see Fig. 6.11) in

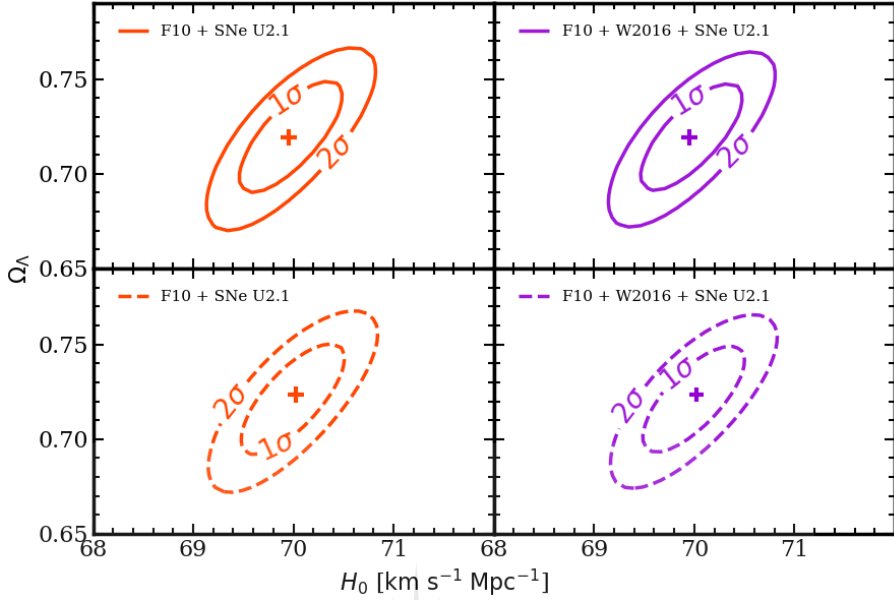


Figure 6.11 The same as Fig. 6.7 but with the SNe U2.1 sample (Suzuki et al., 2012). The top and bottom panels correspond to the GRBs samples with all redshifts and with redshifts > 1.414 , respectively.

these cases thanks to the much larger weight of the SNe U2.1 sample. Fig. 6.12 shows the Hubble diagram constructed with the SNe U2.1 together with F10 and W2016 samples. The top panel includes all GRBs and the bottom panel includes GRBs with $z > 1.414$, respectively. The black solid line represents the distance moduli $\mu(z)$ obtained with the best-fit cosmological parameters obtained from the respective joint analysis.

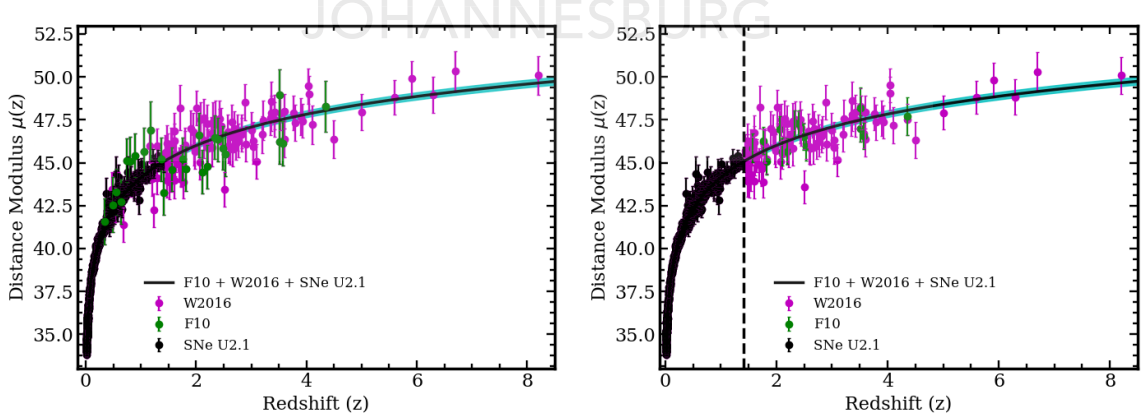


Figure 6.12 Combined SNe and GRB Hubble diagram for the F10 + W2016 + SNe U2.1 sample. The top panel includes all GRBs and the bottom panel includes GRBs with $z > 1.414$, respectively. The black lines are plotted using the estimated cosmological parameters obtained from the joint F10 + W2016 + SNe U2.1 data with 1σ confidence regions (cyan), reported in Tab. 6.4. The vertical broken line indicate $z = 1.414$.

6.6 Discussion and Summary

We have performed detailed time-integrated spectral analysis of GRBs detected with *Fermi*-LAT and GBM in 9 years of operation and for which the redshift is known. We found that the Band model (Band et al., 1993) provides the best-fit for 12 out of 26 GRBs in our sample while the SBPL model (Ryde, 1999) provides the best-fit for 4 GRBs (see Tab. 6.1 and Fig. 6.2). Fitting the spectra of other GRBs require BB and/or PL and/or Comp model(s) in addition to the Band or SBPL model. The resulting $E_{i,p}$ of the νF_ν spectra of these GRBs (see Tab. 6.2) varies from 60 ± 2 keV (GRB 091127) to 19334 ± 652 keV (GRB 160509A). The corresponding isotropic-equivalent radiated energy from these bursts within T_{90} ranges from $(1.3 \pm 0.1) \times 10^{52}$ erg (GRB 150514A) to $(435 \pm 6) \times 10^{52}$ erg (GRB 160625B) in the $1\text{--}10^4$ keV energy band E_{iso}^* (F10). Extending the energy band to $1\text{--}10^5$ keV E_{iso}^* (F100), we obtain different minimum and maximum values of $(1.4 \pm 0.1) \times 10^{52}$ erg (GRB 150514A) to $(605 \pm 25) \times 10^{52}$ erg (GRB 080916C), respectively. We used standard cosmological parameters, consistent with Planck results, to calculate these isotropic-equivalent energies.

We find that the $E_{i,p}\text{--}E_{iso}$ correlation for the *Fermi* LGRBs is rather strong and only the short GRB 090510 appears as an outlier (see Fig. 6.5 and Tab. 6.3). We did not use this burst in the rest of our analysis. The best-fit Amati relation for the LGRBs can be expressed as

$$\frac{E_{iso}}{10^{52} \text{ erg}} = 10^{1.67 \pm 0.16} \left(\frac{E_{i,p}}{950 \text{ keV}} \right)^{1.16 \pm 0.37},$$

where E_{iso} is calculated in the $1\text{--}10^4$ keV energy band. The accuracy of the fits to the Amati relation may be limited by our ignorance of its physical origin. The lack of bursts with a high E_{iso} and a low $E_{i,p}$ have a physical origin, while events with a low E_{iso} and a high $E_{i,p}$ may escape detection, as explored by Heussaff et al. (2013). Indeed, a full standardization of GRBs would require a better understanding of the non statistical scattering of the GRBs positions in the $E_{i,p}\text{--}E_{iso}$ plane. In our analysis, we thus used an ad-hoc uncertainty σ_{ext} (see Eqs. 4.30 and 4.31) that represents these hidden physical parameters.

Our fit to the W2016 sample (94 LGRBs) and the joint *Fermi* + W2016 sample (119 LGRBs) also resulted in parameter values compatible with other fits, although the errors on the parameters for these samples are smaller due to larger sample sizes. There are 14 LGRBs in the *Fermi* sample with redshift $z > 1.414$, which is the redshift up to which SNe Type Ia have been observed. Then, we fit this high-redshift sub-sample with the Amati relation and check whether the parameters k and m evolve with the GRB redshift (see Fig. 6.6). It is interesting to note, however, that almost half of the *Fermi*-LAT detected GRBs are at redshift $z < 1.414$. By combining the high-redshift GRBs from the *Fermi* and W2016 samples (total 98 GRBs at $z > 1.414$) we could obtain a good fit to the Amati relation. The resulting fit parameters are similar to the parameters obtained from the complete *Fermi* + W2016 sample, thus we see no evidence for an evolution of the best-fit Amati correlation parameters as a function of redshift.

We have performed a χ^2 estimator to constrain the Hubble parameter H_0 and dark-energy density Ω_Λ in a flat Λ CDM universe by using the distance modulus $\mu = 5 \log(d_L/\text{Mpc}) + 25$, where the luminosity distance d_L can be expressed in terms of $E_{\text{i,p}}$ and E_{iso} through the Amati relation. Thus GRBs are assumed standard cosmological candles, following the Amati relation fits. This method has been used by many authors (see, e.g., [Amati et al., 2008](#); [Tsutsui et al., 2009](#); [Wang et al., 2016](#); [Demianski et al., 2017](#)), however, is somewhat circular problem in the sense that E_{iso} is calculated assuming particular values of H_0 and Ω_Λ in the first place. Nevertheless, we follow this method adopted by previous authors for illustration purpose and to explore the sensitivity of the Amati relation to cosmological parameters. We find that the normalization of the Amati relation depends strongly on the initial choice of H_0 and is linearly proportional to it. On the other hand, the initial choice of Ω_Λ has a mild effect on both the normalization and slope of the Amati relation. In principle, the circularity problem could be solved by fitting the Amati relation and cosmological parameters simultaneously. Recently, some model-independent techniques were proposed to calibrate GRBs to avoid the circularity problem, such as the Bayesian method ([Firmani et al., 2005](#)), the scatter method ([Ghirlanda et al., 2004b](#)), the luminosity distance method [Ghirlanda et al. \(2004a\)](#); [Liang & Zhang \(2005\)](#), Markov Chain Monte Carlo (MCMC) method ([Li et al., 2008](#)), cosmological global fitting analysis method ([Li et al., 2008](#); [Graziani, 2011](#); [Ghirlanda, 2009](#); [Wang et al., 2016](#)), etc.. Unfortunately, these techniques can not completely overcome the circularity problem so far. A large sample of GRBs with less scatter in the $E_{\text{i,p}} - E_{\text{iso}}$ correlation will be useful in future for this study.

Because of a small sample size and of its limited range in redshift, the *Fermi* GRBs alone cannot constrain the cosmological parameters (see Tab. 6.4 and Fig. 6.7). Our analysis of the W2016 sample gives H_0 and Ω_Λ values consistent with the Planck results but with large errors. A joint analysis of *Fermi* + W2016 sample could not constrain Ω_Λ but using GRBs with $z > 1.414$ only we could constrain H_0 and Ω_Λ , albeit with large errors. Next, we have combined GRB samples (*Fermi* and W2016) with the SNe U2.1 sample ([Suzuki et al., 2012](#)) and obtained the cosmological parameters (see Fig. 6.11) of $H_0 = 69.95^{+0.53}_{-0.47} \text{ km s}^{-1} \text{ Mpc}^{-1}$ and $\Omega_\Lambda = 0.72 \pm 0.03$. We have also fitted cosmological parameters using GRBs with $z > 1.414$ and SNe U2.1 sample obtaining $H_0 = 70.03^{+0.46}_{-0.54} \text{ km s}^{-1} \text{ Mpc}^{-1}$ and $\Omega_\Lambda = 0.72 \pm 0.03$. Subsequently, we have plotted the Hubble diagram up to redshift $z = 8.2$ using these best-fit values, together with the GRB and SNe data (see Fig. 6.12). GRBs have the potential to trace cosmological parameters. The phenomenological Amati relation provides a window to explore this idea. At present, the quality of the correlation is poor to make a big impact in the cosmological study with GRBs but possibilities remain open with future big data sets.

SUMMARY AND FUTURE DIRECTIONS

Contents

7.1	Summary of results	121
7.1.1	Cosmological constraints from calibrated Yonetoku relation	122
7.1.2	Cosmological constraints from calibrated Amati relation	123
7.2	Future directions	125

7.1 Summary of results

GRBs are bright and hence can be found at cosmological distances. If emission from GRBs can be standardized, like SNe Type Ia (Riess et al., 1998; Perlmutter et al., 1999; Perlmutter & Schmidt, 2003), they can allow us to probe the furthest reaches of the universe. The physics of GRB prompt emission and the robustness of the analysis methods aimed to standardize them for cosmology still remain an open question. However, a combination of new instruments that provide the large spectral coverage and a growing number of GRBs with known redshift may increase the accuracy in the estimate of cosmological parameters using GRBs. The properties of GRB prompt emission is mainly obtained from the T_{90} or T_{peak} time-integrated spectral modeling of the bursts. In this regard, useful properties of GRBs are the existence of phenomenological correlations among the observed quantities emitted by long GRBs. These relations are found between the spectral properties and energetics, of which one is strongly dependent on the cosmological model. LGRBs may serve as standard candles to constrain cosmological parameters by probing the Hubble diagram well beyond the range of redshift currently accessible using SNe Type Ia.

In order to constrain the cosmological parameters we used correlations obtained from the well-fitted parameters of the LGRB spectra between the redshift-corrected energy $E_{i,p}$ at which a typical GRB νF_ν spectrum peaks and the isotropic peak luminosity (L_{iso}) in the cosmological rest frame, the so-called Yonetoku relation (Yonetoku et al., 2004). Moreover, we applied the

Amati relation (Amati et al., 2002; Amati, 2006b; Amati et al., 2008; Tsutsui et al., 2009), which links between the isotropic-equivalent energy E_{iso} released within T_{90} and the intrinsic peak energy $E_{i,p}$. These correlations are relevant to standardize GRBs for understanding cosmology via γ -ray observations. However, there is no consensus yet on the physical interpretation of these correlations. The possible presence of selection effects, lack of sufficient sample of GRBs with known redshift, the limited energy range provided by previous telescopes are also the main issues against validation of these correlations and use it as a cosmological tool. The dispersion of GRBs around the power-law best-fit line is somewhat large but encourage the use of GRBs as cosmological standard candles. Selection effects including detector artifacts may also play a significant role in the study of the Amati and Yonetoku correlations. Nevertheless, the strong correlation of $E_{i,p}$ with L_{iso} or E_{iso} found in several studies have not precluded their use as cosmological standard candles.

7.1.1 Cosmological constraints from calibrated Yonetoku relation

Application of GRBs as cosmological tools can be utilized by using the calibrated Yonetoku relation up to high redshifts. Below we present the results obtained from the $E_{i,p}$ - L_{iso} correlation fit parameters and discuss constraints on the Hubble parameter H_0 and dark-energy density Ω_Λ .

The investigation of phenomenological correlations between the spectral properties and energetics are discussed in details in Chapter §4. It includes the estimation of the Yonetoku fit parameters by using the maximum likelihood statistical method (Eq. 4.31) and its error computation (Eq. 4.33) in 1σ confidence interval. The linearized form of the Yonetoku relation is given in Eq. (4.37). By using the fit parameters of Yonetoku relation, we can derive an explicit formulation of the distance modulus μ (Eq. 4.49) and its uncertainty (Eq. 4.50) to construct the Hubble diagram. We can use χ^2 expression give in Eq. (4.52) to constrain the H_0 and Ω_Λ in a flat Λ CDM universe by using the distance modulus $\mu = 5 \log(d_L/\text{Mpc}) + 25$, where the luminosity distance d_L can be expressed in terms of $E_{i,p}$ and L_{iso} through the Yonetoku relation. After the formulation of maximum likelihood function, derivation of distance modulus and χ^2 function in Chapter §4, it has been applied to the samples of GRBs detected either with the *Swift*-BAT or *Fermi*-GBM or with both instruments as referred to in Chapter §5.

- In order to use a quality data set of GBM, we include the GRBs in the sample for which their spectral fitting parameters are constrained from the Band, SBPL and Comp spectral models. Among these GRBs, we have identified 76 GRBs ($F_{\text{best-model}}$) with measured redshift (i.e., from $z = 0.3285$ to $z = 5.283$) that have the spectral peak energy or break energy with a best-fit model. For the *Swift*-BAT GRBs with measured redshift, we identified acceptable spectral fitting parameters obtained from the Comp model and power low (PL) model. Since the value of spectral peak energy is not available for BAT GRBs fitted with PL model, we only consider 38 GRBs with known redshift (i.e., from $z = 0.2115$ to $z = 5.4636$) constrained by Comp model (S_{Comp}).

- The computation of L_{iso} as in Eq. (5.2) is done for each of the GRBs by using the parameters obtained from the spectral-fit integrated over the T_{peak} of the GRB spectrum. The results of L_{iso} and $E_{i,p}$ obtained from the best-fit spectral models for GBM and BAT samples are reported in Tabs. 5.1 and 5.2, respectively. The value of index from the best-fit Yonetoku relation for GBM sample ($F_{\text{best-model}}$) is about 1.56 ± 0.35 with the extrinsic systematics value of $\sigma_{\text{ext}} = 0.53 \pm 0.09$ while the index of BAT sample (S_{Comp}) $m = 2.69 \pm 0.65$ with slightly smaller value of $\sigma_{\text{ext}} = 0.31 \pm 0.15$. This indicates that the slope of S_{Comp} is steeper than the slope of $F_{\text{best-model}}$ and other samples reported in Tab. 5.3. The indices and extrinsic parameters obtained from the best-fit values of Yonetoku relation for GBM analysis are consistent with the previous work of Schaefer & Collazzi (2007); Lin et al. (2016). We also found that the L_{iso} of GBM sample is higher than the BAT sample as shown in Fig. 5.8.
- The correlation between L_{iso} and $E_{i,p}$ for the samples of GRBs (Tab. 5.3), we found a significant Pearson's correlation coefficients, $\rho_{pE_{i,p},L_{\text{iso}}}$ that ranges from 0.67 to 0.83. The partial correlation coefficients between $E_{i,p}$ and L_{iso} by removing the effect of redshift are also found between 0.52 and 0.75.
- From the best-fit parameters of Yonetoku relation we estimated H_0 with $\Omega_\Lambda \in (0.0, 0.85)$ for different samples of GBM and BAT GRBs. The obtained values of H_0 are comparable (Tab. 5.4). However, with the present GBM and BAT samples of GRBs alone, H_0 and Ω_Λ cannot be meaningfully constrained. The obtained values of H_0 and Ω_Λ from $FS_{\text{best-model}}$ sample combining with the latest SNe Type Ia data provide $H_0 = 69.908^{+0.533}_{-0.517} \text{ km s}^{-1} \text{ Mpc}^{-1}$ and $\Omega_\Lambda = 0.715^{+0.027}_{-0.030}$ in 1σ confidence intervals. The obtained result in 1σ confidence level is consistent with the currently acceptable ranges of H_0 and Ω_Λ (Riess et al., 2018; Planck Collaboration et al., 2018) but the errors on parameters are rather large that arise due to the large extrinsic systematics scattering associated to the simulated sample.
- Subsequently, we have constructed an extended Hubble diagram up to redshift 5.46 using the best-fit values, together with the GBM and BAT GRBs combining with the latest SNe Type Ia data (Fig. 5.11).

7.1.2 Cosmological constraints from calibrated Amati relation

Another important part of this thesis work deals with the Amati relation computed from the spectral analysis of 26 *Fermi*-LAT GRBs with known redshifts. These GRBs were detected by the *Fermi*-LAT during its nine years of operations from July 2008 to September 2017. We have performed a detailed time-integrated spectral analysis over T_{90} duration of these bright bursts with GBM and LAT Pass 8 data. Since Pass 8 data allow us to use photons below 100 MeV, we have extended the spectra analysis of LAT down to 30 MeV by considering the energy dispersion since it is large below 100 MeV. Here, we mention several possible lines of investigation:

- In addition to the Band or SBPL model, fitting the spectra of several GRBs require BB

and/or PL and/or Comp model(s). Thus extending the computation of E_{iso} to the 100 MeV range, which was not collectively used to study the Amati relation so far. The corresponding E_{iso} from these bursts ranges from $\sim 1.3 \times 10^{52}$ erg (GRB 150514A) to $\sim 4.35 \times 10^{54}$ erg (GRB 160625B) in the 1– 10^4 keV energy band, E_{iso}^* (F10). Extending the energy band to 1– 10^5 keV, E_{iso}^* (F100), we obtained different minimum and maximum values of $\sim 1.4 \times 10^{52}$ erg (GRB 150514A) to $\sim 6.05 \times 10^{54}$ erg (GRB 080916C), respectively as reported in Tab.6.2.

- The maximum likelihood statistical method (Eq. 4.31) used for the estimation of the fit parameters of Amati relation are discussed in details in Chapter §4. We have also derived an explicit formulation for the distance modulus (Eq. 4.45) for the construction of an extended Hubble diagram from the calibrated parameters of the Amati relation, Eq. (4.50), with its error given in Eq. (4.51). A χ^2 expression (Eq. 4.52) is also presented in this chapter, which used to constrain H_0 and Ω_Λ in a flat universe with Λ CDM model. Then, it has been applied to the sample of 9 years of *Fermi*-LAT GRBs as referred to in Chapter §6.
- We found that the Amati relation is satisfied by the 25 LGRBs, with fitting parameters similar to the previous studies that used data from different satellite experiments, while the only short GRB 090510 is an outlier. The Amati relation best-fits to the full F10 and F100 samples for the LGRBs can be expressed as

$$\frac{E_{\text{iso}}}{10^{52} \text{ erg}} = \begin{cases} 10^{1.67 \pm 0.16} \left(\frac{E_{\text{i,p}}}{950 \text{ keV}} \right)^{1.16 \pm 0.37}, & \text{for } E_{\text{iso}}^*(\text{F10}) \\ 10^{1.73 \pm 0.18} \left(\frac{E_{\text{i,p}}}{950 \text{ keV}} \right)^{1.25 \pm 0.33}, & \text{for } E_{\text{iso}}^*(\text{F100}). \end{cases}$$

The obtained values of normalization k and slope m for these samples are comparable including their extrinsic errors σ_{ext} (Tab. 6.3). Nevertheless, there is a perceptible difference for the parameter k between the F10 or F100 sample and the W2016 ($k = 1.19 \pm 0.08$) or F10+W2016 ($k = 1.31 \pm 0.07$) sample. We have also found a high significance partial correlation coefficient $\rho_{E_{\text{i,p}}, E_{\text{iso}}, z}$ of 0.65 and 0.70 for samples F10 and F100, respectively.

- For the *Fermi* GRBs alone, we are limited by a small sample size to constrain the cosmological parameters (e.g., Tab. 6.4 and Fig. 6.7). The analysis of W2016 (94 LGRBs) sample provides $H_0 = 68_{-23}^{+26} \text{ km s}^{-1} \text{ Mpc}^{-1}$ and $\Omega_\Lambda = 0.69_{-0.69}^{+0.20}$ values consistent with the currently acceptable ranges of those cosmological parameters (Riess et al., 2018; Planck Collaboration et al., 2018) but with large error. We have combined GRB samples (*Fermi* and W2016) with the SNe U2.1 sample (Suzuki et al., 2012) and obtained the cosmological parameters (e.g., Fig. 6.11) as

$$\begin{cases} H_0 = 69.95_{-0.45}^{+0.54}; \Omega_\Lambda = 0.72 \pm 0.03, & \text{for full sample} \\ H_0 = 70.03_{-0.54}^{+0.48}; \Omega_\Lambda = 0.72 \pm 0.03 & \text{for } z > 1.414. \end{cases}$$

Afterwards, we have plotted an extended Hubble diagram up to a redshift of $z = 8.2$ using these best-fit values, together with the GRB and SNe data (Fig. 6.12).

- We have also studied the sensitivity of the Amati relation to the initial choice of cosmological parameters, H_0 and Ω_Λ . We explored that the normalization of the Amati relation strongly depends on the initial choice of H_0 while the initial choice of Ω_Λ has a mild effect on both the normalization and slope of the relation. The mild dependence on Ω_Λ results from the fact that the luminosity and isotropic emitted energy depend more strongly on H_0 than Ω_Λ .

We have performed a detailed time-integrated spectral analysis of GRBs co-detected by GBM and LAT on board the *Fermi* satellite. Thus covering a wide energy range, in which multiple components are required to fit the spectra of a number of GRBs. We found that the time-integrated spectra of 12 out of 25 GRBs are best-modeled with the Band function, which may suggest a common origin for emissions detected by *Fermi*-LAT/GBM. Some GRBs require the superposition of a MeV component and an extra power-law component. Since we performed our spectral analysis over T_{90} duration, the constrained extra power-law component may not due to the late prompt emission (i.e., the afterglow phase). Hence, the existence of high-energy spectral components uncertain the true underlying empirical Amati relation which is due to the properties of prompt emission. The results from our work indicate that phenomenological correlations among the spectral properties and energetics such as Amati relation for long GRBs can potentially be useful to standardize GRBs for cosmological studies up to high redshifts.

7.2 Future directions

One of the most important results of our spectral analysis was obtaining a quality data set of the keV–MeV to GeV emission of GRBs from the *Fermi*-GBM/LAT observation for the analysis of phenomenological correlations. However, due to small sample size and of its limited range in redshift, the *Fermi* GRBs cannot constrain the cosmological parameters adequately. A sample of GRBs from the *Swift*-BAT observation and another sample of the W2016 data are used to study the correlation as well.

In the calibrations of the Yonetoku (see Chapter §5) and the Amati (see Chapter §6) relations, the L_{iso} and E_{iso} are calculated for the given values of H_0 and Ω_Λ , respectively that arises the so-called circularity problem. One could assume a cosmological model in the first place, which would be required for the study of correlation to probe the cosmological parameters. In future, in order to fully take into account this circularity problem, the correlations should be further tested through an extensive maximum likelihood analysis method that has allowed us to jointly fit the calibration and cosmological model. Due to the paucity of the data sets and circularity problems mentioned above, to employ a more robust $E_{\text{i,p}}-L_{\text{iso}}$ or $E_{\text{i,p}}-E_{\text{iso}}$ correlation study as a cosmological probe we require a high-quality data set which will reduce the scattering in the correlation. Better calibration of these correlations will be possible with a future mission, such as SVOM (scheduled for launch in 2021), which will perform spectral measurements of prompt GRB emission in a broader energy range with respect to the *Swift*-BAT instrument and will provide a

large number of GRBs with measured redshift. The sensitivity of both the Yonetoku and Amati relations and other phenomenological relations to cosmological model for different samples of GRBs will be explored in our future work.

I would also like to study the sensitivity of the upcoming Cherenkov Telescope Array (CTA) to GRBs (see Sec. §2.5), which is the next generation of ground-based γ -ray telescopes. It will allow us to explore very high-energy γ -rays from 20 GeV–100 TeV energies, beyond the *Fermi*-LAT γ -ray detected energy range (i.e., 20 MeV – \gtrsim 300 GeV). The highest energy for GRB γ -ray detected by *Fermi*-LAT was 96 GeV. The CTA telescopes will increase the sensitivity for the deep observations, which is expected to boost the detection rates of GRB at highest energies. In future, I would like to determine the sensitivity and investigate the expected detection rate of CTA by extrapolating high-energy flux from the *Fermi*-LAT GRBs shown in Fig. 2.11. Besides, I would like to investigate the multi-wavelength properties of GRBs observed with high fluence from the space-based observatories, the *Fermi* and *Swift* as well as from ground-based such as MeerKAT/Square Kilometre Array (SKA)¹, The Southern African Large Telescope (SALT)², Mobile Astronomical System of TElescope Robots (MASTER, Lipunov et al., 2004), Large Synoptic Survey Telescope (LSST, Tuell et al., 2010), HESS and CTA.



¹<https://www.ska.ac.za/gallery/meerkat/>

²<https://www.saao.ac.za/science/facilities/telescopes/salt/>



DERIVATION OF SBPL

A.1 Smoothly-Broken Power Law

We derive a smoothly broken power law (Ryde, 1999), having a lower energy power law index α , smoothly transferred into a higher energy power law with index β . The change of index can be described by a negative hyperbolic tangent function with its logarithmic derivative changes from α to β

$$y = -\lambda_1 \tanh(x) + \lambda_2, \quad (\text{A.1})$$

where $y = d \log N(E) / d \log E$, $x = 1/\sigma \log(E/E_0)$. Here λ_1 and λ_2 are positive constants and E_0 is the e-folding energy. Since $\alpha > \beta$, the value of constants illustrated in Fig. A.1 give us $\lambda_1 = (\alpha - \beta)/2$ and $\lambda_2 = (\alpha + \beta)/2$. Then the tangent function in Eq. A.1 can be written as

$$\frac{d \log N_{\text{sbpl}}(E)}{d(\log E)} = \frac{\beta - \alpha}{2} \tanh\left(\frac{\log(E/E_0)}{\sigma}\right) + \frac{\alpha + \beta}{2}, \quad (\text{A.2})$$

where $N_{\text{sbpl}}(E)$ is the flux of photon energy E and σ is the break scale in decades of energy fixed at 0.3. Integrating Eq. (A.2), we can obtain

$$\begin{aligned} d \log N_{\text{sbpl}}(E) &= \frac{\beta - \alpha}{2} \int \tanh\left(\frac{\log(E/E_0)}{\sigma}\right) d(\log E) + \frac{\alpha + \beta}{2} \int d(\log E), \\ &= \frac{\beta - \alpha}{2} \ln\left(\cosh\frac{\log(E/E_0)}{\sigma}\right) \sigma + \frac{\alpha + \beta}{2} \log E + C, \end{aligned} \quad (\text{A.3})$$

where C is the integration constant, which can be obtained using the boundary condition $N_{\text{sbpl}}(E) = A_{\text{sbpl}}$ when $E = E_{\text{dec}}$. Here A_{sbpl} is the normalization defined at $E_{\text{dec}} = 100$ keV. Then the energy flux is given by

$$N_{\text{sbpl}}(E) = 10^{\frac{\beta - \alpha}{2} \sigma \ln\left(\cosh\frac{\log(100 \text{ keV}/E_0)}{\sigma}\right) + \frac{\alpha + \beta}{2} \log E + C'} = A_{\text{sbpl}}, \quad (\text{A.4})$$

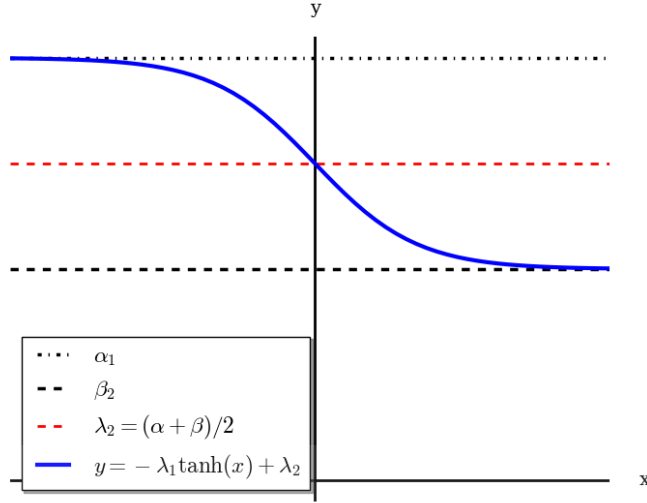


Figure A.1 The index changes from α to β .

$$C' = A_{\text{sbpl}} \times 10^{\frac{\alpha - \beta}{2} \sigma \ln \left(\cosh \frac{\log(100 \text{ keV}/E_0)}{\sigma} \right) (100 \text{ keV})^{-\frac{\alpha + \beta}{2}}} \quad (\text{A.5})$$

Then Eq. (A.4) yields

$$\begin{aligned} N_{\text{sbpl}}(E) &= A_{\text{sbpl}} \times 10^{\frac{\beta - \alpha}{2} \sigma \left[\ln \left(\cosh \frac{\log(100 \text{ keV}/E_0)}{\sigma} \right) - \ln \left(\cosh \frac{\log(100 \text{ keV}/E_0)}{\sigma} \right) \right] \left(\frac{E}{100 \text{ keV}} \right)^{\frac{\alpha + \beta}{2}}}, \\ &= A_{\text{sbpl}} \left(\frac{E}{100 \text{ keV}} \right)^{\frac{\alpha + \beta}{2}} 10^{(\alpha - \alpha_p)}, \end{aligned} \quad (\text{A.6})$$

where

$$\begin{cases} a = \frac{1}{2} \sigma(\beta - \alpha) \ln \left(\frac{e^r + e^{-r}}{2} \right), & a_p = \frac{1}{2} \sigma(\beta - \alpha) \ln \left(\frac{e^{r_p} + e^{-r_p}}{2} \right), \\ r = \frac{\log(E/E_0)}{\sigma}, & r_p = \frac{\log(100 \text{ keV}/E_0)}{\sigma}. \end{cases} \quad (\text{A.7})$$

The peak energy of the vF_v spectrum is at

$$E_p = E_0 \times 10^{\left(\frac{1}{2} \sigma \ln \left[\frac{\alpha + 2}{-\beta - 2} \right] \right)}, \text{ only valid for } \left| \frac{\alpha + 2}{-\beta - 2} \right| < 1. \quad (\text{A.8})$$

THE *Fermi*-GBM AND *Swift*-BAT SPECTRAL FITTING PARAMETERS, AND REANALYSIS OF W2016 DATA

Contents

B.1	The best-fit spectral parameters of the <i>Swift</i> -BAT sample	129
B.2	The best-fit spectral parameters of the <i>Fermi</i> -GBM sample	130
B.3	The Comp (F_{Comp}) spectral fitting parameters of the <i>Fermi</i> -GBM sample	133
B.4	The Band (F_{Band}) spectral fitting parameters of the <i>Fermi</i> -GBM sample	135
B.5	Reanalysis of W2016 data	137

B.1 The best-fit spectral parameters of the *Swift*-BAT sample

Table B.1 The result of the Comp spectral fitting parameters of the *Swift*-BAT sample integrated over T_{peak} for 38 GRBs (e.g., *Swift*-BAT catalog, Lien et al., 2016). The z , L_{iso} and μ for each GRB is listed in Tab. 5.2.

GRB Name	Model	T_{peak} Interval (s)	γ	E_p (keV)
GRB 170705A	Comp	13.41 - 14.41	-0.92 ± 0.22	161.3 ± 87.9
GRB 150314A	Comp	0.06 - 1.06	-0.47 ± 0.17	248.9 ± 102.2
GRB 140506A	Comp	0.0 - 1.0	-0.53 ± 0.6	100.4 ± 55.0
GRB 140206A	Comp	60.8 - 61.8	-0.54 ± 0.18	115.6 ± 15.1
GRB 130427A	Comp	-43.42 - -42.42	-0.5 ± 0.1	467.4 ± 213.1
GRB 130420A	Comp	110.67 - 111.67	-1.03 ± 0.49	58.0 ± 15.6
GRB 121128A	Comp	21.68 - 22.68	-0.5 ± 0.22	107.7 ± 16.2
GRB 120811C	Comp	5.27 - 6.27	-1.02 ± 0.42	60.1 ± 13.2

Continued on next page

APPENDIX B. THE *FERMI*-GBM AND *SWIFT*-BAT SPECTRAL FITTING PARAMETERS, AND REANALYSIS OF W2016 DATA

Table B.1 – Continued from previous page

GRB 120729A	Comp	0.04 - 1.04	-0.78 ± 0.52	65.0 ± 17.4
GRB 120712A	Comp	7.51 - 8.51	-0.13 ± 0.74	99.7 ± 55.8
GRB 120624B	Comp	138.06 - 139.06	-0.5 ± 0.33	185.9 ± 152.1
GRB 120119A	Comp	8.98 - 9.98	-0.78 ± 0.23	197.6 ± 143.0
GRB 110731A	Comp	-0.27 - 0.73	-0.77 ± 0.22	135.2 ± 39.8
GRB 110715A	Comp	1.86 - 2.86	-0.98 ± 0.13	152.0 ± 32.6
GRB 110503A	Comp	-0.12 - 0.88	-0.16 ± 0.33	130.2 ± 31.0
GRB 100906A	Comp	10.48 - 11.48	-1.01 ± 0.27	138.4 ± 99.8
GRB 100814A	Comp	4.21 - 5.21	0.41 ± 0.54	155.9 ± 58.9
GRB 100621A	Comp	24.46 - 25.46	-0.95 ± 0.21	90.6 ± 14.6
GRB 091029	Comp	19.12 - 20.12	-0.93 ± 0.65	53.2 ± 18.3
GRB 090424	Comp	-0.1 - 0.9	-0.98 ± 0.19	183.4 ± 102.1
GRB 081222	Comp	3.67 - 4.67	-0.79 ± 0.22	166.3 ± 77.3
GRB 080916A	Comp	1.25 - 2.25	-0.16 ± 0.45	138.3 ± 64.4
GRB 080413B	Comp	-0.26 - 0.74	-0.94 ± 0.27	111.3 ± 40.6
GRB 071010B	Comp	1.4 - 2.4	-1.0 ± 0.27	68.5 ± 9.4
GRB 070508	Comp	10.85 - 11.85	-0.68 ± 0.16	213.5 ± 71.1
GRB 061222A	Comp	86.24 - 87.24	-0.49 ± 0.21	225.8 ± 113.9
GRB 060927	Comp	0.22 - 1.22	-0.29 ± 0.43	130.2 ± 60.6
GRB 060908	Comp	0.54 - 1.54	-0.27 ± 0.6	123.0 ± 88.1
GRB 060719	Comp	0.37 - 1.37	-0.68 ± 0.67	54.8 ± 12.0
GRB 060306	Comp	0.18 - 1.18	-0.82 ± 0.37	111.5 ± 58.0
GRB 060206	Comp	2.19 - 3.19	-0.91 ± 0.39	81.8 ± 27.3
GRB 060117	Comp	11.14 - 12.14	-0.94 ± 0.17	100.9 ± 13.3
GRB 060111A	Comp	4.31 - 5.31	-0.52 ± 0.62	86.0 ± 45.4
GRB 050922C	Comp	-0.08 - 0.92	-0.89 ± 0.28	146.5 ± 107.2
GRB 050502B	Comp	0.22 - 1.22	-0.11 ± 0.72	73.7 ± 21.6
GRB 050401	Comp	24.27 - 25.27	-0.07 ± 0.65	108.0 ± 40.3
GRB 050318	Comp	28.58 - 29.58	-0.81 ± 0.44	67.3 ± 16.3
GRB 050219A	Comp	9.68 - 10.68	-0.14 ± 0.67	111.1 ± 57.9

Notes: γ is the photon index of Comp model. E_p is the Comp model peak energy.

B.2 The best-fit spectral parameters of the *Fermi*-GBM sample

B.2. THE BEST-FIT SPECTRAL PARAMETERS OF THE *FERMI*-GBM SAMPLE

Table B.2 The result of the best-fit spectral fitting parameters of the *Fermi*-GBM sample integrated over T_{peak} for 76 GRBs (e.g., *Fermi*-GBM catalog, [Gruber et al., 2014](#); [von Kienlin et al., 2014](#); [Narayana Bhat et al., 2016a](#)). The z , L_{iso} and μ for each GRB is listed in Tab. 5.1.

GRB Name	Best-model	T_{peak} Interval (s)	γ	E_p (keV)
GRB 170903534	Comp	0.0 - 1.02	-1.29 ± 0.15	181.6 ± 52.7
GRB 170705115	Comp	9.22 - 10.24	-0.84 ± 0.06	207.8 ± 12.5
GRB 170607971	Comp	2.05 - 3.07	-1.37 ± 0.08	221.1 ± 36.9
GRB 170405777	Comp	29.7 - 30.72	-0.73 ± 0.05	381.3 ± 28.1
GRB 161129300	Comp	26.62 - 27.65	-0.87 ± 0.12	272.6 ± 57.0
GRB 161117066	Comp	115.71 - 116.74	-0.87 ± 0.16	73.5 ± 5.7
GRB 161014522	Comp	7.17 - 8.19	-0.49 ± 0.15	197.42 ± 22.1
GRB 160629930	Comp	14.34 - 15.36	-0.75 ± 0.11	239.1 ± 29.3
GRB 151027166	Comp	0.0 - 1.02	-0.99 ± 0.07	317.8 ± 43.4
GRB 150821406	Comp	15.36 - 16.38	-0.94 ± 0.06	390.7 ± 47.5
GRB 150514774	Comp	1.02 - 2.05	-0.97 ± 0.1	62.2 ± 2.6
GRB 150301818	Comp	3.07 - 4.1	-0.95 ± 0.15	172.35 ± 26.6
GRB 141225959	Comp	2.05 - 3.07	-0.01 ± 0.36	252.8 ± 46.01
GRB 141221338	Comp	0.0 - 1.02	-1.08 ± 0.13	328.1 ± 80.6
GRB 141220252	Comp	0.0 - 1.02	-0.52 ± 0.07	214.6 ± 11.5
GRB 141004973	Comp	0.0 - 1.02	-1.33 ± 0.12	140.4 ± 25.4
GRB 140907672	Comp	9.22 - 10.24	-0.64 ± 0.22	113.1 ± 13.7
GRB 140808038	Comp	0.0 - 1.02	-0.23 ± 0.13	157.4 ± 10.8
GRB 140703026	Comp	10.24 - 11.26	-0.77 ± 0.15	271.9 ± 46.3
GRB 140620219	Comp	6.14 - 7.17	-0.91 ± 0.21	92.5 ± 12.0
GRB 140606133	Comp	1.02 - 2.05	-1.26 ± 0.05	845.1 ± 219.3
GRB 140512814	Comp	129.02 - 130.05	-1.0 ± 0.05	579.8 ± 79.0
GRB 140506880	Comp	0.0 - 1.02	-0.7 ± 0.12	172.5 ± 14.5
GRB 140423356	Comp	-2.05 - -1.02	-0.69 ± 0.26	250.4 ± 65.2
GRB 140304557	Comp	7.17 - 8.19	-0.92 ± 0.26	295.3 ± 107.3
GRB 140213807	Comp	6.14 - 7.17	-0.94 ± 0.04	92.4 ± 2.7
GRB 131105087	Comp	106.5 - 107.52	-1.03 ± 0.06	449.5 ± 64.6
GRB 131011741	Comp	4.1 - 5.12	-0.86 ± 0.16	402.0 ± 97.2
GRB 121128212	Comp	8.19 - 9.22	-0.47 ± 0.1	115.5 ± 6.0
GRB 120907017	Comp	-1.02 - 0.0	-0.94 ± 0.3	133.9 ± 31.8
GRB 120716712	Comp	0.0 - 1.02	-0.83 ± 0.1	169.0 ± 16.7
GRB 120624933	Comp	11.26 - 12.29	-0.83 ± 0.04	797.0 ± 74.9
GRB 120326056	Comp	1.02 - 2.05	-1.08 ± 0.13	77.7 ± 7.0
GRB 120119170	Comp	14.34 - 15.36	-0.91 ± 0.05	328.4 ± 25.4

Continued on next page

APPENDIX B. THE *FERMI*-GBM AND *SWIFT*-BAT SPECTRAL FITTING PARAMETERS, AND REANALYSIS OF W2016 DATA

Table B.2 – Continued from previous page

GRB 110731465	Comp	0.0 - 1.02	-0.96 ± 0.07	176.3 ± 11.5	
GRB 110213220	Comp	18.43 - 19.46	-1.16 ± 0.09	92.2 ± 7.2	
GRB 100906576	Comp	10.24 - 11.26	-0.81 ± 0.09	207.0 ± 20.9	
GRB 100816026	Comp	1.02 - 2.05	-0.37 ± 0.09	138.9 ± 6.9	
GRB 100728439	Comp	2.05 - 3.07	-0.93 ± 0.19	122.9 ± 20.5	
GRB 100728095	Comp	81.92 - 82.94	-0.53 ± 0.08	511.0 ± 48.0	
GRB 100704149	Comp	3.07 - 4.1	-0.55 ± 0.12	260.6 ± 29.1	
GRB 100615083	Comp	10.24 - 11.26	-0.87 ± 0.14	89.9 ± 8.0	
GRB 100414097	Comp	23.55 - 24.58	-0.75 ± 0.04	522.5 ± 32.4	
GRB 091208410	Comp	8.19 - 9.22	-1.09 ± 0.06	191.2 ± 16.2	
GRB 091020900	Comp	2.05 - 3.07	-1.13 ± 0.09	656.7 ± 154.0	
GRB 090618353	Comp	63.49 - 64.51	-0.96 ± 0.03	447.5 ± 20.2	
GRB 090424592	Comp	1.02 - 2.05	-0.86 ± 0.02	207.9 ± 4.5	
GRB 090328401	Comp	23.55 - 24.58	-0.77 ± 0.04	463.2 ± 29.7	
GRB 090323002	Comp	65.54 - 66.56	-0.55 ± 0.06	396.0 ± 27.2	
GRB 090113778	Comp	0.0 - 1.02	-0.58 ± 0.2	201.7 ± 30.2	
GRB 090102122	Comp	15.62 - 16.64	-0.27 ± 0.07	377.7 ± 22.3	
GRB 081222204	Comp	3.07 - 4.1	-0.8 ± 0.07	197.9 ± 14.7	
GRB 081221681	Comp	20.48 - 21.5	-0.36 ± 0.06	119.1 ± 3.8	
GRB 081008832	Comp	15.36 - 16.38	-0.65 ± 0.28	163.5 ± 37.7	
GRB 080916406	Comp	2.05 - 3.07	-0.39 ± 0.15	239.1 ± 27.9	
GRB 080916009	Comp	2.05 - 3.07	-0.77 ± 0.06	525.1 ± 55.6	
GRB 080810549	Comp	23.55 - 24.58	-1.13 ± 0.16	625.9 ± 240.2	
GRB 080804972	Comp	1.02 - 2.05	-0.22 ± 0.21	172.2 ± 20.1	
GRB Name	Best-model	T_{peak} Interval (s)	α	β	E_p (keV)
GRB 171010792	Band	33.79 - 34.82	-0.82 ± 0.02	-2.44 ± 0.08	299.5 ± 12.1
GRB 170214649	Band	61.44 - 62.46	-0.7 ± 0.07	-1.96 ± 0.12	455.2 ± 74.2
GRB 160625945	Band	188.45 - 189.47	-0.5 ± 0.01	-2.05 ± 0.02	593.7 ± 15.2
GRB 160509374	Band	16.38 - 17.41	-0.75 ± 0.02	-2.26 ± 0.07	345.3 ± 15.3
GRB 150403913	Band	11.26 - 12.29	-0.67 ± 0.03	-2.19 ± 0.08	509.3 ± 34.6
GRB 150314205	Band	2.05 - 3.07	-0.41 ± 0.03	-2.54 ± 0.09	298.0 ± 10.0
GRB 141028455	Band	12.29 - 13.31	-0.66 ± 0.05	-2.3 ± 0.18	438.6 ± 35.0
GRB 140508128	Band	4.1 - 5.12	-0.55 ± 0.04	-2.43 ± 0.09	376.3 ± 19.0
GRB 131231198	Band	22.53 - 23.55	-0.79 ± 0.02	-2.66 ± 0.13	312.6 ± 11.1
GRB 131108862	Band	0.0 - 1.02	-0.6 ± 0.06	-1.94 ± 0.07	332.6 ± 32.1
GRB 130518580	Band	25.6 - 26.62	-0.73 ± 0.03	-2.13 ± 0.08	469.0 ± 33.4
GRB 130427324	Band	8.19 - 9.22	-0.45 ± 0.01	-3.13 ± 0.04	717.6 ± 6.0
GRB 091003191	Band	18.43 - 19.46	-0.6 ± 0.04	-2.33 ± 0.15	393.5 ± 27.1

Continued on next page

B.3. THE COMP (F_{Comp}) SPECTRAL FITTING PARAMETERS OF THE *FERMI*-GBM SAMPLE

Table B.2 – Continued from previous page

GRB 090926181	Band	3.07 - 4.1	-0.46 ± 0.02	-2.68 ± 0.14	346.8 ± 10.9	
GRB 081121858	Band	6.14 - 7.17	-0.21 ± 0.31	-1.77 ± 0.12	194.6 ± 45.4	
GRB Name	Best-model	T_{peak} Interval (s)	α	β	E_0 (keV)	E_p (keV)
GRB 140206304	sbpl	5.120 - 6.144	-0.24 ± 0.22	-2.60 ± 0.13	71.5 ± 8.6	112.5 ± 4.1
GRB 120711115	sbpl	95.232 - 96.256	-0.92 ± 0.03	-2.20 ± 0.09	706.8 ± 107.0	1274.2 ± 49.5
GRB 091127976	sbpl	0.000 - 1.024	-0.74 ± 0.09	-2.33 ± 0.04	35.3 ± 2.7	56.1 ± 1.3

Notes: γ is the photon index of Comp model. E_p is the peak energy of Band, Comp and sbpl models.

B.3 The Comp (F_{Comp}) spectral fitting parameters of the *Fermi*-GBM sample

Table B.3 The result of the Comp (F_{Comp}) spectral fitting parameters of the *Fermi*-GBM sample integrated over T_{peak} for 90 GRBs (e.g., *Fermi*-GBM catalog, [Gruber et al., 2014](#); [von Kienlin et al., 2014](#); [Narayana Bhat et al., 2016a](#)).

GBM Name	z	Model	T_{peak} (s)	γ	E_p (keV)	L_{iso} (10^{52} erg s $^{-1}$)	$\mu \pm \sigma_\mu$
GRB 171222684	2.409	Comp	64.51 - 65.54	-2.02 ± 0.02	388.2 ± 3.6	1.1 ± 0.18	48.7 ± 1.3
GRB 171010792	0.3285	Comp	33.79 - 34.82	-0.9 ± 0.02	360.6 ± 9.4	0.82 ± 0.03	42.0 ± 1.3
GRB 170903534	0.886	Comp	0.0 - 1.02	-1.29 ± 0.15	181.6 ± 52.7	0.25 ± 0.08	45.3 ± 1.5
GRB 170705115	2.01	Comp	9.22 - 10.24	-0.84 ± 0.06	207.8 ± 12.5	9.27 ± 0.98	44.6 ± 1.3
GRB 170607971	0.557	Comp	2.05 - 3.07	-1.37 ± 0.08	221.1 ± 36.9	0.24 ± 0.04	44.1 ± 1.4
GRB 170405777	3.51	Comp	29.7 - 30.72	-0.73 ± 0.05	381.3 ± 28.1	43.7 ± 4.76	46.2 ± 1.3
GRB 170214649	2.53	Comp	61.44 - 62.46	-0.78 ± 0.04	614.9 ± 47.5	31.5 ± 3.15	46.1 ± 1.3
GRB 170113420	1.968	Comp	-1.02 - 0.0	-1.23 ± 0.47	207.8 ± 85.4	1.08 ± 0.66	46.9 ± 1.6
GRB 161129300	0.645	Comp	26.62 - 27.65	-0.87 ± 0.12	272.6 ± 57.0	0.16 ± 0.04	45.4 ± 1.4
GRB 161117066	1.549	Comp	115.71 - 116.74	-0.87 ± 0.16	73.5 ± 5.7	1.21 ± 0.37	44.0 ± 1.5
GRB 161017745	2.013	Comp	4.1 - 5.12	-1.22 ± 0.15	402.6 ± 189.4	2.81 ± 1.19	47.1 ± 1.6
GRB 161014522	2.823	Comp	7.17 - 8.19	-0.49 ± 0.15	197.4 ± 22.1	5.08 ± 1.28	46.5 ± 1.4
GRB 160804065	0.736	Comp	0.0 - 1.02	-1.23 ± 0.24	133.3 ± 43.2	0.10 ± 0.05	45.1 ± 1.6
GRB 160629930	3.332	Comp	14.34 - 15.36	-0.75 ± 0.11	239.1 ± 29.3	8.68 ± 1.79	46.9 ± 1.3
GRB 160625945	1.406	Comp	188.45 - 189.47	-0.77 ± 0.01	1253.4 ± 24.3	171.0 ± 3.99	43.3 ± 1.4
GRB 160509374	1.17	Comp	16.38 - 17.41	-0.84 ± 0.02	437.3 ± 11.9	13.9 ± 0.52	43.5 ± 1.3
GRB 151027166	0.81	Comp	0.0 - 1.02	-0.99 ± 0.07	317.8 ± 43.4	0.58 ± 0.10	45.0 ± 1.4
GRB 150821406	0.755	Comp	15.36 - 16.38	-0.94 ± 0.06	390.7 ± 47.5	0.60 ± 0.09	45.1 ± 1.3
GRB 150514774	0.807	Comp	1.02 - 2.05	-0.97 ± 0.1	62.2 ± 2.6	0.42 ± 0.09	42.5 ± 1.5

Continued on next page

APPENDIX B. THE *FERMI*-GBM AND *SWIFT*-BAT SPECTRAL FITTING PARAMETERS, AND REANALYSIS OF W2016 DATA

Table B.3 – Continued from previous page

GRB 150403913	2.06	Comp	11.26 - 12.29	-0.76 ± 0.03	652.1 ± 34.6	38.8 ± 2.8	45.2 ± 1.3
GRB 150314205	1.758	Comp	2.05 - 3.07	-0.51 ± 0.02	348.6 ± 8.0	37.0 ± 1.57	43.5 ± 1.3
GRB 150301818	1.5169	Comp	3.07 - 4.1	-0.95 ± 0.15	172.4 ± 26.6	0.81 ± 0.22	45.9 ± 1.4
GRB 141225959	0.915	Comp	2.05 - 3.07	-0.01 ± 0.36	252.8 ± 46.0	0.21 ± 0.10	46.2 ± 1.5
GRB 141221338	1.452	Comp	0.0 - 1.02	-1.08 ± 0.13	328.1 ± 80.6	1.19 ± 0.34	46.4 ± 1.4
GRB 141220252	1.3195	Comp	0.0 - 1.02	-0.52 ± 0.07	214.6 ± 11.5	2.3 ± 0.27	44.6 ± 1.3
GRB 141028455	2.33	Comp	12.29 - 13.31	-0.71 ± 0.04	511.3 ± 34.1	22.2 ± 2.13	45.8 ± 1.3
GRB 141004973	0.573	Comp	0.0 - 1.02	-1.33 ± 0.12	140.4 ± 25.4	0.12 ± 0.03	44.1 ± 1.5
GRB 140907672	1.21	Comp	9.22 - 10.24	-0.64 ± 0.22	113.1 ± 13.7	0.32 ± 0.12	45.3 ± 1.5
GRB 140808038	3.29	Comp	0.0 - 1.02	-0.23 ± 0.13	157.4 ± 10.8	11.1 ± 2.32	45.9 ± 1.3
GRB 140703026	3.14	Comp	10.24 - 11.26	-0.77 ± 0.15	271.9 ± 46.3	6.15 ± 1.68	47.3 ± 1.4
GRB 140620219	2.04	Comp	6.14 - 7.17	-0.91 ± 0.21	92.5 ± 12.0	1.68 ± 0.62	45.1 ± 1.5
GRB 140606133	0.384	Comp	1.02 - 2.05	-1.26 ± 0.05	845.1 ± 219.3	0.18 ± 0.04	45.6 ± 1.4
GRB 140512814	0.725	Comp	129.02 - 130.05	-1.0 ± 0.05	579.8 ± 79.0	0.73 ± 0.11	45.5 ± 1.3
GRB 140508128	1.027	Comp	4.1 - 5.12	-0.65 ± 0.03	454.0 ± 17.4	8.14 ± 0.50	43.6 ± 1.3
GRB 140506880	0.889	Comp	0.0 - 1.02	-0.7 ± 0.12	172.5 ± 14.5	0.79 ± 0.15	44.0 ± 1.4
GRB 140423356	3.26	Comp	-2.05 - -1.02	-0.69 ± 0.26	250.4 ± 65.2	4.33 ± 1.96	47.7 ± 1.5
GRB 140304557	5.283	Comp	7.17 - 8.19	-0.92 ± 0.26	295.3 ± 107.3	12.2 ± 5.92	48.8 ± 1.6
GRB 140213807	1.2076	Comp	6.14 - 7.17	-0.94 ± 0.04	92.4 ± 2.7	2.56 ± 0.219	42.68 ± 1.4
GRB 131231198	0.642	Comp	22.53 - 23.55	-0.84 ± 0.02	347.6 ± 8.3	2.89 ± 0.10	42.7 ± 1.3
GRB 131108862	2.4	Comp	0.0 - 1.02	-0.74 ± 0.04	483.9 ± 33.9	25.3 ± 2.51	45.7 ± 1.3
GRB 131105087	1.69	Comp	106.5 - 107.52	-1.03 ± 0.06	449.5 ± 64.6	3.67 ± 0.58	46.3 ± 1.3
GRB 131011741	1.874	Comp	4.1 - 5.12	-0.86 ± 0.16	402.0 ± 97.2	2.36 ± 0.78	47.0 ± 1.4
GRB 130612141	2.006	Comp	-1.02 - 0.0	-1.2 ± 0.39	64.3 ± 14.5	0.57 ± 0.36	45.6 ± 1.6
GRB 130610133	2.092	Comp	4.1 - 5.12	-1.1 ± 0.29	152.4 ± 38.7	1.12 ± 0.49	46.5 ± 1.5
GRB 130518580	2.488	Comp	25.6 - 26.62	-0.83 ± 0.02	635.7 ± 30.6	77.8 ± 4.62	45.1 ± 1.3
GRB 130427324	0.3399	Comp	8.19 - 9.22	-0.51 ± 0.0	805.5 ± 5.0	11.0 ± 0.11	40.7 ± 1.3
GRB 121211574	1.023	Comp	-1.02 - 0.0	-0.66 ± 0.45	112.6 ± 22.5	0.10 ± 0.07	45.9 ± 1.6
GRB 121128212	2.2	Comp	8.19 - 9.22	-0.47 ± 0.1	115.5 ± 6.0	6.08 ± 1.08	44.4 ± 1.4
GRB 120907017	0.97	Comp	-1.02 - 0.0	-0.94 ± 0.3	133.9 ± 31.8	0.22 ± 0.11	45.2 ± 1.5
GRB 120811649	2.671	Comp	3.07 - 4.1	-0.64 ± 0.39	69.2 ± 9.1	2.63 ± 1.51	45.2 ± 1.5
GRB 120716712	2.48	Comp	0.0 - 1.02	-0.83 ± 0.1	169.0 ± 16.7	5.11 ± 0.97	45.7 ± 1.4
GRB 120624933	2.1974	Comp	11.26 - 12.29	-0.83 ± 0.04	797.0 ± 74.9	26.8 ± 2.97	46.2 ± 1.4
GRB 120326056	1.798	Comp	1.02 - 2.05	-1.08 ± 0.13	77.7 ± 7.0	1.37 ± 0.34	44.5 ± 1.4
GRB 120119170	1.728	Comp	14.34 - 15.36	-0.91 ± 0.05	328.4 ± 25.4	6.61 ± 0.69	45.2 ± 1.3
GRB 120118709	2.943	Comp	5.12 - 6.14	-0.93 ± 0.34	66.9 ± 9.7	1.60 ± 0.80	46.0 ± 1.5
GRB 111107035	2.893	Comp	1.02 - 2.05	-0.74 ± 0.52	142.9 ± 40.3	1.72 ± 1.49	47.2 ± 1.7
GRB 110731465	2.83	Comp	0.0 - 1.02	-0.96 ± 0.07	176.3 ± 11.5	17.9 ± 2.05	45.0 ± 1.3
GRB 110213220	1.4607	Comp	18.43 - 19.46	-1.16 ± 0.09	92.2 ± 7.2	1.98 ± 0.36	43.7 ± 1.4

Continued on next page

B.4. THE BAND (F_{Band}) SPECTRAL FITTING PARAMETERS OF THE *FERMI*-GBM SAMPLE

Table B.3 – Continued from previous page

GRB 110128073	2.339	Comp	-2.05 - -1.02	-0.89 ± 0.36	300.2 ± 127.7	1.21 ± 0.71	48.1 ± 1.6
GRB 110106893	0.618	Comp	6.14 - 7.17	-1.18 ± 0.29	329.6 ± 119.3	0.06 ± 0.02	46.7 ± 1.5
GRB 100906576	1.727	Comp	10.24 - 11.26	-0.81 ± 0.09	207.0 ± 20.9	4.45 ± 0.77	44.8 ± 1.4
GRB 100816026	0.8049	Comp	1.02 - 2.05	-0.37 ± 0.09	138.9 ± 6.9	0.47 ± 0.07	43.8 ± 1.4
GRB 100728439	2.106	Comp	2.05 - 3.07	-0.93 ± 0.19	122.9 ± 20.5	1.83 ± 0.63	45.6 ± 1.4
GRB 100728095	1.567	Comp	81.92 - 82.94	-0.53 ± 0.08	511.0 ± 48.0	5.82 ± 0.90	45.8 ± 1.3
GRB 100704149	3.6	Comp	3.07 - 4.1	-0.55 ± 0.12	260.6 ± 29.1	15.1 ± 3.21	46.8 ± 1.3
GRB 100615083	1.398	Comp	10.24 - 11.26	-0.87 ± 0.14	89.9 ± 8.0	0.81 ± 0.22	44.4 ± 1.5
GRB 100414097	1.368	Comp	23.55 - 24.58	-0.75 ± 0.04	522.5 ± 32.4	7.48 ± 0.65	45.0 ± 1.3
GRB 100413732	3.9	Comp	113.66 - 114.69	-0.26 ± 0.54	282.6 ± 71.9	4.77 ± 2.68	48.5 ± 1.5
GRB 091208410	1.0633	Comp	8.19 - 9.22	-1.09 ± 0.06	191.2 ± 16.2	1.67 ± 0.20	44.0 ± 1.4
GRB 091127976	0.490	Comp	0.0 - 1.02	-1.16 ± 0.03	94.0 ± 2.5	0.52 ± 0.03	41.4 ± 1.5
GRB 091020900	1.71	Comp	2.05 - 3.07	-1.13 ± 0.09	656.7 ± 154.0	3.63 ± 0.79	47.0 ± 1.4
GRB 091003191	0.8969	Comp	18.43 - 19.46	-0.69 ± 0.03	482.0 ± 21.2	4.11 ± 0.27	44.0 ± 1.3
GRB 090926181	2.1062	Comp	3.07 - 4.1	-0.52 ± 0.02	385.6 ± 7.5	68.7 ± 2.39	43.7 ± 1.3
GRB 090618353	0.54	Comp	63.49 - 64.51	-0.96 ± 0.03	447.5 ± 20.2	1.84 ± 0.11	43.0 ± 1.3
GRB 090516353	4.109	Comp	28.67 - 29.7	-1.39 ± 0.15	448.0 ± 354.1	11.6 ± 5.5	48.5 ± 2.0
GRB 090424592	0.544	Comp	1.02 - 2.05	-0.86 ± 0.02	207.9 ± 4.5	1.38 ± 0.05	42.0 ± 1.4
GRB 090423330	8.26	Comp	-2.05 - -1.02	-0.61 ± 0.53	80.5 ± 13.1	14.2 ± 8.65	48.1 ± 1.5
GRB 090328401	0.736	Comp	23.55 - 24.58	-0.77 ± 0.04	463.2 ± 29.7	1.14 ± 0.10	44.6 ± 1.3
GRB 090323002	3.57	Comp	65.54 - 66.56	-0.55 ± 0.06	396.0 ± 27.2	43.8 ± 5.06	46.3 ± 1.3
GRB 090113778	1.7493	Comp	0.0 - 1.02	-0.58 ± 0.2	201.7 ± 30.2	1.04 ± 0.33	46.4 ± 1.4
GRB 090102122	1.547	Comp	15.62 - 16.64	-0.27 ± 0.07	377.7 ± 22.3	4.92 ± 0.60	45.4 ± 1.3
GRB 081222204	2.77	Comp	3.07 - 4.1	-0.8 ± 0.07	197.9 ± 14.7	11.2 ± 1.47	45.6 ± 1.3
GRB 081221681	2.26	Comp	20.48 - 21.5	-0.36 ± 0.06	119.1 ± 3.8	9.88 ± 1.12	44.0 ± 1.4
GRB 081121858	2.512	Comp	6.14 - 7.17	-0.62 ± 0.16	355.8 ± 52.6	8.36 ± 2.11	46.5 ± 1.4
GRB 081008832	1.9685	Comp	15.36 - 16.38	-0.65 ± 0.28	163.5 ± 37.7	0.94 ± 0.45	46.6 ± 1.5
GRB 080916406	0.689	Comp	2.05 - 3.07	-0.39 ± 0.15	239.1 ± 27.9	0.18 ± 0.05	45.2 ± 1.4
GRB 080916009	4.35	Comp	2.05 - 3.07	-0.77 ± 0.06	525.1 ± 55.6	83.9 ± 11.4	46.9 ± 1.4
GRB 080905705	2.3739	Comp	0.0 - 1.02	-0.74 ± 0.43	184.6 ± 47.8	1.1 ± 0.48	47.4 ± 1.5
GRB 080810549	3.3604	Comp	23.55 - 24.58	-1.13 ± 0.16	625.9 ± 240.2	10.5 ± 3.6	48.4 ± 1.6
GRB 080804972	2.2045	Comp	1.02 - 2.05	-0.22 ± 0.21	172.2 ± 20.1	1.96 ± 0.64	46.3 ± 1.4

Notes: γ is the photon index of Comp model. E_p is the Comp peak energy.

B.4 The Band (F_{Band}) spectral fitting parameters of the *Fermi*-GBM sample

APPENDIX B. THE *FERMI*-GBM AND *SWIFT*-BAT SPECTRAL FITTING PARAMETERS, AND REANALYSIS OF W2016 DATA

Table B.4 The result of the Band (F_{Band}) spectral fitting parameters of the *Fermi*-GBM sample integrated over T_{peak} for 46 GRBs (e.g., *Fermi*-GBM catalog, [Gruber et al., 2014](#); [von Kienlin et al., 2014](#); [Narayana Bhat et al., 2016a](#)).

GRB Name	z	Model	T_{peak} (s)	α	β	E_p (keV)	L_{iso} (10^{52} erg s $^{-1}$)	$\mu \pm \sigma_\mu$
GRB 171010792	0.3285	Band	33.79 - 34.82	-0.82 ± 0.02	-2.44 ± 0.08	299.5 ± 12.1	1.0 ± 0.1	42.6 ± 1.1
GRB 170705115	2.01	Band	9.22 - 10.24	-0.69 ± 0.09	-2.44 ± 0.25	166.6 ± 15.1	11.0 ± 2.5	45.1 ± 1.1
GRB 170607971	0.557	Band	2.05 - 3.07	-1.18 ± 0.13	-2.13 ± 0.19	130.5 ± 27.5	0.3 ± 0.1	44.1 ± 1.3
GRB 170405777	3.51	Band	29.7 - 30.72	-0.67 ± 0.07	-2.25 ± 0.32	323.9 ± 41.2	49.6 ± 10.2	46.7 ± 1.1
GRB 170214649	2.53	Band	61.44 - 62.46	-0.7 ± 0.07	-1.96 ± 0.12	455.2 ± 74.2	35.6 ± 6.7	46.4 ± 1.2
GRB 160625945	1.406	Band	188.5 - 189.5	-0.5 ± 0.01	-2.05 ± 0.02	593.7 ± 15.2	150.0 ± 5.6	43.0 ± 1.1
GRB 160509374	1.17	Band	16.38 - 17.41	-0.75 ± 0.02	-2.26 ± 0.07	345.3 ± 15.3	16.8 ± 1.2	43.9 ± 1.1
GRB 151027166	0.81	Band	0.0 - 1.02	-0.86 ± 0.1	-2.05 ± 0.19	224.1 ± 31.2	0.8 ± 0.3	45.1 ± 1.2
GRB 150821406	0.755	Band	15.36 - 16.38	-0.84 ± 0.09	-2.13 ± 0.33	290.6 ± 50.9	0.8 ± 0.3	45.4 ± 1.2
GRB 150514774	0.807	Band	1.02 - 2.05	-0.77 ± 0.15	-2.77 ± 0.28	55.1 ± 3.8	0.5 ± 0.2	43.4 ± 1.5
GRB 150403913	2.06	Band	11.26 - 12.29	-0.67 ± 0.03	-2.19 ± 0.08	509.3 ± 34.6	42.4 ± 3.9	45.6 ± 1.1
GRB 150314205	1.758	Band	2.05 - 3.07	-0.41 ± 0.03	-2.54 ± 0.09	298.0 ± 10.0	43.2 ± 3.1	44.1 ± 1.1
GRB 141221338	1.452	Band	0.0 - 1.02	-1.04 ± 0.18	-3.31 ± 7.81	305.8 ± 60.71	1.2 ± 0.9	47.3 ± 1.4
GRB 141028455	2.33	Band	12.29 - 13.31	-0.66 ± 0.05	-2.3 ± 0.18	438.6 ± 35.0	25.1 ± 3.1	46.4 ± 1.1
GRB 140808038	3.29	Band	0.0 - 1.02	-0.11 ± 0.16	-2.91 ± 0.82	144.1 ± 15.1	12.6 ± 4.9	46.6 ± 1.2
GRB 140801792	1.32	Band	1.02 - 2.05	0.03 ± 0.08	-3.78 ± 0.77	122.5 ± 4.2	2.9 ± 0.5	44.5 ± 1.2
GRB 140508128	1.027	Band	4.1 - 5.12	-0.55 ± 0.04	-2.43 ± 0.09	376.3 ± 19.0	9.7 ± 0.9	44.1 ± 1.1
GRB 140506880	0.889	Band	0.0 - 1.02	-0.49 ± 0.2	-2.44 ± 0.42	138.9 ± 16.5	1.0 ± 0.5	44.5 ± 1.3
GRB 140423356	3.26	Band	-2.05 - 1.02	-0.45 ± 0.41	-1.76 ± 0.52	159.6 ± 48.8	7.2 ± 6.5	47.4 ± 1.6
GRB 140213807	1.2076	Band	6.14 - 7.17	-0.84 ± 0.06	-2.89 ± 0.21	84.2 ± 3.2	2.8 ± 0.4	43.6 ± 1.3
GRB 140206304	2.73	Band	5.12 - 6.14	0.64 ± 0.21	-2.5 ± 0.15	112.1 ± 7.9	18.9 ± 7.7	45.1 ± 1.2
GRB 131231198	0.642	Band	22.53 - 23.55	-0.79 ± 0.02	-2.66 ± 0.13	312.7 ± 11.1	3.3 ± 0.2	43.4 ± 1.1
GRB 131108862	2.4	Band	0.0 - 1.02	-0.6 ± 0.06	-1.94 ± 0.07	332.6 ± 32.1	31.2 ± 4.4	45.8 ± 1.1
GRB 131011741	1.874	Band	4.1 - 5.12	-0.47 ± 0.43	-1.63 ± 0.13	168.2 ± 87.7	4.0 ± 3.9	46.0 ± 1.8
GRB 130518580	2.488	Band	25.6 - 26.62	-0.73 ± 0.03	-2.13 ± 0.08	469.0 ± 33.4	81.6 ± 7.2	45.4 ± 1.1
GRB 130427324	0.3399	Band	8.19 - 9.22	-0.45 ± 0.01	-3.13 ± 0.04	717.6 ± 6.0	11.4 ± 0.2	41.4 ± 1.1
GRB 120716712	2.48	Band	0.0 - 1.02	-0.39 ± 0.21	-2.14 ± 0.17	105.9 ± 16.8	7.0 ± 3.4	45.7 ± 1.3
GRB 120711115	1.41	Band	95.23 - 96.26	-0.83 ± 0.04	-2.21 ± 0.11	1360.8 ± 160.8	20.5 ± 2.4	46.6 ± 1.2
GRB 120624933	2.1974	Band	11.26 - 12.29	-0.79 ± 0.05	-2.34 ± 0.23	683.9 ± 79.5	27.3 ± 3.7	46.9 ± 1.2
GRB 120119170	1.728	Band	14.34 - 15.36	-0.84 ± 0.07	-2.35 ± 0.36	274.2 ± 29.5	7.9 ± 1.7	45.7 ± 1.1
GRB 110731465	2.83	Band	0.0 - 1.02	-0.96 ± 0.06	-4.38 ± 6.48	176.4 ± 12.9	18.1 ± 3.2	46.0 ± 1.1
GRB 100906576	1.727	Band	10.24 - 11.26	-0.61 ± 0.13	-2.14 ± 0.2	146.7 ± 20.1	6.2 ± 2.4	45.0 ± 1.2
GRB 100816026	0.8049	Band	1.02 - 2.05	-0.3 ± 0.1	-2.71 ± 0.31	130.4 ± 6.8	0.6 ± 0.1	44.6 ± 1.2

Continued on next page

Table B.4 – Continued from previous page

GRB 100728095	1.567	Band	81.92 - 82.94	-0.45 ± 0.09	-2.47 ± 0.38	445.7 ± 56.0	6.7 ± 1.6	46.3 ± 1.1
GRB 100704149	3.6	Band	3.07 - 4.1	-0.51 ± 0.12	-2.56 ± 1.97	241.6 ± 51.5	17.6 ± 12.4	47.5 ± 1.4
GRB 100414097	1.368	Band	23.55 - 24.58	-0.73 ± 0.05	-2.53 ± 0.65	480.6 ± 39.7	8.5 ± 1.8	45.7 ± 1.1
GRB 091208410	1.0633	Band	8.19 - 9.22	-0.95 ± 0.08	-2.2 ± 0.15	141.1 ± 15.4	2.2 ± 0.5	44.3 ± 1.2
GRB 091127976	0.490	Band	0.0 - 1.02	-0.51 ± 0.09	-2.27 ± 0.04	55.4 ± 2.6	0.7 ± 0.2	41.5 ± 1.5
GRB 091020900	1.71	Band	2.05 - 3.07	-0.91 ± 0.21	-1.67 ± 0.13	238.9 ± 101.9	4.6 ± 2.5	46.1 ± 1.4
GRB 091003191	0.8969	Band	18.43 - 19.46	-0.6 ± 0.04	-2.33 ± 0.15	393.5 ± 27.1	5.0 ± 0.6	44.5 ± 1.1
GRB 090926181	2.1062	Band	3.07 - 4.1	-0.46 ± 0.02	-2.68 ± 0.14	346.8 ± 10.8	76.7 ± 5.0	44.4 ± 1.1
GRB 090618353	0.54	Band	63.49 - 64.51	-0.94 ± 0.03	-2.87 ± 0.3	424.8 ± 24.5	2.0 ± 0.2	43.9 ± 1.1
GRB 090424592	0.544	Band	1.02 - 2.05	-0.83 ± 0.02	-3.04 ± 0.24	195.6 ± 6.4	1.5 ± 0.1	43.0 ± 1.2
GRB 090328401	0.736	Band	23.55 - 24.58	-0.77 ± 0.04	-4.46 ± 7.08	463.0 ± 31.0	1.2 ± 0.2	45.6 ± 1.1
GRB 081221681	2.26	Band	20.48 - 21.5	-0.32 ± 0.07	-3.88 ± 6.85	116.5 ± 4.4	10.2 ± 5.0	45.1 ± 1.2
GRB 081121858	2.512	Band	6.14 - 7.17	-0.21 ± 0.31	-1.77 ± 0.12	194.6 ± 45.4	12.6 ± 6.4	46.1 ± 1.3

B.5 Reanalysis of W2016 data

The dataset analyzed by Wang et al. (2016) contains 151 entries, until GRB 140213A, combining new data with old data from Amati et al. (2008) and Amati et al. (2009). Six *Fermi* GRBs which are common with our sample are GRB 080916C, GRB 090323, GRB 090902B, GRB 090926A, GRB 130427A, and GRB 130518A. A number of GRBs in Wang et al. (2016) are also counted twice. Here we have reanalyzed 94 GRBs (W2016 sample) from this data set which are not in our *Fermi*-LAT/GBM GRB sample and are not counted twice. The bolometric fluence S_{bolo} reported by Wang et al. (2016) has been converted to E_{iso} using the standard cosmological parameters and are reported in Table B.5 together with $E_{\text{i,p}}$. The E_{iso} has been calculated in the 1–10⁴ keV range.

Table B.5 The W2016 sample of 94 GRBs with E_{iso} updated from Amati et al. (2008, 2009); Wang et al. (2016). Instruments: SW = *Suzaku*-WAM, KW = *Konus*-Wind, SB = *Swift*-BAT, FG = *Fermi* GBM, HET = HETE-2, GRO = CGRO/BATSE and SAX = *BeppeSAX*

GRB Name	Instruments	z	$E_{\text{i,p}}$ (keV)	S_{bolo} (10 ⁻⁵ erg/cm ²)	E_{iso} (10 ⁵² erg)	$\mu \pm \sigma_\mu$
GRB 140213A	FG	1.21	176.6 ± 4.4	2.5 ± 0.0	9.9 ± 0.2	44.0 ± 1.0
GRB 140206A	FG	2.73	447.6 ± 22.4	1.7 ± 0.0	29.1 ± 0.5	46.1 ± 1.0
GRB 131117A	SB	4.04	221.9 ± 37.3	0.1 ± 0.0	1.6 ± 0.3	49.5 ± 1.0
GRB 131105A	FG	1.69	547.7 ± 83.5	4.8 ± 0.2	35.0 ± 1.2	44.9 ± 1.0
GRB 131030A	KW	1.29	405.9 ± 22.9	1.1 ± 0.1	4.7 ± 0.4	46.0 ± 1.0
GRB 130907A	KW	1.24	881.8 ± 24.6	75.2 ± 4.8	308.4 ± 19.5	42.2 ± 1.0
GRB 130831A	KW	0.48	81.4 ± 5.9	1.3 ± 0.1	0.8 ± 0.0	43.4 ± 1.0
GRB 130701A	KW	1.16	191.8 ± 8.6	0.5 ± 0.0	1.7 ± 0.1	46.0 ± 1.0
GRB 130612	FG	2.01	186.1 ± 31.6	0.1 ± 0.0	0.8 ± 0.1	48.2 ± 1.0
GRB 130610	FG	2.09	911.8 ± 132.7	0.8 ± 0.1	8.9 ± 0.5	47.5 ± 1.0

Continued on next page

APPENDIX B. THE *FERMI*-GBM AND *SWIFT*-BAT SPECTRAL FITTING PARAMETERS, AND REANALYSIS OF W2016 DATA

Table B.5 – Continued from previous page

GRB 130606	KW	5.91	2031.5 ± 483.7	0.5 ± 0.1	28.6 ± 5.3	49.9 ± 1.0
GRB 130514	KW/SB	3.6	496.8 ± 151.8	1.9 ± 0.3	51.0 ± 6.8	46.4 ± 1.1
GRB 130505	KW	2.27	2063.4 ± 101.4	4.6 ± 0.1	57.1 ± 1.1	46.7 ± 1.0
GRB 130420A	FG	1.3	128.6 ± 6.9	1.7 ± 0.1	7.8 ± 0.3	44.1 ± 1.0
GRB 130408	KW	3.76	1003.9 ± 138.0	1.0 ± 0.2	28.8 ± 5.0	47.9 ± 1.1
GRB 130215	FG	0.6	247.5 ± 100.6	4.8 ± 0.1	4.6 ± 0.1	43.4 ± 1.1
GRB 121128	KW	2.2	243.2 ± 12.8	0.9 ± 0.1	10.3 ± 0.8	46.0 ± 1.0
GRB 120922	SB	3.1	156.6 ± 0.0	1.6 ± 0.2	33.8 ± 3.8	45.1 ± 1.0
GRB 120909	KW	3.93	1651.6 ± 123.3	2.7 ± 0.2	84.0 ± 7.2	47.4 ± 1.0
GRB 120811C	SB	2.67	157.5 ± 20.9	0.7 ± 0.1	12.3 ± 1.2	45.8 ± 1.0
GRB 120802	SB	3.8	274.3 ± 93.0	0.4 ± 0.1	12.7 ± 2.1	47.3 ± 1.1
GRB 120724	SB	1.48	68.5 ± 18.6	0.2 ± 0.0	0.9 ± 0.1	46.1 ± 1.1
GRB 120326	FG	1.8	130.0 ± 10.3	0.4 ± 0.0	3.6 ± 0.2	45.9 ± 1.0
GRB 120119	KW	1.73	417.4 ± 54.6	4.6 ± 0.6	35.5 ± 4.5	44.6 ± 1.0
GRB 111209	KW	0.68	519.9 ± 88.9	69.5 ± 8.7	85.8 ± 10.8	41.4 ± 1.0
GRB 111107	FG	2.89	420.4 ± 124.6	0.2 ± 0.0	3.4 ± 0.6	48.5 ± 1.1
GRB 111008	KW	5.0	894.0 ± 240.0	1.1 ± 0.1	48.1 ± 5.0	48.0 ± 1.0
GRB 110818	FG	3.36	1117.5 ± 241.1	1.1 ± 0.1	25.5 ± 1.9	47.9 ± 1.0
GRB 110731	KW	2.83	1164.3 ± 49.8	2.5 ± 0.0	45.9 ± 0.2	46.8 ± 1.0
GRB 110715	KW	0.82	218.4 ± 20.9	2.7 ± 0.2	4.9 ± 0.4	44.0 ± 1.0
GRB 110503	KW	1.61	572.3 ± 51.0	2.8 ± 0.2	18.6 ± 1.4	45.5 ± 1.0
GRB 110422	KW	1.77	421.0 ± 13.9	9.3 ± 0.0	74.7 ± 0.2	43.9 ± 1.0
GRB 110213	KW	1.46	223.9 ± 70.1	1.6 ± 0.2	8.7 ± 1.3	45.0 ± 1.1
GRB 110205	KW/SB/SW	2.22	740.6 ± 322.0	3.3 ± 0.7	39.9 ± 8.2	45.8 ± 1.1
GRB 100906	KW	1.73	387.2 ± 244.1	3.6 ± 0.6	27.4 ± 4.2	44.8 ± 1.2
GRB 100814	KW	1.44	312.3 ± 48.8	1.4 ± 0.2	7.6 ± 1.3	45.5 ± 1.0
GRB 100704	KW	3.6	809.6 ± 135.7	0.7 ± 0.1	19.0 ± 1.9	48.0 ± 1.0
GRB 100621	KW	0.54	146.5 ± 23.9	5.8 ± 0.6	4.4 ± 0.5	42.5 ± 1.0
GRB 100413	SW	3.9	1783.6 ± 374.9	2.4 ± 0.8	72.8 ± 23.8	47.7 ± 1.1
GRB 091029	SB	2.752	230.0 ± 66.0	0.5 ± 0.0	8.2 ± 0.8	46.8 ± 1.0
GRB 091020	SB	1.71	280.0 ± 190.0	0.1 ± 0.03	0.8 ± 0.3	48.2 ± 1.3
GRB 090812	SB	2.452	2000.0 ± 700.0	3.1 ± 0.5	44.0 ± 7.6	47.1 ± 1.1
GRB 090715B	SB	3.0	536.0 ± 172.0	1.1 ± 0.2	22.0 ± 3.4	46.9 ± 1.1
GRB 090516	SB	4.109	971.0 ± 390.0	2.0 ± 0.4	65.7 ± 12.7	47.2 ± 1.1
GRB 090423	FG	8.2	491.0 ± 200.0	0.1 ± 0.0	11.2 ± 3.0	50.1 ± 1.1
GRB 090418	KW/SB	1.608	1567 ± 384	2.4 ± 0.6	15.8 ± 4.0	46.8 ± 1.1
GRB 090102	KW	1.547	1149.0 ± 166.0	3.5 ± 0.6	21.7 ± 3.9	46.0 ± 1.0
GRB 081222	FG	2.77	505.0 ± 34.0	1.7 ± 0.2	29.4 ± 3.0	46.3 ± 1.0
GRB 081121	KW	2.512	47.2 ± 1.1	1.7 ± 0.3	25.5 ± 4.9	43.4 ± 1.0
GRB 081118	SB/FG	2.58	147.0 ± 14.0	0.3 ± 0.1	4.2 ± 0.9	46.8 ± 1.0
GRB 081028	SB	3.038	234.0 ± 93.0	0.8 ± 0.1	16.7 ± 2.0	46.3 ± 1.1
GRB 081008	SB	1.9685	261.0 ± 52.0	1.0 ± 0.1	9.3 ± 0.9	45.9 ± 1.0
GRB 080913	KW/SB	6.695	710.0 ± 350.0	0.1 ± 0.0	8.4 ± 2.5	50.3 ± 1.2
GRB 080810	FG	3.35	1470.0 ± 180.0	1.8 ± 0.2	44.0 ± 4.8	47.6 ± 1.0
GRB 080721	KW	2.591	1741.0 ± 227.0	7.9 ± 1.4	123.6 ± 21.6	46.0 ± 1.0

Continued on next page

B.5. REANALYSIS OF W2016 DATA

Table B.5 – Continued from previous page

GRB 080607	KW	3.036	1691.0 ± 226.0	9.0 ± 0.5	184.1 ± 9.9	45.9 ± 1.0
GRB 080605	KW	1.6398	650.0 ± 55.0	3.4 ± 0.3	23.7 ± 2.0	45.4 ± 1.0
GRB 080603B	KW	2.69	376.0 ± 100.0	0.6 ± 0.1	10.7 ± 1.0	47.0 ± 1.0
GRB 080514B	KW	1.8	627.0 ± 65.0	2.0 ± 0.5	16.8 ± 4.0	46.0 ± 1.0
GRB 080413	SW/SB	2.433	584.0 ± 180.0	0.6 ± 0.1	7.9 ± 2.0	47.6 ± 1.1
GRB 080319C	KW	1.95	906.0 ± 272.0	1.5 ± 0.3	14.3 ± 2.9	46.8 ± 1.1
GRB 071020	KW	2.145	1013.0 ± 160.0	0.9 ± 0.4	9.9 ± 4.5	47.6 ± 1.1
GRB 071003	KW	1.604	2077 ± 286	5.32 ± 0.6	35.6 ± 3.9	46.3 ± 1.0
GRB 070125	KW	1.547	934.0 ± 148.0	13.3 ± 1.3	83.1 ± 8.1	44.3 ± 1.0
GRB 060927	SB	5.6	475.0 ± 47.0	0.3 ± 0.0	14.5 ± 2.2	48.8 ± 1.0
GRB 060908	SB	2.43	514.0 ± 102.0	0.7 ± 0.1	10.3 ± 1.0	47.1 ± 1.0
GRB 060707	SB	3.425	279.0 ± 28.0	0.2 ± 0.0	5.8 ± 1.0	47.9 ± 1.0
GRB 060526	SB	3.21	105.0 ± 21.0	0.1 ± 0.1	2.7 ± 1.4	47.5 ± 1.2
GRB 060418	KW	1.489	572.0 ± 143.0	2.3 ± 0.5	13.4 ± 2.9	45.6 ± 1.1
GRB 060206	SB	4.048	394.0 ± 46.0	0.1 ± 0.0	4.6 ± 1.0	49.0 ± 1.0
GRB 060124	KW	2.296	784.0 ± 285.0	3.4 ± 0.5	43.4 ± 6.4	45.9 ± 1.1
GRB 060115	SB	3.53	285.0 ± 34.0	0.3 ± 0.0	6.6 ± 1.1	47.9 ± 1.0
GRB 051109A	KW	2.346	539.0 ± 200.0	0.5 ± 0.1	6.8 ± 0.7	47.5 ± 1.1
GRB 050922C	HET	2.198	415.0 ± 111.0	0.5 ± 0.2	5.6 ± 1.9	47.3 ± 1.1
GRB 050904	KW/SB	6.29	3178 ± 1094.0	2.0 ± 0.2	127.7 ± 12.8	49.0 ± 1.1
GRB 050820	KW	2.612	1325.0 ± 277.0	6.4 ± 0.5	102.1 ± 8.0	45.9 ± 1.0
GRB 050603	KW	2.821	1333.0 ± 107.0	3.5 ± 0.2	63.6 ± 3.6	46.6 ± 1.0
GRB 050401	KW	2.9	467.0 ± 110.0	1.9 ± 0.4	36.2 ± 7.6	46.1 ± 1.1
GRB 050318	SB	1.44	115.0 ± 25.0	0.4 ± 0.0	2.3 ± 0.2	45.6 ± 1.0
GRB 040912	HET	1.563	44.0 ± 33.0	0.2 ± 0.1	1.3 ± 0.4	45.3 ± 1.4
GRB 030429	HET	2.65	128.0 ± 26.0	0.1 ± 0.0	2.3 ± 0.3	47.4 ± 1.0
GRB 030328	KW/HET	1.52	328.0 ± 55.0	6.4 ± 0.6	38.7 ± 3.6	43.9 ± 1.0
GRB 030323	HET	3.37	270.0 ± 113.0	0.1 ± 0.0	2.9 ± 1.0	48.6 ± 1.2
GRB 030226	HET	1.98	289.0 ± 66.0	1.3 ± 0.1	12.8 ± 1.0	45.7 ± 1.0
GRB 021004	HET	2.3	266.0 ± 117.0	0.3 ± 0.0	3.5 ± 0.5	47.4 ± 1.1
GRB 020127	HET	1.9	290.0 ± 100.0	0.4 ± 0.0	3.5 ± 0.1	47.0 ± 1.1
GRB 020124	HET/KW	3.2	448.0 ± 148.0	1.2 ± 0.1	26.9 ± 2.2	46.6 ± 1.1
GRB 011211	SAX	2.14	186.0 ± 24.0	0.5 ± 0.1	5.6 ± 0.7	46.3 ± 1.0
GRB 010222	KW	1.48	766.0 ± 30.0	14.6 ± 1.5	83.9 ± 8.6	44.0 ± 1.0
GRB 000926	KW	2.07	310.0 ± 20.0	2.6 ± 0.6	27.6 ± 6.4	45.0 ± 1.0
GRB 000131	GRO/KW	4.5	987.0 ± 416.0	4.8 ± 0.8	181.4 ± 30.9	46.4 ± 1.1
GRB 990510	SAX	1.619	423.0 ± 42.0	2.6 ± 0.4	17.7 ± 2.7	45.2 ± 1.0
GRB 990123	GRO/SAX/KW	1.6	1724.0 ± 466.0	35.8 ± 5.8	238.1 ± 38.6	44.0 ± 1.1
GRB 971214	SAX	3.42	685.0 ± 133.0	0.9 ± 0.1	21.7 ± 2.8	47.5 ± 1.0

DECORRELATION ENERGY AND MULTIVARIATE NORMAL DISTRIBUTION

Contents

C.1	The decorrelation energy	141
C.1.1	The computed decorrelation energy for different samples	142
C.1.2	The plots of the computed decorrelation energy for different samples .	143
C.2	Multivariate normal distribution and correlation	144

C.1 The decorrelation energy

In the previous sub-section §4.4.3 we have discussed the decorrelation energy and the butterfly plot, made from the lower and upper boundaries (i.e., $\pm\sigma_y$ defined in Eq. 4.38) around the best-fit. Now we will discuss some example that have been introduced to obtained the value of the decorrelation energy. As a preliminary, we chose the *Fermi*-GBM sample and performed the power law curve-fit. This results the estimated parameters: $k = 50.91 \pm 0.133$ and $m = 2.125 \pm 0.128$ with the covariance matrix

$$\text{cov} = \begin{bmatrix} 0.0176 & -0.0165 \\ -0.0165 & 0.0165 \end{bmatrix}.$$

Then $E_{0,\text{dec}}$ calculated as:

$$\begin{aligned} E_{0,\text{dec}} &= 10^{-\frac{C_{km}}{\sigma_m^2}} \text{ keV}, \\ &= 100 \times 10^{(\frac{0.016514}{0.0165})} \text{ keV}, \\ &= 1001.87 \approx 1000 \text{ keV}. \end{aligned} \tag{C.1}$$

We can plot the butterfly by making the lower and upper boundaries using σ_y ,

$$y = k + mx \pm \sigma_y. \tag{C.2}$$

The butterfly band can be sketched (see App. C.1.2) from the lower and upper boundaries of σ_y around fitting line of $y = k + mx$. For all samples used in the analysis of the Yonetoku and Amati relations, we computed including C_{km} , σ_m , x_{dec} and $E_{0,dec}$, which are reported in Tab. C.1.1.

C.1.1 The computed decorrelation energy for different samples

Table C.1 The result of curve fitting of the *Fermi*-GBM and *Swift*-BAT samples.

Sample	Model	Number of GRBs	C_{km}	σ_m^2	x_{dec}	$E_{0,dec}$ (keV)
GBM	Comp	90	-0.0165	0.0165	1.00086	1002 \approx 1000
	Band	46	-0.0688	0.0718	0.95765	907 \approx 900
	Best-model	78	-0.0172	0.0204	0.84320	697 \approx 700
BAT	Comp	38	-0.0513	0.0997	0.51462	327 \approx 350
GBM and BAT	Best-model	106	-0.0180	0.02474	0.72707	533 \approx 550



C.1.2 The plots of the computed decorrelation energy for different samples

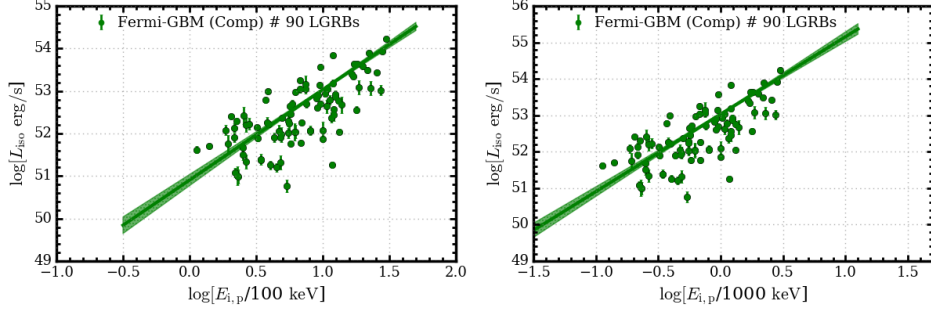


Figure C.1 *Fermi*-GBM sample with the Comp model of 90 GRBs. *Left panel* – The Yonetoku plane using the reference energy of $E_0 = 100 \text{ keV}$. *Right panel* – The Yonetoku plane after the decorrelation energy $E_{0,\text{dec}} = 1000 \text{ keV}$ is used.

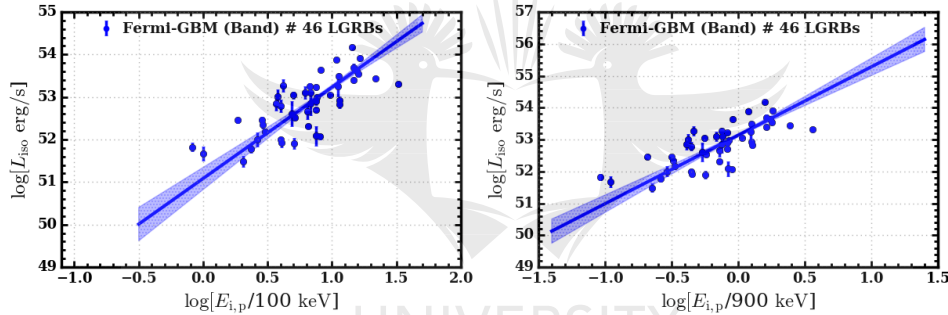


Figure C.2 *Fermi*-GBM sample with the Band spectral fitting model of 46 GRBs. *Left panel* – The Yonetoku plane using the reference energy of $E_0 = 100 \text{ keV}$. *Right panel* – The Yonetoku plane after the decorrelation energy $E_{0,\text{dec}} = 900 \text{ keV}$ is used.

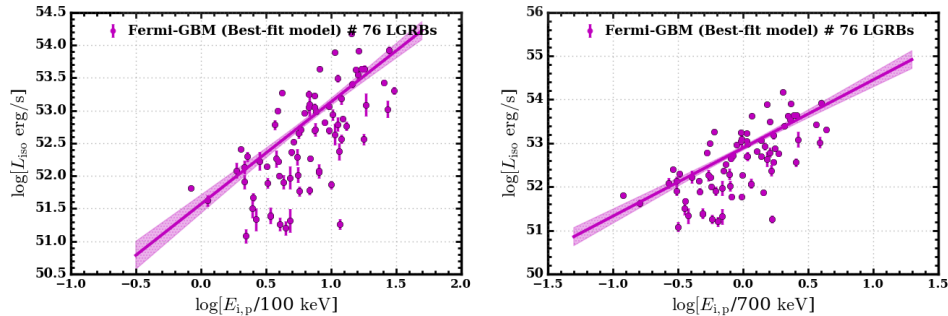


Figure C.3 *Fermi*-GBM sample with the best-fit spectral fitting model of 76 GRBs. *Left panel* – The Yonetoku plane using the reference energy of $E_0 = 100 \text{ keV}$. *Right panel* – The Yonetoku plane after the decorrelation energy $E_{0,\text{dec}} = 700 \text{ keV}$ is used.

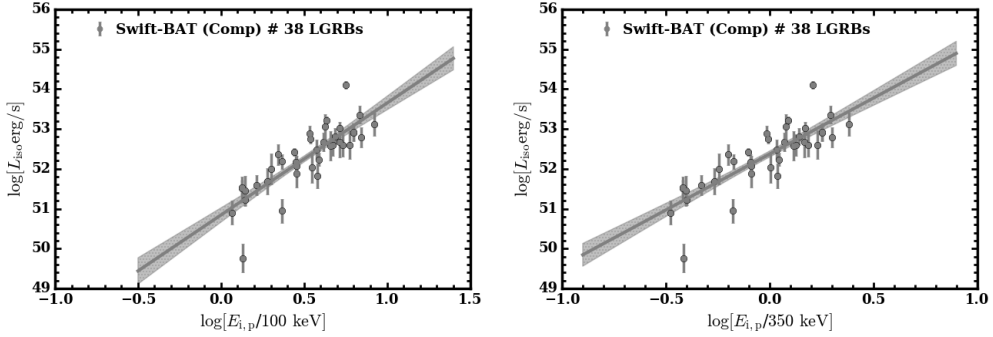


Figure C.4 *Swift-BAT* sample with the Comp spectral fitting model of 38 GRBs. *Left panel* – The Yonetoku plane using the reference energy of $E_0 = 100$ keV. *Right panel* – The Yonetoku plane after the decorrelation energy $E_{0,\text{dec}} = 350$ keV is used.

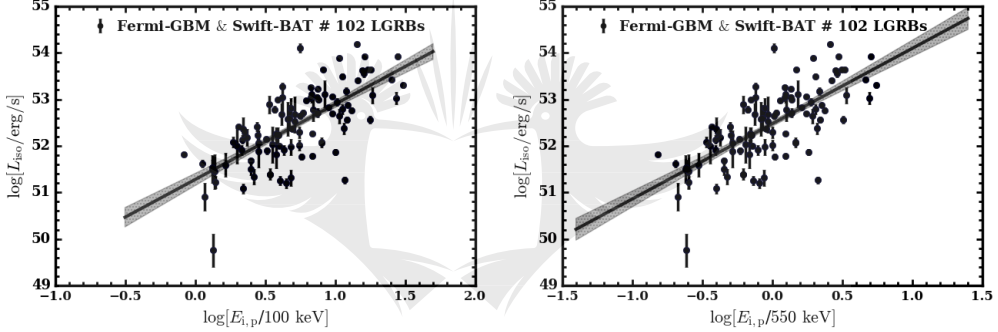


Figure C.5 *Fermi-GBM* and *Swift-BAT* samples with the best-fit model spectral fitting model of 102 GRBs. *Left panel* – The Yonetoku plane using the reference energy of $E_0 = 100$ keV. *Right panel* – The Yonetoku plane after the decorrelation energy $E_{0,\text{dec}} = 550$ keV is used.

C.2 Multivariate normal distribution and correlation

Here, we give a brief explanation of a multivariate normal (or Gaussian) distribution (MVN, [Do, 2008](#)). An important example of constructing a confidence interval is when the data consists of more than one measurements of parameter being estimated that follows the MVN distribution. For a set of 10,000 random variables x with mean \bar{x} and covariance matrix $V_{ij} = \text{cov}[x_i, x_j]$ for k -dimensional vectors we compute the density function of the MVN distribution as

$$F(x; \bar{x}, V) = \frac{1}{(2\pi)^{k/2}|V|^{1/2}} \exp\left(-\frac{1}{2}(x - \bar{x})^T V^{-1}(x - \bar{x})\right), \quad (\text{C.3})$$

where $(2\pi)^{k/2}|V|^{1/2}$ is the normalization constant and the determinant $|V| > 0$ is the variance.

Correlation (Corr)

The correlation coefficient ρ_{ij} between two variables i and j with means \bar{i} and \bar{j} and standard deviations σ_i and σ_j is given as

$$\rho_{ij} = \text{corr}(i, j) = \frac{\text{cov}(i, j)}{\sigma_i \sigma_j} = \frac{E[(i - \sigma_i)(j - \sigma_j)]}{\sigma_i \sigma_j}, \quad (\text{C.4})$$

where E is the expectation value operator and $\text{cov}(i, j)$ is the covariance of the two variables. This equation also called the Pearson product-moment correlation coefficient (ρ_p , Bevington et al., 1993). The Spearman's rank correlation coefficient (ρ_{sp} , Spearman, 1904) also describes the relationship between two variables based on the statistical ranking between two variables $r(i)$ and $r(j)$ given as follow:

$$\rho_{sp} = \frac{\text{cov}[r(i), r(j)]}{\sigma_{r(i)} \sigma_{r(j)}}, \quad (\text{C.5})$$

where $\text{cov}[r(i), r(j)]$ is the covariance of Pearson correlation, but applied to the rank variables, $\sigma_{r(i)}$ and $\sigma_{r(j)}$ are the standard deviations of the rank variables. In general, the Pearson correlation coefficients measure linear relationships while the Spearman's correlation coefficient measure a monotonic relationships. Both ρ_p and ρ_{sp} have the values between +1 and -1, where 1 is positive linear correlation, 0 is no linear correlation, and -1 is negative linear correlation.

Using the RMFIT software package, the GRB photon spectral fitting provide, the normed covariance matrix (i.e. the correlation coefficient matrix, ρ_{ij}) of the symmetric array numbers in the form

$$\rho_{ij} = \begin{bmatrix} 1.0 & \rho_{12} & \rho_{13} & \cdots & \rho_{1j} \\ \rho_{21} & 1.0 & \rho_{23} & \cdots & \rho_{2j} \\ \rho_{31} & \rho_{32} & 1.0 & \cdots & \rho_{3j} \\ \vdots & \vdots & \vdots & \ddots & \vdots \\ \rho_{i1} & \rho_{i2} & \rho_{i3} & \cdots & 1.0 \end{bmatrix}. \quad (\text{C.6})$$

The correlation of a variable with itself is one. Then the covariance matrix in terms of the correlation is given as

$$\text{cov}(\sigma_i, \sigma_j) = \sigma_{ij} = \rho_{ij} \sigma_i \sigma_j. \quad (\text{C.7})$$

The covariance of the data

$$\text{cov}(\sigma_i, \sigma_j) = \begin{bmatrix} \sigma_1^2 & \rho_{12}\sigma_1\sigma_2 & \rho_{13}\sigma_1\sigma_3 & \cdots & \rho_{1j}\sigma_1\sigma_j \\ \rho_{21}\sigma_2\sigma_1 & \sigma_2^2 & \rho_{23}\sigma_2\sigma_3 & \cdots & \rho_{2j}\sigma_2\sigma_j \\ \rho_{31}\sigma_3\sigma_1 & \rho_{32}\sigma_3\sigma_2 & \sigma_3^2 & \cdots & \rho_{3j}\sigma_3\sigma_j \\ \vdots & \vdots & \vdots & \ddots & \vdots \\ \rho_{i1}\sigma_i\sigma_1 & \rho_{i2}\sigma_i\sigma_2 & \rho_{i3}\sigma_i\sigma_3 & \cdots & \sigma_i\sigma_j \end{bmatrix}. \quad (\text{C.8})$$

Using the covariance from eq. C.8 and the values of the parameters obtained from the best-fit photon model of GRB prompt emission, we can model 1σ -limit error using the MVN distribution.



LIST OF PUBLICATIONS

Part of the research work presented in this thesis has already appeared or will appear in international accredited journal or peer-reviewed conference proceedings.

Publications on reviews with international accredited journal

- Dirirsa F. F., Razzaque S., Piron F., et al., 2019 “*Spectral analysis of Fermi-LAT gamma-ray bursts with known redshift and their potential use as cosmological standard candles*”, ApJ, 887, 1. doi: 10.3847/1538-4357/ab4e11
- Acciari, V.A., et al. 2019, “Observation of inverse Compton emission from a long γ -ray burst”, Nature 575, 459–463 doi:10.1038/s41586-019-1754-6
- Ajello M. et al., 2019 “*A Decade of Gamma-Ray Bursts Observed by Fermi-LAT: The Second GRB Catalog*”, ApJ, 878, 1. <https://arxiv.org/abs/1906.11403>
- Ackermann M. et al., 2018, “*Unresolved Gamma-Ray Sky through its Angular Power Spectrum*”, Phys. Rev. Lett., 121, 241101. <https://arxiv.org/abs/1812.02079>
- Ajello M., et al, 2019, “*Fermi and Swift Observations of GRB 190114C: Tracing the Evolution of High-Energy Emission from Prompt to Afterglow*”, ApJ (Accepted), <https://arXiv:1909.10605>
- Ajello M., et al., 2019, “*Bright γ -ray flares observed in GRB 131108A*”, ApJ (Accepted), <https://arxiv.org/abs/1911.04642>
- Abdollahi S., et al., 2019, “*Fermi Large Area Telescope Fourth Source Catalog*”, ApJ (Submitted), <https://arxiv.org/abs/1902.10045>
- Dirirsa F. F., Razzaque, S., Preece R., Omodei, N., et al., “*Fermi Observations of the Bright LAT GRB 160625B*”, the first draft is submitted to the public board of the *Fermi* collaboration. Manuscript will be submitted to MNRAS.

Peer-reviewed conference proceedings

- Dirirsa F. F. & Razzaque S., “*Yonetoku relation of Fermi-GBM and Swift-BAT Gamma-ray bursts*”, Proceedings of the 6th Annual Conference on HEASA2018, Parys, Free State, South Africa, PoS (2019) p.012.
- Dirirsa F. F. & Razzaque S., “*Correlation between intrinsic peak luminosity and spectral peak energy for energetic Fermi GRBs*”, Proceedings of the 5th Annual Conference on HEASA2017, PoS (2018) p.002.

LIST OF PUBLICATIONS

- Dirirsa F. F., Razzaque S. and Piron F., on behalf of the *Fermi*-LAT Collaboration, “*Spectral analysis of Fermi-LAT gamma-ray bursts with known redshift and their potential use as cosmological standard candles*”, Proceedings of the 62nd Annual Conference SAIP2017
- Dirirsa F. F., & *Fermi*-LAT Collaboration. 2016, “*Fermi Observations of the Bright LAT GRB 160625B*”, in Proceedings of the 4th Annual Conference on HEASA2016, 25-26 August, 2016, SAAO, Cape Town, South Africa, PoS (2017): 004.
- Dirirsa F. F. & Razzaque S., on behalf of the *Fermi*-LAT Collaboration, “*Isotropic energy and luminosity correlations with spectral peak energy for five long GRBs*”, Proceedings of the 61st Annual Conference SAIP2016, ISBN: 978-0-620-77094-1
- Dirirsa F. F. & Razzaque S., “*Gamma ray bursts (GRBs) as probes of Cosmological Parameters*”, Proceedings of SALT Science Conference 2015 -SSC2015-1-5 June, 2015, POS (SSC2015) 066
- Dirirsa F. F., Britto R. J. & Razzaque S., on behalf of the *Fermi*-LAT Collaboration, “*Spectral studies of flaring quasar PKS 1424-418 above 100 MeV with Fermi-LAT*”, Proceedings of the 60th Annual Conference SAIP2015, pp. 284 - 289. ISBN: 978-0-620-70714-5

LAT GRBs published in GCN circulars

- Ohno M., Longo F., Arimoto M., Axelsson M., and Dirirsa F., 2019, *GRB 190731A: Fermi-LAT detection*, GRB Coordinates Network, Circular Service, No. 25244, #1
- Axelsson M., Longo F., Arimoto M. and Dirirsa F., 2019, *GRB 190511A: Fermi-LAT detection*, GRB Coordinates Network, Circular Service, No. 24483, #1
- Dirirsa F., & Ohno M. 2018, *GRB 181231A: Fermi-LAT detection*, GRB Coordinates Network, Circular Service, No. 23597, #1
- Dirirsa F., & Bissaldi E. 2018, *GRB 180210A: Fermi-LAT detection*, GRB Coordinates Network, Circular Service, No. 22408, #1
- Dirirsa F., Vianello G., Tak D., Racusin J., & Kocevski D. 2017, *GRB 170206A: Fermi-LAT detection*, GRB Coordinates Network, Circular Service, No. 20617, #1
- Racusin J., Dirirsa F., Longo F., McEnery J., & Vianello G., 2016, *GRB 160816A: Fermi-LAT detection*, GRB Coordinates Network, Circular Service, No. 19802, #1
- Dirirsa F., Vianello G., Racusin J., & Axelsson M., 2016, *GRB 160625B: Fermi-LAT refined analysis*, GRB Coordinates Network, Circular Service, No. 19586, #1
- Vianello G., Dirirsa F., Omodei N., et al. 2016, *GRB 160623A / Galactic transient: Fermi-LAT detection*, GRB Coordinates Network, Circular Service, No. 19553, #1
- Axelsson M., Bissaldi E., McEnery J., Dirirsa F., & Burgess J. 2016, *GRB 160521B: Fermi-LAT detection*, GRB Coordinates Network, Circular Service, No. 19444, #1
- Longo F., Bissaldi E., Vianello G., Moretti, Omodei N. Bregeon J., Dirirsa F., et al. 2016, *GRB 160509A: Fermi-LAT refined analysis*, GRB Coordinates Network, Circular Service, No. 19413, #1

BIBLIOGRAPHY

- Abbott B. P., et al., 2017, *The Astrophysical Journal Letters*, **848**, L13
- Abdo A. A., et al., 2009, *The Astrophysical Journal Letters*, **706**, L138
- Ackermann M., et al., 2010, *The Astrophysical Journal*, **716**, 1178
- Ackermann M., et al., 2011, *The Astrophysical Journal*, **729**, 114
- Ackermann M., et al., 2012, *The Astrophysical Journal Supplement*, **203**, 4
- Ackermann M., et al., 2013a, *The Astrophysical Journal Supplement*, **209**, 11
- Ackermann M., et al., 2013b, *The Astrophysical Journal*, **771**, 57
- Actis M., et al., 2011, *Experimental Astronomy*, **32**, 193
- Afonso P., et al., 2011, *Astronomy & Astrophysics*, **526**, A154
- Aharonian F., et al., 2009, *Astronomy & Astrophysics*, **495**, 505
- Amati L., 2006a, *Monthly Notices of the Royal Astronomical Society*, **372**, 233
- Amati L., 2006b, *Monthly Notices of the Royal Astronomical Society*, **372**, 233
- Amati L., et al., 2002, *Astronomy & Astrophysics*, **390**, 81
- Amati L., Guidorzi C., Frontera F., Della Valle M., Finelli F., Landi R., Montanari E., 2008, *Monthly Notices of the Royal Astronomical Society*, **391**, 577
- Amati L., Frontera F., Guidorzi C., 2009, *Astronomy & Astrophysics*, **508**, 173
- Atteia J. L., et al., 1987, *The Astrophysical Journal Supplement Series*, **64**, 305
- Atteia J.-L., et al., 2017, *The Astrophysical Journal*, **837**, 119
- Atwood W. B., et al., 2009, *The Astrophysical Journal*, **697**, 1071
- Atwood W., et al., 2013, preprint, ([arXiv:1303.3514](https://arxiv.org/abs/1303.3514))
- Axelsson M., et al., 2012, *The Astrophysical Journal Letters*, **757**, L31

BIBLIOGRAPHY

- Axelsson M., Bissaldi E., McEnery J., Dirirsa F., Burgess J. M., 2016, GRB Coordinates Network, [19444, 1](#)
- Axelsson M., Longo F., Arimoto M., Dirirsa F., 2019, GRB Coordinates Network, [24483, 1](#)
- Band D., et al., 1993, [The Astrophysical Journal, 413, 281](#)
- Barkana R., Loeb A., 2001, [Physics Reports, 349, 125](#)
- Barthelmy S. D., Butterworth P., Cline T. L., Gehrels N., Fishman G. J., Kouveliotou C., Meegan C. A., 1995, [Astrophysics and Space Science, 231, 235](#)
- Barthelmy S. D., et al., 2005, [Space Science Reviews, 120, 143](#)
- Bennett C. L., et al., 2013, [The Astrophysical Journal Supplement Series, 208, 20](#)
- Berger E., 2011, GRB Coordinates Network, [12193, 1](#)
- Berger E., Mulchaey J., 2005, GRB Coordinates Network, [3122, 1](#)
- Berger E., Rauch M., 2008, GRB Coordinates Network, [8542, 1](#)
- Bevington P. R., Robinson D. K., Blair J. M., Mallinckrodt A. J., McKay S., 1993, Computers in Physics, [7, 415](#)
- Bissaldi E., Omodei N., Vianello G., Kocevski D., Fermi-LAT Collaboration 2017, in Proceedings of the 7th International Fermi Symposium, held 15-20 October 2017, in Garmisch-Partenkirchen, Germany (IFS2017), id.65. p. 65
- Bloom J. S., Djorgovski S. G., Kulkarni S. R., Frail D. A., 1998, [The Astrophysical Journal Letters, 507, L25](#)
- Boella G., Butler R. C., Perola G. C., Piro L., Scarsi L., Bleeker J. A. M., 1997, [Astronomy & Astrophysics, Supplement, 122, 299](#)
- Bregeon J., Charles E., M. Wood for the Fermi-LAT collaboration 2013, preprint, ([arXiv:1304.5456](#))
- Briggs M. S., et al., 1996, [The Astrophysical Journal, 459, 40](#)
- Briggs M. S., Pendleton G. N., Kippen R. M., Brainerd J. J., Hurley K., Connaughton V., Meegan C. A., 1999a, [The Astrophysical Journal, Supplement, 122, 503](#)
- Briggs M. S., et al., 1999b, [The Astrophysical Journal, 524, 82](#)
- Bromm V., Schaefer B. E., 1999, [The Astrophysical Journal, 520, 661](#)
- Burrows D. N., et al., 2005, [Space Science Reviews, 120, 165](#)

BIBLIOGRAPHY

- Butler N. R., Kocevski D., Bloom J. S., Curtis J. L., 2007, [The Astrophysical Journal](#), **671**, 656
- Butler N. R., Kocevski D., Bloom J. S., 2009, [The Astrophysical Journal](#), **694**, 76
- Butler N. R., Bloom J. S., Poznanski D., 2010, [The Astrophysical Journal](#), **711**, 495
- Campana S., Grupe D., 2010, GRB Coordinates Network, [10940](#), 1
- Cano Z., Malesani D., de Ugarte Postigo A., Izzo L., Thoene C. C., Castro-Rodriguez N., 2016, GRB Coordinates Network, [20245](#), 1
- Cardone V. F., Capozziello S., Dainotti M. G., 2009, [Monthly Notices of the Royal Astronomical Society](#), **400**, 775
- Carroll S. M., 2001, [Living Reviews in Relativity](#), **4**, 1
- Cash W., 1979, [The Astrophysical Journal](#), **228**, 939
- Castro-Tirado A. J., et al., 2014a, GRB Coordinates Network, [16505](#), 1
- Castro-Tirado A. J., Gorosabel J., Garcia-Rodriguez A., 2014b, GRB Coordinates Network, [16797](#), 1
- Castro-Tirado A. J., et al., 2016, GRB Coordinates Network, [19632](#), 1
- Cavallo G., Rees M. J., 1978, [Monthly Notices of the Royal Astronomical Society](#), **183**, 359
- Cenko S. B., Cucchiara A., Fox D. B., Berger E., Price P. A., 2007, GRB Coordinates Network, [6888](#), 1
- Cenko S. B., Rau A., Salvato M., 2009a, GRB Coordinates Network, [8773](#), 1
- Cenko S. B., Bloom J. S., Morgan A. N., Perley D. A., 2009b, GRB Coordinates Network, [9053](#), 1
- Cenko S. B., Perley D. A., Junkkarinen V., Burbidge M., Diego U. S., Miller K., 2009c, GRB Coordinates Network, [9518](#), 1
- Cherenkov Telescope Array Consortium T., et al., 2017, preprint, ([arXiv:1709.07997](#))
- Chornock R., Perley D. A., Cenko S. B., Bloom J. S., 2009a, GRB Coordinates Network, [9028](#), 1
- Chornock R., Perley D. A., Cenko S. B., Bloom J. S., 2009b, GRB Coordinates Network, [9028](#), 1
- Chornock R., Perley D. A., Cenko S. B., Bloom J. S., 2009c, GRB Coordinates Network, [9243](#), 1
- Chornock R., Perley D. A., Cobb B. E., 2009d, GRB Coordinates Network, [10100](#), 1
- Christensen N., 2018, Encyclopedia of Modern Optics, p. 432

BIBLIOGRAPHY

- Collazzi A. C., Schaefer B. E., Goldstein A., Preece R. D., 2012, *The Astrophysical Journal*, **747**, 39
- Cordier B., Götz D., Motch C., 2018, preprint, ([arXiv:1802.01681](https://arxiv.org/abs/1802.01681))
- Costa E., et al., 1997, *Nature*, **387**, 783
- Cucchiara A., 2010, GRB Coordinates Network, **10608**, 1
- Cucchiara A., 2014, GRB Coordinates Network, **15652**, 1
- Cucchiara A., Prochaska J. X., 2012, GRB Coordinates Network, **12865**, 1
- Cucchiara A., Fox D. B., Cenko S. B., Berger E., 2008a, GRB Coordinates Network, **8065**, 1
- Cucchiara A., Fox D. B., Cenko S. B., Berger E., 2008b, GRB Coordinates Network, **8346**, 1
- Cucchiara A., Fox D. B., Cenko S. B., Berger E., 2008c, GRB Coordinates Network, **8713**, 1
- Cucchiara A., Fox D. B., Tanvir N., Berger E., 2009a, GRB Coordinates Network, **9873**, 1
- Cucchiara A., Fox D. B., Cenko S. B., Tanvir N., Berger E., 2009b, GRB Coordinates Network, **10031**, 1
- Cucchiara A., Fox D., Levan A., Tanvir N., 2009c, GRB Coordinates Network, **10202**, 1
- Cucchiara A., et al., 2011, *The Astrophysical Journal*, **736**, 7
- D'Agostini G., 2005, Fits, and especially linear fits, with errors on both axes, extra variance of the data points and other complications ([arXiv:physics/0511182](https://arxiv.org/abs/physics/0511182))
- D'Elia V., et al., 2015, GRB Coordinates Network, **18187**, 1
- Dai Z. G., Liang E. W., Xu D., 2004, *The Astrophysical Journal Letters*, **612**, L101
- Dainotti M. G., Amati L., 2018, *Publications of the Astronomical Society of the Pacific*, **130**, 051001
- Davis J. E., 2001, *The Astrophysical Journal*, **548**, 1010
- Debono I., Smoot G. F., 2016, *Universe*, **2**, 23
- Demianski M., Piedipalumbo E., 2011, *Monthly Notices of the Royal Astronomical Society*, **415**, 3580
- Demianski M., Piedipalumbo E., Sawant D., Amati L., 2017, *Astronomy & Astrophysics*, **598**, A112

- Dirirsa F., Bissaldi E., 2018, GRB Coordinates Network, [22408](#), 1
- Dirirsa F. F., Fermi-LAT Collaboration 2016, in Proceedings of the 4th Annual Conference on High Energy Astrophysics in Southern Africa (HEASA 2016). 25-26 August. p. 4
- Dirirsa F., Ohno M., 2018, GRB Coordinates Network, [23597](#), 1
- Dirirsa F. F., Razzaque S., 2015, in SALT Science Conference 2015 (SSC2015). p. 66
- Dirirsa F., Vianello G., Racusin J., Axelsson M., 2016, GRB Coordinates Network, [19586](#), 1
- Dirirsa F. F., Razzaque S., Frédéric P., 2017a, The Proceedings of the 62nd Annual Conference of the South African Institute of Physics (SAIP2017), pp [184 – 289](#)
- Dirirsa F., Vianello G., Tak D., Racusin J., Kocevski D., 2017b, GRB Coordinates Network, 20617, 1
- Dirirsa F. F., et al., 2019, Spectral analysis of Fermi-LAT gamma-ray bursts with known redshift and their potential use as cosmological standard candles ([arXiv:1910.07009](#))
- Do C. B., 2008, Section Notes, Lecture on Machine Learning, CS, 229
- Eichler D., Levinson A., 2004, [The Astrophysical Journal Letter](#), **614**, L13
- Eichler D., Livio M., Piran T., Schramm D. N., 1989, [Nature](#), **340**, 126
- Eisenstein D. J., et al., 2005, [The Astrophysical Journal](#), **633**, 560
- Fenimore E. E., Ramirez-Ruiz E., 2000, Redshifts For 220 BATSE Gamma-Ray Bursts Determined by Variability and the Cosmological Consequences ([arXiv:astro-ph/0004176](#))
- Fermi.gsfc.nasa.gov 2017, https://fermi.gsfc.nasa.gov/ssc/observations/types/grbs/lat_grbs/
- Feroci M., et al., 2007, [Nuclear Instruments and Methods in Physics Research A](#), **581**, 728
- Firmani C., Ghisellini G., Ghirlanda G., Avila-Reese V., 2005, [Monthly Notices of the RAS](#), **360**, L1
- Fishman G. J., Meegan C. A., 1995, [Annual Review of Astron and Astrophys](#), **33**, 415
- Fishman G. J., Meegan C. A., Parnell T. A., Wilson R. B., Paciesas W., Mateson J. L., Cline T. L., Teegarden B. J., 1985, in Jones F. C., ed., International Cosmic Ray Conference Vol. 3, 19th International Cosmic Ray Conference (ICRC19).
- Fitzpatrick G., McBreen S., Connaughton V., Briggs M., 2012, in Space Telescopes and Instrumentation 2012: Ultraviolet to Gamma Ray. p. 84433B ([arXiv:1210.5369](#)), doi:[10.1117/12.928036](#)

BIBLIOGRAPHY

- Flores H., et al., 2010, GRB Coordinates Network, [11317](#), 1
- Fox D. W., et al., 2003, [The Astrophysical Journal Letters](#), [586](#), L5
- Fox D. B., et al., 2005, [Nature](#), [437](#), 845
- Frail D. A., Kulkarni S. R., Nicastro L., Feroci M., Taylor G. B., 1997, [Nature](#), [389](#), 261
- Friedmann A., 1922, [Zeitschrift fur Physik](#), [10](#), 377
- Frieman J. A., Turner M. S., Huterer D., 2008, [Annu. Rev. Astron. Astrophys.](#), [46](#), 385
- Funk S., Hinton J. A., CTA Consortium 2013, [Astroparticle Physics](#), [43](#), 348
- Fynbo J. P. U., et al., 2005, GRB Coordinates Network, [3176](#)
- Fynbo J. P. U., Limousin M., Castro Cerón J. M., Jensen B. L., Naranen J., 2006, GRB Coordinates Network, [4692](#), 1
- Fynbo J. P. U., Malesani D., Hjorth J., Sollerman J., Thoene C. C., 2008, GRB Coordinates Network, [8254](#), 1
- Fynbo J. P. U., et al., 2009, [The Astrophysical Journal Supplement Series](#), [185](#), 526
- Fynbo J. P. U., Xu D., Jakobsson P., Armstrong D., Cardenes R., 2012, GRB Coordinates Network, [13632](#), 1
- Fynbo J. P. U., Tanvir N. R., Jakobsson P., Xu D., Malesani D., Milvang-Jensen B., 2014, GRB Coordinates Network, [16217](#), 1
- Galama T. J., et al., 1999, [Astronomy and Astrophysics Supplement Series](#), [138](#), 465
- Galli M., et al., 2013, [Astronomy & Astrophysics](#), [553](#), A33
- Gehrels N., 2004, in Schoenfelder V., Lichti G., Winkler C., eds, ESA Special Publication Vol. 552, 5th INTEGRAL Workshop on the INTEGRAL Universe. p. 777
- Gehrels N., Razzaque S., 2013, [Frontiers of Physics](#), [8](#), 661
- Gehrels N., et al., 2005, [Nature](#), [437](#), 851
- Gehrels N., Ramirez-Ruiz E., Fox D. B., 2009, [Annual Review of Astron and Astrophys.](#), [47](#), 567
- Ghirlanda G., 2009, in Giobbi G., Tornambe A., Raimondo G., Limongi M., Antonelli L. A., Menci N., Brocato E., eds, American Institute of Physics Conference Series Vol. 1111, American Institute of Physics Conference Series. pp 579–586 ([arXiv:0908.1930](#)), doi:[10.1063/1.3141613](#)
- Ghirlanda G., Celotti A., Ghisellini G., 2003, [Astronomy & Astrophysics](#), [406](#), 879

BIBLIOGRAPHY

- Ghirlanda G., Ghisellini G., Lazzati D., Firmani C., 2004a, *The Astrophysical Journal Letters*, **613**, L13
- Ghirlanda G., Ghisellini G., Lazzati D., 2004b, *The Astrophysical Journal*, **616**, 331
- Ghirlanda G., Ghisellini G., Firmani C., 2005, *Monthly Notices of the Royal Astronomical Society*, **361**, L10
- Ghirlanda G., Ghisellini G., Firmani C., 2006, *New Journal of Physics*, **8**, 123
- Ghirlanda G., Nava L., Ghisellini G., Firmani C., Cabrera J. I., 2008, *Monthly Notices of the Royal Astronomical Society*, **387**, 319
- Ghirlanda G., Nava L., Ghisellini G., Celotti A., Firmani C., 2009, *Astronomy & Astrophysics*, **496**, 585
- Ghirlanda G., Nava L., Ghisellini G., 2010, *Astronomy & Astrophysics*, **511**, A43
- Ghirlanda G., Nava L., Ghisellini G., Celotti A., Burlon D., Covino S., Melandri A., 2012a, *Monthly Notices of the Royal Astronomical Society*, **420**, 483
- Ghirlanda G., et al., 2012b, *Monthly Notices of the Royal Astronomical Society*, **422**, 2553
- Gilmore R. C., Madau P., Primack J. R., Somerville R. S., Haardt F., 2009, *Monthly Notices of the Royal Astronomical Society*, **399**, 1694
- Gilmore R. C., Bouvier A., Connaughton V., Goldstein A., Otte N., Primack J. R., Williams D. A., 2013, *Experimental Astronomy*, **35**, 413
- Giuliani A., et al., 2008, *Astronomy & Astrophysics*, **491**, L25
- Goldstein A., et al., 2012, *The Astrophysical Journal Supplement Series*, **199**, 19
- Golenetskii S. V., Mazets E. P., Aptekar R. L., Ilinskii V. N., 1983, *Nature*, **306**, 451
- Gomboc A., 2012, *Contemporary Physics*, **53**, 339
- Gompertz B. P., O'Brien P. T., Wynn G. A., 2014, *Monthly Notices of the Royal Astronomical Society*, **438**, 240
- González M. M., Dingus B. L., Kaneko Y., Preece R. D., Dermer C. D., Briggs M. S., 2003, *Nature*, **424**, 749
- Gorosabel J., de Ugarte Postigo A., Thoene C., Perley D., Garcia Rodriguez A., 2014a, GRB Coordinates Network, **16671**, 1

BIBLIOGRAPHY

- Gorosabel J., de Ugarte Postigo A., Thoene C. C., Tanvir N., Fynbo J. P. U., Garcia-Alvarez D., Perez-Romero A., 2014b, GRB Coordinates Network, [17234](#), 1
- Graziani C., 2011, [New Astronomy](#), **16**, 57
- Greiner J., et al., 2009, [Astronomy & Astrophysics](#), **498**, 89
- Greiner J., Rau A., Schady P., Saviane I., Cenko B., 2012, GRB Coordinates Network, [13493](#), 1
- Groot P. J., et al., 1997, IAU Circ., **6588**
- Groot P. J., et al., 1998, [The Astrophysical Journal Letters](#), **493**, L27
- Gruber D., et al., 2014, [The Astrophysical Journal](#), **211**, 12
- Guiriec S., et al., 2011, [The Astrophysical Journal Letters](#), **727**, L33
- Guiriec S., et al., 2013, [The Astrophysical Journal](#), **770**, 32
- Guiriec S., et al., 2015a, [The Astrophysical Journal](#), **807**, 148
- Guiriec S., Mochkovitch R., Piran T., Daigne F., Kouveliotou C., Racusin J., Gehrels N., McEnery J., 2015b, [The Astrophysical Journal](#), **814**, 10
- Hakkila J., Giblin T. W., Norris J. P., Fragile P. C., Bonnell J. T., 2008, [Astrophysical Journal, Letters](#), **677**, L81
- Heussaff V., Atteia J.-L., Zolnierowski Y., 2013, [Astronomy & Astrophysics](#), **557**, A100
- Hinshaw G., et al., 2013, [The Astrophysical Journal Supplement Series](#), **208**, 19
- Hinton J. A., et al., 2004, [New Astronomy Reviews](#), **48**, 331
- Hjorth J., et al., 2003, [Nature](#), **423**, 847
- Hogg D. W., 1999, arXiv e-prints, [pp astro-ph/9905116](#)
- Hogg D. W., Bovy J., Lang D., 2010, arXiv e-prints, [p. arXiv:1008.4686](#)
- Holland S. T., Page K. L., 2008, GRB Coordinates Network, [8095](#), 1
- Host Lyman-alpha 2006, Preliminary Keck GRB Host Project, [p.](http://www.astro.caltech.edu/grbhosts/)
<http://www.astro.caltech.edu/grbhosts/>
- Howell E. J., Coward D. M., 2013, [Monthly Notices of the Royal Astronomical Society](#), **428**, 167
- Hunt L. K., et al., 2014, [Astronomy & Astrophysics](#), **565**, A112
- Hurley K., et al., 1994, [Nature](#), **372**, 652

- Hutchins J. B., 1976, [The Astrophysical Journal](#), **205**, 103
- Jakobsson P., Fynbo J. P. U., Paraficz D., Telting J., Jensen B. L., Hjorth J., Castro Cerón J. M., 2005, GRB Coordinates Network, [4029](#), 1
- Jakobsson P., et al., 2007, GRB Coordinates Network, [6398](#), 1
- Jakobsson P., et al., 2012, [The Astrophysical Journal](#), **752**, 62
- Jeong S., Sanchez-Ramirez R., Gorosabel J., Castro-Tirado A., 2014, GRB Coordinates Network, [15936](#), 1
- Jimenez R., Verde L., Treu T., Stern D., 2003, [The Astrophysical Journal](#), **593**, 622
- Jones D. O., et al., 2013, [The Astrophysical Journal](#), **768**, 166
- Kaneko Y., Preece R. D., Briggs M. S., Paciesas W. S., Meegan C. A., Band D. L., 2006, [The Astrophysical Journal Supplement Series](#), **166**, 298
- Kankare E., et al., 2017, GRB Coordinates Network, [22002](#), 1
- Kasliwal M. M., Cenko S. B., Singer L. P., 2014, GRB Coordinates Network, [16425](#), 1
- Klebesadel R. W., Strong I. B., Olson R. A., 1973, [The Astrophysical Journal Letters](#), **182**, L85
- Kocevski D., 2012, [The Astrophysical Journal](#), **747**, 146
- Kouveliotou C., Meegan C. A., Fishman G. J., Bhat N. P., Briggs M. S., Koshut T. M., Paciesas W. S., Pendleton G. N., 1993, [The Astrophysical Journal Letters](#), **413**, L101
- Krayzel F., et al., 2013, preprint, ([arXiv:1307.6461](#))
- Krisciunas K., Phillips M. M., Suntzeff N. B., 2004, [The Astrophysical Journal Letters](#), **602**, L81
- Kruehler T., Greiner J., Kann D. A., 2010, GRB Coordinates Network, [14500](#), 1
- Kruehler T., Malesani D., Xu D., Fynbo J. P. U., Levan A. J., Tanvir N. R., D'Elia V., Perley D., 2013, GRB Coordinates Network, [14264](#), 1
- Kruehler T., Schady P., Greiner J., Tanvir N. R., 2017, GRB Coordinates Network, [20686](#), 1
- Krühler T., et al., 2012, [The Astrophysical Journal](#), **758**, 46
- Kulkarni S. R., et al., 1998, [Nature](#), **395**, 663
- Levan A. J., Cenko S. B., Perley D. A., Tanvir N. R., 2013, GRB Coordinates Network, [14455](#), 1
- Levan A. J., et al., 2014, [The Astrophysical Journal](#), **781**, 13

BIBLIOGRAPHY

- Levinson A., Eichler D., 2005, *The Astrophysical Journal Letter*, **629**, L13
- Li L.-X., 2007, *Monthly Notices of the RAS*, **379**, L55
- Li H., Xia J.-Q., Liu J., Zhao G.-B., Fan Z.-H., Zhang X., 2008, *The Astrophysical Journal*, **680**, 92
- Liang E., Zhang B., 2005, *The Astrophysical Journal*, **633**, 611
- Lien A., et al., 2016, *The Astrophysical Journal*, **829**, 7
- Lin H.-N., Li X., Chang Z., 2016, *Monthly Notices of the Royal Astronomical Society*, **459**, 2501
- Lipunov V. M., et al., 2004, *Astronomische Nachrichten*, **325**, 580
- Longo F., et al., 2016, GRB Coordinates Network, **19413**, 1
- MacFadyen A. I., Woosley S. E., 1999, *The Astrophysical Journal*, **524**, 262
- Malesani D., et al., 2004, *The Astrophysical Journal, Letters*, **609**, L5
- Malesani D., et al., 2009, GRB Coordinates Network, **9942**, 1
- Malesani D., et al., 2014, GRB Coordinates Network, **15800**, 1
- Malesani D., Kruehler T., Heintz K. E., Fynbo J. P. U., 2016, GRB Coordinates Network, **20180**, 1
- Mas-Hesse J. M., et al., 2003, *Astronomy & Astrophysics*, **411**, L261
- Mattox J. R., et al., 1996, *The Astrophysical Journal*, **461**, 396
- Mazzali P. A., et al., 2006, *Nature*, **442**, 1018
- Meegan C. A., et al., 1996, *The Astrophysical Journal, Supplement*, **106**, 65
- Meegan C., et al., 2009, *The Astrophysical Journal*, **702**, 791
- Mészáros P., 1998, in Meegan C. A., Preece R. D., Koshut T. M., eds, American Institute of Physics Conference Series Vol. 428, Gamma-Ray Bursts, 4th Hunstville Symposium. pp 647–656 ([arXiv:astro-ph/9711354](https://arxiv.org/abs/astro-ph/9711354)), doi:[10.1063/1.55394](https://doi.org/10.1063/1.55394)
- Mészáros P., 2002, *Annual Review of Astron and Astrophys*, **40**, 137
- Milne P. A., Cenko S. B., 2011, GRB Coordinates Network, **11708**, 1
- Milvang-Jensen B., et al., 2010, GRB Coordinates Network, **10876**, 1
- Moiseev A. A., Hartman R. C., Johnson T. E., Ormes J. F., Thompson D. J., 2005, International Cosmic Ray Conference, **5**, 419

- Narayana Bhat P., et al., 2016a, *The Astrophysical Journal*, **223**, 28
- Narayana Bhat P., et al., 2016b, *The Astrophysical Journal, Supplement*, **223**, 28
- Nava L., Ghirlanda G., Ghisellini G., 2009, in Meegan C., Kouveliotou C., Gehrels N., eds, American Institute of Physics Conference Series Vol. 1133, American Institute of Physics Conference Series. pp 350–355 ([arXiv:0902.1522](https://arxiv.org/abs/0902.1522)), doi:[10.1063/1.3155917](https://doi.org/10.1063/1.3155917)
- Niel M., Hurley K., Vedrenne G., Estkhulin I. V., Melioranskii A. S., 1976, *Astrophysics & Space Science*, **42**, 99
- Norris J. P., 2002, *The Astrophysical Journal*, **579**, 386
- Norris J. P., Bonnell J. T., 2006, *The Astrophysical Journal*, **643**, 266
- Norris J. P., Marani G. F., Bonnell J. T., 2000, *The Astrophysical Journal*, **534**, 248
- Nousek J. A., et al., 2006, *The Astrophysical Journal*, **642**, 389
- O'Meara J., Chen H.-W., Prochaska J. X., 2010, GRB Coordinates Network, [11089](#), 1
- Oesch P. A., et al., 2016, *The Astrophysical Journal*, **819**, 129
- Ohno M., Longo F., Arimoto M., Axelsson M., Dirirsa F., 2019, GRB Coordinates Network, [25244](#), 1
- Paciesas W. S., et al., 1999, *The Astrophysical Journal, Supplement*, **122**, 465
- Panaiteescu A., 2009, *Monthly Notices of the Royal Astronomical Society*, **393**, 1010
- Paul J., Wei J., Basa S., Zhang S.-N., 2011, *Comptes Rendus Physique*, **12**, 298
- Pelassa V., Preece R., Piron F., Omodei N., Guiriec S., 2010, arXiv e-prints, p. [arXiv:1002.2617](https://arxiv.org/abs/1002.2617)
- Perley D. A., et al., 2009, *The Astronomical Journal*, **138**, 1690
- Perley D. A., Cao Y., Cenko S. B., 2014, GRB Coordinates Network, [17228](#), 1
- Perley D. A., Hillenbrand L., Prochaska J. X., 2015, GRB Coordinates Network, [18487](#), 1
- Perlmutter S., Schmidt B. P., 2003, in Weiler K., ed., Lecture Notes in Physics, Berlin Springer Verlag Vol. 598, Supernovae and Gamma-Ray Bursters. pp 195–217 ([arXiv:astro-ph/0303428](https://arxiv.org/abs/astro-ph/0303428)), doi:[10.1007/3-540-45863-8_11](https://doi.org/10.1007/3-540-45863-8_11)
- Perlmutter S., et al., 1999, *The Astrophysical Journal*, **517**, 565
- Petrosian V., Kitanidis E., Kocevski D., 2015, *The Astrophysical Journal*, **806**, 44

BIBLIOGRAPHY

- Piran T., 1999, [Physics Reports](#), **314**, 575
- Piran T., 2002, [Science](#), **295**, 986
- Piranomonte S., Vergani S. D., Malesani D., Fynbo J. P. U., Wiersema K., Kaper L., 2011, GRB Coordinates Network, [12164](#), 1
- Piron F., 2016, [Comptes Rendus Physique](#), **17**, 617
- Pizzichini G., Ferrero P., Gianotti F., Morelli E., HETE Science Team 2004, Memorie della Societa Astronomica Italiana Supplementi, [5](#), 166
- Planck Collaboration et al., 2018, preprint, ([arXiv:1807.06209](#))
- Produit N., 2003, International Cosmic Ray Conference, [5](#), 2701
- Pugliese V., Xu D., Tanvir N. R., Wiersema K., Fynbo J. P. U., Milvang-Jensen B., D'Elia V., 2015, GRB Coordinates Network, [17672](#), 1
- Racusin J. L., Dirirsa F., Longo F., McEnery J., Vianello G., 2016, GRB Coordinates Network, [19802](#), 1
- Rau A., Kienlin A. V., Hurley K., Lichti G. G., 2005, [Astronomy & Astrophysics](#), **438**, 1175
- Rau A., McBreen S., Kruehler T., 2009, GRB Coordinates Network, [9353](#), 1
- Rau A., Kruehler T., Greiner J., 2013, GRB Coordinates Network, [15330](#), 1
- Read J. I., 2014, [Journal of Physics G Nuclear Physics](#), **41**, 063101
- Rees M. J., Meszaros P., 1992, [Monthly Notices of the Royal Astronomical Society](#), **258**, 41P
- Reichart D. E., Lamb D. Q., Fenimore E. E., Ramirez-Ruiz E., Cline T. L., Hurley K., 2001, [The Astrophysical Journal](#), **552**, 57
- Ricker G. R., et al., 2003, in Ricker G. R., Vanderspek R. K., eds, American Institute of Physics Conference Series Vol. 662, Gamma-Ray Burst and Afterglow Astronomy 2001: A Workshop Celebrating the First Year of the HETE Mission. pp 3–16, [doi:10.1063/1.1579291](#)
- Riess A. G., et al., 1998, [The Astronomical Journal](#), **116**, 1009
- Riess A. G., et al., 2018, [The Astrophysical Journal](#), **861**, 126
- Robert N., Jerry B., 2000, <https://apod.nasa.gov/apod/ap000702.html>
- Ruiz-Velasco A. E., et al., 2007, [The Astrophysical Journal](#), **669**, 1
- Ryde F., 1999, [Astrophysical Letters and Communications](#), **39**, 281

- Ryde F., 2004, *The Astrophysical Journal*, **614**, 827
- Salvaterra R., et al., 2012, *The Astrophysical Journal*, **749**, 68
- Sanchez-Ramirez R., Gorosabel J., de Ugarte Postigo A., Gonzalez Perez J. M., 2012, GRB Coordinates Network, [13723](#), 1
- Sanchez-Ramirez R., Gorosabel J., Castro-Tirado A. J., Cepa J., Gomez-Velarde G., 2013, GRB Coordinates Network, [14685](#), 1
- Schaefer B. E., Collazzi A. C., 2007, *The Astrophysical Journal Letters*, **656**, L53
- Schulze S., Wiersema K., Xu D., Fynbo J. P. U., 2014, GRB Coordinates Network, [15831](#), 1
- Singer L. P., et al., 2015, *The Astrophysical Journal*, **806**, 52
- Soderberg A. M., et al., 2006, *Nature*, **442**, 1014
- Sommer M., et al., 1994, *The Astrophysical Journal Letters*, **422**, L63
- Spearman C., 1904, *The American Journal of Psychology*, **15**, 72
- Spergel D. N., et al., 2003, *The Astrophysical Journal Supplement Series*, **148**, 175
- Stanek K. Z., et al., 2003, *The Astrophysical Journal Letters*, **591**, L17
- Suzuki N., et al., 2012, *The Astrophysical Journal*, **746**, 85
- Svinkin D. S., et al., 2016, *The Astrophysical Journal Supplement Series*, **224**, 10
- Swift-XRT 2018, http://www.swift.ac.uk/xrt_curves/
- Tanvir N. R., Ball J., 2012, GRB Coordinates Network, [13532](#), 1
- Tanvir N. R., et al., 2010a, GRB Coordinates Network, [11123](#), 1
- Tanvir N. R., Wiersema K., Levan A. J., 2010b, GRB Coordinates Network, [11230](#), 1
- Tanvir N. R., Wiersema K., Levan A. J., Cenko S. B., Geballe T., 2011, GRB Coordinates Network, [12225](#), 1
- Tanvir N. R., Wiersema K., Levan A. J., Fox D., Fruchter A., Krogsrud D., 2012a, GRB Coordinates Network, [13441](#), 1
- Tanvir N. R., Levan A. J., Matulonis T., 2012b, GRB Coordinates Network, [14009](#), 1
- Tanvir N. R., Levan A. J., Wiersema K., Petric A., Chiboucas K., Miller J., 2014, GRB Coordinates Network, [16150](#), 1

BIBLIOGRAPHY

- Tanvir N. R., et al., 2016, GRB Coordinates Network, [19419, 1](#)
- Tavani M., et al., 2006, in Society of Photo-Optical Instrumentation Engineers (SPIE) Conference Series. p. 626603, [doi:10.1117/12.673207](#)
- Tello J. C., Sanchez-Ramirez R., Gorosabel J., Castro-Tirado A. J., Rivero M. A., Gomez-Velarde G., Klotz A., 2012, GRB Coordinates Network, [13118, 1](#)
- Terekhov M. M., Aptekar R. L., Frederiks D. D., Golenetskii S. V., Il'Inskii V. N., Mazets E. P., 1998, in Meegan C. A., Preece R. D., Koshut T. M., eds, American Institute of Physics Conference Series Vol. 428, Gamma-Ray Bursts, 4th Hunstville Symposium. pp 894–898, [doi:10.1063/1.55416](#)
- Thompson D. J., et al., 1993, [The Astrophysical Journal, Supplement](#), **86**, 629
- Thompson D. J., Bertsch D. L., O'Neal Jr. R. H., 2005, [The Astrophysical Journal, Supplement](#), **157**, 324
- Thompson C., Meszaros P., Rees M. J., 2007, [The Astrophysical Journal](#), **666**, 1012
- Tierney D., et al., 2013, [Astronomy & Astrophysics](#), **550**, A102
- Tsutsui R., Nakamura T., Yonetoku D., Murakami T., Kodama Y., Takahashi K., 2009, [Journal of Cosmology and Astroparticle Physics](#), **8**, 015
- Tsvetkova A., et al., 2017, [The Astrophysical Journal](#), **850**, 161
- Tuell M. T., Martin H. M., Burge J. H., Gressler W. J., Zhao C., 2010, in Proceedings of SPIE. p. 77392V, [doi:10.1117/12.857358](#)
- Ubertini P., et al., 2003, [Astronomy & Astrophysics](#), **411**, L131
- Ukwatta T. N., et al., 2012, [Monthly Notices of the Royal Astronomical Society](#), **419**, 614
- Vedrenne G., et al., 2003, [Astronomy & Astrophysics](#), **411**, L63
- Vianello G., Omodei N., Fermi/LAT collaboration 2015, preprint, ([arXiv:1502.03122](#))
- Vianello G., Dirirsa F., Omodei N., Racusin J. L., Axelsson M., Kocevski D., 2016, GRB Coordinates Network, [19553, 1](#)
- Vreeswijk P. M., Thoene C. C., Malesani D., Fynbo J. P. U., Hjorth J., Jakobsson P., Tanvir N. R., Levan A. J., 2008, GRB Coordinates Network, [7601, 1](#)
- Wang J. S., Wang F. Y., Cheng K. S., Dai Z. G., 2016, [Astronomy & Astrophysics](#), **585**, A68
- Watson A. A., 2011, [Nuclear Physics B Proceedings Supplements](#), **212**, 13

- Wiersema K., Tanvir N. R., Cucchiara A., Levan A. J., Fox D., 2009, GRB Coordinates Network, [10263](#), 1
- Wilks S. S., 1938, *The Annals of Mathematical Statistics*, 9, 60
- Winkler C., et al., 2003, [Astronomy & Astrophysics](#), [411](#), L1
- Wood-Vasey W. M., et al., 2008, [The Astrophysical Journal](#), [689](#), 377
- Xu D., et al., 2009, GRB Coordinates Network, [10053](#), 1
- Xu D., Fynbo J. P. U., D'Elia V., Tanvir N. R., 2012, GRB Coordinates Network, [13460](#), 1
- Xu D., Malesani D., Tanvir N., Kruehler T., Fynbo J., 2013, GRB Coordinates Network, [15450](#), 1
- Xu D., Levan A. J., Fynbo J. P. U., Tanvir N. R., D'Elia V., Malesani D., 2014, GRB Coordinates Network, [16983](#), 1
- Xu D., Malesani D., Fynbo J. P. U., Tanvir N. R., Levan A. J., Perley D. A., 2016, GRB Coordinates Network, [19600](#), 1
- Yamaoka K., et al., 2009, *Publications of the Astronomical Society of Japan*, 61, S35
- Yamaoka K., et al., 2017, *Publications of the Astronomical Society of Japan*, 69, R2
- Yonetoku D., Murakami T., Nakamura T., Yamazaki R., Inoue A. K., Ioka K., 2004, [The Astrophysical Journal](#), [609](#), 935
- Yonetoku D., Murakami T., Tsutsui R., Nakamura T., Morihara Y., Takahashi K., 2010, *Publications of the Astronomical Society of Japan*, 62, 1495
- Yu H.-F., et al., 2016, [Astronomy & Astrophysics](#), [588](#), A135
- Zeh A., Klose S., Hartmann D. H., 2004, [The Astrophysical Journal](#), [609](#), 952
- Zhang B., Fan Y. Z., Dyks J., Kobayashi S., Mészáros P., Burrows D. N., Nousek J. A., Gehrels N., 2006, [The Astrophysical Journal](#), [642](#), 354
- Zhang F.-W., Shao L., Yan J.-Z., Wei D.-M., 2012a, [The Astrophysical Journal](#), [750](#), 88
- Zhang Z. B., Chen D. Y., Huang Y. F., 2012b, [The Astrophysical Journal](#), [755](#), 55
- Zhang B., Lü H.-J., Liang E.-W., 2016, [Space Science Reviews](#), [202](#), 3
- Zitouni H., Guessoum N., Azzam W. J., 2014, [Astrophysics and Space Science](#), [351](#), 267
- de Ugarte Postigo A., et al., 2006, [The Astrophysical Journal Letters](#), [648](#), L83

BIBLIOGRAPHY

- de Ugarte Postigo A., Castro-Tirado A. J., Tello J. C., Cabrera Lavers A., Reverte D., 2011, GRB Coordinates Network, [11993, 1](#)
- de Ugarte Postigo A., et al., 2013a, *Astronomy & Astrophysics*, **557**, L18
- de Ugarte Postigo A., Tanvir N., Sanchez-Ramirez R., Thoene C. C., Gorosabel J., Fynbo J. P. U., 2013b, GRB Coordinates Network, [14437, 1](#)
- de Ugarte Postigo A., Thoene C. C., Gorosabel J., Sanchez-Ramirez R., Fynbo J. P. U., Tanvir N. R., Cabrera-Lavers A., Garcia A., 2013c, GRB Coordinates Network, [15470, 1](#)
- de Ugarte Postigo A., et al., 2014a, GRB Coordinates Network, [16310, 1](#)
- de Ugarte Postigo A., et al., 2014b, GRB Coordinates Network, [16902, 1](#)
- de Ugarte Postigo A., Thoene C. C., Gorosabel J., Tanvir N., Fynbo J. P. U., Peshev P., Gomez Velarde G., Perez Valladares D., 2014c, GRB Coordinates Network, [17198, 1](#)
- de Ugarte Postigo A., Kruehler T., Flores H., Fynbo J. P. U., 2015a, GRB Coordinates Network, [17523, 1](#)
- de Ugarte Postigo A., et al., 2015b, GRB Coordinates Network, [17583, 1](#)
- de Ugarte Postigo A., Xu D., Malesani D., Tanvir N. R., 2015c, GRB Coordinates Network, [17822, 1](#)
- de Ugarte Postigo A., Thoene C., Izzo L., Kann D. A., Peshev P., Tejero A., 2016, GRB Coordinates Network, [20043, 1](#)
- de Ugarte Postigo A., Kann D. A., Thoene C. C., Izzo L., Tanvir N. R., Lombardi G., Marante A., 2017a, GRB Coordinates Network, [20990, 1](#)
- de Ugarte Postigo L., Izzo C., Thoene Z., Cano J. P. U., 2017b, GRB Coordinates Network, [21240, 1](#)
- de Ugarte Postigo A., Kann D. A., Izzo L., Thoene C. C., 2017c, GRB Coordinates Network, [21298, 1](#)
- de Ugarte Postigo A., Izzo L., Thoene C. C., Kann D. A., Heintz K. E., Castro-Rodriguez N., Marante A., 2017d, GRB Coordinates Network, [21799, 1](#)
- von Kienlin A., et al., 2014, *The Astrophysical Journal Supplement Series*, **211**, 13